APPLICATION OF SCATTERING MODELS TO OPTICAL SURFACE INSPECTION

Author: COLIN D OBRAY

A thesis presented in the Department of Systems Science, The City University, for the Degree of Doctor of Philosophy.

February 1983

Poor quality print in original

PAGE NUMBERS ARE CUT OFF IN THE ORIGINAL

CONTENTS

ILLUSTRATIONS

CHAPTER 2

CHAPTER 4

CHAPTER 7

ACKNOWLEDGEMENTS

I am indebted to Professor L Finkelstein of the Department of Physics of City University, for not only directing the study, but also for his continual promptings and patience during the completion of this thesis.

I also acknowledge my debt to [redacted], formerly of the Department of Systems Science of City University during the initial supervision of the project.

Due recognition must also be given to the SIRA Institute and to the British Steel Corporation, for their collaborative assistance and support throughout this, and related projects.

My thanks also extend to a number of workers of the Systems Science Department, too numerous to mention individually, and to several colleagues at Lanchester Polytechnic, in particular to [redacted] and [redacted], for use of their profile analysis and plotting facilities.

Last, but not least, I would like to thank [redacted] for coping so well with a difficult, and at times ambiguous manuscript.

DECLARATION

I grant powers of discretion to the City University Librarian to allow this thesis to be copied in whole or in part without further reference to me. This permission covers only single copies made for study purposes, subject to normal conditions of acknowledgement.

ABSTRACT

For some time optical scanning devices have been employed to automatically inspect sheet surface material, frequently operating in wholly or semi-empirical fashion.

Geometrical and physical optics give rise to a MIRROR FACET MODEL and a KIRCHHOFF WAVE THEORY MODEL of light scattering from a rough surface, respectively. The two models represent transfer functions of surface topography into polar diagram description of light scatter.

Polar diagram predictions, under the mirror facet and wave theory régimes, have been formulated on the basis of a variety of periodic and random surfaces, and hence compared and constrasted.

A moving sensor rig, operating under computer control, automatically recorded the intensity of the back scattered field from metal specimens, arising from an incident laser beam. Subsequently an appropriate region of the surface specimens was mapped, using a talysurf-10 stylus instrument and logged as a series of parallel profiles.

On the basis of these data the predictive powers of the two models were examined.

For the order of surface roughness examined (0.05 μm ∿ 0.5 μm) there was considerable evidence of a dominant geometrical component of light scattering, although the facet model could not be substantiated directly due to metrological difficulties associated with the computation of slope statistics. The two-dimensional Kirchhoff model, based on area information, however, was validated, and in some circumstances the one-dimensional Kirchhoff model, derived on a single surface profile, provided valuable

predictive information on surface defects.

Studies into the statistical distributions of light scatter, relevant to applications of instrument design, surface flaw detection and surface texture parameter estimation were conducted.

Utilising the compiled data bases, the project reports simple robust procedures for extracting surface information in real time, by a non-destructive, non-contacting method employing modest technology.

CHAPTER 1

INTRODUCTION

The Instrument Systems Centre at City University, working in collaboration with a number of other bodies, is investigating automatic inspection techniques for monitoring industrial processes. One particular application being studied is the automatic inspection of continuously moving surfaces, such as steel sheet from a rolling mill. At first, interest mainly concerned the detection, delineation and classification of surface flaws, but latterly much attention has centred upon surface texture specification, measurement and control.

Optical scanning systems, whereby the surface material is systematically scanned by an interrogating laser beam, are attractive for a variety of reasons (fully catalogued in Chapter 2 : The Inspection Problem). The SIRA Institute has developed a scanning system for the automatic detection of surface defects. The data gathering system carries much unutilised surface texture information. A key objective of the thesis was to determine the exact nature of this surface texture information, to process and quantify it as an integral part of an on-line quality assessment and control system. (The industrial background of the study is set out in full in Chapter 2.)

A necessary step in this process was to investigate the physics of the laser beam/surface texture interaction. The interaction was modelled by two theoretically distinct mechanisms : (i) a simple ray theory of scattering and (ii) a complex wave theory of electromagnetic scattering.

One aim of the study was to investigate both theories with the objective of determining to what extent they explain observed and measured scattering phenomena, and provide a basis for on-line surface roughness assessment algorithms. Both models are formally introduced in Chapter 4, and their validation is discussed in Chapter 7. The models are not novel but have not been formally validated, largely because of problems of excessive data gathering, especially with regard to mapping a region of specimen surface material. A by-product of the work has been to establish a semi-automatic, computer-aided approach to the data acquistion of scattered laser beam intensity information, and digitised surface roughness topography measurement. These procedures are fully described and documented in Chapter 5.

Chapter 6 is devoted to the presentation and some statistical analysis of these data. The data is pictorially displayed in a variety of ways: one and two-dimensional plots of laser scans, isometric and contour maps of surface topography, originally preserved on microfilm and subsequently copied for inclusion within the text.

Intensity scatter distributions are the subject of Chapter 8.

The design of the data gathering system of optical scanning devises is basically of one of two types:-

type (i) : one or several fixed transducers which monitor the varying reflected intensity field as the subject surface material is physically moved beneath its or their field of view,

type (ii) : a scanning sensor which scans the intensity field reflected from stationary or moving subject material.

Both types of system have been studied and a number of results and effects have demanded attention. Were the effects real phenomena of the laser/rough surface interaction or an apparent phenomena, that is to say a consequence of some design feature of the instrument? The scatter distributions, as monitored by both moving and stationary scanners, are investigated with the specific aim of resolving such issues and harnessing such acquired knowledge to the applications of instrument design, defect detection and surface texture definition.

These applications are given due coverage in Chapter 9, although where there is a lack of concrete data (for instance when the problem has been raised by a colleague), of necessity the application methods are only outlined.

A prior discussion which puts the work of the thesis in context and gives the hitherto state of the art, is described in Chapter 3 in the form of a review of optical methods of surface inspection. In view of the particular industrial application of interest to us, greatest attention is given to methods capable of investigating the dynamic problem of moving steel sheet. Methods of tackling the static problem, interferomic methods of examining specimens in situ for example, are only touched upon.

The main conclusions arising from the investigation are reported in full in Chapter 10. However they may be summarised briefly as follows:

(1) The Kirchhoff wave theory model of light scattering has been validated for a variety of metal surfaces - copper, brass, steel, surfaces all of the order of 0.1-0.5μm RMS roughness height.

(2) The electrical properties of the surfaces need not be included in the mode, since a model based on the assumption of perfect conductivity proved more than adequate.

(3) For surfaces of the above order of (Type (C)) roughness, scattering is believed to be largely geometric, although the simple facet model itself proved an inadequate predictor.

(4) In the case of isotropic surface material, light scattering was demonstrated to be an area property and the one-dimensional Kirchhoff model was deficient. In view of (3), the two-dimensional Kirchhoff model alone has the required transfer function to convert input surface topography into a realistic output intensity scattering distribution.

(5) For smoother, Type (B) surfaces, the Kirchhoff model could not give a point-by-point fit, although the scattered field is still capable of explanation in terms of the surface statistics.

(6) The project has reaffirmed the ability to extract surface parameters from light scattered data, and has allowed for more robust algorithms to be implemented.

(7) The theory of scattering for non-Gaussian surface has been extended to cover the case of Poisson distributed surface heights amongst others.

(8) Applications in the area of defect detection have been furthered by suggesting distribution-based methods of thresholding, and in the application of scattering models to problems of defect recognition. The feasibility of using polar diagram information has been demonstrated in the course of studying scratch and indentation defects. Despite theoretical reservations, the prediction models show some potential for investigating defect features. The indication is that this potential is limited at present by the quality of the surface topography data base.

CHAPTER 2

THE INSPECTION PROBLEM

Abstract

The development of modern technologies has demanded improved control of surface texture of industrial components, arising principally out of a realisation that improvement in surface finish leads to increased performance and/or increased life.

How should we in fact determine surface properties be they phsio-chemical or topographic? Direct methods, whereby we measure the characteristic directly, may have serious disadvantages. For instance the action of a stylus on a fine surface impairs the surface finish. In such situations it is desirable to resort to the subterfuge of indirect methods, whereby for example an energy stream is projected at the surface, and the interaction of the steam with the surface is observed. Interpretation of the output in terms of surface properties closes the loop.

Optical scanning systems is one such class of indirect method with proven industrial capability.

2.1 The Need for Surface Inspection

In the steel industry a fundamental quality control task is the detection of defects. Plainly scratches, gorges, dents, rust spots, etc. could render a particular sheet unfit for a particular function. For example, certain gross surface flaws persist and show through paint finishes and a particular sheet having such flaws would be unacceptable to the car body industry. The same sheet however might be suitable for a washing machine

pressing.

The influence of surface finish on the ability of a component to function satisfactorily is still improperly understood in many areas of application. Functional properties such as fatigue resistance, load-carrying capacity, resistance to wear or corrosion etc. depend critically upon material properties such as hardness, reaction to heat etc., in addition to topographic properties. However with increased understanding of the influence of surface roughness on functioning, there has consequently developed a desire to specify surface finish more closely.

For example, in order to moderate or avoid contact with surfaces, lubrication is of prime importance. The ability of a surface to hold a lubricating film and to channel and distribute the film into the high pressure areas during a press forming operation say, is very much dependent on the surface texture. In this application too smooth a surface finish results in scoring during press working.

Again we may wish to mask irrelevant surface blemishes or to enhance the acceptance of a lacquer with a matt surface texture. In many applications we wish to improve the surface finish: to reduce friction or wear in contact, to inhibit corrosion, etc. At all events we need to control surface texture which necessitates careful monitoring of surface material in production.

2.2 Surface Assessment: Requirements and Methods

Assured of a general need for surface inspection, we must specify the industrial requirements more closely and consider which inspection techniques are appropriate to

those requirements.

Plainly we must detect surface flaws and classify them. Detection alone is not enough, since certain flaws are acceptable for some functions but not for others. Inspection of unacceptable flaws must be 100%; that is to say the whole of the surface material must be scruitinised. A practical consequence of 100% inspection in real time is that the inspection system must be automatic.

In general, surface flaws are manifest as gross deviations from mean surface material. Rust spots, surface pitting of intercrystalline corrosion, mechanical handling defects dents, scratches, gouges, etc. would be accompanied by macro changes in the surface topography. However, there are also low contrast troublesome defects such as "sticker-end-wrench" whose superimposed mechanical profile properties are of the order of the micro mechanical structure. To resolve such defects as this we would need to focus part of any interrogating system upon the micro-structure, since it is not solely gross surface flaws which impinge upon the functional properties of a surface.

As we have already indicated, surface texture as a whole needs to be considered and closely controlled for many areas of application. In fact 100% inspection of surface texture is often required since inconsistency of texture creates problems in fabrication for instance. Press rigs can be set up to accommodate coarsely textured surfaces but difficulties arise if a surface has a wide range of texture, since set-up conditions may not be adjusted in the course of a production run. Large

variability in material or lubrication frequently leads to difficulties in production control and a large scrap rate.

We may summarise our remarks as follows:
The requirements of a surface inspection scheme are that

(i) there should be 100% inspection conducted in real time,

(ii) the system should have the ability to sense those surface properties which relate to functional properties,

(iii) the inspection process should in no way degrade the surface.

Concomitant benefits of such an automatic scheme is the facility for continuous feed-back control of the production process, the objectivity of assessment and the means of providing a guarantee of the functional capability of surfaces.

The methods available for measuring surface finish are comparative or by direct measurement. Indirect methods are attempts to assess the surface texture by observation or feel of the surface and include optical, capacitance and pneumatic methods. Direct methods enable a numerical value to be placed on the surface finish and include stylus probe techniques and interferomic methods.

On-line inspection of fast moving surfaces meeting requirements (i) and (iii) dictates that some form of optical scanning device be used.

Requirement (ii) is an open question, since for many applications it is obscure which surface parameters affect functional performance. The transfer behaviour of optical instruments with regard to surface topography is

a subject of this investigation. We should note in passing that a stylus probe instrument, usually taken as a reference device, also has a transfer behaviour since the output is filtered by the stylus point and we should question therefore the wavelengths that a stylus can sense. The radius of a stylus tip is usually about 2.5 μm, whereas optical methods could be thought to have an equivalent stylus radius related to the wavelength of the incident light.

A simplified systems engineering approach to the overall problem is detailed in figure 2.2.1 below:

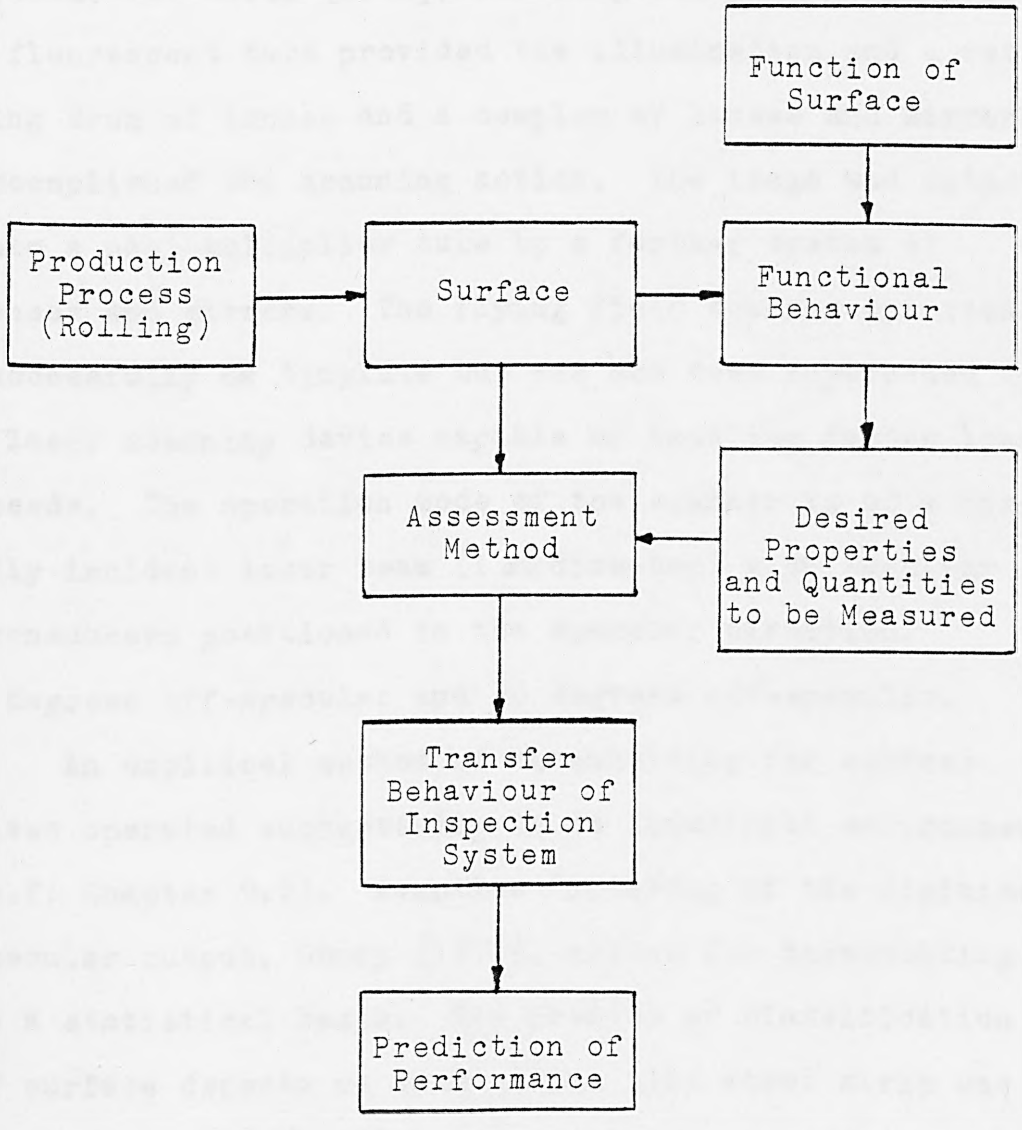

FIG. 2.2.1. Schematic Diagram of Surface Assessment

2.3 Optical Scanning Devices

The elements of an optical scanning system are basically (i) a controlled source of illumination, (ii) a set of light sensitive transducers and (iii) a computer interface for interpretation of the transducer outputs. The usual procedure is that the surface material moves continuously beneath a light source whose collimated beam scans the width of the material. Light back scattered from the surface falls within the field of view of fixed sensors.

The SIRA Institute developed a flying field scanner system, see Brook [1971], for inspecting sheet material. A fluorescent tube provided the illumination and a rotating drum of lenses and a complex of lenses and mirrors accomplished the scanning action. The image was output onto a photomultiplier tube by a further system of lenses and mirrors. The flying field scanner operated successfully on tinplate but has now been superseded by a laser scanning device capable of handling faster line speeds. The operation mode of the scanner is of a normally incident laser beam (1 mm diameter) with receiver transducers positioned in the specular direction, 5 degrees off-specular and 30 degrees off-specular.

An empirical method of thresholding for surface flaws operated successfully in an industrial environment (c.f. Chapter 9.2). Adaptive filtering of the digitised specular output, Obray [1973], allows for thresholding on a statistical basis. The problem of classification of surface defects on cold-rolled mild steel strip was tackled by Hill [1977]. Defect classes were drawn up in discussion with industrial users. Hill's approach was to

monitor the delineation, shape and depth of defect signal on an optical scan using a matched filter bank, complemented by defect trigger records of successive scans. The signal processing involved is not inconsiderable but high contrast gross defects were well differentiated. However some low contrast defects were not resolved.

Formulating the output from the three SIRA sensors as a vector signal $\underline{V}$ of dimension three, and utilising the dispersion matrix of $\underline{V}$, Norton-Wayne [1982], constructed a weighting function of its elements to maximise the contrast of a particularly troublesome low constrast defect namely 'sticker-end-wrench'. With this algorithm 'sticker-end-wrench' could be successfully detected.

2.4 Conclusion

The requirement of real-time inspection of fast moving surfaces coupled with the advantages of non-contacting methods has motivated research into optical scanning devices. Previous work, carried out by the SIRA institute and the Department of Systems Science at the City University has endorsed the feasibility of such devices on-line, and has indicated the power of polar diagram information in defect classification. Their work further fostered the belief that complete polar diagram information would be invaluable.

CHAPTER 3

REVIEW OF LITERATURE ON THE INTERACTION OF LIGHT WITH ROUGH SURFACES AND OPTICAL METHODS OF INSPECTION

Abstract

Mindful of the advantages of non-contacting and non-destructive testing methods, we review the available literature on the interaction of light with rough surfaces and optical methods of surface inspection. Incidentally, Welford [1977] provides an excellent overview of the subject.

Source papers covering the theoretical background physics of the problem are reviewed as well as the literature concerned with applications. The majority of papers dealing with applications are addressed to the problem of surface roughness assessment and in many cases are aimed at providing an optical alternative to the talysurf. The problem of defect detection and classification does not figure so prominantly in the literature but some important contributions to this field are noted.

3.1 Theoretical

Twersky [1957], Ament [1956], Beckmann [1957], Du Castel and Spizzichino [1962] and others developed scattering theories on the basis of various model surfaces. Twersky's concept of a rough surface was that of a regular or irregular distribution of protuberances on a perfectly conducting plane; Ament's consisted of randomly spaced half-planes, whilst Beckmann described a half-plane facet model by a Markov chain. Du Castel and Spizzichino's surface has a number of brilliant points/unit area from which originated the scattered field. The ideas

elucidated in these early papers are relevant to both a facet view of scattering as well as to a wave theory approach,although the model surfaces in most cases are unrealistic.

Beckmann [1963] developed a theory appropriate to laser light for both strong and weak scatters and is recalled in some detail in Chapter 4: the average properties of the far field distribution are calculated on the basis of a Gaussian rough surface and that the Kirchhoff approximation, namely that the field at any point of the surface is approximately the field that would be present on the tangent plane at that point, is valid. Our interest is primarily concerned with reflected light, but in passing we note that Chandley and Welford [1975] reformulated Beckmann's results to accommodate transmissive scattering by transparent surfaces such as ground glass.

The Beckmann theory also described the nature of the distribution of the far field random component about the ensemble average (deterministic component). If the phase distribution of wavelets arising from the surface is uniform, the amplitude of the scattered field has a Rayleigh probability density. In Appendix 8B, the associated field intensity distribution is shown to be negative exponential (although this result may also be found in Dainty [1970]). Incoherent phase conditions are met in the case of very rough surfaces. The random component is given the term speckle and averaging measurements obtained with coherent light effectively removes speckle effects which carry little relevant information about the surface.

Beckmann [1963] exhausted the case of scattering from a Gaussian height surface with a Gaussian auto-correlation function of surface heights. He extended this in Beckmann [1973] to cover the case of scattering from a surface possessing a negative exponential height distribution, whilst retaining a Gaussian auto-correlation function of surface heights. (In Chapter 8 scattering from a surface exclusively defined by negative exponential functions is considered and the theory of scattering from non-Gaussian surfaces is further developed by considering the case of surface with a gamma height distribution.) Negative exponential and Lorentzian auto-correlation functions, in conjuction with Gaussian first order statistics, have been used by Chandley [1976].

Results for strong scatters are given a comprehensive treatment in Chapter 8 and have been explored by other authors (e.g. Miller et al [1975]). Miller's treatment introduces a correlation function of the phase of the scattered light and calculates the intensity of the speckle pattern in the far and near fields.

Several researchers have investigated further the theory of speckle: Jakemann and Pusey [1973a], [1973b], [1975], Escamilla [1978], Hariharan [1977], Ross and Fiddy [1978], Pederson [1976], etc. In the Miller theory it was assumed that there were many scattering centres in the illuminated area which allowed the central limit theorem of statistical theory to be invoked. Jakeman and Pusey, Escamilla extend speckle theory when this is not the case. Both the Beckmann and Miller approaches for strongly scattering surfaces, lead to the classical result for far-field speckle patterns (sometimes referred to as

the spatial speckle correlation function) of Gaussian statistics of complex amplitude. Jakemann and Pusey show that the far-field no longer exhibits Gaussian statistics if there are few scattering centres in the illuminated area. Ross and Fiddy argue that the classical theory which leads to the negative exponential distribution for speckle intensity is in fact a limiting case, which although may be an adequate approximation in many cases, does not describe speckle patterns in general. In Chapter 8 we report measurements taken at SIRA on cold rolled steel strip which demonstrate negative exponential statistics, although experimental verification of first and second order speckle pattern statistics was confirmed in McKechnie [1974]. The usual description of intensity distributions relate to the intensity at a point, as distinct from the laser speckle measured with a finite aperture. Assuming Gaussian models for both the far field spatial speckle correlation function and for the spatial profile of the detector, Stansberg [1981b], shows that a Gamma distribution describes the speckle intensity for a one-dimensional (slit) aperture. Pederson investigated speckle intensity variance arising from various model surfaces which suggested limitations as to its usefulness in surface roughness studies. However if partially coherent illumination is utilised useful information is carried in the speckle statistics (see Stansberg [1981a] for example).

For laser light the speckle contrast defined as σ_I/μ_I, the ratio of the standard deviation to the mean of the speckle intensity, is unity as prescribed by the negative exponential distribution. If a surface is

simultaneously illuminated by two monochromatic sources of wavelengths λ and $\lambda + \delta\lambda$ say, then for small $\delta\lambda$ the two speckle patterns have a non-zero correlation. The dependence of the far-field speckle correlation on surface roughness was first discussed by Goodman [1963] and later investigated by Parry [1975]. The speckle contrast falls from unity with increasing surface height variance, consistent with experimental results reported by Sprague [1972].

We note in passing that the speckle contrast, σ_I/μ_I for a gamma distribution

$$\frac{1}{b}\left(\frac{I}{b}\right)^{\beta-1} \exp\left(-\frac{I}{b}\right) \Big/ \Gamma(\beta) \quad , \quad I > 0$$

is $1/\sqrt{\beta} < 1$, for $\beta > 1$.

The reduction of speckle contrast as we decrease the coherence of the incident beam is as expected. If a surface is illuminated with incoherent light then the speckle phenomenon disappears entirely, and the variation in the far-field is due to surface noise. The series of SIRA measurements showed a reduction in the speckle contrast by a factor of 2 if incoherent illumination was used instead of coherent illumination. Welford [1977] presents an approximate theory for partially coherent beam scatter.

The variation of speckle contrast was studied from a theoretical viewpoint by Esamilla [1978] to explain experimental work by Fujii and Asakura [1977] which showed that speckle contrast increases when the radius of the focused laser beam is reduced. A maximum contrast is reached when

the spot radius is approximately equal to the correlation length of surface heights, whereupon the contrast starts to decrease. Chandley and Escamilla [1979], report speckle contrast measurements for a wide range of scatterers. The indication from their work is that for a fixed correlation length, the maximum contrast appears at progressively smaller values of the spot radius, as the standard deviation of surface roughness heights increases.

The partial depolarisation of a polarised incident laser beam by a rough surface also reduces speckle contrast as shown by Hariharan [1977].

We note finally Leader's [1971] contribution to the theory of scattering from surfaces of finite conductivity, which represents a more rigourous treatment than Beckmann's original work. In subsequent papers [1976], [1979], Leader develops a theory to investigate surfaces described by a two-scale roughness model and predicts the mutual coherence function for typical surface parameters.

3.2 Optical Estimation of Surface Roughness

A number of instruments (Glossmeters) measure in one or two fixed directions and relate these measurements empirically to surface roughness. An early attempt to relate light measurements to surface roughness on a theoretical basis was by Bennett and Porteous [1961]. They used infra-red radiation to cope with strong scatters as indeed did Thwaite [1982] some twenty years later. Their measurements of the RMS height (σ) agreed with those obtained from stylus profiles within a factor of 2. (c.f. Chapter 7).

More recently, Mundy and Porter [1981] use the half-power point for estimating the mean surface roughness

slope (σ/T) (c.f. Chapter 9.3). Their methodology is based on several unstated assumptions, namely a strongly scattering Gaussian surface.

Berny [1976] studied weak scatters and drew on Beckmann's results to obtain estimates of σ and correlation length (T). Composite model surfaces which included a periodic component were also studied. The paper also describes an optical profilometer with a spot size of less than 1 μm with which to sense the surface. The specular intensity of the reflected beam from a specimen, was normalised with respect to that using a near optical flat of the same material and reflectance. Berny's work echoes that of Hildebrand et al [1973] both in concept and instrumentation.

A recent paper by Milana and Rasello [1981] presented an optical method for on-line evaluation of machined surfaces. Again measurements were normalised with respect to a standard surface of the same surface material, with known RMS roughness, σ_r, and correlation, T_r. The underlying theory was the one-dimensional Beckmann theory applied to grooved periodic surfaces with a superimposed random component. Estimation of the RMS height was via a calibration curve.

Chandley [1976a] measured the central specular peak arising from ground glass material of 0.1 - 1 μm roughness. He used wide angle illumination $\theta_1 = \theta_2 \sim 80$ degrees to derive an estimate of σ, which compared well with stylus measurements, and also sensed the off-specular region to obtain an estimate of T. In a subsequent paper Chandley [1976b] estimated the autocorrelation of surface heights. As in our studies, Chandley found that the Gaussian auto-

correlation model was inappropriate, but obtained good agreement between his derived function and that obtained using stylus profiles. See also Elson and Bennett [1979] for a similar treatise.

Tanner [1976a], [1976b] investigated lapped and ground mild steel surfaces. The surface height distributions of his specimens were significantly non-Gaussian, and his paper includes a theoretical model to account for such distributions.

Many researchers have investigated the contrast of far field speckle : Fujii et al [1976], Fujii and Lit [1978], Leger et al [1975], Bitz [1978], Stansberg [1981a], etc. Fujii et al [1976] measured the contrast of the far field as a function of the surface roughness and the illuminated area, and in a subsequent paper measured surface roughness from dichromatic speckle patterns. Leger et al and Bitz investigations are suitable for on-line measurement of σ since they employed coherent light. Both studied the correlation between two speckle patterns due to two different angles of incident laser light. The supporting theory was based on Gaussian surfaces. Stansberg [1981a] used the fact that the correlation between two speckle patterns of different wavelengths of incident light are equally dependent on the RMS roughness, and except for some high contrast values achieved fair agreement with theory.

The potential to extend the range of surface height measurement using a suitable bandwidth of polychromatic light was exploited by Parry [1974]. The qualitative validation of theory contained in this paper was later augmented in Parry [1975], in his studies of ground glass

under multiline laser illumination. Fair agreement between measurements of first order speckle statistics and talysurf profile statistics was achieved.

Interferomic and light scattering results for the surface spectral density function (SDF) were compared by Stover [1975], whereas Thwaite [1982] compared the SDF obtained by optical Fourier transforms with calculations from profile measurements. The use of a linear diode array transducer set-up, and infra red incident radiation, to increase the sensitivity range to surface roughness, were features of Thwaite's experiments.

A means of estimating the surface profile by comparing the phase change between a surface reflected laser beam and reference beam was devised by Smolka and Candell [1978]. The two beams were scanned by a photodetector by a rotating beam splitter. Smolka and Candell conclude that the instrument is suitable for large scale rough surfaces of the order 1-50 μm, and describe their methodology as falling between the more elaborate interferomic schemes and mechanical contact schemes.

3.3 Defect Detection and Classification

An analysis of surface flaw detection is given by Sawatari [1971]. He used an oblique illumination technique, and after filtering out the specular reflection component, examined the scattered light to detect surface flaws (c.f. Chapter 9.2).

The theory of Beckmann, modified by a notational change introduced by Horn [1975], has been used by Mundy [1979] to provide an image analysis method of computer modelling of a metal surface, and for detecting surface defects. A scattering ratio, S, was defined as the natural

logarithm of the ratio of the scattered intensity at grazing and normal incidences as the discriminant function. Mundy's results showed that S provided good contrast to defects.

His methodology was pursued in a paper with Porter, namely Porter and Mundy [1981], where they considered in particular the detection of a scratch on a metal surface. The observation angle was taken along the direction of the incident light whilst the specimen was rotated through 5 degree increments and the image intensity was recorded at each stage. The scratch roughness can be related to plate roughness by determining the angle of incidence for which the contrast is zero.

Mundy's technique is not suitable for on-line defect measurement and neither is Berny's [1976] device, which in addition to measuring surface roughness is reportedly able to measure the width and depth of surface defects. Berny's instrument is described as being capable of giving quick qualitative examinations in series production.

The work at City University, on defect detection and classification algorithms, on data obtained by the SIRA laser scanner for on-line use has been reviewed in Chapter 2.3 and will not be reiterated here.

CHAPTER 4

MATHEMATICAL MODELS OF ELECTROMAGNETIC SCATTERING

Abstract

Two mathematical models of electromagnetic scattering are postulated:

(1) A simple ray theory model in which the reflecting surface is thought of as a composite of optically perfect mirror facets, scattering incident rays according to the elementary law of physics - "angle of reflection equals angle of incidence".

(2) A wave theory model in which the wave nature of the incident radiation, together with the electrical properties of the metal surface and the consequent interaction, are taken into account.

Here a detailed description of the models is given, sufficient for their prediction of the back scattered field from a metal surface. Comparisons between the two models are drawn on the basis of predicted polar diagrams obtainable from deterministic and stochastic profile surfaces.

When the mechanical roughness structure is large compared with the wave-length of light, ($\lambda << \Lambda$, in the case of deterministic, periodic profiles, $g >> 1 (\Rightarrow \lambda < \sigma)$ for stochastic profiles), the models converge in some measure. The ordered phase characteristics of periodic profiles however, ensures only partial convergence in respect of preferred directions of scatter. For very rough random surfaces, the scattered field is incoherent and is modelled purely by the probability density function of profile slopes, and the two scattering models are equivalent. An elegant proof based on the inversion theorem

of characteristic functions is detailed.

4.1 The Mirror Facet Model

4.1.1 The Mirror Facet Concept of a Rough Surface

A surface can be conceived as a composition of plane elementary facets, randomly orientated in space. The facet shape need not be precisely defined except that it will, of necessity, be polygonal, due to the planar requirement. Each facet furthermore, functions as an ideal mirror, reflecting a ray pencil of light according to the well-known law: that angle of reflection equals the angle of incidence.

We first of all focus our attention upon the simple ray theory approach and the so-called MIRROR FACET model.

In this approach, the total scattered field is the aggregate of n elementary rays scattered from n individual facets. The wave nature of the incident radiation is ignored so that each ray does not possess a phase characteristic. There is, consequently, no mutual interference of individual (waves) rays, and reflected rays simply reinforce one another. Additionally, the total scattered field is not considered to be a vector field: the intensity of the field scattered in a given direction is proportional to the number of rays reflected in that direction, and does not include resolved components in that direction of otherwise reflected rays. The distribution of the scattered radiation is thus effectively a scalar rather than a vector field. The most elementary rough surface facet model is a 2-dimensional profile of plane facets:

Such a profile is defined mathematically by regularly spaced ordinates, and the simple geometrical laws of reflection provide an easy algorithm for computing those rays falling within a one degree (or finer) receiver angle. Rays which are reflected downwards into the metal surface are "lost", whilst rays which suffer a secondary reflection are "hidden" from the sensor and subsequently ignored.

A natural extension to a 3-dimensional surface, an important progression if less rigidly anisotropic surfaces are to be modelled, is a 3-dimensional "grid" array of plane mirror facets:

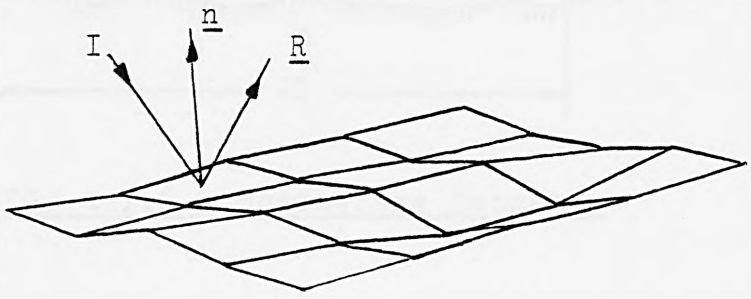

FIG. 4.1.1. Facet Scattering

Surface definition consists of a series of parallel profile ordinate data. Computation of the scattered field is again relatively straightforward apart from determining those rays which have secondary reflections.

Before discussing the wave characteristics of light and the formulation of an alternative model of light scattering, the surface roughness statistics immediately accessible from the mirror facet model are outlined. This affords a convenient opportunity

to introduce the scattering geometry, and to formulate many of the geometrical relationships associated with algorithms pertaining to simple ray scattering theory.

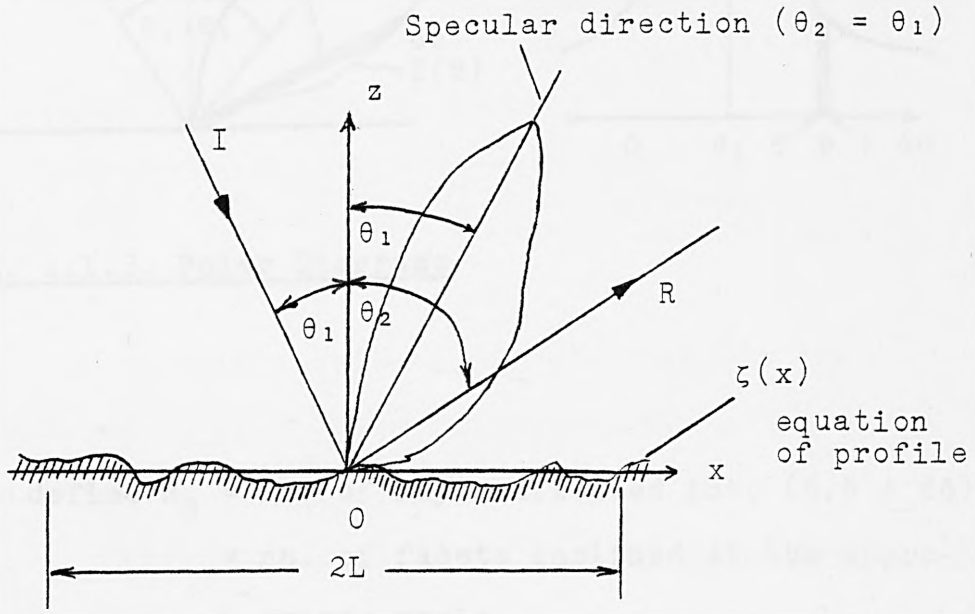

FIG. 4.1.2. Scattering Geometry

θ_1 = angle of incidence of laser beam ;
beam has wavelength λ (= 0.628 μm) ;
laser spot typically, 2 mm in diameter,
illuminates a portion of surface (-L,L);
θ_2 = angle of observation.

4.1.2. One-Dimensional Profile Facet Model Reflection

Consider the plane polar diagram of the scattering of incident light, I,into reflection angles θ:

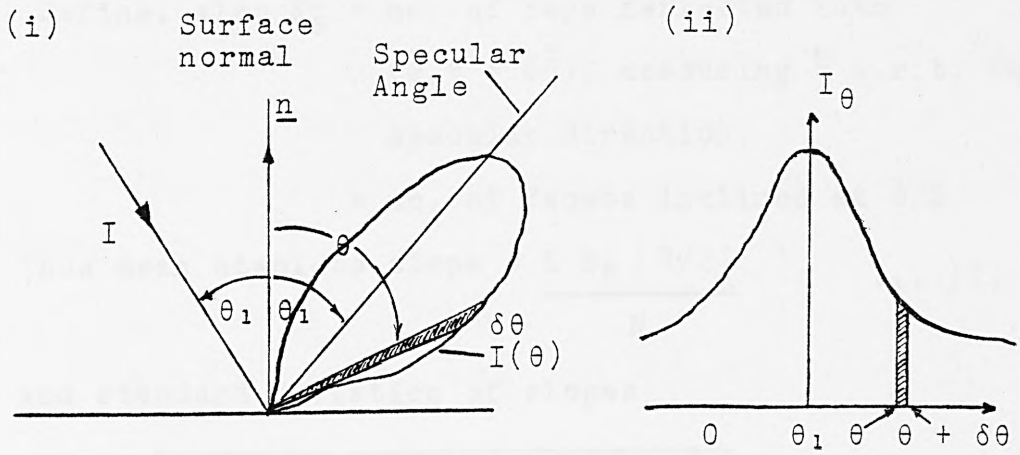

FIG. 4.1.3. Polar Diagrams

Here, define N_θ = no. of rays reflected into $(\theta, \theta + \delta\theta)$
= no. of facets inclined at the appropriate angle.

Consider also scattering of the incident ray, I, by a typical facet inclined at $\tilde{\theta}/2$ to the mean plane. The reflected ray, R, is reflected at angle $\tilde{\theta}$ with respect to the specular direction, as shown in Fig. 4.1.4 (i) and (ii) below:

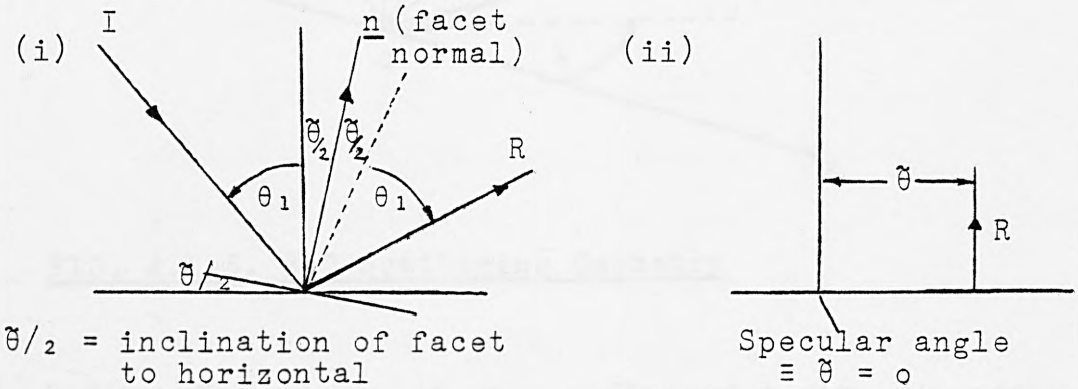

FIG. 4.1.4. Facet Scattering

Define, also $N_{\tilde{\theta}}$ = no. of rays reflected into $(\tilde{\theta}, \tilde{\theta} + \delta\tilde{\theta})$, measuring $\tilde{\theta}$ w.r.t. the specular direction.

= no. of facets inclined at $\tilde{\theta}/2$

Thus mean absolute slope $= \dfrac{\Sigma\, N_{\tilde{\theta}}\, |\,\tilde{\theta}/2|}{N}$ ....(1)

and standard deviation of slopes

$$= \sqrt{\frac{1}{N-1}\left\{\Sigma\,(N_{\tilde{\theta}}\,\tilde{\theta}/2)^2 - (\Sigma\, N_{\tilde{\theta}}\,\tilde{\theta}/2)^2/N\right\}} \quad \text{where} \quad \text{....(2)}$$

$N = \Sigma\, N_{\tilde{\theta}}$

A three-dimensional surface analysis can be formulated to provide corresponding surface slope statistics.

4.1.3. Two-Dimensional Surface Facet Model Reflection

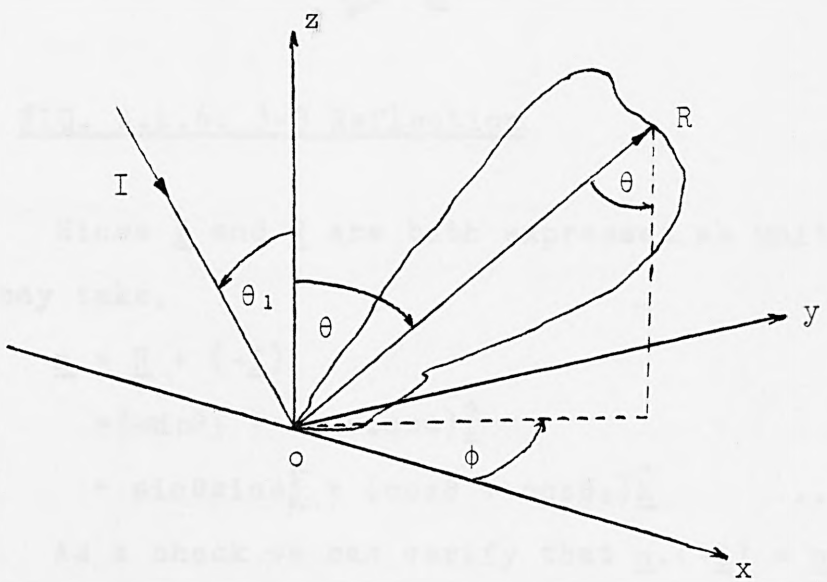

FIG. 4.1.5. 3-D Scattering Geometry

Define, $N_{\theta,\phi}$ = no. of rays reflected in the direction $(\theta \to \theta + \delta\theta,\ \phi \to \phi + \delta\phi)$

= no. of plane facets inclined at the appropriate angle.

Because of the additional complexity, it is best to adopt a vector analysis approach, in order to determine the distribution of facet slopes.

With respect to the above system of co-ordinate axes,

$$\underline{I} = \sin\theta_1\hat{\underline{i}} - \cos\theta_1\hat{\underline{k}} \qquad \ldots.(3)$$

$$\underline{R} = \sin\theta\cos\phi\hat{\underline{i}} + \sin\theta\sin\phi\hat{\underline{j}} + \cos\theta\hat{\underline{k}} \qquad \ldots.(4)$$

A normal, $\underline{n}$, to a facet giving a reflected ray in the direction of $\underline{R}$, lies in the plane of $\underline{I}$ and $\underline{R}$ and bisects the angle between them.

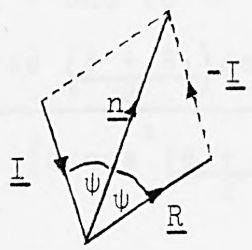

FIG. 4.1.6. 3-D Reflection

Since $\underline{I}$ and $\underline{R}$ are both expressed as unit vectors we may take,

$$\underline{n} = \underline{R} + (-\underline{I})$$

$$= (-\sin\theta_1 + \sin\theta\cos\phi)\hat{\underline{i}}$$

$$+ \sin\theta\sin\phi\hat{\underline{j}} + (\cos\theta + \cos\theta_1)\hat{\underline{k}} \qquad \ldots.(5)$$

As a check we can verify that $\underline{n}.(-\underline{I}) = \underline{n}.\underline{R}$

(both are equal to $1 + \cos\theta_1\cos\theta - \sin\theta_1\sin\theta\cos\phi$)

Now the angle between the plane of the facet and the reference mean plane, $\tilde{\theta}$, say, equals the angle between the normals.

Thus, $\underline{n}.\hat{\underline{k}} = |\underline{n}|\cos\tilde{\theta}$

$$= \cos\theta + \cos\theta_1 \qquad \ldots.(6)$$

But $|\underline{n}|^2 = (-\sin\theta_1 + \sin\theta\cos\phi)^2 + \sin^2\theta\sin^2\phi$

$+ (\cos\theta + \cos\theta_1)^2$

$= \sin^2\theta_1 - 2\sin\theta_1\sin\theta\cos\phi + \sin^2\theta\cos^2\phi$

$+ \sin^2\theta\sin^2\phi + \cos^2\theta + 2\cos\theta\cos\theta_1 + \cos^2\theta_1$

$= 2 + 2\cos\theta\cos\theta_1 - 2\sin\theta_1\sin\theta\cos\phi$ ....(7)

Thus $\cos\tilde{\theta} = \dfrac{(\cos\theta + \cos\theta_1)}{\{2 + 2\cos\theta\cos\theta_1 - 2\sin\theta_1\sin\theta\cos\phi\}^{\frac{1}{2}}}$ ....(8)

As another check on the computation, take $\phi = o$.

Whence $\cos\tilde{\theta} = \dfrac{\cos\theta + \cos\theta_1}{[2 + 2\cos(\theta + \theta_1)]^{\frac{1}{2}}}$ ....(9)

$= \dfrac{\cos\theta + \cos\theta_1}{[2\{1 + \cos(\theta + \theta_1)\}]^{\frac{1}{2}}}$

$= \dfrac{2\cos\left\{\frac{\theta + \theta_1}{2}\right\}\cos\left\{\frac{\theta - \theta_1}{2}\right\}}{\left[4\cos^2\left\{\frac{\theta + \theta_1}{2}\right\}\right]^{\frac{1}{2}}}$ ....(10)

$\Longrightarrow \tilde{\theta} = \dfrac{\theta - \theta_1}{2}$ ....(11)

The analysis has reduced to that of the two-dimensional profile and the geometry found to be valid.

Here the mean absolute slope

$$= \frac{1}{N}\sum_{\theta}\sum_{\phi} N_{\theta,\phi}\,|\tilde{\theta}| \qquad \text{....(12)}$$

where $\tilde{\theta}$ is given by eqn (8) and the sums extend over all angles which contain reflected rays. N is the total number of plane facets.

4.2 The Wave Theory Model

4.2.1. One-Dimensional Wave Theory Model

The essential difference between this model and the mirror facet model, is that the wave characteristics of the incident electromagnetic radiation are taken into account. The wavelength, direction of polarisation of the incident beam, together with the electrical properties of the surface material, are features fully integrated into a comprehensive scattering theory.

Here the resultant scattered field is a vector sum of wavefronts arising from elementary scatterers (facets). If a wavefront has amplitude A_j and phase ϕ_j, then the resultant field from N individual scatterers is:

$$U = re^{i\psi} = \sum_{j=1}^{N} A_j e^{i\phi_j} \qquad \ldots.(13)$$

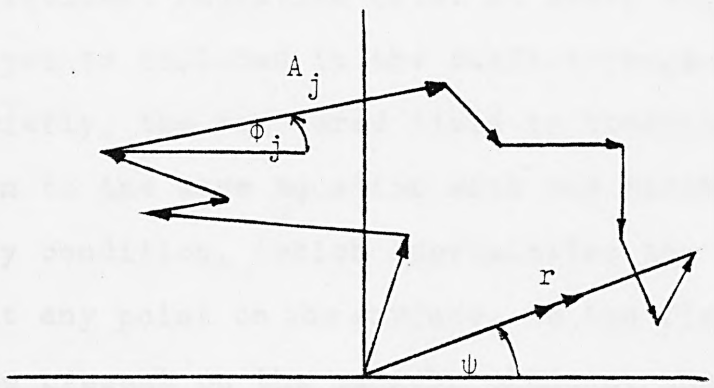

FIG. 4.2.1. Resultant field

The wavefronts mutually interfere, and visual effects of light and dark speckle images occur.

As in 4.1, if the surface definition is a 2-dimensional profile, or a series of parallel profiles, the scattered field can be calculated according to a

KIRCHHOFF WAVE THEORY MODEL, demanding much the same computational complexity as did the mirror facet model. That is, if the topography of the illuminated surface is specified precisely, the scattered radiation can be computed. We may either assume that the surface material is perfectly conducting, or take into account the reflectivity properties of the surface material.

We should be aware however, that in spite of the apparent comprehensiveness of the model, certain simplifying assumptions were made, so that the accompanying mathematics would be tractable, namely:

(i) shadowing and multiple scattering may be neglected,

(ii) the incident plane wave is linearly polarised,

(iii) the radius of curvature of the irregularities is large compared with the wavelength of the incident radiation (i.e. no sharp edges or points included in the surface roughness).

Briefly, the scattered field is obtained as a solution to the wave equation with the Kirchhoff boundary condition, (which approximates the incident field at any point on the surface, to the field that would be present on the tangent plane at that point). The Kirchhoff method is physically reasonable if assumption (iii) above is met. The procedure is fairly robust however, and solutions may still be adequate approximates even though (iii) is violated.

The definitive text on the KIRCHHOFF THEORY MODEL is to be found in Beckmann [1963]. In this chapter essential results are summarised and pronounced upon, since we need to know precisely the mechanism by which

surface topography determines polar diagrams, according to the Kirchhoff wave theory model.

The scattering coefficient is defined as, the ratio of the reflected field, to the field reflected in the specular direction, by a smooth perfectly conducting plane of the same dimensions, under the same illumination.

With reference to the scattering geometry of Fig. 4.1.2., the scattering coefficient, ρ, for a perfect conductor with $L>>\lambda$ and the incident beam horizontally or vertically polarised is,

$$\rho(\theta_2) = \frac{F_2}{2L} \int_{-L}^{L} e^{i\underline{v}\cdot\underline{r}} dx \qquad \ldots.(14)$$

$$= \frac{F_2}{2L} \int_{-L}^{L} e^{i(v_x x + v_z \zeta(x))} dx \qquad \ldots.(15)$$

where F_2 is a pure function of the incidence and observer angles θ_1 and θ_2, namely

$$F_2 = \sec\theta_1 . \frac{1 + \cos(\theta_1 + \theta_2)}{\cos\theta_1 + \cos\theta_2} ,$$

$$v_x = \frac{2\pi}{\lambda} (\sin\theta_1 - \sin\theta_2) \; ; \; v_z = -\frac{2\pi}{\lambda} (\cos\theta_1 + \cos\theta_2).$$

Here λ is the wavelength of the incident radiation, taking the source to be coherent and monochromatic. Typically the source is a helium neon laser and λ = 628 A°.

From eqn (15), given the profile curve, $\zeta(x)$, the integral may be computed and the scattering coefficient ρ determined for various θ_2, yielding the complete polar diagram.

If the surface material has finite conductivity, the expression for $\rho(\theta_2)$ is of the form:

$$\rho(\theta_2) = \frac{1}{4L\cos\theta_1}\int_{-L}^{L}(a\zeta' - b)e^{iv_x x + iv_z \zeta}dx \quad ....(16)$$

where the terms a and b are given by

$$a = (1 - R)\sin\theta_1 + (1 + R)\sin\theta_2 \quad ....(17)$$

$$b = (1 - R)\cos\theta_2 - (1 - R)\cos\theta_1 \quad ....(18)$$

The reflectivity coefficient R, depends on the material, the local angle of incidence and the direction of the plane of polarisation.

4.2.2. Two-Dimensional Wave Theory Model

The extension to the case when the surface is defined as a surface sheet $\zeta(x,y)$ is straightforward:

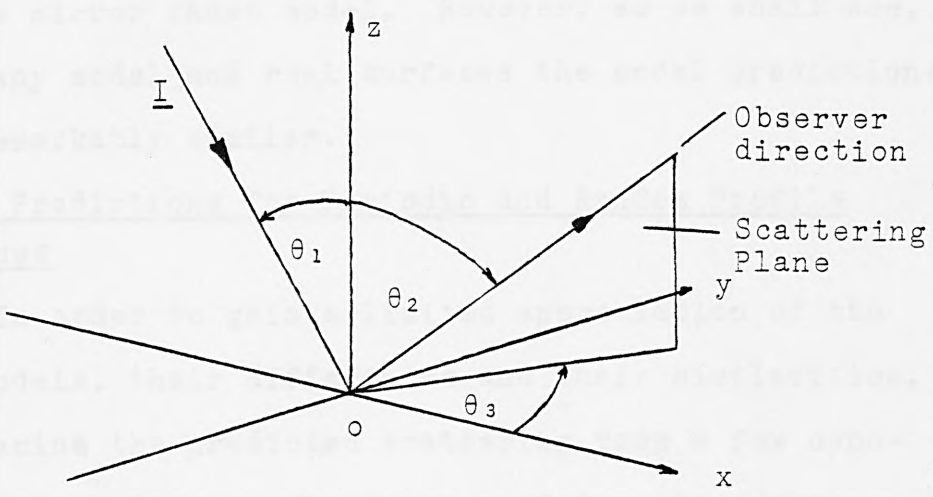

FIG. 4.2.2. 3-D Scattering Geometry

The coefficient of scattering for a perfectly conducting surface is:

$$\rho(\theta_2,\theta_3) = \frac{F_3}{A}\iint_A e^{i\underline{v}\cdot\underline{r}}\,dx\,dy \quad ....(19)$$

$$= \frac{F_3}{A}\iint_A e^{i(v_x x + v_y y + v_z \zeta)}\,dx\,dy \quad ....(20)$$

Here, A is the area of the sheet under illumination;

$$F_3 = \frac{1 + \cos\theta_1\cos\theta_2 - \sin\theta_1\sin\theta_2\cos\theta_3}{\cos\theta_1(\cos\theta_1 + \cos\theta_2)} \quad ;$$

$$v_x = \frac{2\pi}{\lambda}(\sin\theta_1 - \sin\theta_2\cos\theta_3) \; ; \quad v_y = -\frac{2\pi}{\lambda}\sin\theta_2\sin\theta_3$$

and $$v_z = -\frac{2\pi}{\lambda}(\cos\theta_1 + \cos\theta_2).$$

The scattered field for a finitely conducting sheet surface may be derived, although we do not state it here.

We see from eqns (15) and (20) for ρ, that the exact surface geometries $\zeta(x)$, $\zeta(x,y)$ are involved in the computations. Prima facie, the wave theory model offers a better prospect of recovering more surface geometry information, than appears possible from the simple mirror facet model. However, as we shall see, for many model and real surfaces the model predictions are remarkably similar.

4.3 Model Predictions for Periodic and Random Profile Surfaces

In order to gain a limited appreciation of the two models, their differences and their similarities, we examine the predicted scattering from a few hypothetical surfaces. Where appropriate, the juxstaposition of the facet model and the wave theory model analyses, enables comparisons to be seen more readily. In all cases, with regard to the wave theory model we shall consider the model surfaces to be perfectly conducting and $L >> \lambda$ so that the 'edge' effects may be neglected.

① Inclined Optical Flats

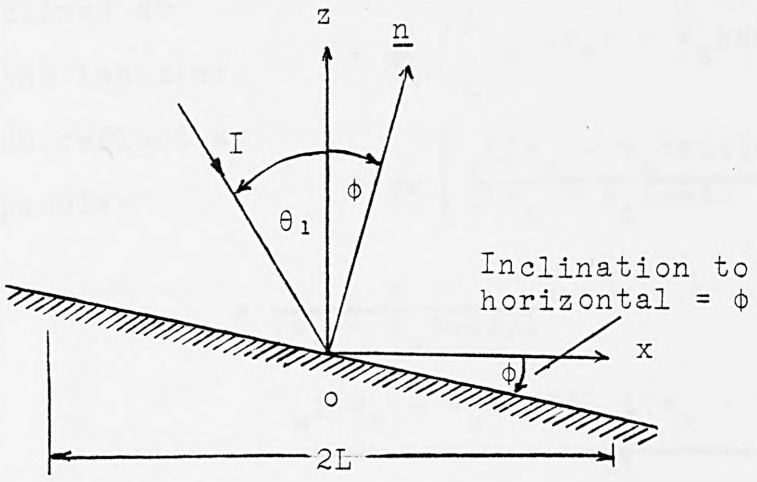

Facet Model

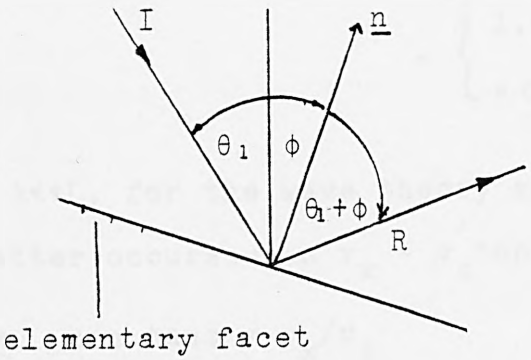

Wave Theory Model

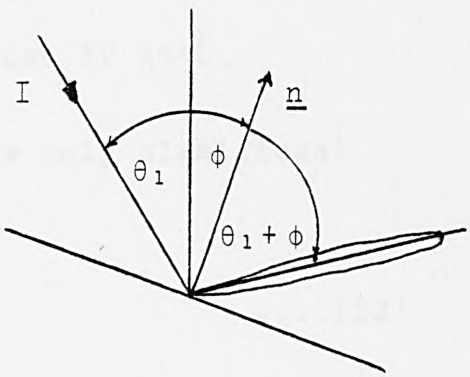

FIG. 4.3.1. Scattering from an Optical Flat

Plainly, since for all elementary facets, the normal is inclined at $(\theta_1 + \phi)$ to the incident ray; they each reflect a ray in the specular direction

$$\rho(\theta_2) = \frac{F}{2L}\int_{-L}^{L} e^{i\underline{v}\cdot\underline{r}}\,dx$$

$$= \frac{F}{2L}\int_{-L}^{L} e^{i(v_x x - v_z \tan\phi x)}\,dx$$

$$= \frac{F}{2L}\left[\frac{e^{i(v_x - v_z\tan\phi)x}}{i(v_x - v_z\tan\phi)}\right]_{-L}^{L}$$

$$= \frac{F}{(v_x - v_x\tan\phi)L}x$$

$$\{\frac{e^{i(v_x - v_z\tan\phi)L} \; \overset{-e}{i(v_x - v_z\tan\phi)(-L)}}{2i}\}$$

$$= \frac{F\,\sin(v_x - v_z\tan\phi)L}{(v_x - v_z\tan\phi)L}$$

$$= F\,\mathrm{sinc}(v_x - v_z\tan\phi)L \qquad ....(21)$$

$$(\mathrm{sinc}\ x = \frac{\sin x}{x})$$

$$= \begin{cases} 1, v_z - v_z\tan\phi = 0 \\ \simeq 0 \ \text{otherwise if } \lambda << L. \end{cases}$$

If $\lambda << L$, for the wave theory model, the only significant scatter occurs when $v_x - v_z\tan\phi = 0$.

i.e. when $\tan\phi = v_x/v_z$ ....(22)

$$= \frac{2\pi/\lambda\ (\sin\theta_1 - \sin\theta_2)}{-2\pi/\lambda\ (\cos\theta_1 + \cos\theta_2)}$$

$$= \frac{-2\cos(\frac{\theta_1 + \theta_2}{2})\sin(\frac{\theta_1 - \theta_2}{2})}{2\cos(\frac{\theta_1 + \theta_2}{2})\cos(\frac{\theta_1 - \theta_2}{2})}$$

$$= -\tan\frac{(\theta_1 - \theta_2)}{2} \qquad ....(23)$$

$$\longrightarrow \quad -\phi = \frac{\theta_1 - \theta_2}{2}$$

$$\theta_2 = \theta_1 + 2\phi \quad \text{w.r.t. the co-ordinate axiz z}$$

Thus both theories confine scattering to the specular direction. This agreement can be explained intuitively by a simple ray diagram. For reflected wavefronts in the direction $\theta_2 = \theta_1 + 2\phi$, there is zero path difference, and so waves reflected from elementary facets are in phase and simply reinforce one another.

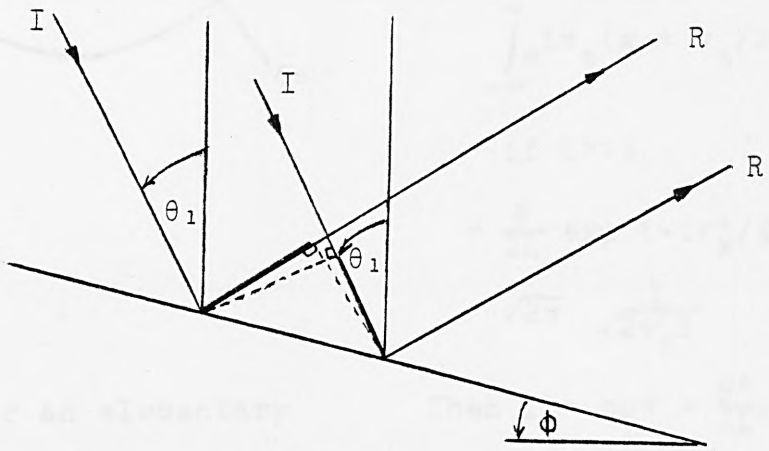

FIG. 4.3.2. Ray Diagram for Optical Flat

② Parabolic Reflector

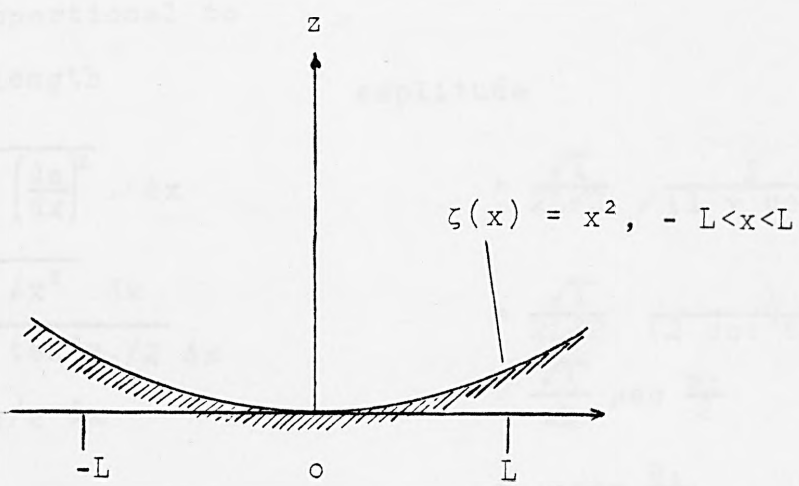

FIG. 4.3.3. Parabolic Reflector

Facet Model

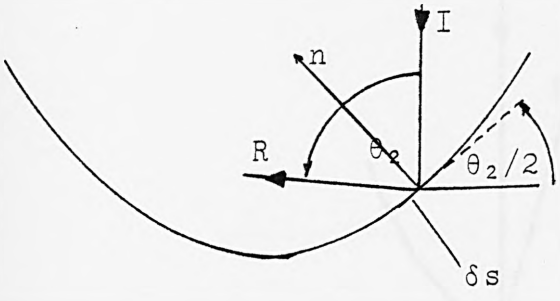

Consider an elementary facet δs inclined at $\theta_2/2$ to a normally incident beam. For the facet model approach the number of rays reflected in direction θ_2 will be proportional to the facet length

$$\delta s \simeq \sqrt{1 + \left(\frac{dz}{dx}\right)^2} \cdot \delta x$$

$$= \sqrt{1 + 4x^2} \quad \delta x$$

$$\sqrt{1 + \tan^2\theta_2/2}\ \delta x$$

$$= \sec\theta_2/2\ \delta x$$

Wave Theory Model

$$\rho = \frac{F}{2L} \int_{-L}^{L} e^{i(v_x x + v_z x^2)} dx$$

$$= \frac{F}{2L} \int_{-L}^{L} \exp\{iv_z(x + v_x/2v_x)^2$$

$$-iv_x^2/4v_z\}\, dx$$

$$\simeq \frac{F}{2L} \exp(-iv_x^2/4v_z) \cdot$$

$$\int_{-\infty}^{\infty} e^{iv_z(x + v_x/2v_z)^2} dx$$

if $L \gg \lambda$

$$= \frac{F}{2L} \exp\,(-iv_x^2/4v_z) \cdot$$

$$\sqrt{2\pi}\ \frac{1}{\sqrt{2v_z i}} \qquad \ldots.(24)$$

Then $I = \rho\rho^* = \frac{F^2}{4L^2} \cdot \frac{\pi}{v_z}$ ....(25)

$$= \frac{F^2}{4L^2} \cdot \frac{\lambda}{2} \frac{1}{(\cos\theta_1 + \cos\theta_2)}$$

....(26)

For normal incidence, ($\theta_1 = 0$)

$$I = \frac{\lambda}{8L^2} \cdot \frac{1}{(1 + \cos\theta_2)}, \text{ and}$$

....(27)

amplitude

$$= \frac{\sqrt{\lambda}}{2L\sqrt{2}}\ \sqrt{\frac{1}{(1 + \cos\theta_2)}}$$

....(28)

$$= \frac{\sqrt{\lambda}}{2L\sqrt{2}}\ \frac{1}{(2\cos^2\theta_2/2)^{\frac{1}{2}}}$$

$$= \frac{\sqrt{\lambda}}{4L} \sec\frac{\theta_2}{2}$$

$$\propto \sec\frac{\theta_2}{2} \qquad \ldots.(29)$$

Using simple ray theory arguments, since a normal beam is directed parallel to the principal axis of a parabolic

mirror, all rays are reflected through the focus $(0,\frac{1}{4})$.

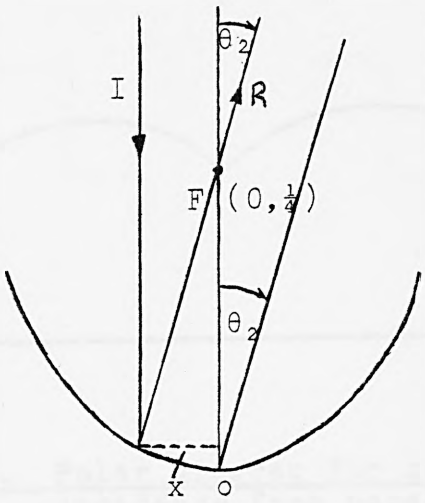

FIG. 4.3.4. Ray Diagram for Parabolic Reflector

In the far field, the amplitude at θ_2, varies as $\sec\theta_2/2$ according to the wave theory model. From simple geometry, (according to the facet theory) $\tan\theta_2 = x/(OF - x^2)$

$$\tan\theta_2 = x/(OF - x^2)$$

$$= \frac{x}{\frac{1}{4} - x^2} = \frac{4x}{1 - 4x^2}$$

$$\text{Thus} \quad \cos\theta_2 = 2\cos^2\theta_2/2 = \frac{1-4x^2}{1+4x^2}$$

$$1 + \cos\theta_2 = 2\cos^2\theta_2/2 = \frac{2}{1+4x^2}$$

$$\Longrightarrow \frac{\sec\theta_2}{2} = \sqrt{1+4x^2}$$

Thus the amplitude distribution predicted by the wave theory model corresponds with the power distribution predicted by the facet theory.

To gain some insight into the above results, consider the following disgression:-

If n coherent waves of equal power are all in phase the total power is proportional to n^2, since the total power

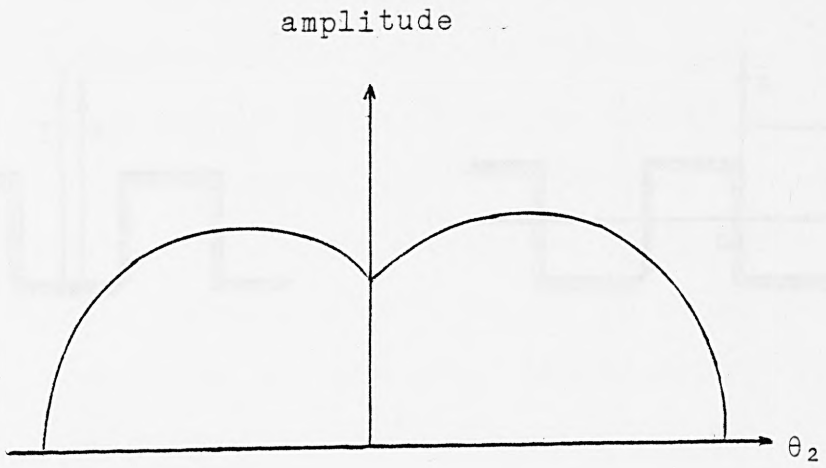

FIG. 4.3.5. Polar diagram for scattering at normal incidence from parabolic reflector

density of coherent waves is obtained by summing the individual fields vectorially. In contrast, the mean power densities of incoherent waves may be added algebraically, and the mean total power of n incoherent waves is proportional to n. The facet model is thus appropriate to the case of incoherent illumination.

We now explore two strictly periodic surfaces

4.3.1 Periodic Profile Surfaces

③ Rectangular Corrugations

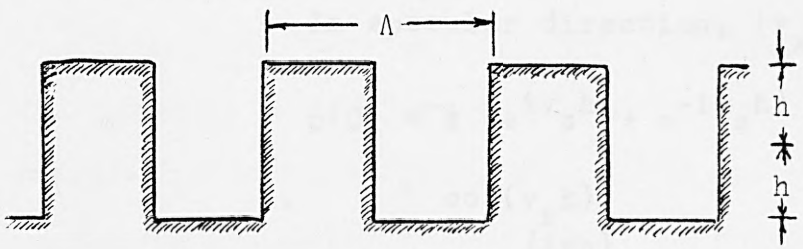

FIG. 4.3.6. Rectangular Corrugation

Suppose that the illumination is directed normal to the surface thereby avoiding problems of shadowing.

Facet Model

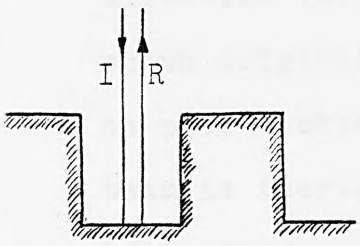

Wave Theory Model

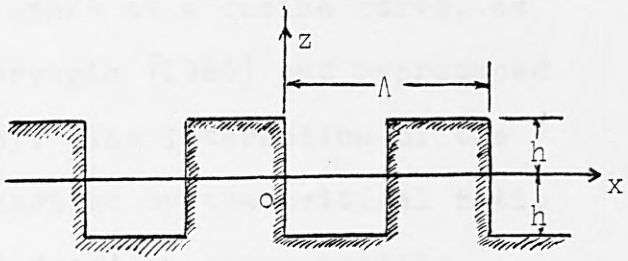

We could take the number of elementary facets to be $4L/\Lambda$ (Λ is the period of the surface corrugations). All facets return a reflected ray back along the incident path. The facet model cannot distinguish between surfaces (1) and (3) if illumination is normal.

$$\rho(\theta_2) = \frac{F}{2L}\int_{-L}^{L} e^{iv_x x + iv_z z}\,dx$$

$$= \frac{F}{2L}\cdot\frac{2L}{\Lambda}\left\{\int_0^{\Lambda/2} e^{-iv_z h + iv_x x}\,dx + \int_{\Lambda/2}^{\Lambda} e^{iv_z h + iv_x x}\,dx\right\}$$

$$= \frac{F}{\Lambda}\left\{e^{-iv_z h}\left[\frac{1}{iv_x}e^{iv_x x}\right]_0^{\Lambda/2} + e^{iv_z h}\left[\frac{1}{iv_x}e^{iv_x x}\right]_{\Lambda/2}^{\Lambda}\right\}$$

$$= \frac{F}{\Lambda i v_x}\left\{e^{-iv_z h}\left(e^{iv_x \Lambda/2}-1\right) + e^{iv_z h}\left(e^{iv_x \Lambda} - e^{iv_x \Lambda/2}\right)\right\}$$

$$= \frac{F}{\Lambda i v_x}\left(e^{iv_x \Lambda/2}-1\right)\cdot\left(e^{-iv_z h} + e^{iv_z h}e^{iv_x \Lambda/2}\right)$$

In specular direction, ($v_x = 0$),

$$\rho(0) = \tfrac{1}{2}\left(e^{iv_z h} + e^{-iv_z h}\right)$$

$$= \cos(v_z h)$$

$$= \cos\left(\frac{4\pi h}{\lambda}\right) \qquad \ldots.(30)$$

$$I(0) = \cos^2\left(\frac{4\pi h}{\lambda}\right) \qquad \ldots.(31)$$

The coefficient of scattering in the specular direction varies with $4\pi h/\lambda$ as a cosine curve, as shown originally by Deryugin [1960] and reproduced on p63, Beckmann [1963]. The interaction of the beam is therefore summarised by the critical ratio h/λ. There are four 'edges' in every profile period and so, strictly, the Kirchhoff wave theory approach is invalid. However Deryugin shows the Kirchhoff method to be a good approximation of an exact evaluation of the scatter.

Intuitively, the path difference of adjacent wavefronts reflected from the surface will be $4h$, and for the case $4h = \lambda/2$, the fronts will totally interfere with each other and the intensity falls to zero.

Widening the discussion to periodic profiles, $\zeta(x)$, in general, we may write $\zeta(x) = \zeta(x + \Lambda)$, which implies periodicity of $\exp(iv_x x + iv_z \zeta)$ for $v_x \Lambda = 2\pi m$ where m is any integer. Since $v_x = \frac{2\pi}{\lambda}(\sin\theta_1 - \sin\theta_2)$, in Beckmann's notation, $\sin\theta_{2m} = \sin\theta + \frac{\lambda}{\Lambda}$, which defines the directions of the side lobes of the scatter distributions of polar diagrams.

For $\Lambda << \lambda$ (very smooth surfaces) there is only the specular lobe (corresponding to $m = 0$) and the surface reflects specularly, regardless of the roughness parameter h; for $\lambda << \Lambda$ there are a multiplicity of lobes and the incident wave is scattered completely; for $\lambda \tilde{\sim} \Lambda$ there are a few significant side lobes and the polar diagram structure is more

informative. This is the condition of resonance where the wavelength of the interrogating beam is matched to the wavelength of the surface roughness, we shall return to this theme later. (c.f. Chapter 9.1.)

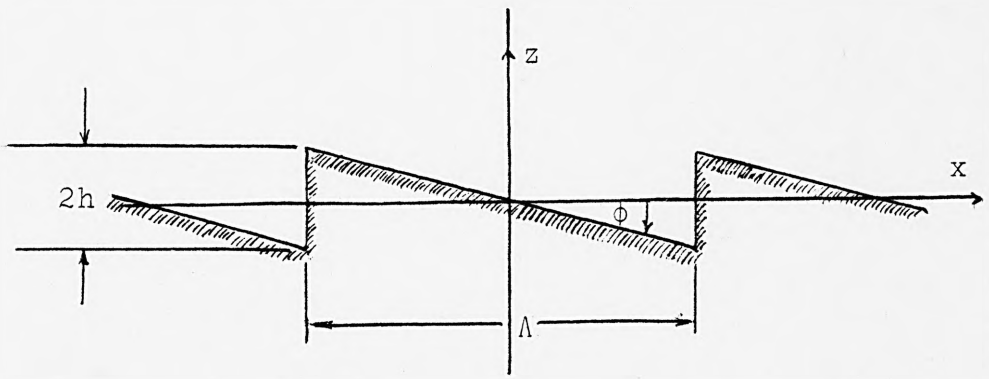

FIG. 4.3.7. Saw-Tooth Profile

Suppose there are (2n + 1) periods in 2L, i.e. $(2n + 1)\Lambda = 2L$ and that shadowing and secondary reflection effects may be ignored.

Facet Model

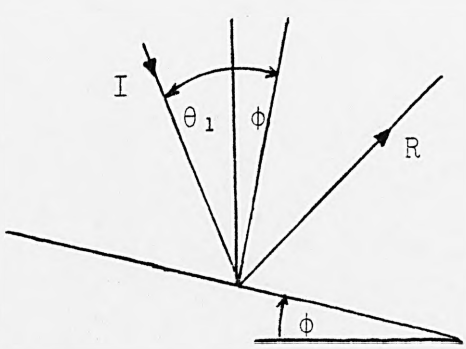

Wave Theory Model

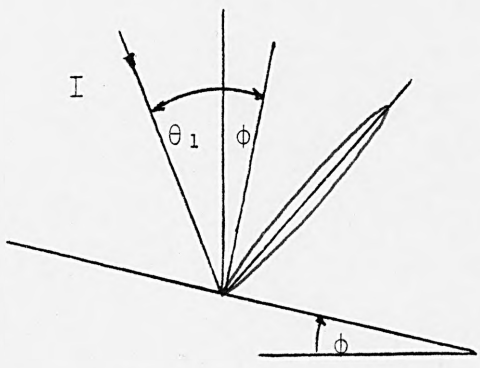

Again, all $(2n + 1)$ profile teeth are inclined at $(\theta_1 + \phi)$ to the incident beam, so that the scattered field is a sum of $(2n + 1)$ elementary rays in the specular direction

$$\rho = \frac{F}{2L}\int_{-L}^{L} e^{i\underline{v}\cdot\underline{r}}\,dx$$

$$= \frac{F}{(2n+1)}\,\mathrm{sinc}(v_x - v_z\tan\phi)\Lambda/2 \cdot \left[1 + n\cos(v_x\Lambda)\right] \quad \ldots.(32)$$

(from Appendix 4B)

We suppose that $(2n + 1)\Lambda = 2L$ and that $\Lambda >> \lambda$.

Although the wave theory restricts scattering to within a small angle of specular direction, for a given tilt, ϕ, of the profile teeth, the intensity in this direction will vary dramatically with the wavelength Λ and in this respect, the model descriptions of the scatter remain distinct.

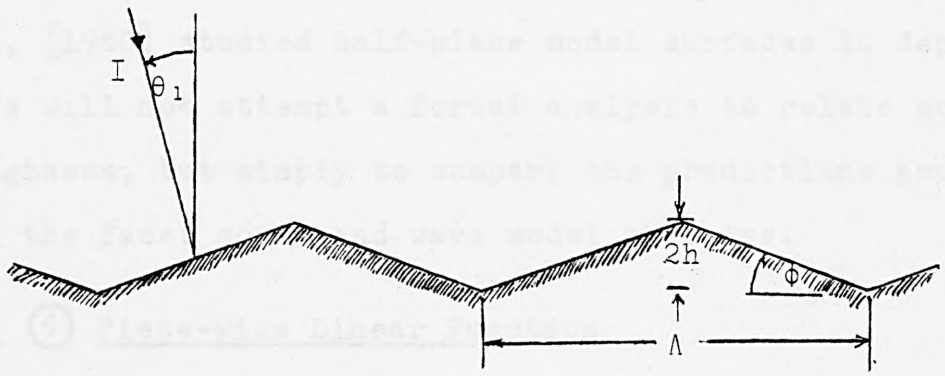

FIG. 4.3.8. Saw-Tooth Profile

The saw-tooth profile above, for normal or near normal incidence, should not give rise to the complications of shadowing or secondary reflections, for suitable h and Λ. For general scattering angles θ_2, the integration is straightforward and may be referred to in Appendix 4B.

(The result for the preferred scattering angles θ_{2m} may be found in Beckmann [1963] p.58.)

$$\rho(\theta_2) = \frac{Fe^{iv_z h}}{2i} \{ \left[\sin (v_x + v_z \tan\phi)\frac{\Lambda}{4} - i\cos(v_x + v_z \tan\phi)\frac{\Lambda}{4} \right] .\mathrm{sinc}(v_x + v_z \tan\phi)\frac{\Lambda}{4} - \left[\sin(v_x - v_z\tan\phi)\frac{\Lambda}{4} - i\cos(v_x - v_z\tan\phi)\frac{\Lambda}{4} \right] .\mathrm{sinc}(v_x - v_z\tan\phi)\frac{\Lambda}{4} \}$$

For $\Lambda >> \lambda$, the sinc(.) terms vanish except in the close proximity of (.) = 0, i.e. at $\frac{v_x}{v_z} = \pm \tan\phi = \pm \frac{4h}{\Lambda}$. Proceeding as on p53, this leads to the two angles specified by the tilt facets of the geometrical profile.

By way of generalisation and to bridge sections 4.3.1. and 4.3.2. we consider a piece-wise linear function profile: effectively a mirror facet model surface, although possibly envisaged as an approximation to a real surface. Ament [1956], [1960] studied half-plane model surfaces in depth: here we will not attempt a formal analysis to relate scatter to roughness, but simply to compare the predictions according to the facet model and wave model theories.

⑤ Piece-wise Linear Function

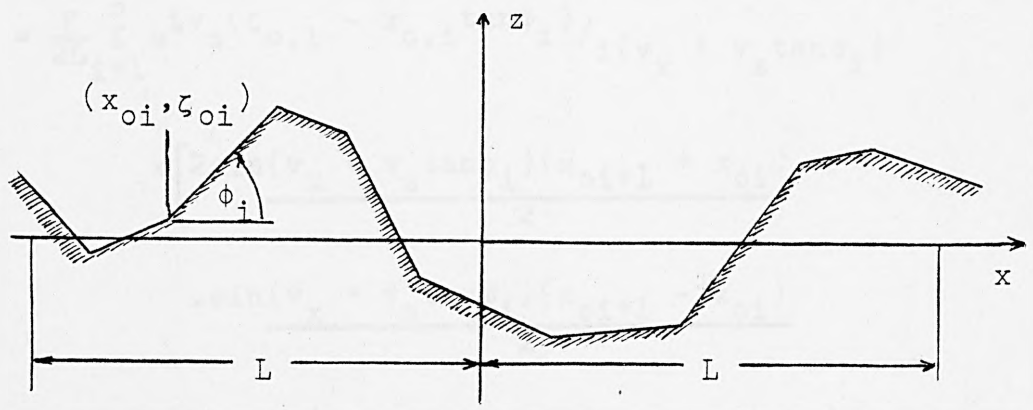

FIG. 4.3.9. Piece-wise Linear Profile

A facet profile, $\zeta(x)$ can be written as

$\zeta(x) = \zeta_{o,i} + \tan\phi_i(x - x_{o,i})$, $x_{o,i} < x < x_{o,i+1}$ with

$\zeta_{o,i+1} = \zeta_{o,1} + \tan\phi_i(x_{o,i+1} - x_{o,i})$ to ensure continuity.

Then

$$\rho(\theta_2) = \frac{F}{2L}\int_{-L}^{L} e^{i(\underline{v}\cdot\underline{r})}dx$$

$$= \frac{F}{2L}\sum_{i=1}^{n}\int_{x_{o,i}}^{x_{o,i+1}} e^{i[v_x x + v_x(\zeta_{o,i} + \tan\phi_i(x - x_{o,i}))]}dx$$

$$= \frac{F}{2L}\sum_{i=1}^{n} e^{iv_z(\zeta_{o,i} - x_{o,i}\tan\phi_i)}\int_{x_{o,i}}^{x_{o,i+1}} e^{i(v_x + \tan\phi_i v_z)x}dx$$

$$= \frac{F}{2L}\sum_{i=1}^{n} \frac{e^{iv_z(\zeta_{o,i} - x_{o,i}\tan\phi_i)}}{i(v_x + v_z\tan\phi_i)}\left[e^{i(v_x + \tan\phi_i v_z)x}\right]_{x_{o,i}}^{x_{o,i+1}}$$

$$= \frac{F}{2L}\sum_{i=1}^{n} e^{iv_z(\zeta_{o,i} - x_{o,i}\tan\phi_i)} \times \left[\frac{e^{i(v_x + \tan\phi_i v_z)x_{o,i+1}} - e^{i(v_x + \tan\phi_i v_z)x_{o,i}}}{i(v_x + v_z\tan\phi_i)}\right]$$

$$= \frac{F}{2L}\sum_{i=1}^{n} e^{iv_z(\zeta_{o,i} - x_{o,i}\tan\phi_i)}$$

$$\times\left[\frac{\cos\{(v_x + v_z\tan\phi_i)x_{o,i+1}\} - \cos\{(v_x + v_z\tan\phi_i)x_{o,i}\}}{i(v_x + v_z\tan\phi_i)}\right.$$

$$\left. + \frac{i\sin\{(v_x + v_z\tan\phi_i)x_{o,i+1}\} - \sin\{(v_x + v_z\tan\phi_i)x_{o,i}\}}{i(v_x + v_z\tan\phi_i)}\right]$$

$$= \frac{F}{2L}\sum_{i=1}^{n} e^{iv_z(\zeta_{o,i} - x_{o,i}\tan\phi_i)} / i(v_x + v_z\tan\phi_i)$$

$$\times\left[2\sin\frac{(v_x + v_z\tan\phi_i)(x_{oi+1} + x_{oi})}{2}\right.$$

$$\cdot\sin\frac{(v_x + v_z\tan\phi_i)(x_{oi+1} - x_{oi})}{2}$$

$$+ i\,2\cos\frac{(v_x + v_z\tan\phi_i)(x_{o,i+1} + x_{oi})}{2}$$

$$\left.\cdot\sin\frac{(v_x + v_z\tan\phi_i)(x_{oi+1} - x_{oi})}{2}\right]$$

$$= \frac{F}{L} \sum_{i=1}^{n} e^{iv_z(\zeta_{o,i} - x_{o,i}\tan\phi_i)}$$

$$x\left[\cos \frac{(v_x + v_z\tan\phi_i)(x_{o,i+1} + x_{o,i})}{2}\right.$$

$$\left. - i\sin \frac{(v_x + v_z\tan\phi_i)(x_{o,i+1} + x_{o,i})}{2}\right]$$

$$x \sin \frac{(v_x + v_z\tan\phi_i)(x_{o,i+1} - x_{o,i})/2}{(v_x + v_z\tan\phi_i)} \qquad \ldots.(33)$$

with $(x_{o,i+1} - x_{o,i}) >> \lambda$, the contribution from the i^{th} facet vanishes except for $v_x + v_z\tan\phi_i = 0$.

i.e. the scattering coefficient vanishes except for the contributions at specific angles as dictated by the individual facets. Thus the angular dispersion of the two scattering theories coincide for large roughness structure profiles, but the phase information carried by the wave model, maintains distinct polar diagram definition in received amplitude or intensity.

4.3.2. Random Profile Surfaces

Beckmann [1963] contains a detailed account of both periodic and random profile analysis. The case of a surface possessing a Gaussian height distribution is described in full. We recap on the normal theory as necessary to extend the methodology, and examine the important special case of a surface possessing a negative exponential of heights. (c.f. Fig. 4.3.11.) which illustrates a surface profile from a plateau-honed surface where typically the profile peaks are 'shorn flat', and the associated highly skewed negative exponential height distribution). This special case is treated in more detail, along with other cases citing surfaces possessing non-Gaussian profile statistics, in Chapter 8.3. We conclude the comparison of the two scattering models by demonstrating the convergence of mirror facet and wave theory models, for very rough surfaces in general. Tanner [1980] claims to have demonstrated this in an earlier paper, Tanner [1976], but on close examination he uses simple ray facet theory arguments.

The discussion of random profile analysis employing the Kirchhoff wave theory model now proceeds as follows:

For a perfectly conducting, one-dimensionally rough surface (with zero mean height), the coefficient of scattering is

$$\rho(\theta_2) = \frac{F}{2L}\int_{-L}^{L} e^{i(v_x x + v_z \zeta(x))}dx$$

Taking expectations,

$$E[\rho(\theta_2)] = \frac{F}{2L}\int_{-L}^{L} e^{iv_x x} E(e^{iv_z \zeta})dx \qquad ....(34)$$

$$= \frac{F}{2L}\chi(v_z)\int_{-L}^{L} e^{iv_x x}dx$$

$$= F\,\chi(v_z)\,\mathrm{sinc}\, v_x L \qquad ....(35)$$

$$= F\,\chi(v_z)\rho_o, \text{ say where } \rho_o = \mathrm{sinc}\, v_x L$$

and we have introduced the <u>characteristic function</u> $\chi(v_z)$ of $w(z)$, the probability density function of surface heights.

The general result, for the standardised intensity distribution reflected from a surface as defined above is

$$I(\theta_2) = E[\rho\rho^*]$$

$$= \rho_o^2\chi(v_z)\chi^*(v_z) +$$

$$\frac{F}{2L}\int_{-L}^{L} e^{iv_x\tau}[\chi_2(v_z, -v_z;\tau) - \chi(v_z)\chi^*(v_z)]d\tau \qquad ....(36)$$

where $\chi_2(v_z, -v_z;\tau)$ is the joint characteristic function of surface heights z_1 and z_2 separated by a distance τ. the first term gives a significant contribution only in the specular direction, and then only for very smooth surfaces, in which case it is manifest by a specular spike, whilst the second term can then be thought of as the off-specular component.

⑥ <u>Case of Normal Surface Height Distribution</u>

In brief, $w(z) \sim \frac{1}{\sqrt{2\pi}}\frac{1}{\sigma} e^{-z^2/2\sigma^2}$, with σ the standard deviation of surface heights. The derived characteristic function in this case

$$\chi(v_z) = e^{-\frac{1}{2}\sigma^2 v_z^2} = e^{-\frac{1}{2}g} \qquad ....(37)$$

where, in keeping with Beckmann's notation,

$g = \sigma^2 v_z^2$, a useful categorising parameter.

The joint density $w(z_1, z_2)$ is bivariate normal with correlation C say, viz:

$$w(z_1, z_1) = \frac{1}{2\pi\sigma^2\sqrt{1 - C^2}} \exp\left[-\frac{(z_1^2 - 2Cz_1z_2 + z_2^2)}{2\sigma^2(1 - C^2)} \right]$$

from which, ...(38)

$$\chi_2(v_z, -v_z) = \exp\left[-v_z^2\sigma^2(1 - C)\right] = e^{-g(1 - C)}$$

....(39)

Thus, for a Gaussian surface,

$$I(\theta_2) = \rho o^2 e^{-g} + \frac{F^2}{2L}\int_{-L}^{L} e^{iv_x\tau}\left[e^{-g\left[1 - C(\tau)\right]} - e^{-g} \right] d\tau$$

....(40)

The usual procedure is to assume a Gaussian form of autocorrelation function : $C(\tau) = e^{-\tau^2/T^2}$ where T is defined as the correlation length. Under this assumption,

$$I(\theta_2) = \rho o^2 e^{-g} + \frac{F^2}{2L}\int_{-L}^{L} e^{iv_x\tau} e^{-g}\{e^{gC(\tau)} - 1\}\, dz$$

....(41)

$$= \rho o^2 e^{-g} + \frac{F^2}{2L}\int_{-L}^{L} e^{iv_x\tau}\, e^{-g} \sum_{m=1}^{\infty} \frac{g^m}{m!}\, e^{-m\tau^2/T^2}\, d\tau$$

....(42)

For type (A) surfaces $g \ll 1$, i.e. very smooth surfaces, only take the first term of the series : for type (B) surfaces $g \sim 1$, i.e. moderately smooth, take as many terms as necessary : for type (C) surfaces $g \gg 1$, i.e. rough surfaces, use "saddle point" integration. (Type (A) surfaces are discussed later in Chapter 8.2.2 and Type (B) in Chapter 8.2.1 and 8.3).

Let us consider for the moment the case $g \gg 1$

$$I(\theta_2) \to \frac{F^2}{2L}\int_{-\infty}^{\infty} e^{iv_x\tau}\, g^{-g(1 - C(\tau))}\, d\tau, \text{ since}$$

....(43)

the first term above is negligible, and only near

$\tau = 0$ do we have any significant contribution to the integral. In which case $C(\tau) = e^{-\tau^2/T^2} \simeq 1 - \tau^2/T^2$.

$$\therefore I(\theta_2) \simeq \frac{F^2}{2L} \int_{-\infty}^{\infty} e^{iv_x\tau}\, e^{-g\left[1 - (1 - \tau^2/T^2)\right]} d\tau \quad \ldots.(44)$$

$$= \frac{F^2}{2L} \int_{-\infty}^{\infty} e^{iv_x\tau}\, e^{-g\tau^2/T^2} d\tau$$

$$= \frac{F^2}{L} \int_{-\infty}^{\infty} \cos(v_x\tau) e^{-g\tau^2/T^2} d\tau$$

$$= \frac{TF^2}{L}\sqrt{\frac{\pi}{g}} \exp\left(-\frac{v_x^2 T^2}{4g}\right) \quad \ldots.(45)$$

(c.f. Ryzhik and Gradstein [1957])

$$= \frac{TF^2}{Lv_z}\frac{\sqrt{\pi}}{\sigma} \exp\left(-\frac{T^2 v_x^2}{4\sigma^2 v_z^2}\right)$$

$$= \frac{TF^2\sqrt{\pi}}{Lv_z\sigma} \cdot \exp\left(-\frac{T^2}{4\sigma^2}\tan^2\tilde{\theta}/2\right) \quad \tilde{\theta} = \theta_1 - \theta_2$$

$$\simeq \frac{TF^2\sqrt{\pi}}{Lv_z\sigma} \cdot \exp\left(-\frac{T^2\tilde{\theta}^2}{16\sigma^2}\right) \quad \ldots.(46)$$

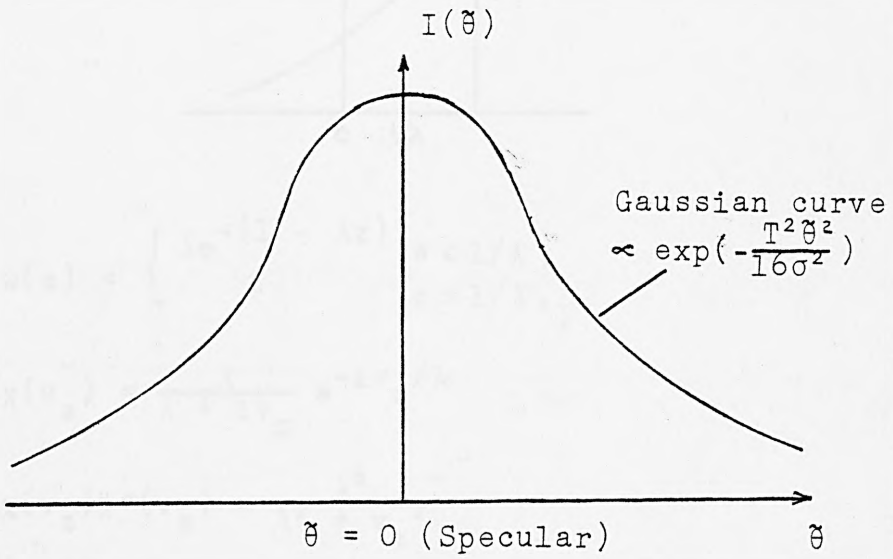

FIG. 4.3.10. Scattering from Rough Type (C) Surface having Gaussian Height Distribution

If we "normalise" the intensity curve the "variance" = $8\sigma^2/T^2$. [N.B. the curve represents the expected intensity at angle $\tilde{\theta}$ away from specular, and

must not be confused with the usual interpretation as a random variable frequency curve.]

For a Gaussian height surface, $N(0,\sigma^2)$ and $C(\tau) = e^{-\tau^2/T^2}$, the distribution of slopes is $N(0,2\sigma^2/T^2)$ (c.f. Appendix 8I or Beckmann [1963] p.193 for full justification) and furthermore the distribution of inclinations (ψ) of roughness facets, will be approximately $N(0,2\sigma^2/T^2)$. Since facets inclined at $\tilde{\theta}/2$ will reflect into $\tilde{\theta}$, we can interpret the above results according to the mirror facet view of scattering, namely, that the intensity at angle $\tilde{\theta}$, is directly proportional to the number of facets inclined at the appropriate angle $\tilde{\theta}/2$.

⑦ Case of Negative Exponential Distribution

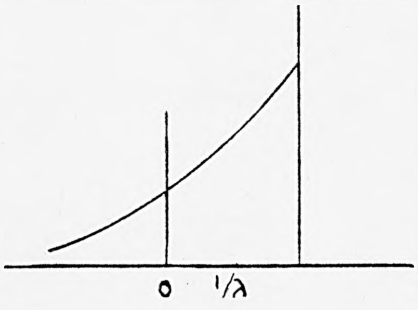

Take $w(z) = \begin{cases} \lambda e^{-(1 - \lambda z)} & z < 1/\lambda, \\ & z > 1/\lambda. \end{cases}$

Then $\chi(v_z) = \frac{\lambda}{\lambda + iv_z} e^{-iv_z/\lambda}$

and $\chi(v_z)\chi^*(v_z) = \frac{\lambda^2}{\lambda^2 + v_z^2}$

i.e. $\chi(v_z)\chi^*(v_z) = \frac{1}{1 + v_z^2/\lambda^2} = \frac{1}{1 + \sigma^2 v_z^2} = \frac{1}{1 + g}$

The full treatment for this particular surface height distribution is found in Chapter 8.3, where the above and following results are described in detail.

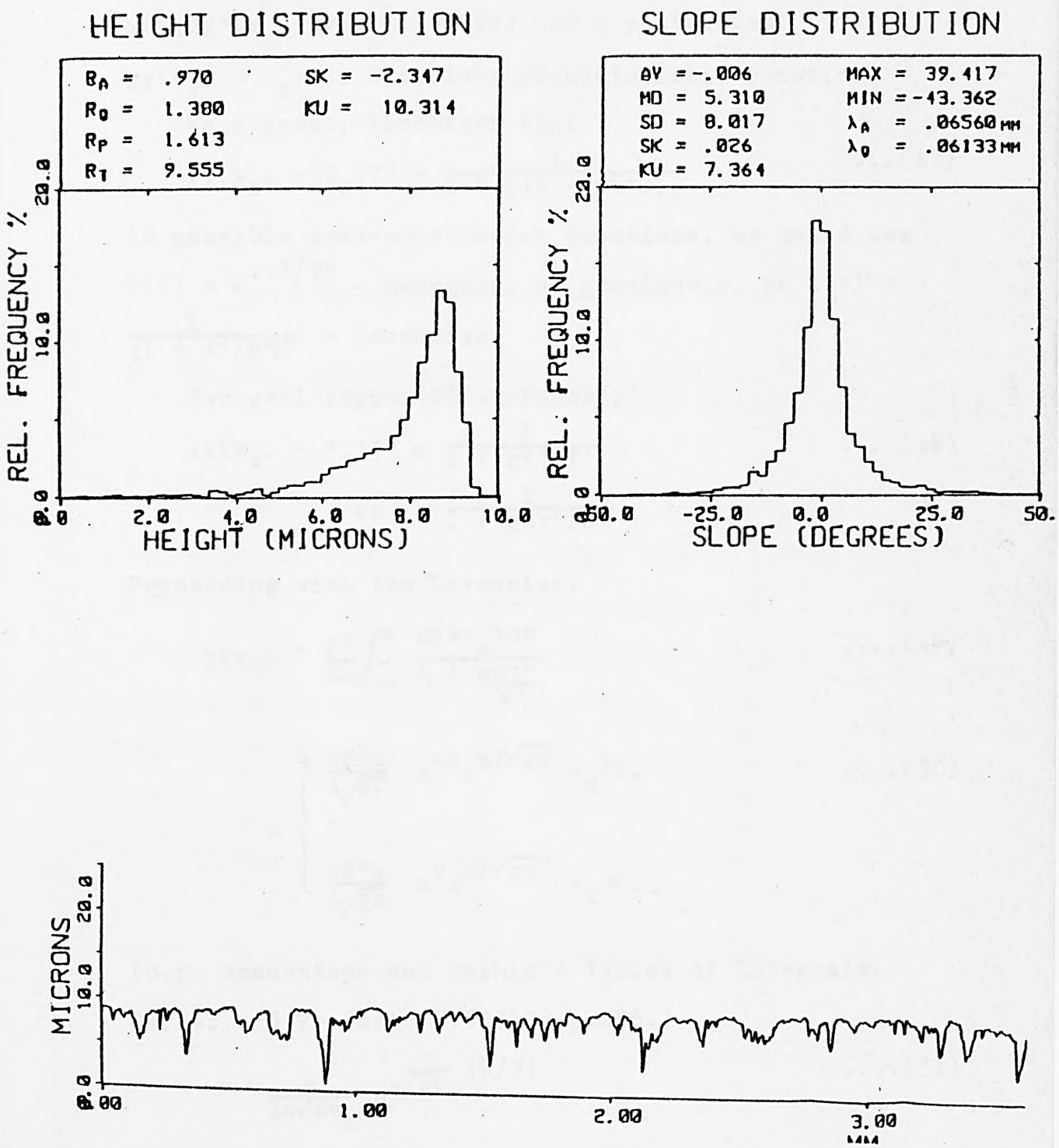

FIG. 4.3.11. Surface Profile, Height and Slope Distributions from a Plateau - Honed Surface

The author's heuristic procedure is to replace g in $\chi(v_z)\chi^*(v_z)$ by $g\,[1 - C(\tau)]$ as a postulated $\chi_2(v_z, -v_z;\tau)$, bivariate characteristic function.

We suggest, therefore that

$$\chi_2(v_z, -v_z;\tau) = \frac{1}{1 + g[1 - C(\tau)]} \qquad \ldots.(47)$$

As possible auto-correlation functions, we could use $C(\tau) = e^{-\tau^2/T^2}$ - Gaussian, as previously, or $C(\tau) = \frac{1}{[1 + \tau^2/a^2]^m}$ - Lorenzian.

For $g \gg 1$ (type (C) surfaces),

$$\chi_2(v_z, -v_z;\tau) \simeq \frac{1}{1 + g\tau^2/T^2} \qquad \ldots.(48)$$

$$\text{or} \simeq \frac{1}{1 + gm\tau^2/a^2}$$

Proceeding with the Lorenzian,

$$I(\theta_2) \sim \frac{F^2}{2L}\int_{-\infty}^{\infty} \frac{\cos v_x \tau d\tau}{1 + \frac{gm\tau^2}{a^2}} \qquad \ldots.(49)$$

$$= \begin{cases} \frac{\pi F^2 a}{4\sqrt{gm}}\, e^{-v_x a/\sqrt{gm}} & v_x > 0, \\ \frac{\pi F^2 a}{4\sqrt{gm}}\, e^{v_x a/\sqrt{gm}} & v_x < o. \end{cases} \qquad \ldots.(50)$$

(c.f. Gradshteyn and Ryzhik's Tables of Integrals Series and Products 3.723(2) p.406.)

$$\sim \frac{a}{4\sigma\sqrt{m}v_z}\, e^{-\frac{a}{\sqrt{m}\sigma}|\theta/2|} \qquad \ldots.(51)$$

i.e. a Laplacian scatter distribution curve.

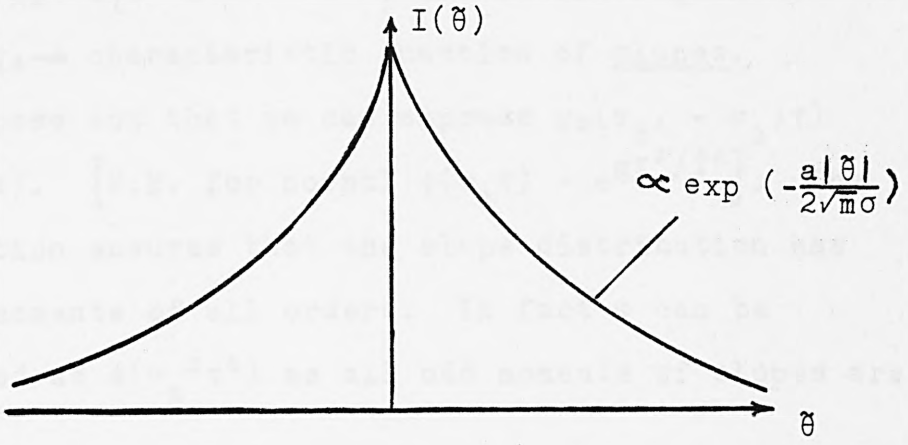

FIG. 4.3.12. Scattering from Rough Type (C) Surface with Negative Exponential Height Distribution

The difference of two negative exponentials in Laplacian (c.f. p.272 Kendall and Stuart [1969] Ex.11.15 a = 1) and we may conclude that this is the case for the distribution of slopes. The geometric interpretation therefore, is exactly the same as for the normal case, and so the facet model applies under these conditions also.

⑧ General Type C Surface

We formally generalise these results for Type (C) surfaces, with the aid of the inversion theorem of characteristic functions:

"If f(x) and $\phi(t)$ are p.d.f. and characteristic functions of a random variable X i.e. by definition $\phi(t) = \int_{-\infty}^{\infty} f(x)\, e^{ixt} dx$ then $f(x) = \frac{1}{2\pi} \int_{-\infty}^{\infty} \phi(t) e^{-ixt} dt$."

(p.95 Kendall and Stuart [1969].)

For a Type (C) surface,

$$I(\theta_2) = \frac{F}{2L} \int_{-\infty}^{\infty} e^{iv_x \tau} \chi_2(v_z, -v_z; \tau)\, d\tau .$$

Recall, $\chi_2 = E\left[e^{iv_z(z_1 - z_2)}\right]$ and in the region of $\tau = 0$, $\chi_2 \rightarrow$ characteristic function of slopes.

Suppose now that we can express $\chi_2(v_z, -v_z;\tau)$ as $\phi(v_z\tau)$. $\left[\text{N.B. for normal } \phi(v_z\tau) = e^{g\tau^2/T^2}\right]$. The supposition ensures that the slope distribution has finite moments of all orders. In fact ϕ can be expressed as $\phi(v_z{}^2\tau^2)$ as all odd moments of slopes are zero.

$$\text{Then, } I(\theta_2) = \frac{F^2}{2L}\int_{-\infty}^{\infty} e^{iv_x\tau}\phi(v_z\tau)d\tau \qquad \ldots.(52)$$

Write $t = v_z\tau$; $dt = v_z d\tau$

$$\therefore \quad I(\theta_2) = \frac{F^2}{2L}\int_{-\infty}^{\infty} e^{i\left[v_x t/v_z\right]}\phi(t)\,\frac{dt}{v_z}$$

$$= \frac{F^2}{2Lv_z}\int_{-\infty}^{\infty} e^{i(\tan\theta/2)t}\phi(t)dt$$

$$\sim \frac{F^2}{2Lv_z}\int_{-\infty}^{\infty} e^{i(\theta/2)t}\phi(t)dt \qquad \ldots.(53)$$

$$\text{INVERT } I(\theta_2) = \frac{F^2}{2Lv_z}\,2\pi\, f(\theta/2) \quad \text{where } f(.) \qquad \ldots.(54)$$

is the p.d.f. of slopes and thus SCATTERING IS GEOMETRICAL FOR ANY TYPE (C) g>>1 ROUGH SURFACE FOR WHICH THE ABOVE CONDITIONS ARE MET.

4.3.3. Mixed Roughness Models

Both beam scattering models are relevant to the following two illustrations of mixed rough surface models. Firstly, consider a model surface where a random Gaussian component is superimposed on a deterministic grooved component, to give the model profile shown:

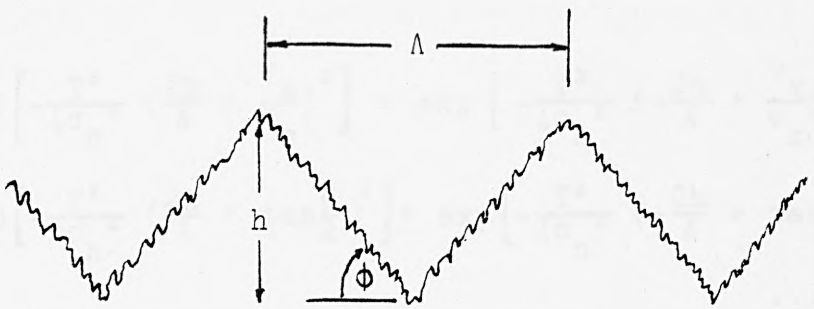

FIG. 4.3.13. Mixed Roughness Model Profile

Milana and Rasello [1981] introduced such a model, and suggested that the deterministic component is due to the shape of the tool forming the surface, whilst the random component is attributable to the cutting action.

Then $\rho\rho^* = \frac{F^2}{4L^2} \iint e^{iv_x(x_1 - x_2) + iv_z\{(\zeta_1 - \zeta_2) + \eta_1 - \eta_2\}} dx_1 dx_2$ ....(55)

where η_1, η_2 are Gaussian variates.

Taking mean values, and using the saddle point method:

$$E[\rho\rho^*] = \frac{F^2}{4L}\{\int_{-\infty}^{\infty} e^{iv_x\tau + iv_z\frac{2h}{\Lambda}\tau}.E(e^{iv_z(\eta_1 - \eta_2)})d\tau + \int_{\infty}^{\infty} e^{iv_x\tau - iv_z\frac{2h\tau}{\Lambda}}.E(e^{iv_z(\eta_1 - \eta_2)})d\tau\} \quad ....(56)$$

$$= \frac{F^2}{4L}\{\int_{-\infty}^{\infty} e^{i(v_x + v_z\frac{2h}{\Lambda})\tau}\ e^{-\sigma_n^2 v_z^2 \tau^2/T^2} d\tau + \int_{-\infty}^{\infty} e^{i(v_x - v_z\frac{2h}{\Lambda})\tau}\ e^{-\sigma_n^2 v_z^2 \tau^2/T^2} d\tau$$

$$= \frac{F^2}{2L}\{\int_{o}^{\infty} \cos(v_x + v_z\frac{2h}{\Lambda})\tau\ e^{-\sigma_n^2 v_z^2 \tau^2/T^2} d\tau + \int_{o}^{\infty} \cos(v_x - v\frac{2h}{\Lambda})\tau\ e^{-\sigma_n^2 v_z^2 \tau^2/T^2} d\tau$$

$$= \frac{F^2\, T\sqrt{\pi}}{2L\sigma_n v_z}\left\{ e^{-(v_x + v_z\frac{2h}{\Lambda})^2/4\sigma_n^2 v_z^2/T^2} + e^{-(v_x - v_z\frac{2h}{\Lambda})^2/4\sigma_n^2 v_z^2/T^2}\right\}$$

$$= \frac{F^2\, T\sqrt{\pi}}{2L\sigma_n v_z}\left\{ \exp\left[-\frac{T^2}{4\sigma_n^2}\left(\frac{2h}{\Lambda} + \frac{v_x}{v_z}\right)^2\right] + \exp\left[-\frac{T^2}{4\sigma_n^2}\left(-\frac{2h}{\Lambda} + \frac{v_x}{v_z}\right)^2\right]\right\}$$

$$= \frac{F^2\, T\sqrt{\pi}}{2L\sigma_n v_z}\left\{ \exp\left[-\frac{T^2}{4\sigma_n^2}\left(\frac{2h}{\Lambda} + \tan\frac{\tilde{\theta}}{2}\right)^2\right] + \exp\left[-\frac{T^2}{4\sigma_n^2}\left(-\frac{2h}{\Lambda} + \tan\frac{\tilde{\theta}}{2}\right)^2\right]\right\}$$

....(57)

Thus the mean scattered field in approximately the sum of two Gaussians. In particular, the specular intensity at ($\tilde{\theta} = 0$) is

$$\frac{F^2 T\sqrt{\pi}}{L\sigma_n v_z} \exp\left[-\frac{T^2 h^2}{\sigma_n^2 \Lambda^2}\right] \qquad ....(58)$$

a result utilised by Milana and Rasello [1981].

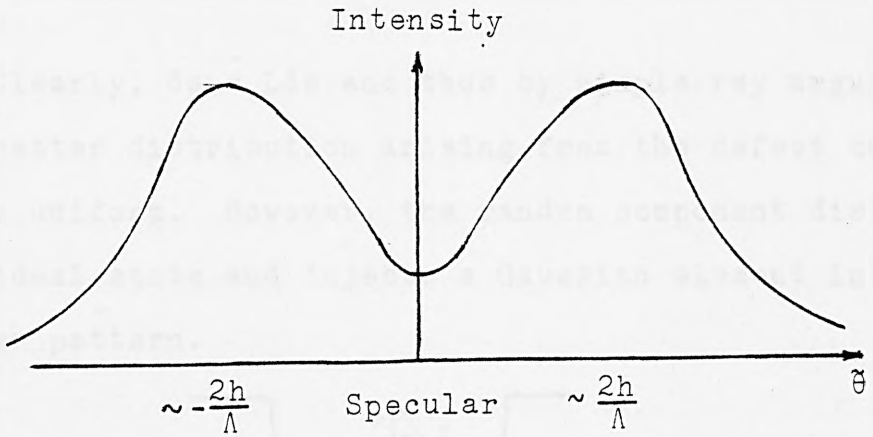

FIG. 4.3.14. Mean Total Intensity for Grooved Surfaces

If we set h = 0 in (57) we have the case of incoherent scattering from a Gaussian surface, as discussed previously.

We see that the deterministic component governs the location of the scattering modes, whilst the spread of the scatter is dictated by the random term.

Secondly, consider the modelling of a large struc-

ture defect on a rough surface, that is, a deterministic defect component with superimposed random surface roughness.

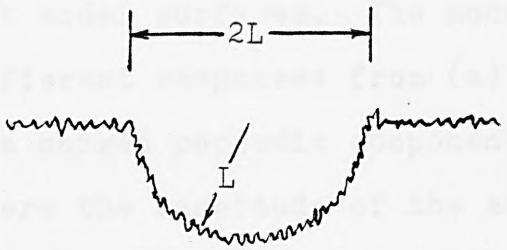

FIG. 4.3.15. Semi-Circular Defect with Surface Noise

Clearly, $\delta s = L\delta\phi$ and thus by simple ray arguments, the scatter distribution arising from the defect component is uniform. However, the random component disturbs this ideal state and injects a Gaussian element into the scatter pattern.

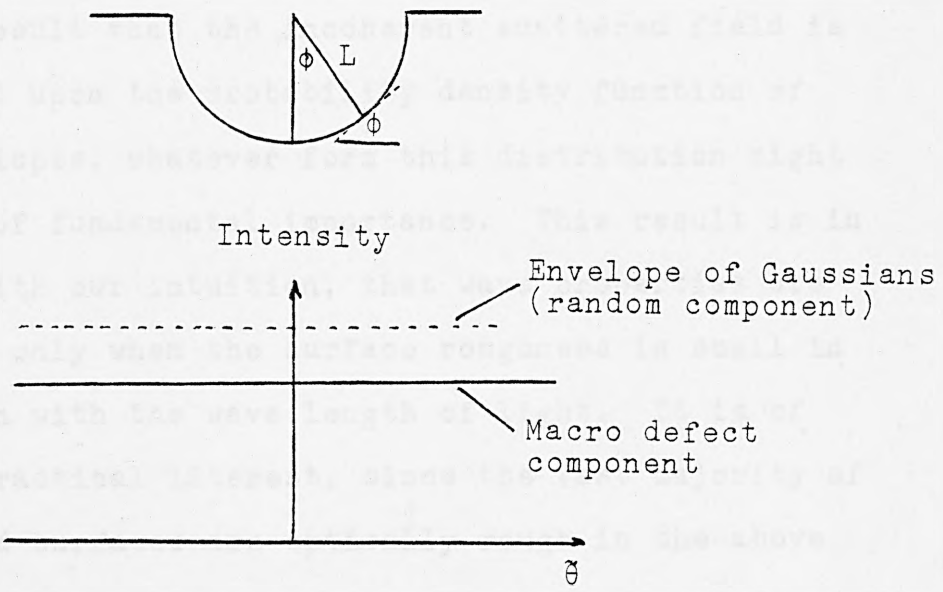

FIG. 4.3.16. Mean Total Intensity from Semi-Circular Indentation

4.4 Conclusions

Although differing fundamentally in several important mathematical respects, the MIRROR FACET and the WAVE THEORY models substantially agree when applied to important model surfaces. The models predict significantly different responses from (a) profile surfaces possessing a marked periodic component or (b) from profiles where the magnitude of the surface roughness is comparable with, or less than the wavelength of light.

The "in-phase" characteristics of reflected wavefronts associated with type (a) and the beam interaction with the fine structure of (b) are plainly dominant in the case of the wave theory model.

For surface profiles possessing a large mechanical roughness structure the models exhibit close agreement. For very rough purely random surfaces (type (c) surfaces with $g>>1$ as defined earlier : in practical terms this means surfaces with $\sigma>0.2\mu m$ for normal incidence), the general result that the incoherent scattered field is consequent upon the probability density function of surface slopes, whatever form this distribution might take, is of fundamental importance. This result is in keeping with our intuition, that wave properties are important only when the surface roughness is small in comparison with the wave length of light. It is of immense practical interest, since the vast majority of engineered surfaces are optically rough in the above sense.

APPENDIX 4A

Glossary of Terms and Symbols

Refer to Chapter 4.1. p42 for the scattering geometry.

$$v_x = \frac{2\pi}{\lambda}(\sin\theta_1 - \sin\theta_2) \quad (v_x = 0 \text{ in specular direction})$$

$$v_z = -\frac{2\pi}{\lambda}(\cos\theta_1 + \cos\theta_2)$$

$$F = \frac{\sec\theta_1(1 + \cos(\theta_1 + \theta_2))}{\cos\theta_1 + \cos\theta_2} \; ; \; F = 1 \text{ in specular direction}$$

N.B. F = 1 for normal incidence.

$$\rho_o^2 = \sin^2 c\, v_x L \qquad \left(\text{sinc} v_x L = \frac{\sin v_x L}{v_x L}\right)$$

$\zeta(x)$ = profile equation

σ^2 = variance of height distribution

$w(z)$ = p.d.f. of surface height

$\chi(\;)$ = characteristic function of surface height

i.e. $$\chi(v_z) = \int_{-\infty}^{\infty} w(z)\, e^{iv_z z}\, dz$$

$C(\tau)$ = autocorrelation function of surface height

T = correlation length

i.e. given by $C(T) = 1/e$

$W(z_1, z_2)$ = joint distribution of surface height

$\chi_2(v_z, -v_z)$ = joint characteristic function of surface height

i.e. $$\chi_2(v_z, -v_z) = \int_{-\infty}^{\infty}\int_{-\infty}^{\infty} W(z_1, -z_2)\, e^{iv_z(z_1 - z_2)}\, dz_1 dz_2$$

$$g = v_z^2 \sigma^2.$$

The magnitude of g characterises the surface:

Type (A) $g \ll 1$	:	Type (B) $g \sim 1$	:	Type (C) $g \gg 1$
very smooth		moderately rough		rough

APPENDIX 4B

(4) Saw-Tooth Profiles

(i) Consider firstly a surface waveform consisting of just three inclined optical flats. (The methodology will then be generalised to consider 2n+1 such flats.)

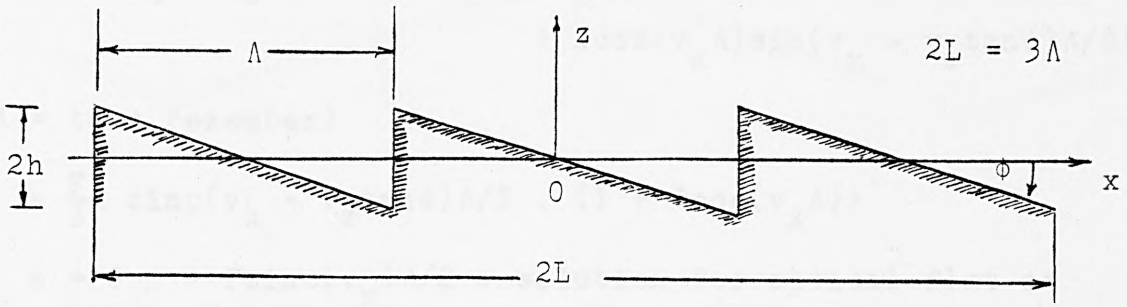

$$= \frac{F}{2L}\int_{-L}^{L} e^{i(\underline{v}.\underline{r})}dx$$

$$= \frac{F}{2L}\{\int_{-3\Lambda/2}^{-\Lambda/2} e^{i(v_x x + v_z(-2h - x\tan\phi)}dx + \int_{-\Lambda/2}^{\Lambda/2} e^{i(v_x x + v_z \tan\phi)}dx + \int_{\Lambda/2}^{3\Lambda/2} e^{i(v_x x + v_z(2h - x\tan\phi)}dx\}$$

$$= \frac{F}{3\Lambda}\left[e^{-i2hv_z}\int_{-3\Lambda/2}^{-\Lambda/2} G(x)dx + \int_{-\Lambda/2}^{\Lambda/2} G(x)dx + e^{i2hv_z}\int_{\Lambda/2}^{3\Lambda/2} G(x)dx\right]$$

on expressing the integrand $e^{i(v_x - v_z\tan\phi)x}$ as $G(x)$

If we write $\int G(x)dx = H(x)$ $\left(= \frac{e^{i(v_x - v_z\tan\phi)x}}{i(v_x - v_z\tan\phi)}\right)$ then

$$\rho = \frac{F}{3\Lambda}\left[e^{-i2hv_z}\{H(-\Lambda/2) - H(-3\Lambda/2)\} + H(\Lambda/2) - H(-\Lambda/2) + e^{i2hv_z}\{H(3\Lambda/2) - H(\Lambda/2)\}\right]$$

Rearranging and pairing appropriate terms,

$$\rho = \frac{2F}{3\Lambda(v_x - v_z\tan\phi)}\{\sin(v_x - v_z\tan\phi)\Lambda/2 + \sin[(v_x - v_z\tan\phi)3\Lambda/2 + 2hv_z] - \sin[(v_x - v_z\tan\phi)\Lambda/2 + 2hv_z]\}$$

$$\rho = \frac{2F}{3\Lambda(v_x - v_z\tan\phi)}\{\sin(v_x - v_z\tan\phi)\Lambda/2 + 2\cos(v_x\Lambda)\sin(v_x - v_z\tan\phi)\Lambda/2\}$$

($2h/\Lambda = \tan\phi$ remember)

$$= \frac{F}{3}.\,\mathrm{sinc}(v_x - v_z\tan\phi)\Lambda/2\,.\,\{1 + 2\cos(v_x\Lambda)\}$$

N.B. $\phi \to 0$ $\rho \to F\mathrm{sinc}(v_x)\Lambda/2$: solution for optical flat at normal incidence.

Only non-zero contribution is in direction specified by $v_x - v_z\tan\phi = 0$ i.e. $\theta_2 = \theta_1 + 2\phi$, the specular direction.

Again, considering simple ray principles,

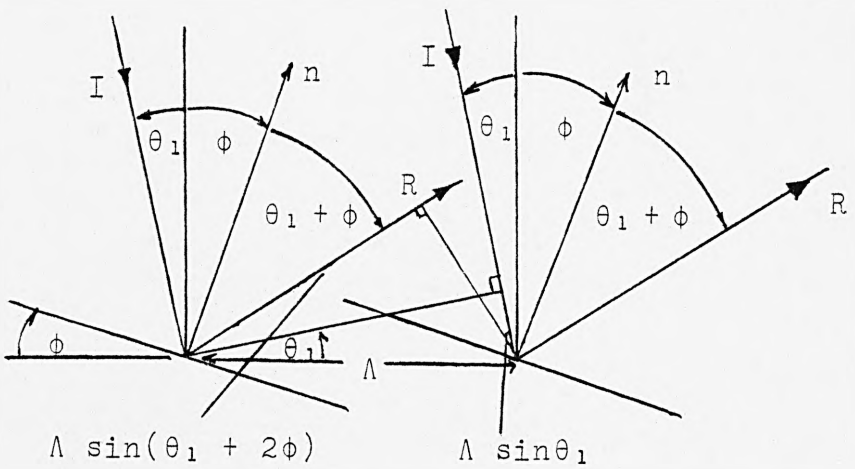

Path difference of reflected rays

$$= \Lambda\sin(\theta_1 + 2\phi) - \Lambda\sin\theta_1$$

$$= \Lambda(\sin(\theta_1 + 2\phi) - \sin\theta_1)$$

$$= \Lambda v_x \cdot \frac{\lambda}{2\pi} = m\lambda \quad \text{for m an integer} \Rightarrow \Lambda v_x = 2\pi m$$

i.e. in phase condition for reinforcement

(ii)

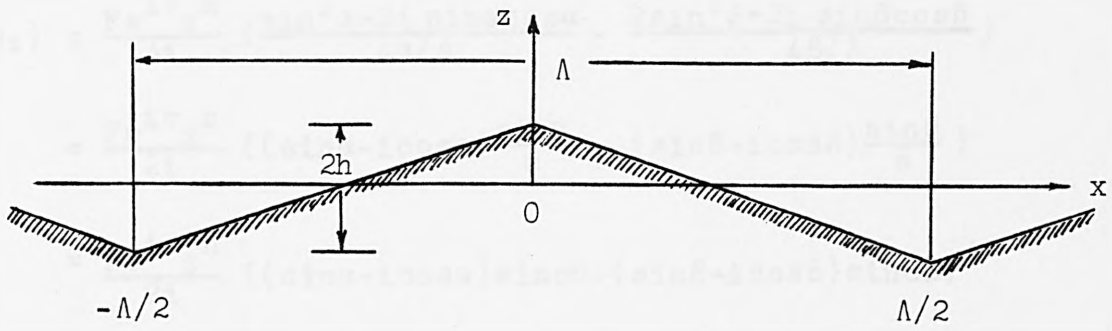

$$\rho(\theta_2) = \frac{F}{\Lambda}\left\{\int_{-\Lambda/2}^{o} e^{i\{v_x x + v_z(h + x\tan\phi)\}}dx + \int_{o}^{\Lambda/2} e^{i\{v_x x + v_z(h - x\tan\phi)\}}dx\right.$$

$$= \frac{F}{\Lambda} e^{iv_z h}\left\{\int_{-\Lambda/2}^{o} e^{i(v_x + v_z\tan\phi)x}\,dx + \int_{o}^{\Lambda/2} e^{i(v_x - x\tan\phi)x}\,dx\right\}$$

$$= \frac{F}{\Lambda} e^{iv_z h}\left\{\frac{1 - e^{-i(v_x + v_z\tan\phi)\Lambda/2}}{i(v_x + v_z\tan\phi)} + \frac{e^{i(v_x - v_z\tan\phi)\Lambda/2} - 1}{i(v_x - v_z\tan\phi)}\right\}$$

$$= \frac{Fe^{iv_x h}}{\Lambda i}\left\{\frac{1 - \cos(v_x + v_z\tan\phi)\Lambda/2 - i\sin(v_x + v_z\tan\phi)\Lambda/2}{(v_x + v_z\tan\phi)} + \frac{\cos(v_x - v_z\tan\phi)\Lambda/2 - 1 + i\sin(v_x - v_z\tan\phi)\Lambda/2}{(v_x - v_z\tan\phi)}\right\}$$

Write $(v_x + v_z\tan\phi)\frac{\Lambda}{4} = \alpha$ and $(v_x - v_z\tan\phi)\frac{\Lambda}{4} = \beta$ to shorten the expressions.

$$\rho(\theta_2) = \frac{Fe^{iv_z h}}{\Lambda i}\left\{\frac{\sin^2\alpha - 2i\sin\alpha\cos\alpha}{4\alpha/\Lambda} - \frac{2\sin^2\beta + 2i\sin\beta\cos\beta}{4\beta/\Lambda}\right\}$$

$$= \frac{Fe^{iv_x h}}{2i}\left\{(\sin\alpha - i\cos\alpha)\frac{\sin\alpha}{\alpha} - (\sin\beta - i\cos\beta)\frac{\sin\beta}{\beta}\right\}$$

$$= \frac{Fe^{iv_z h}}{2i}\left\{(\sin\alpha - i\cos\alpha)\operatorname{sinc}\alpha - (\sin\beta - i\cos\beta)\operatorname{sinc}\beta\right\}$$

For $\Lambda >> \lambda$, the sinc(.) terms vanish except in the close proximity of (.) = 0.

CHAPTER 5

DATA ACQUISITION BY EXPERIMENTAL RIGS

Abstract

The experimental work for this study was conducted in two parts:

(i) The back scatter radiation from a rough surface arising from an interrogating source of electro-magnetic radiation was recorded. A number of metal surfaces was studied for which polar diagrams were obtained. The experimental methods involved in the recording of three-dimensional polar diagrams are described, and the associated hardware and software of a semi-automated system of data gathering is fully documented.

(ii) Three-dimensional surface topography data was collected and collated. The design, construction and interfacing of a semi-automatic system for mapping a metal surface is described. The system incorporated a standard talysurf-10 stylus probe instrument to record data as a series of profile traces, (parallel if desired - manual set up allows for any configuration of traces to be recorded). On-line digitisation and recording were achieved. The talysurf-10 is capable of mapping any region with a defining dimension of up to 50 mm, whilst transference of data to magnetic tape virtually places no limit on the number of height samples which may be acquired.

5.1 Recording Back Scatter Intensity Data

5.1.1 Introduction

The distribution of the field of the back scatter radiation from a rough surface, depends intimately on the surface properties. The two models described in Chapter 4 attempt to quantify this relationship. With the long-term aim of investigating the validity of both models, a sequence of experiments was conducted on various specimens of different material: brass, copper, mild steel, etc., whose surface had been ground or rolled flat. Various grades of finish were investigated and in some instances 'defects' were deliberately introduced : scratch marks were made by scoring the surface and in others, circular indentations of controlled depth and diameter were made using appropriate bits.

5.1.2 The Laser Rig

For a number of reasons a laser beam was used as the interrogating signal: a laser beam is easily controlled as a fine pencil of parallel rays to be focused upon a clearly definable region of surface, as well as being the tool of several investigations into the general area of surface inspection, some of which were reported in Chapters 2 and 3. A helium-neon laser of 628A^{o} was used, being both safe to operate and cheap in terms of its capital cost and use of power. The laser projected a circular beam of 2 mm diameter coherent light. Such a coherent source of monochromatic light, as opposed to a source of white light, gives rise to 'speckle' phenomena due to interference effects. The illuminated region appears to be composed of alternate light and dark areas as the consequence of the wavefronts interfering with

one another. Transducers measuring the scattered field need to average the intensity of the reflected beam over a sufficient number of speckles.

The experimental rig shown in the diagram below 5.1.1 was adapted from previous users' rigs (this study formed part of a continuing programme of work conducted at the City University), and consequently some limiting features of the design follow from the fact that the rig was not entirely purpose built. The apparatus was mounted on an optical bench with the laser at one end. Once various alignment procedures had been pursued the laser was locked into position. It would have been highly advantageous to be able to rotate the laser beam to achieve greater flexibility.

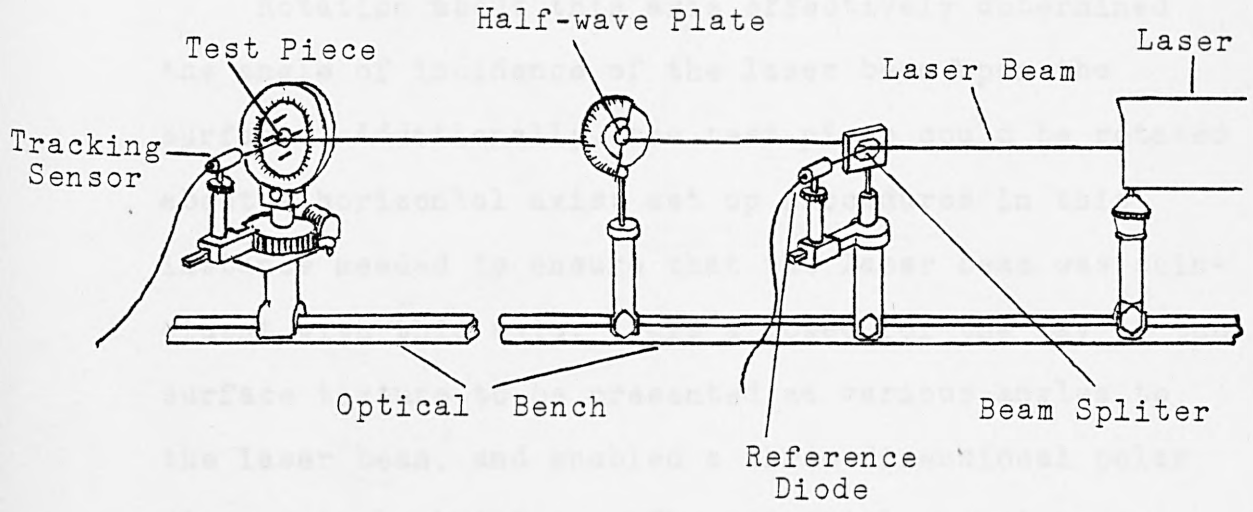

FIG. 5.1.1. THE LASER RIG : Illustrative layout of apparatus. (Not to scale.)

However this would have been an extremely difficult design feature to incorporate. The full set-up operations are described later in the form of an operations manual; for the moment we shall concern ourselves purely with the essential hardware constituting the rig.

A parallel beam of plane polarised light was split: one half provided a reference beam of the laser output and was monitored by a photo diode, the other half encountered a half-wave plate which could rotate the plane of polarisation. A θ^{o} rotation of the plate resulted in a $2\theta^{o}$ rotation of the plane of polarisation. The polarised beam incident upon the specimen was back scattered and the scattered field recorded by a second photo diode sensor. Care needed to be taken when mounting the specimen within its housing to ensure that the vertical axis of rotation of the mounting was in the plane of the test piece.

Rotation about this axis effectively determined the angle of incidence of the laser beam upon the surface. Additionally, the test piece could be rotated about a horizontal axis: set up procedures in this instance needed to ensure that the laser beam was coincident with this axis. This allowed for the lay of the surface texture to be presented at various angles to the laser beam, and enabled a three-dimensional polar diagram to be built up. The essential geometry as described is illustrated in Fig. 5.1.2.

5.1.3. The Semi-Automated System

A semi-automated system of data gathering was devised to remove, in large measure, the tedium of data

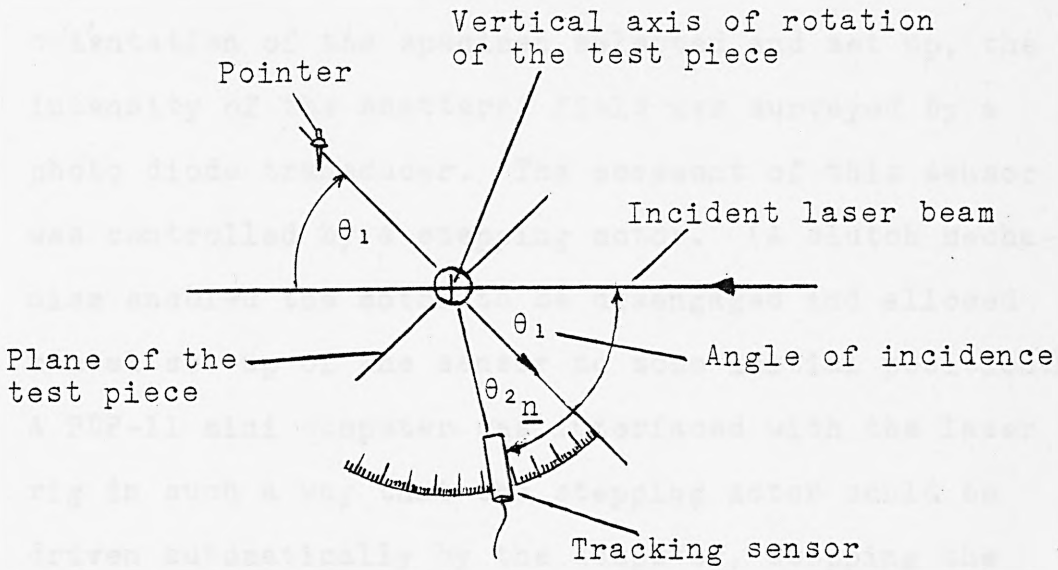

(i) Horizontal configuration

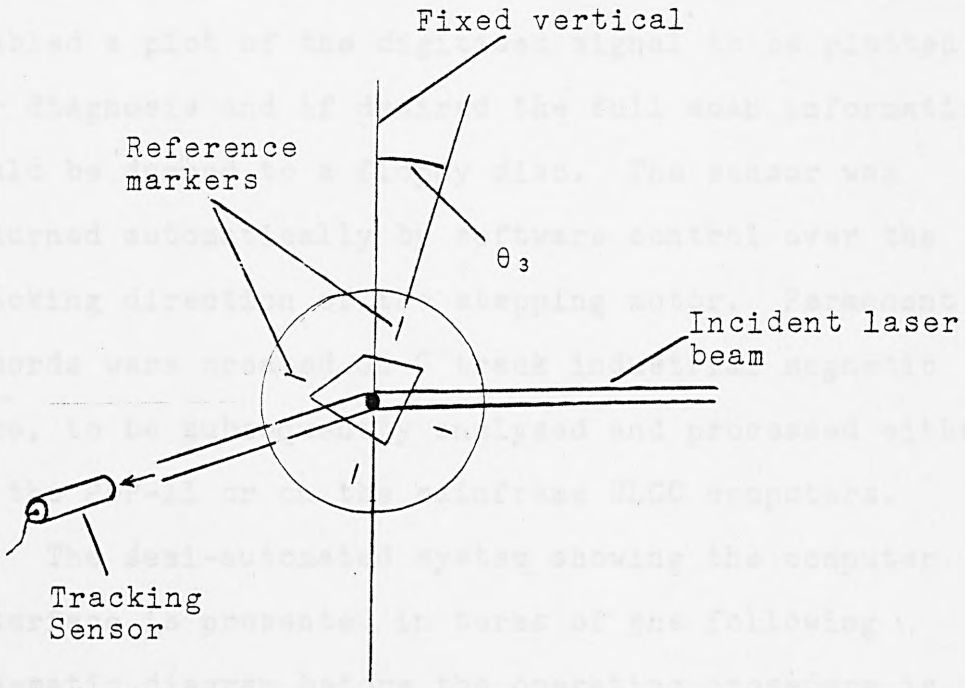

(ii) Vertical configuration

FIG. 5.1.2. Incident Geometry of the Laser beam on the test piece

gathering. With the laser and test piece correctly adjusted, i.e. the appropriate angles of incidence and orientation of the specimen selected and set up, the intensity of the scattered field was surveyed by a photo diode transducer. The movement of this sensor was controlled by a stepping motor. (A clutch mechanism enabled the motor to be disengaged and allowed manual set-up of the sensor to some initial position.) A PDP-11 mini computer was interfaced with the laser rig in such a way that the stepping motor could be driven automatically by the computer, stepping the sensor through appropriate sampling intervals. The sensor information was digitised automatically at the ADC board and thence recorded into core. At the same sample instants, the reference sensor information was recorded for immediate comparison. Computer graphics enabled a plot of the digitised signal to be plotted for diagnosis and if desired the full scan information could be dumped to a floppy disc. The sensor was returned automatically by software control over the tracking direction of the stepping motor. Permanent records were created on 7 track industrial magnetic tape, to be subsequently analysed and processed either on the PDP-11 or on the mainframe ULCC computers.

The semi-automated system showing the computer interface is presented in terms of the following schematic diagram before the operating procedure is described in more detail.

5.1.4. Laser Rig Operation, Data Acqusition and Recording

A sample worksheet of operations is provided in

Fig. 5.1.4. whilst a flow chart of the total system operational procedure is given in Fig. 5.1.5.

We now examine the utilisation of the laser rig and the technical details of the experimentation.

Full program documentation is listed in Appendix 5A.

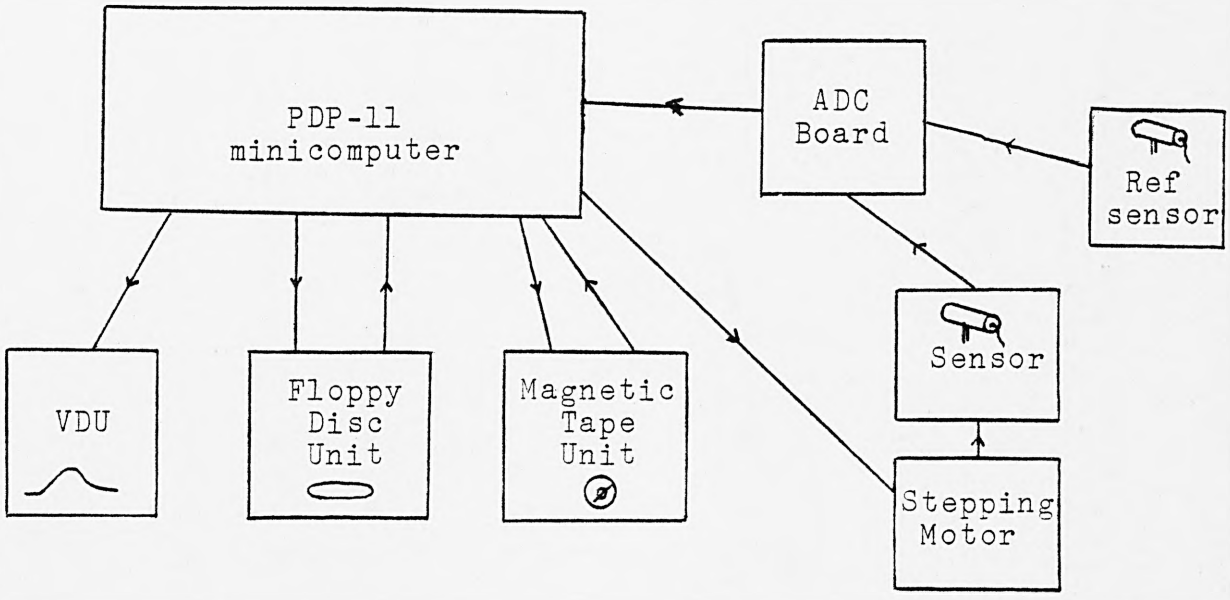

FIG. 5.1.3. Schematic Diagram of the Semi-Automatic Recording System

A. Preliminary Checks Completed?

(i) Alignment of laser spot
(ii) Test piece flat and in axial plane
(iii) Sensors adjusted for maximum response with appropriate gain settings.
(iv) Channels correctly selected.

B. Laser Rig Set-up Sheet

(i) Specimen Identifier Label

(ii) Choice of graphics scale parameters (run information only)

Gain Channel 0 ☐ Gain Channel 1 ☐

Graph Scale ☐ Diff. Magnification ☐

(iii) Rig Set-up variables

(a) θ_1 = ☐

Angle of incidence selected and mounting locked in position. ☐

(b) θ_3 = ☐ $\frac{1}{2}\lambda$-plate ☐

Set-up initial orientation of test piece and corresponding setting of $\frac{1}{2}\lambda$-plate.

(c) Number of (steps) θ_2's n = ☐

(d) Initial (set-up) value of θ_2 = ☐

C. Run

$\theta_3{}^\circ$	$\frac{1}{2}\lambda$	Tick	$\theta_3{}^\circ$	$\frac{1}{2}\lambda$	Tick	$\theta_3{}^\circ$	$\frac{1}{2}\lambda$	Tick

D. Next Step

Set up new θ_1 etc. or close file.

File closed ☐

FIG. 5.1.4. Laser Rig Worksheet

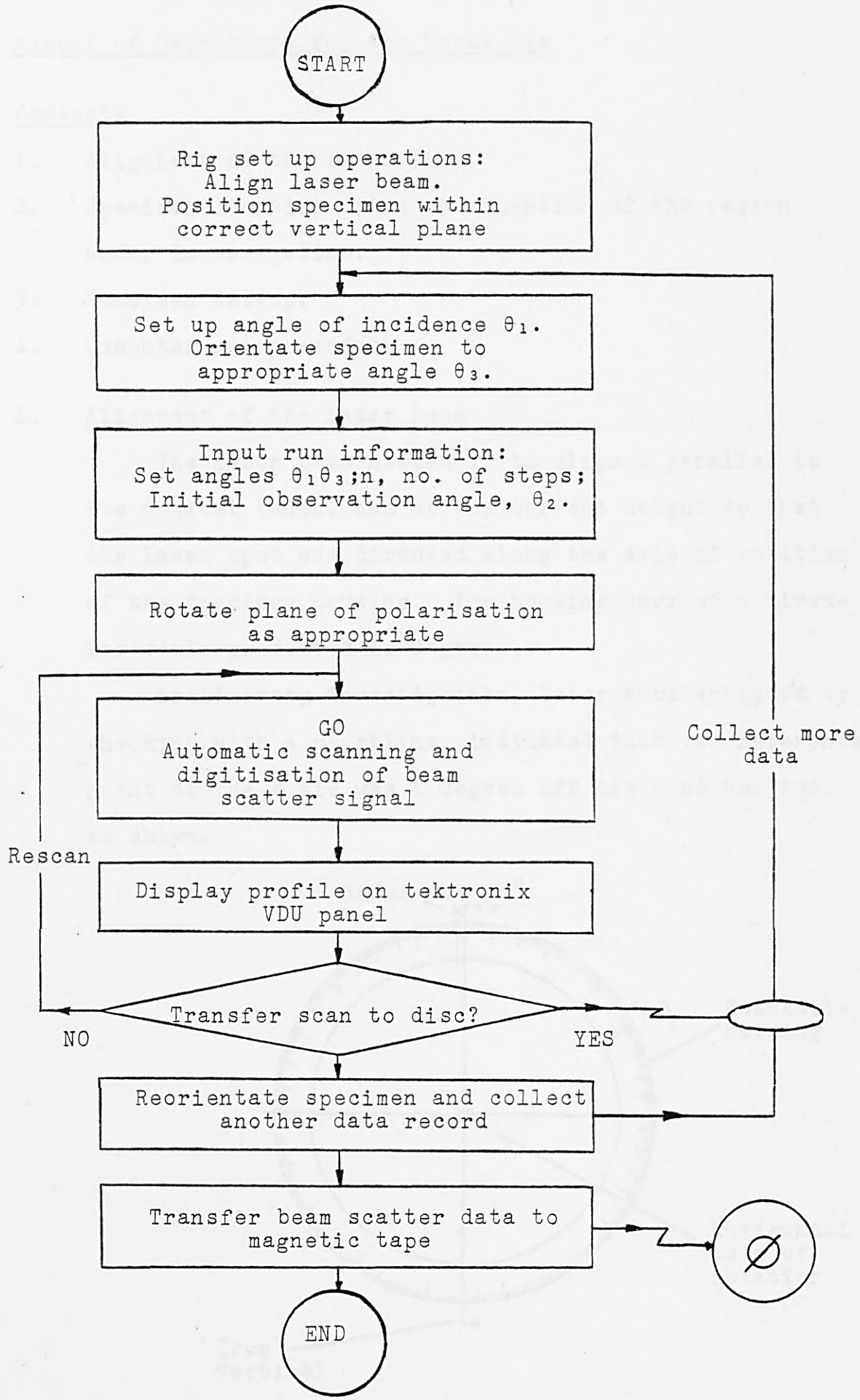

FIG. 5.1.5. Flow Chart of Operations of the Laser Rig

Manual of Operations for the Laser Rig

Contents

1. Alignment of the laser beam.
2. Specimen identification and location of the region under investigation.
3. Specimen set-up.
4. Computer run procedure.

1. Alignment of the laser beam

The laser beam needed to be aligned parallel to the optical bench, and at the correct height so that the laser spot was directed along the axis of rotation of the specimen housing. The housing carried a circular scale graduated in degrees.

Preliminary investigation, later substantiated by checking with a plumbline, indicated that the reference point of the scale was 1 degree off the true vertical as shown.

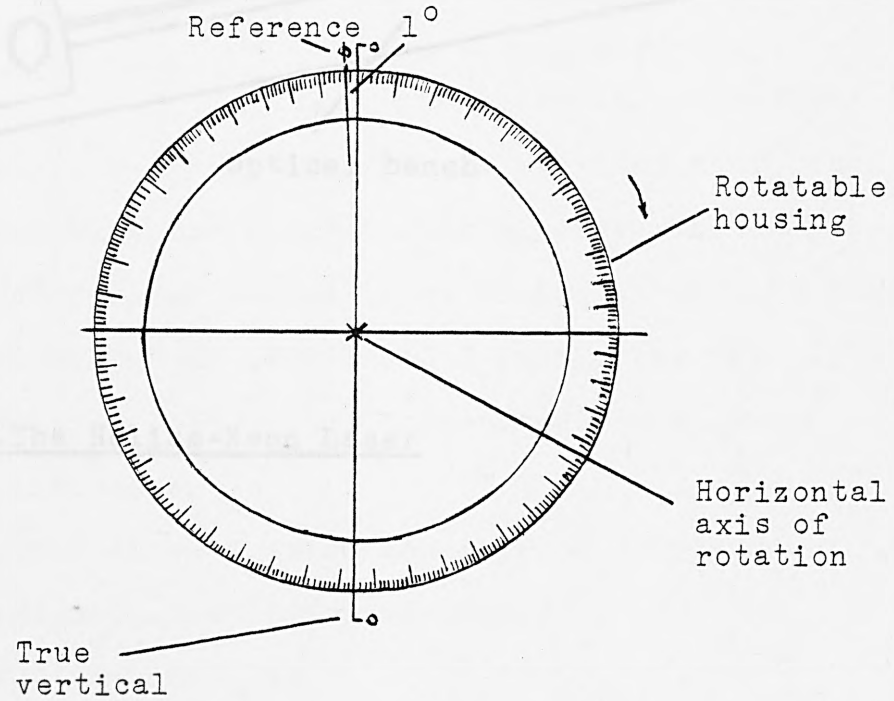

FIG. 5.1.6. Rotation Axes of Specimen Housing

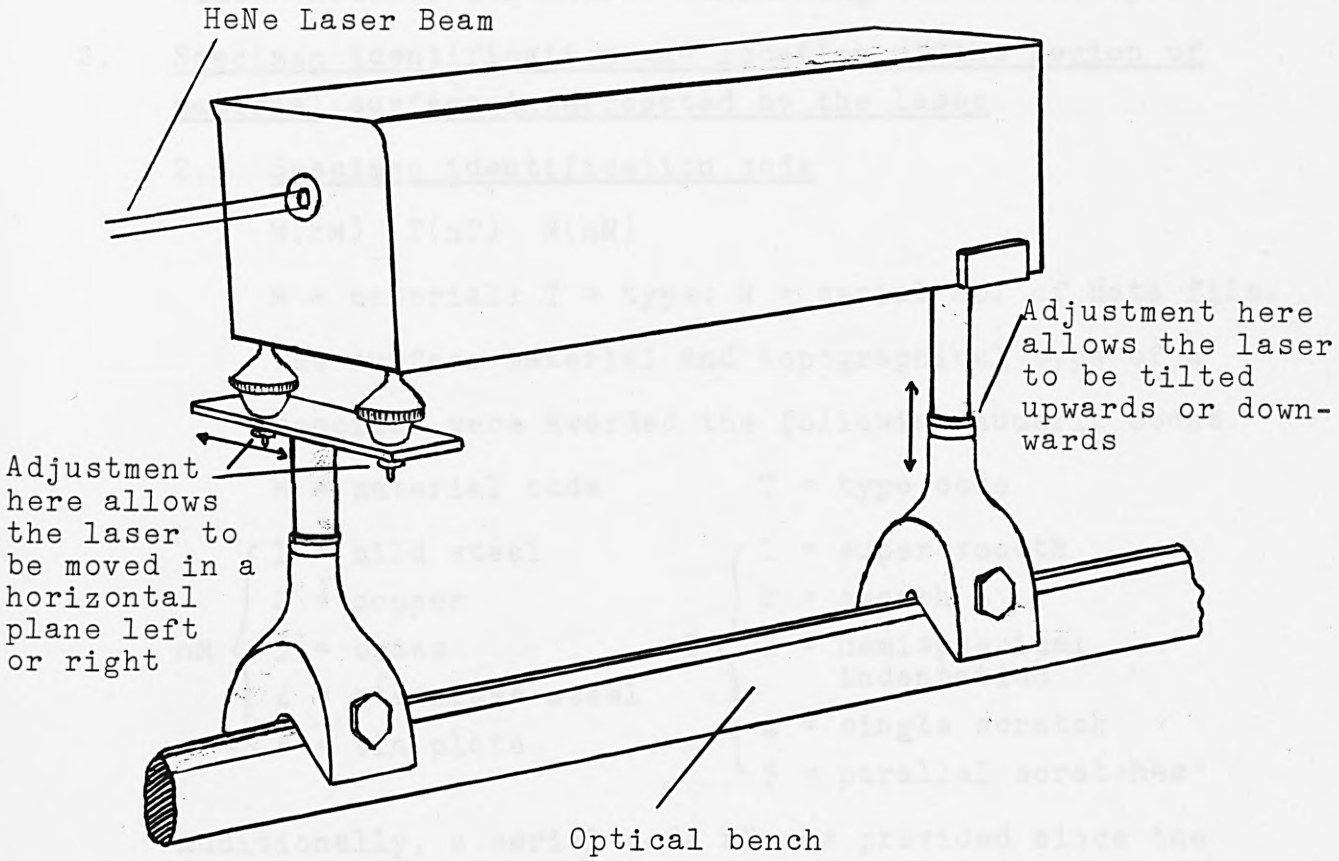

FIG. 5.1.7.The Helium-Neon Laser

Adjustment of the laser was made so that the spot was centred on the true horizontal line and parallel with the optical bench, using the "pin-hole" plate and adjustment screws on the front and back columns of the laser.

Locking rings were then secured in position. (Once aligned the beam ought to be set up for all time - however continuous monitoring was necessary.)

2. Specimen identification and location of the region of material surface interrogated by the laser

2.1 Specimen identification code

M(nM) T(nT) N(nN)

M = material; T = type; N = serial no. of data file.

The surface material and topographical type of a specimen were awarded the following numeric codes.

M = material code

nM
- 1 = mild steel
- 2 = copper
- 3 = brass
- 4 = stainless steel
- 5 = tin plate

T = type code

nT
- 1 = super smooth
- 2 = smooth
- 3 = hemispherical indentation
- 4 = single scratch
- 5 = parallel scratches

Additionally, a serial code nN was provided since the data acquisition for a particular specimen was lengthy, and the data volume needed to be broken up into 'blocks'. The serial number nN identified a particular data file but in practice frequently corresponded to a given angle of incidence.

Laser scatter files created and held on floppy discs are addressed in the following manner:

M(nM)T(nT)N(nN).LST

2.2 Location of the region to be scrutinised by the laser beam

Location marks were made and numbered so as to define the orientation of the specimen in the manner shown. The marks locate the 'centre' of the region of interest. As described in 5.2, a square region, (dimensions 3 mm x 3 mm), was mapped by a talysurf-10 machine. Parallel profiles were traced over the metal surface in the direction $270^{\circ} \rightarrow 90^{\circ}$, and it was necessary to relocate, as precisely as possible, the area covered by the laser spot.

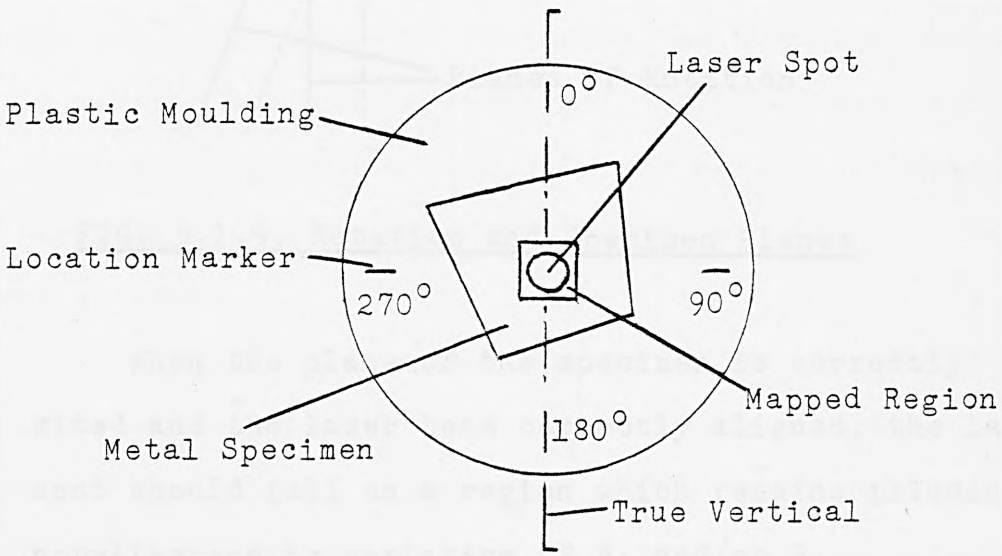

FIG. 5.1.8 Location of the Laser Spot

3. Specimen Set-up

Four spring-loaded screws were adjusted so that the surface of the test piece included the fixed vertical axis of rotation of the housing. (We recall that this mode of rotation governs variation of the angle of incidence.) A micrometer depth gauge was employed to facilitate the adjustment.

As a check, once the adjustment has been made, the incident laser spot should not appear to drift to and fro as θ_1 varies (see diagram).

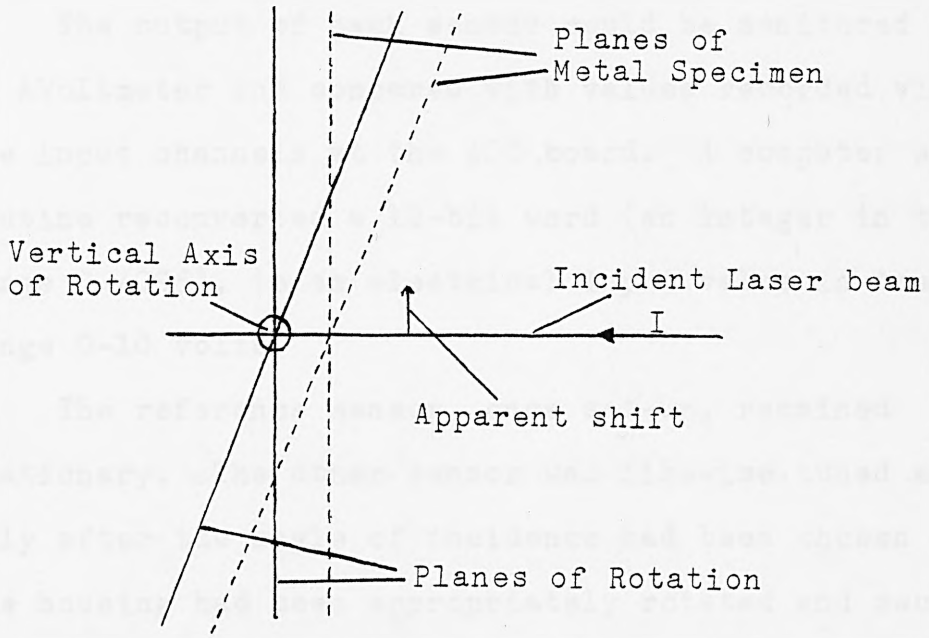

FIG. 5.1.9. Rotation and Specimen Planes

When the plane of the specimen is correctly sited and the laser beam correctly aligned, the laser spot should fall on a region which remains illuminated notwithstanding variation of θ_1 and/or θ_3.

4. Computer Run Procedure

The computer software is fully described in the Appendix 5A with a detailed operations manual for running the data acquisition and data recording program LASDAT.FOR. Here we describe the tuning of the sensors and the formulations of certain transformations for converting scale readings or settings taken at the rig, to incident or scatter geometry configurations.

The two photo-diode sensors had fine adjustment screws which could raise or lower them vertically, as well as being mounted on horizontal arms which allowed for rotation in the horizontal plane. (See Fig. 5.1.12)

The output of each sensor could be monitored by an AVoltmeter and compared with values recorded via the input channels at the ADC board. A computer sub-routine reconverted a 12-bit word (an integer in the range 0-4095), to an electrical input value in the range 0-10 volts.

The reference sensor, once set-up, remained stationary. The other sensor was likewise tuned manually after the angle of incidence had been chosen and the housing had been appropriately rotated and secured. (A pointer, rigidly attached to the housing, traversed a horizontal scale graduated in degrees, and thus θ_1 was selected.)

The monitoring sensor was moved manually to an off-specular position θ_2 and the clutch engaged. The initial setting of θ_2 was read off from the horizontal circular scale and was such that the forwards (clockwise) action of the stepping motor drove θ_2 through the specular $\theta_2 = \theta_1$ angle. (Incidently 100 steps of the stepping motor propelled the sensor through 4 degrees.)

For the rig, normal incidence coincided with the pointer reading 343 degrees. On this basis, LASDAT.FOR automatically converted pointer readings to the appropriate θ_1, θ_2 angles. viz:

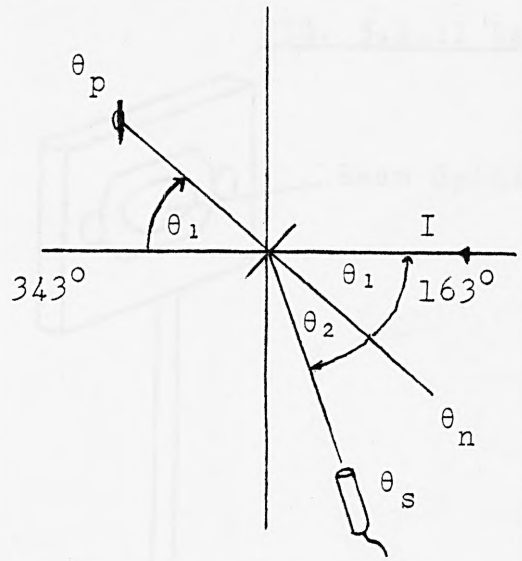

$\theta_1 = 343^\circ - \theta_p$

$\theta_n = 163^\circ - \theta_1$

$\theta_2 = \theta_n - \theta_s$

where θ_p and θ_s are pointer and sensor angles as read directly from the scale, and θ_n defines the direction of the normal.

FIG. 5.1.10. Incident and Scatter Angles

A half-wave plate was employed to govern the plane of polarisation of the laser beam. A circular scale mounted with the plate ensured precise control over this aspect of the incident radiation.

When set-up with the reference set at 72 degrees the half-wave plate provided for an emergent laser beam which was vertically polarised. The fast and slow directions were then mutually orientated at 45 degrees to the vertical.

If desired, the plane of polarisation could be rotated in sympathy with the θ_3 rotation of the specimen (the plane of polarisation rotating with the rotation of the surface texture. The necessary rotation of the half-wave plate for this to be accomplished was displayed during the computer run. For other than normal incidence, the computation is non-trivial and the geometrical background supporting this portion of program software is included in Appendix 5A.

FIG. 5.1.11 Laser Beam Splitting Mirror

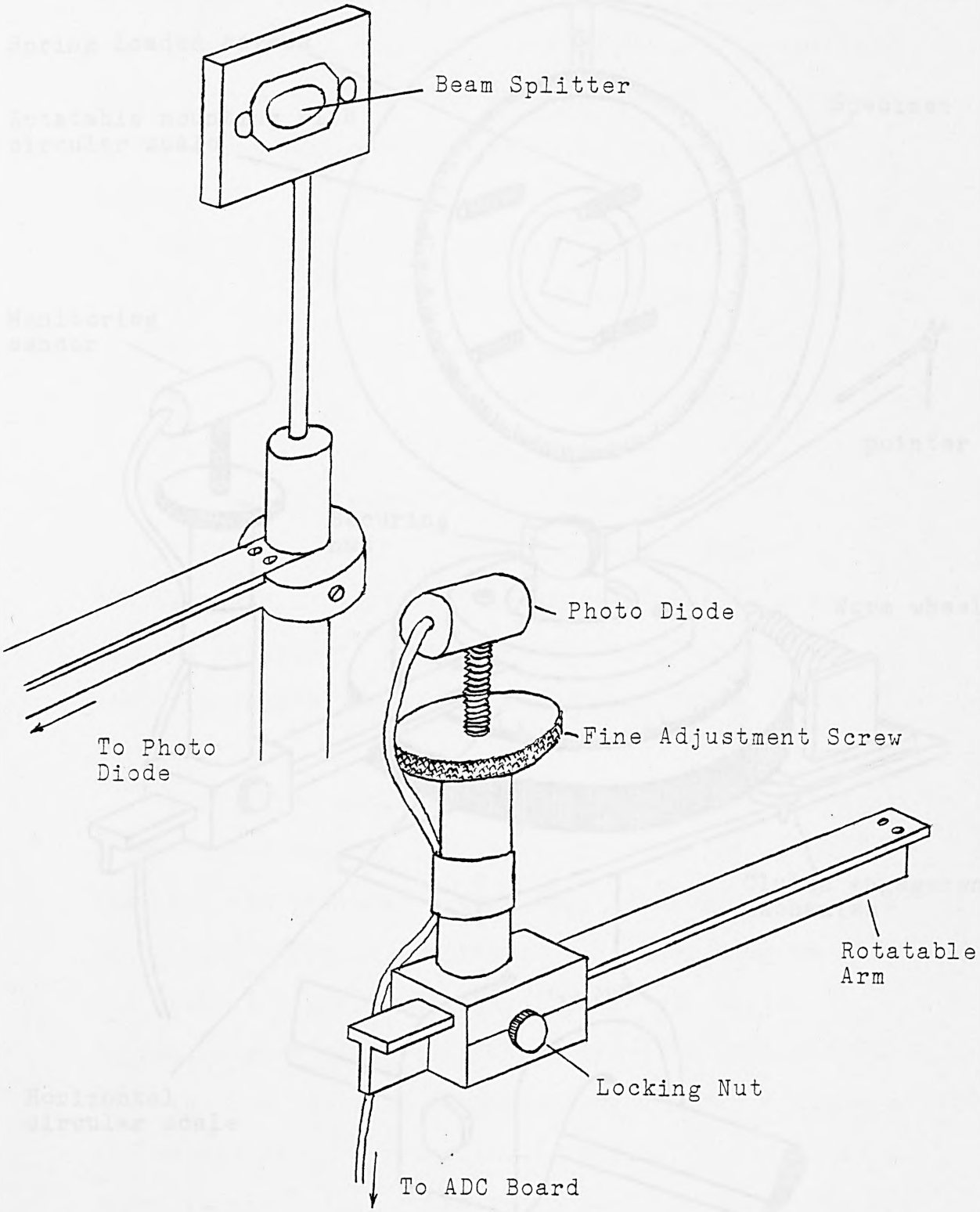

FIG. 5.1.12 Photo Diode Sensor

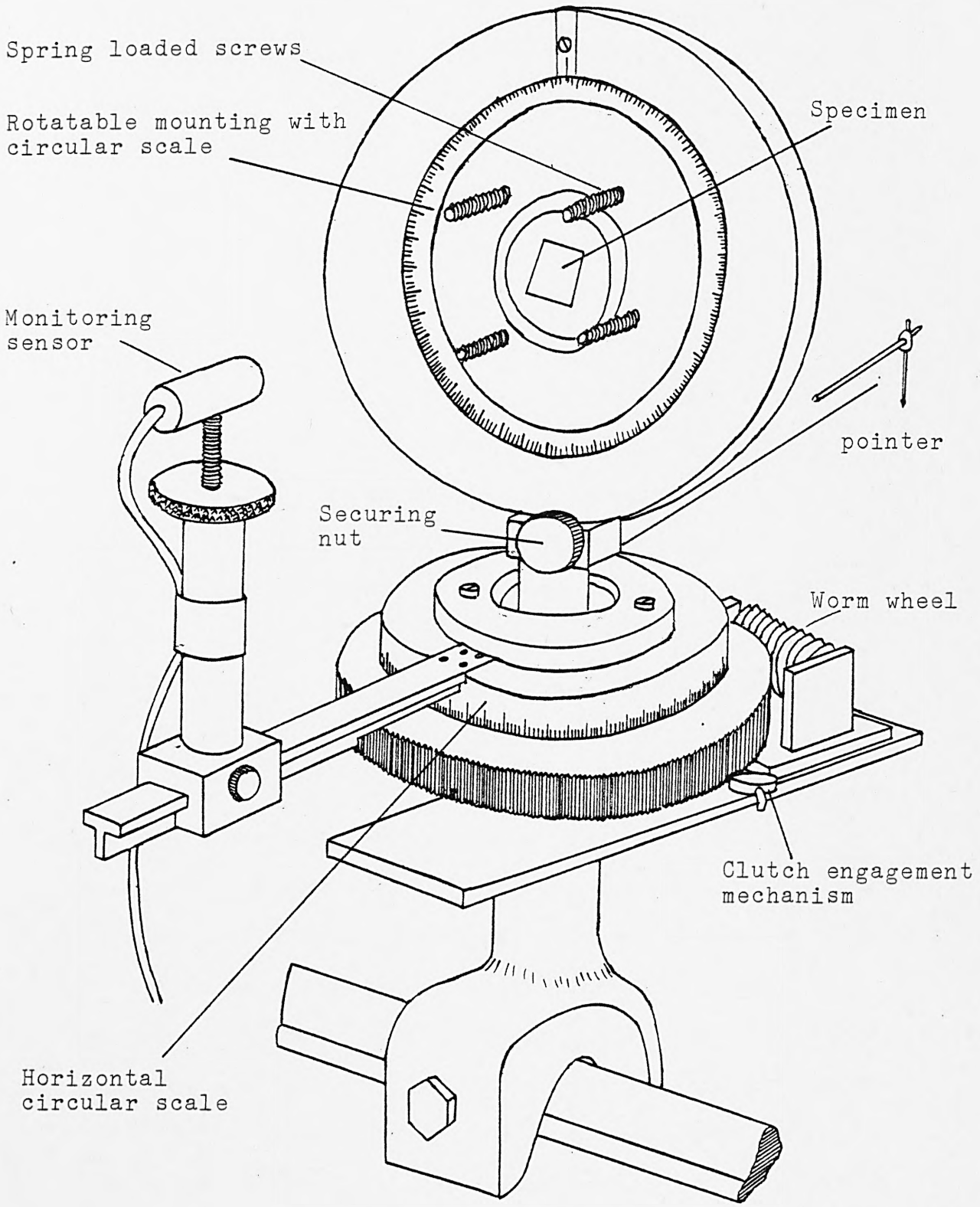

FIG. 5.1.13. Specimen mounting with the stepping motor interface

5. Data Presentation and Display

A hard copy listing of a disc file of laser beam scattering data, created by LASDAT.FOR, is presented below (Table 5.1.1.). The file is headed by an indentifier label and carries essential run set-up information:

SPN M( )T( )N( ) ; identifier label

θ_1 ; angle of incidence

θ_3 ; angle of orientation

n ; number of readings in scan

θ_2 ; initial angle of observation

n - photo diode intensity readings

**** ; file terminator symbol

but consists in essence of beam scatter intensity values (referenced by the laser output), recorded during a single sweep of the scanning photo diode minitor.

SCATGH.FOR computes the angles of observation at which the scatter intensity distribution was sampled, and provides a hard copy listing of the same. The distribution is displayed as a polar diagram plot and also as a graph of intensity against angle. A typical output of SCATGH.FOR is provided (Table 5.1.2. and Fig. 5.1.14.). The range of θ_2 is only 4 degrees and so the picture presented by a broad gaussian-type curve is misleading. The polar plot appears virtually to consist of a single ray. Only by a severe distortion, whereby adjacent angles would be grossly magnified, would such a plot appear otherwise on a VDU display.

```
SPN M3T1N1
  10.0
   0.0
   100
  12.2

0.0194   0.0199   0.0194   0.0201   0.0198   0.0199
0.0202   0.0201   0.0196   0.0201   0.0202   0.0202
0.0202   0.0203   0.0201   0.0203   0.0205   0.0213
0.0217   0.0212   0.0178   0.0173   0.0181   0.0188
0.0194   0.0202   0.0207   0.0216   0.0195   0.0173
0.0188   0.0197   0.0208   0.0191   0.0182   0.0207
0.0285   0.0431   0.0422   0.0438   0.0422   0.0422
0.0423   0.0411   0.0422   0.0433   0.0416   0.0416
0.0432   0.0419   0.0426   0.0422   0.0411   0.0426
0.0439   0.0442   0.0484   0.0657   0.0658   0.0893
0.1115   0.1575   0.2244   0.3088   0.4282   0.6207
0.8691   1.1671   1.5171   1.8490   2.1378   2.3925
2.5082   2.5470   2.4223   2.1425   1.8281   1.3861
1.0916   0.7932   0.5943   0.4250   0.3282   0.2111
0.1531   0.1110   0.0671   0.0431   0.0423   0.0185
0.0208   0.0181   0.0177   0.0216   0.0202   0.0203
0.0201   0.0189   0.0188   0.0177
****
```

TABLE 5.1.1. Beam Scatter Data File created by LASDAT.FOR

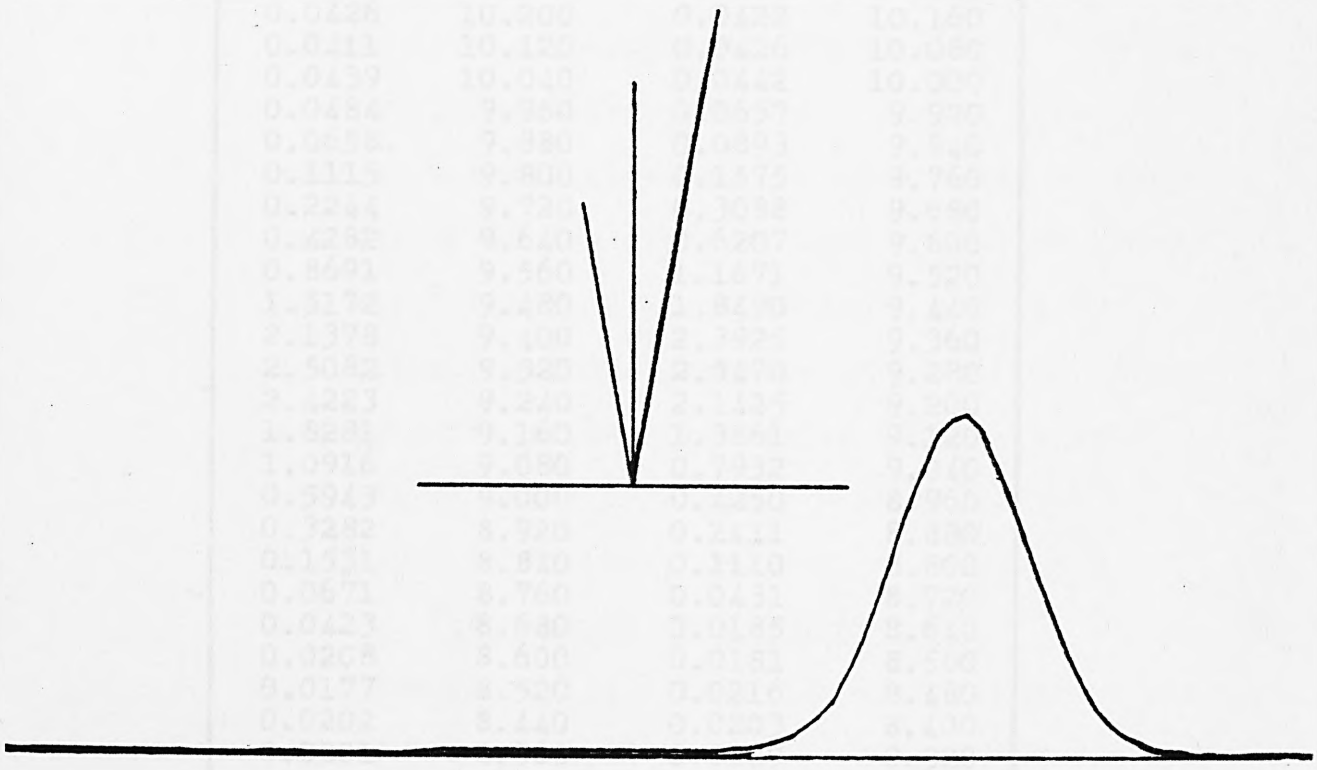

FIG. 5.1.14. Graphical output of the above scan from SCATGH.FOR

SPN M3T1N1
10.0
0.0
100
12.2

INTENSITY	ANGLE	INTENSITY	ANGLE
0.0194	12.200	0.0199	12.160
0.0194	12.120	0.0201	12.080
0.0198	12.040	0.0199	12.000
0.0202	11.960	0.0201	11.920
0.0196	11.880	0.0201	11.840
0.0202	11.800	0.0202	11.760
0.0202	11.720	0.0203	11.680
0.0201	11.640	0.0203	11.600
0.0205	11.560	0.0213	11.520
0.0217	11.480	0.0213	11.440
0.0178	11.400	0.0173	11.360
0.0181	11.320	0.0188	11.280
0.0194	11.240	0.0202	11.200
0.0207	11.160	0.0216	11.120
0.0195	11.080	0.0173	11.040
0.0188	11.000	0.0197	10.960
0.0208	10.920	0.0191	10.880
0.0182	10.840	0.0207	10.800
0.0385	10.760	0.0431	10.720
0.0422	10.680	0.0438	10.640
0.0422	10.600	0.0422	10.560
0.0423	10.520	0.0411	10.480
0.0422	10.440	0.0433	10.400
0.0416	10.360	0.0416	10.320
0.0432	10.280	0.0419	10.240
0.0426	10.200	0.0422	10.160
0.0411	10.120	0.0426	10.080
0.0439	10.040	0.0442	10.000
0.0484	9.960	0.0657	9.920
0.0658	9.880	0.0893	9.840
0.1115	9.800	0.1575	9.760
0.2244	9.720	0.3088	9.680
0.4282	9.640	0.6207	9.600
0.8691	9.560	1.1671	9.520
1.5172	9.480	1.8490	9.440
2.1378	9.400	2.3925	9.360
2.5082	9.320	2.5470	9.280
2.4223	9.240	2.1425	9.200
1.8281	9.160	1.3861	9.120
1.0916	9.080	0.7932	9.040
0.5943	9.000	0.4250	8.960
0.3282	8.920	0.2111	8.880
0.1531	8.840	0.1110	8.800
0.0671	8.760	0.0431	8.720
0.0423	8.680	0.0185	8.640
0.0208	8.600	0.0181	8.560
0.0177	8.520	0.0216	8.480
0.0202	8.440	0.0203	8.400
0.0201	8.360	0.0189	8.320
0.0188	8.280	0.0177	8.240

TABLE 5.1.2. Intensity versus angle: scan data from program SCATGH.FOR.

5.2 Mapping a Small Area of a Metal Surface

5.2.1. Introduction

In recent years a number of workers (such as R. S. Sayles and T. R. Thomas, 1976) have given attention to the problem of recording a three-dimensional map of a small area of a surface in real time. For many applications, when the surface topography is anisotropic, it is unreal to suppose that the three-dimensional geometry of a surface can be adequately expressed in terms of a single profile, or indeed in terms of a few profiles taken in a number of oblique directions. In our study, the mapping of a specimen surface was a necessary concomitant towards predicting the polar diagrams obtained when a particular surface is illuminated by a source of electromagnetic radiation.

It was necessary, since a finite area of surface was illuminated, (in reality an elliptical region of the order of 2 mm by 2.5 mm minor and major axes), to know precisely the three-dimensional surface geometry of the illuminated region. The signal processing of height data, reduced in terms of surface statistics, is discussed in Chapter 6.

5.2.2. The Semi-automated System

The measuring system consisted fundamentally of a Talysurf-10 (Rank Taylor Hobson Ltd., Leicester): a machine which has the feature of a portable traverse unit.

The system was semi-automatic in that at the end of each trace traverse, the stylus was returned manually, and set to the start position for the next trace. However the digitisation of the profile trace record was done automatically, via the ADC interface. It was recorded in core of a PDP-11 minicomputer, and thence intermediately transferred to a floppy disc. A permanent record was then created on a 7-track industrial tape for subsequent processing at leisure on the PDP-11 or, if more sophisticated analysis were required, on a large scale digital computer.

A sample worksheet is reproduced in Fig. 5.2.2 whilst a flowchart of the full operational procedure is given in Fig. 5.2.3.

The semi-automated system is presented in terms of the following schematic diagram before the operating procedure is described in more detail.

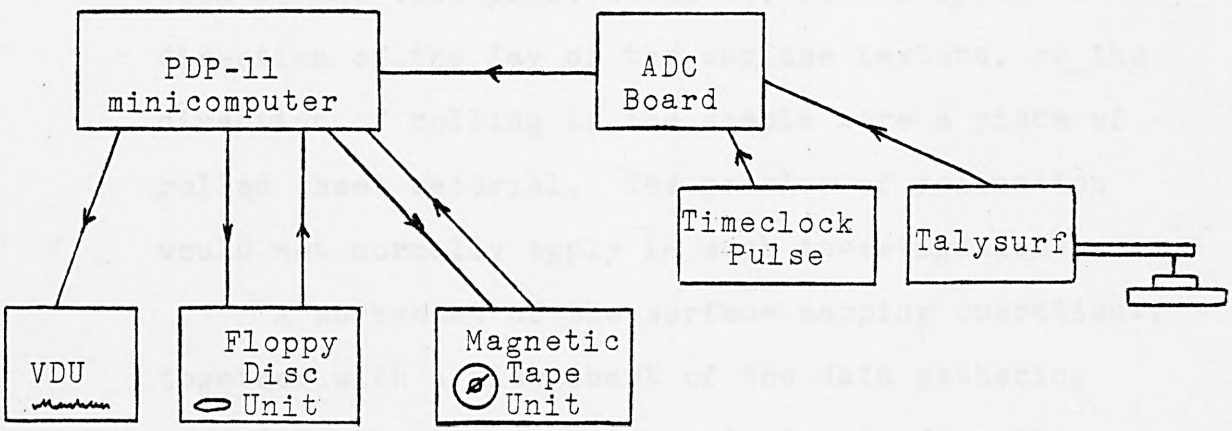

FIG. 5.2.1 Schematic Diagram of the Semi-Automated Mapping System

5.2.3. Operating Procedure, Data Acquisition and Recording

The test piece was marked with four scratch marks which located the centre of the area of the region previously illuminated by the incident laser beam. The specimen mounter block was placed in position. Micrometer screw gauges allowed for movement in two mutually perpendicular directions of the block head. The block aligned such that one direction was parallel to the direction of the stylus traverse; the other direction was thus perpendicular to the direction of traverse. The test piece was was orientated until the stylus traverse was parallel to the requisite scratch marker direction. A traverse length of 3 mm was appropriate for coverage of the formerly illuminated region although 50 mm is the maximum traverse length permitted by the Talysurf-10.

N.B. If a test piece is to be mapped in the context of surface roughness assessment or some such application, then the factors governing the orientation of the test piece would be, for example, the direction of the lay of the surface texture, or the direction of rolling if the sample were a piece of rolled sheet material. The problem of relocation would not normally apply in such investigations.

A worksheet of the surface mapping operations, together with a flow chart of the data gathering and file creation procedures (prior to describing the computer hardware interface) are reproduced.

A. Preliminary Checks Completed?

(i) Specimen held in horizontal plane

(ii) Specimen orientated in requisite direction

(iii) Talysurf-10 set up for trace length and stylus point at map "origin position"

(iv) Clock-pulse generator set up correctly

B. Surface Map Set Up Information

(i) Specimen Identifier label — M | | T | |

(ii) Choice of graphic scale parameter (run information only) Scale:

(iii) No. of samples/trace

(iv) No. of traces

(v) Length of each trace

(vi) Separation of parallel traces

C. Surface Map Run Sheet

Mag. factors V_H = [ ] V_V = [ ]

Run No.	Data Trans.	Run No.	Data Trans.	Run No.	Data Trans
1		15		29	
2		16		30	
3		17		31	
4		18		32	
5		19		33	
6		20		34	
7		21		35	
8		22		36	
9		23		37	
10		24		38	
11		25		39	
12		26		40	
13		27			
14		28			

Map Completed [ ]

FIG. 5.2.2. Surface Mapping Sample Worksheet

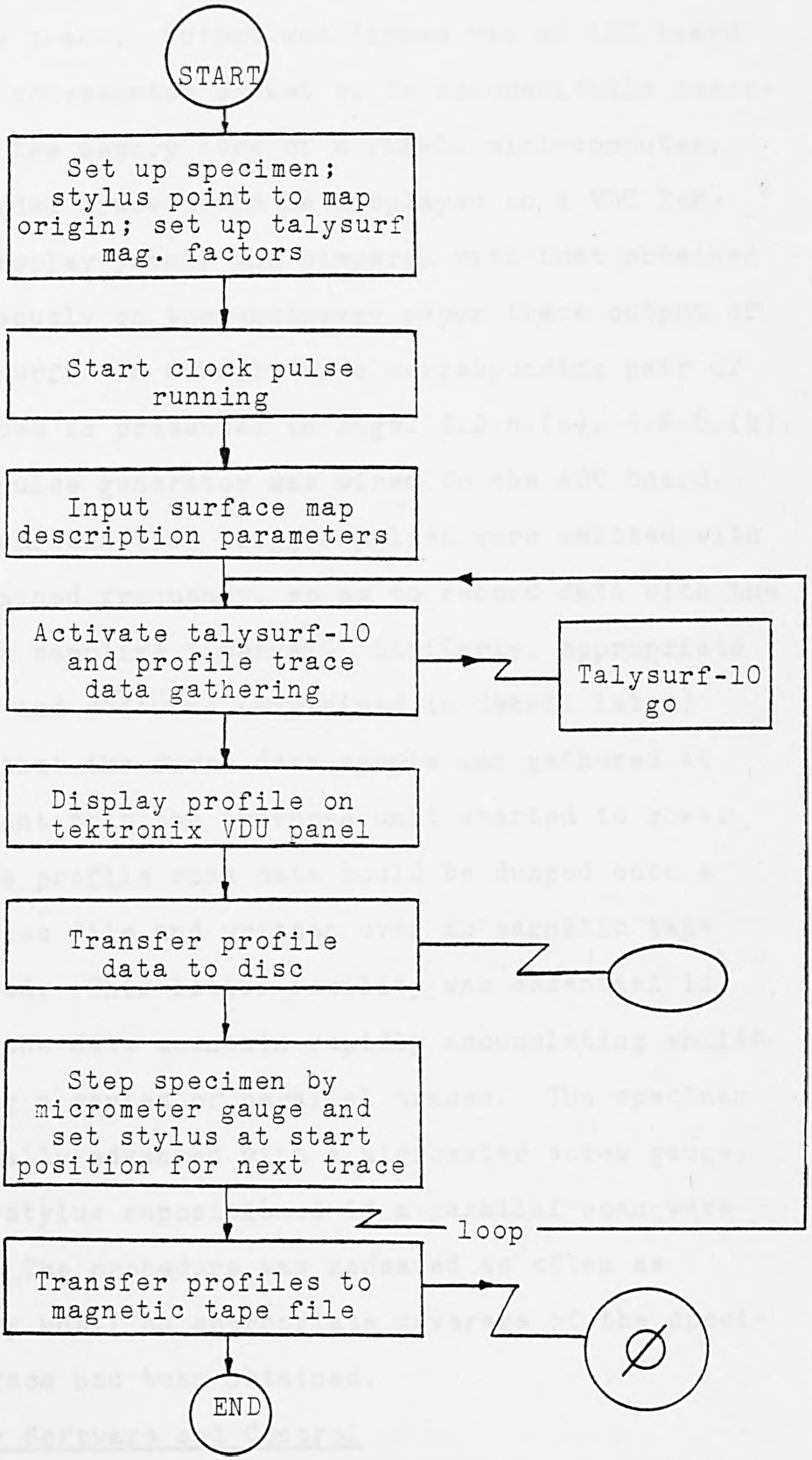

FIG. 5.2.3. Flowchart of Data Gathering and File Creation Procedures

Appropriate profile magnification factors were selected with the talysurf set to automatically record a profile trace. Output was linked via an ADC board from the accessories socket to be automatically recorded into the memory core of a PDP-11 mini-computer. The recorded trace could be displayed on a VDU Tektronix display panel, and compared with that obtained simultaneously on the customary paper trace output of the talysurf. An example of a corresponding pair of such traces is presented in Figs. 5.2.6.(a), 5.2.6.(b).

A pulse generator was wired to the ADC board, and set up such that trigger pulses were emitted with predetermined frequency, so as to record data with the requisite sampling interval. Similarly, appropriate hardware and software (explained in detail later) ensured that the first data sample was gathered at the instant that the traverse unit started to move.

The profile scan data could be dumped onto a floppy disc file and written over to magnetic tape if desired. This latter facility was essential in view of the data mountain rapidly accumulating whilst recording a series of parallel traces. The specimen was manually advanced with a micrometer screw gauge, and the stylus repositioned if a parallel scan were wanted. The procedure was repeated as often as necessary until an appropriate coverage of the specimen surface had been obtained.

Computer Software and Control

Full computer documentation is supplied in Appendix 5B. In brief, an interactive fortran control program SRRMPP.FOR allowed for the input of run set-up infor-

mation, in particular the length of the trace, the number of samples to be collected, and the horizontal magnification factor of the profile. Such information enabled the sampling rate to be determined, given prior knowledge of the speed of traverse obtained from previous timing experiments).

A pulse generator could now be hitched up to the ADC board to transmit a rectangular wave pulse, with frequency equal to that of the sampling rate.

Executive now passed to an assembler subroutine of SRRMPP.FOR namely TALY.MAC. The subroutine awaited notification for data collection which was given when the start button of the talysurf was pressed. Thus the origin point of the digitised profile was synchronised with the start of the surface to be scanned. For completeness this interface is given below.

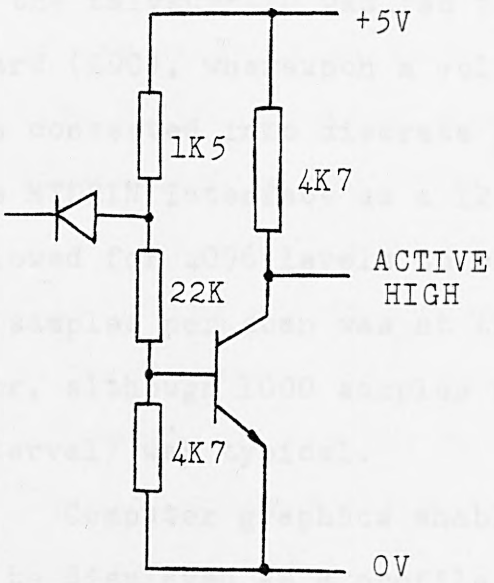

Interfacing to Talysurf 10

A signal indicating the start of a traverse was available on the accessory socket (Pin 10). This output was active low and drove a high gain transistor by a MC671 high output voltage gate.

Diode and Transistor can be any general purpose or switching device.

FIG. 5.2.4. Talysurf 10 Interface

Suitable logic circuitry enabled sampling to be organised in the manner as described.

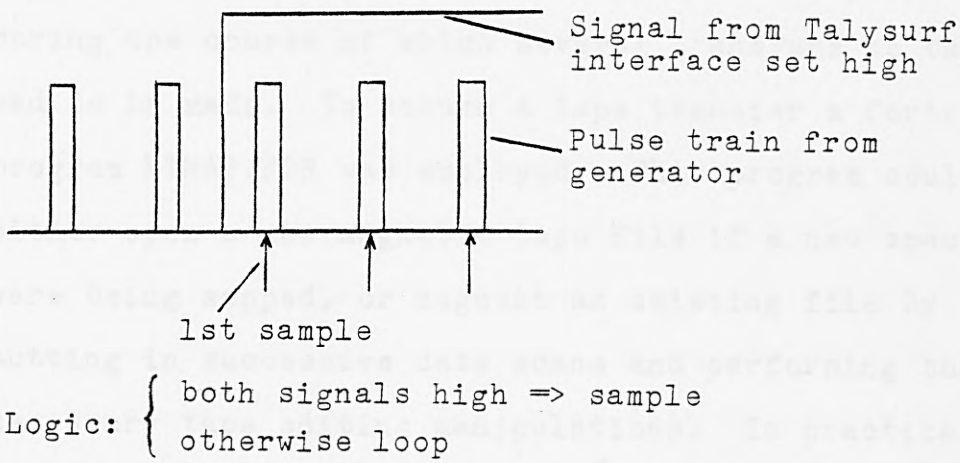

FIG. 5.2.5. Sampling logic diagram

The output voltage from the accessories socket of the talysurf-10 was fed to the analogue-to-digital board (ADC), whereupon a voltage range of -10v to +10v was converted into discrete sets, and was passed via the MTDRIN interface as a 12-bit machine word. This allowed for 4096 levels to be represented. The number of samples per scan was at the discretion of the operator, although 1000 samples over a 3 mm length (3 µm interval) was typical.

Computer graphics enabled the digitised output to be displayed as a profile plot. A semi-permanent record could be kept on transference to a floppy disc from which a hard copy record could be obtained if the file were listed at the printer.

Subsequent scans could be processed similarly. However, the limitations on disc storage dictates that records be dumped on to magnetic tape. To cover a region of $3cm^2$, 100 parallel scans were deployed, during the course of which several transfers to tape had to be made. To secure a tape transfer a fortran program MTMAP.FOR was employed. This program could either open a new magnetic tape file if a new specimen were being mapped, or augment an existing file by butting in successive data scans and performing the necessary tape editing manipulations. In practice, 100 scans of 1000 samples per scan could be gathered and recorded to magnetic tape in about three hours. The limitations to greater efficiency, were the manual set-up interventions necessary in advancing the specimen and returning the stylus prior to each talysurf sweep, and also the relative slowness of somewhat cumbersome magnetic tape handling procedures. However, if the operator chose to bypass graphical and tabular data display options, the rate of data gathering could be enhanced by the order of 30% or so.

The interfacing of the PDP-11 and the magnetic tape drives was such that assembler subroutines needed to be employed. This naturally complicated associated software, but had the advantage of greater flexibility (even allowing for a modest amount of file editing of the tape in situ).

An associated hybrid program MAPMT.FOR was available to read tape files and perspective plots could be plotted on the tektronix panel. However, the resolution of the plot was sufficient for the projection to

be of general interest only. This, added to the fact that the PDP-11 is ill-equipped to process some 100 x 1000 samples, dictates that statistical analysis and pictorial projections fixed on microfilm are more appropriately handled by the ULCC main frame computers.

VDU Data Display

A plot of a digitised profile record is provided, together with the paper trace record output of the talysurf. Differences in their respective magnification factors normally distort the images when trying to draw comparisons. The paper tape trace has been enlarged; the broad similarities of the plots are self-evident. On close examination, the fine detail also corresponds well. The discretisation process of the ADC clearly filtered the electrical signal output of the talysurf-10. However, damping characteristics of the pen recorder also imposed its own filtering, and so neither plot should be regarded as definitive.

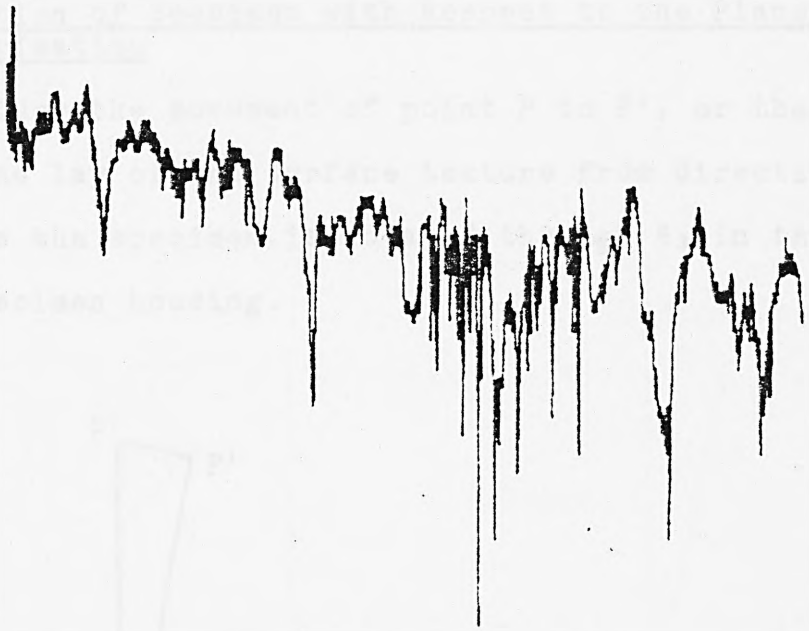

FIG. 5.2.6(a) Plot of Digitised Profile Trace

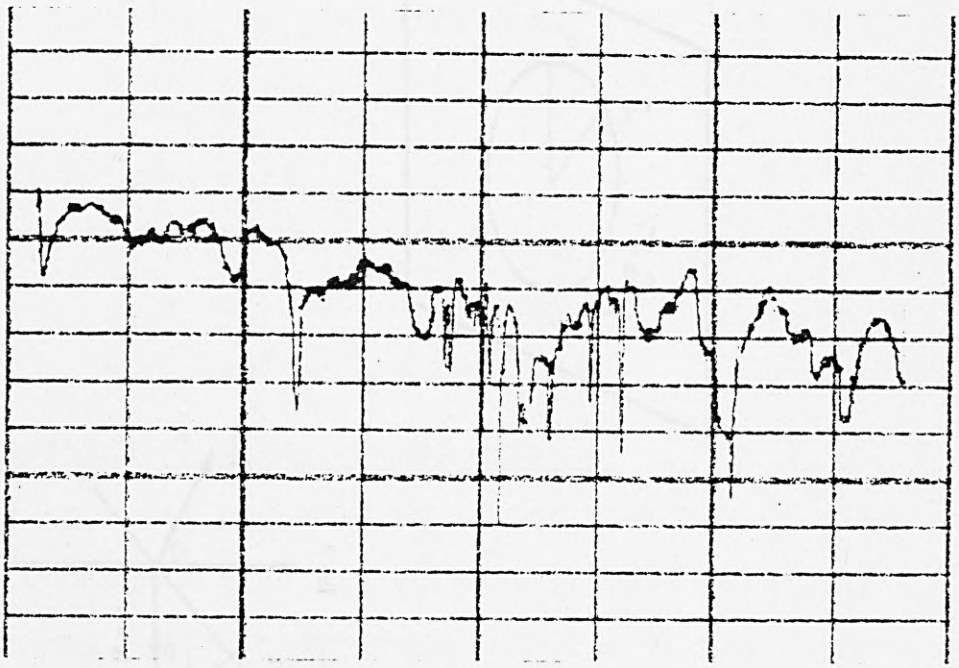

FIG. 5.2.6(b) Talysurf-10 Paper Tape Trace

APPENDIX 5A

5A.1 Rotation of Specimen with Respect to the Plane of Polarisation

Consider the movement of point P to P', or the rotation of the lay of the surface texture from direction OP to OP', as the specimen is rotated through θ_3 in the plane of the specimen housing.

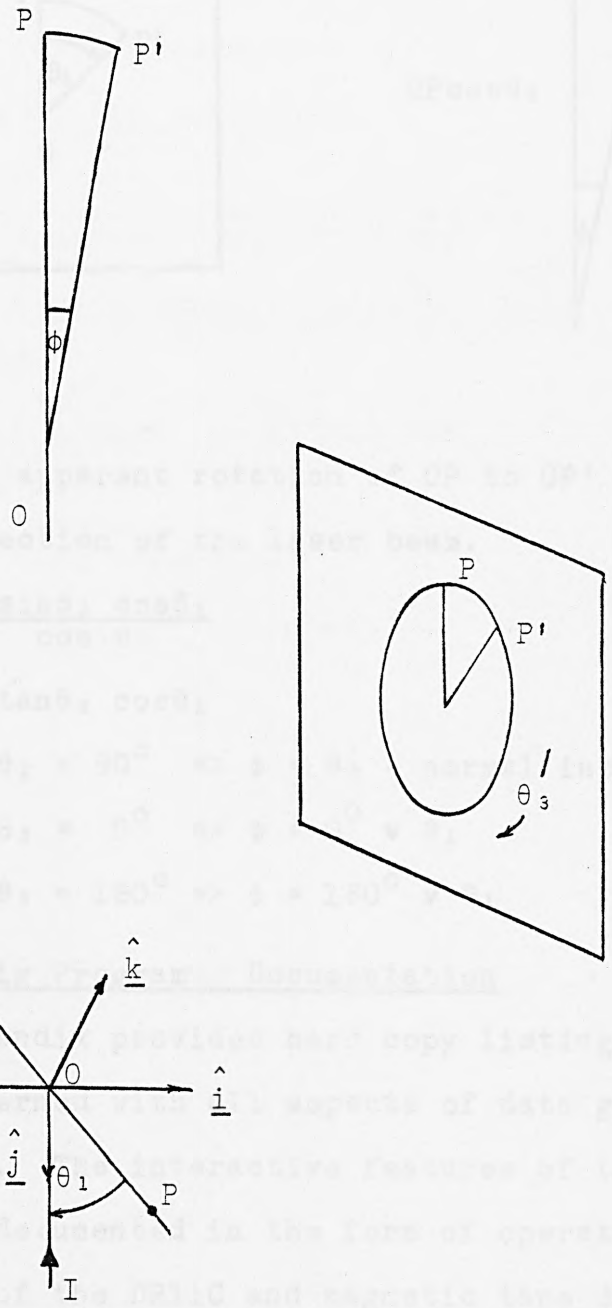

Set up $\hat{i}$, $\hat{j}$, $\hat{k}$ coordinate system. What are the coordinates of P' w.r.t. this system?

$$\underline{OP'} = OP \sin\theta_3 \sin\theta_1 \hat{i} + OP \sin\theta_3 \cos\theta_1 \hat{j} + OP \cos\theta_3 \hat{k}$$

Then from simple geometry,

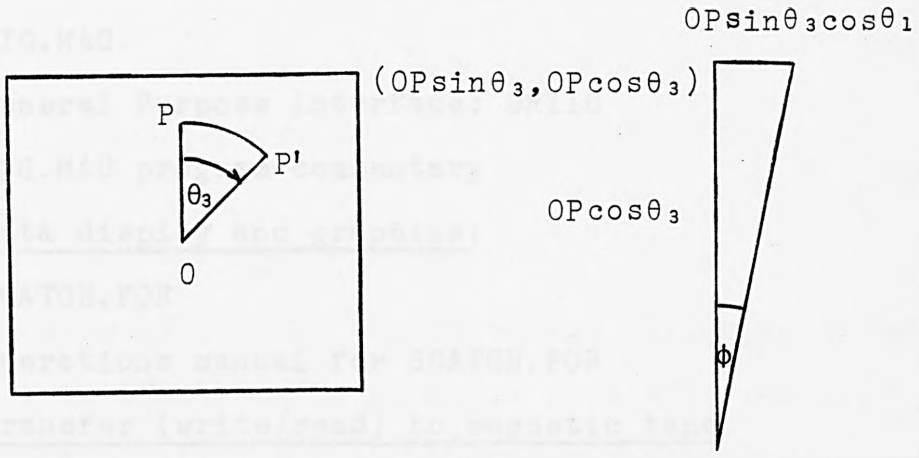

Here ϕ is the apparent rotation of OP to OP' when viewed along the direction of the laser beam.

$$\tan\phi = \frac{\sin\theta_3 \cos\theta_1}{\cos\theta_3}$$

$$\tan\phi = \tan\theta_3 \cos\theta_1$$

check: $\theta_1 = 90^\circ \Rightarrow \phi = \theta_3$ - normal incidence

$\theta_3 = 0^\circ \Rightarrow \phi = 0^\circ \forall \theta_1$

$\theta_3 = 180^\circ \Rightarrow \phi = 180^\circ \forall \theta_1$

5A.2 Laser Rig Program Documentation

This appendix provides hard copy listings of all programs concerned with all aspects of data gathering via the laser rig. The interactive features of the fortran programs are documented in the form of operations manuals. Full details of the DR11C and magnetic tape drive interfaces with the PDP-11 minicomputer are fully described. The assembler subroutines IADCIN and STEP of the macro

program RIG.MAC, which control the data input and stepping motor, require brief exposition.

Program Directory

(a) beam scatter data collection

LASDAT:FOR

Operations manual for LASDAT.FOR

RIG.MAC.

General Purpose Interface: DR11C

RIG.MAC program commentary

(b) data display and graphics:

SCATGH.FOR

Operations manual for SCATGH.FOR

(c) transfer (write/read) to magnetic tape

MTSCAT.FOR

Operations manual for MTSCAT.FOR

MTCRE.MAC.

Magnetic tape interface

MTCRE.MAC program commentary

Program listings
p.119-122
p.131-133
p.136-139
p.154-156
p.161-164
p.168-169
removed for
copyright reasons

PROGRAM

FILENAME LASDAT FOR

ASSOCIATED FILES(S) (1) RIG MAC

DESCRIPTION

The program allows for the automatic recording of beam scatter intensity information as obtained from the experimental rig. Assembler routines IADCIN and STEP, gather data via the ADC board and drive the stepping motor, respectively. Operator interaction allows for the adjustment of the half-wave plate and for the transfer of set-up configuration description information. Repeat scans are displayed graphically and compared for error differences. Validated scans of reflected beam intensity are transferred to a floppy discfile.

Stage	Operation or Display	Action
1	Run program	.RU LASDAT
2	'IDENTIFIER LABEL>'	Type in M,T,N identifier tags (3I1) (Disc file opened)
3	'SCALE FACTOR>'	Type in graphics display factor
4	'DIFFERENCE MAGNIFICATION FACTOR>'	Type in separate mag. factors for examination of differences of replicate scans. (Any missed pulses?)
5	Q('SET THETA?')	Type in angle of incidence
6	'THETA3>'	Type in orientation angle of specimen (F.6.1)
7	'RATE OF DRIVE>'	Type in stepping speed of stepping motor (I6)
8	'NUMBER OF STEPS (NO. OF THETA2S)>'	Type in number of samples to be recorded in the scan
9	'THETA2>'	Type in initial position of scanning diode
10	Q('TRANSFER SET-UP INFORMATION?')	Type Y → Transfer set up information to disc. Otherwise return to stage 5
11	'HALF-WAVE PLATE SETTING>'ϕ	Information only see stage 12
12	'ADJUST HALF-WAVE PLATE'	Program hangs up allowing operator to adjust half-wave plate to angle ϕ stipulated at stage 11
13	'FIRST SCAN'	Information only. Scanning motion of stepping motor is initiated
14	'CHECK ON MIRROR/SENSOR OUTPUT'	Reference sensor output is displayed as a check on rig set-up. Tune sensor as required

Stage	Operation or Display	Action
15	'NOTE THETA2 ANGLE'	Final position of scanning diode may be recorded
16	'FIRST REWIND'	Information only rewinds stepping motor to initial position
17	Q('SECOND SCAN OPTION?')	A replicate scan may be run if desired (Type Y)
18	'SECOND SCAN'	Information only. Duplicate scan is collected
19	'SECOND REWIND'	Information only. Stepping motor rewinds to start position
20	Q('ACCEPT DATA?')	Type Y → data is transferred to floppy disc file. Go to 22
21	Q('RESCAN?')	If data queried, type Y and return to stage 13
22	Q('TERMINATE RUN?')	If yes, type Y → STOP. Otherwise return to stage 5 and continue
23	STOP	

```
NLIST BEX,SEQ

TITLE LASER RIG TEST PROGRAM

GLOBL IADCIN,STEP

MCALL REGDEF

REGDEF

DRCSR=164020
DROUT=DRCSR+2
DRIN=DROUT+2
IADCIN:  CLR   DRCSR

         TST   DRIN

         MOVB  @2(R5),DROUT    ;START ADC

         CLR   R0              ;WASTE SOME TIME

2$:      TST   DRCSR

         BPL   2$

         MOV   DRIN,R0         ;RETURN RESULT

         BIC   #17000,R0       ;CLEAR OFF NOISE

         RTS   PC

STEP:    MOV   #2,R3           ;CLKWISE
         MOV   @4(R5),R2       ;NUMBER OF PULSES
         BEQ   4$
         BPL   1$              ;BRANCH IF ANTICLK

         NEG   R2              ;MAKE POSITIVE
         CLR   R3              ;ANTICLKWISE

1$:      MOV   @2(R5),R1       ;GET PULSE LENGTH
2$:      MOVB  R3,DROUT+1      ;
3$:      DEC   R1              ;LOOP FOR DURATION
         BPL   3$              ;OF PULSE

         DEC   R2
         ENE   1$
4$:      RTS   PC              ;EXIT

         END   IADCIN
```

General Purpose Interface: DR11C

DR11C provides us with three registers on the unibus, these being:

(i) DRCSR: Control and Status register.

(ii) DRIN: A 16 bit input register whose value is determined by user hardware.

(iii) DROUT: A 16 bit read/write output register which can drive user hardware.

The requisite addresses are as follows:

DRCSR = 164020

DROUT = 164022

DRIN = 164024

DRCSR

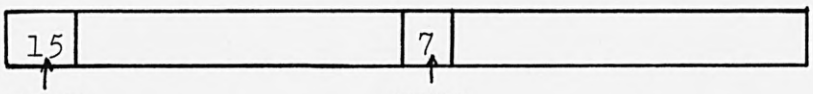

REQB — request B

REQA — request A

ADC end of conversion line sets REQB

DROUT

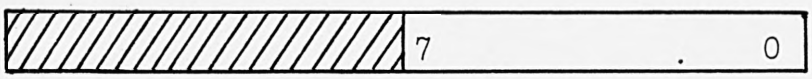

ADC is started whenever the DROUT low order byte (bits 0 → 7) is addressed.

DRIN

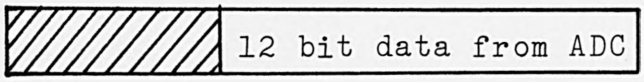

12 bits take 37μs

Reading DRIN buffer (either byte) causes the DT (data transmitted) pulse to be sent

ADC is started whenever the DROUT low order byte (bits 0 - 7) is addressed.

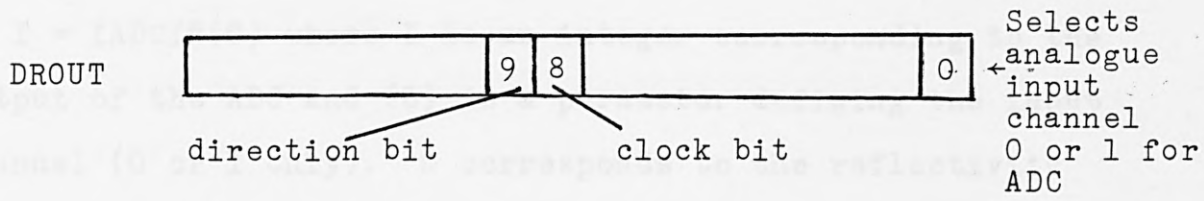

ADC end of conversion line sets REQB.

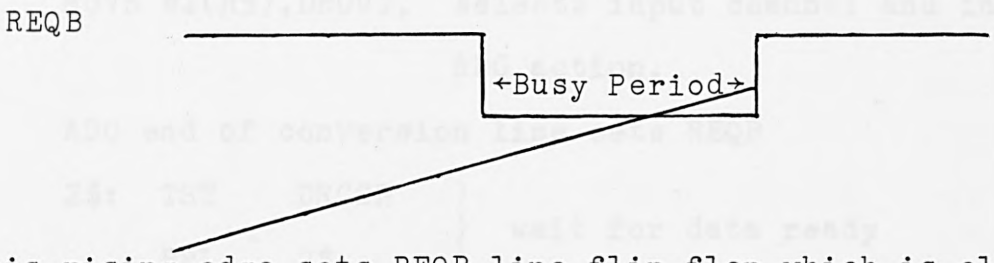

This rising edge sets REQB line flip flop which is cleared by DT pulse from computer.

RIG.MAC program commentary

The assembler program comprises two subroutines, namely IADCIN and STEP. A typical application of the first is I = IADCIN(0) where I is an integer corresponding to the output of the ADC and (0) is a parameter defining the input channel (0 or 1 only). 0 corresponds to the reflectivity intensity sensor monitor and 1 to the reference sensor output.

```
MOVB @2(R5),DROUT,   selects input channel and initiates
                     ADC action.
ADC end of conversion line sets REQB
2$:  TST    DRCSR   )
                    ) wait for data ready
     BPL    2$      )
MOV  DRIN,  RØ       returns data to RØ register
                     and also clears REQB line,
                     whilst
     BIC    #17ØØØØ,RØ clears of any noise, noting
                     that data is a 12-bit word
```

STEP is a subroutine with 2 parameters to control the stepping motion.

Subroutine call: CALL STEP(IRATE,IPULSES). IRATE determines the speed of the stepping motor

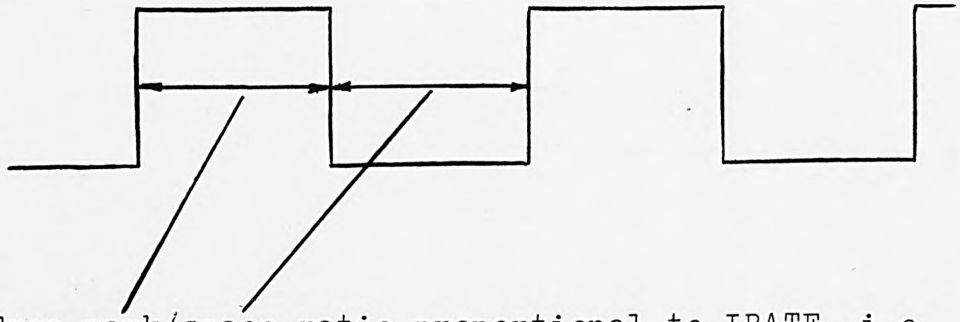

Even mark/space ratio proportional to IRATE, i.e. duration of pulse is proportional to IRATE. IPULSES is the number of complete pulses sent to the motor whilst the sign

of IPULSES determines the stepping action of the motor. More precisely IPULSES = positive, steps motor forwards: IPULSES = negative, steps motor backwards.

```
MOVB  R3, DROUT+1
```

Sets direction bit 9 of DROUT register and initiates stepping motor action.

PROGRAM

FILENAME : SCATGH.FOR

DESCRIPTION

Program reads beam scatter file(s) from disc(s) and displays the intensity distribution, (graph of intensity against receiver angle, and a polar representation), on the Tektronix panel, for cursory examination or for photographic purposes. Hard copy listing of the intensity distribution is also provided.

SCATGH. FOR Operations Manual

Stage	Operation or Display	Action
1	Run program	.RU SCATGH
2	Type in filename for file recall from floppy disc	Type ∇SPN∇M(I1)T(I1)N(I1)
3	'CHECK SPECIMEN LABEL'	Type return if file recalled. Otherwise abort
4	'SCALE FACTOR>'	Type in polar diagram plot magnification factor
5	Q('GRAPH SCALE SATISFACTORY?') Graphical display of polar diagram - may be photo-graphed.	Type Y if representation is satisfactory, other-wise return to stage 4
6	Hard copy listing of intensity versus angle is output from the line printer.	Nil
7	Q('GET NEXT DATA RUN?')	Type Y to continue. Otherwise exit to STOP.
8	Q('CALL ANOTHER DISCFILE?')	Type Y → current disc file is closed and programme re-enters stage 2.
9	Q('ANGLE OF INCIDENCE INCLUDED IN SET-UP INF?')	Type Y if yes. Program returns to stage 2 regardless.
10	STOP	

PROGRAM

FILENAME : MTSCAT.FOR

ASSOCIATED FILE(S) (1) MTCRE.MAC

DESCRIPTION

The program creates a beam scatter data file on magnetic tape. The program allows for disc files to be read and concatenated into a single tape file. The tape has a header label, format

SPN M(NM)T(NT)N(NN)

where NM,NT,NN are all I1 numeric codes,

NM-Material Code (Brass, Copper etc.)

NT-Type Code (Smooth, single scratch, etc.)

NN-Serial Number, usually corresponding to particular angle of incidence.

Stage	Operation or Display	Action
1	Run Program	.RU MTSCAT
2	Q('BYPASS EXISTING FILE(S)?')	Type Y to protect existing mag. tape file(s). Otherwise, type in floppy disc filename identifier SPN M(I1)T(I1)N(I1)
3	Q('DISPLAY FILE DATA?')	Go to read mag. tape program segment - stage 5. Otherwise file is skipped over.
4	FILEMARK DETECTED	Display indicates that EOF marker has been read.
5	Q('FILEMARK DETECTED?')	If no, continue to skip over data blocks.
6	Q('LAST FILE?')	If no, continue to skip files. If yes, return ready for new data transfer (stage 2).
7	'CHECK SPECIMEN LABEL'	Check discfile header label.
8	Q('MODIFY LABEL DESCRIPTION?')	Type Y if yes, otherwise go to stage 10.
9	'MODIFICATION(NN)'	Type in new N(I1) run file identifier.
10	'LABEL UNPACKED'	Information only.
11	Q('TRANSFER LABEL?')	Type Y to pass over header label to mag. tap.
12	Q('TRANSFER ANGLE OF INCIDENCE?')	As above. θ_1 information is transferred.
13	'CHECK ANGLE SET-UP INF.'	Check preliminary run set-up details.
14	'CHECK INTENSITY DATA FOR TRANSFER'	Further pause to examine file data prior to transfer. Go.
15	Q('FILE EXHAUSTED?')	If yes, type Y and go to option at Stage 14.
16	Q('ANGLE OF INCIDENCE IN SET-UP INF?')	Return to 9 or 10 as appropriate.

Stage	Operation or Display	Action
17	Q('OPEN ANOTHER DISCFILE?')	If no, type return. Mag. tape is rewound and read back if desired. If yes, type Y - tape file is closed with a filemark and program returns to stage 4.
18	Q('FILEMARK DETECTED?')	If EOF encountered, return to stage 2.
19	'SET-UP INF.'	Survey set-up information as read over from tape. Continue.
20	Q('CONTINUE MT CHECK?')	Exit is desired.
21	Q('ANGLE OF INCIDENCE IN SET-UP INF?')	Respond as appropriate. Tape file read operation is re-entered.
22	STOP	

```
        .NLIST BEX,SEQ
        .TITLE MAG. TAPE CREATE
        .GLOBL INITMT,MTWRT,MTRD,UNPLAB,PACLAB,CLOMT
        .GLOBL MTEOF

        .MCALL  REGDEF,  PRINT,  EXIT
        .REGDEF

        .MACRO  MTOP     A          ;COMMANDS TO MT
        TSTB    @#MTIN              ;TEST DFU
        BPL     .-4                 ;BACK IF BUSY
        MOVB    #A,@#MTOUT+1        ;SET COMMAND A
        BISB    #GOIN,@#MTOUT+1     ;START EXECUTION
        .ENDM   MTOP

        .MACRO  REWIND              ;REWINDS MT
        MTOP    RWND                ;REWIND
        BIT     #TRRWL,@#MTIN       ;TEST IF REWINDING
        BEQ     .-6                 ;BACK IF SO
        MTINIT                      ;INITIALISE MT
        .ENDM   REWIND

        .MACRO  MTINIT              ;INITIALISE MT
        MTOP    RESET               ;ABORT CURRENT COMMAND
        TSTB    @#MTIN              ;TEST IF DFU BUSY
        BPL     .-4                 ;BACK IF SO
        .ENDM   MTINIT

        .MACRO MESS TEST,?A,?B      ;PRINT TEST MESSAGE
        .PRINT  #A
        BR      B
A:      .ASCIZ  TEXT
        .EVEN
B:
        ENDM    MESS

        MTCSR=164000
        MTOUT=MTCSE+2
        MTIN=MTOUT+2
        PSW=177776
        P7=340

        READY=40000                 ;BIT 14 AT MTIN(TAPE LOADED ETC)
        RESET=200                   ;BIT 15 AT MTOUT(RESET DFU)
        GOIN=100                    ;BIT 14 AT MTOUT(GO)
        WRT=40                      ;BIT 13 AT MTOUT(WRITE)
        RWND=20                     ;BIT 12 AT MTOUT(REWIND)
        RD=0                        ;GO BIT ON ITS OWN=READ FORWARDS
        FOEN=1                      ;ENABLES DFU(SELECTS) AT MTCSR
        LWD=200                     ;BIT 7 AT MTOUT(LAST BYTE)
        TRRWL=20000                 ;TEST BIT 13 AT MTIN(REWIND IN OP?
        PARITY=400                  ;TEST BIT 8 AT MTIN(READ/WRITE ERROR
        FLMARK=2000                 ;TEST BIT 10 AT MTIN(FILEMARK DET?
        EOT=100000                  ;BIT 15 AT MTIN(END-OF-TAPE)
        WFLMK=42                    ;BIT 9 AT MTOUT(WRITE FILEMARK)
        ILLCOM=1000                 ;BIT 9 AT MTIN(ILLEGAL CMD)

INITMT: BIS     #FOEN,@#MTCSR       ;SELECT TAPE DRIVE
        BIT     #READY,@#MTIN       ;DECK READY?
```

```
        BEQ     1$
        JMP     ERRNRD          ;FATAL ERROR, IF NOT
1$:     MTINIT
        REWIND
        RTS     PC

MTWRT:  CMP     (R5)+,#2        ;CHECK FOR LEGAL NO.
        BEQ     1$              ;OF PARAMETERS
        RTS     PC
1$:     MOV     (R5),R0         ;BUFFER ARRAY POINTER TO R0
        MOV     @2(R5),R1       ;NO. OF 'SAMPLES' TO R1
        CMP     #ID,R0          ;WRITE LABLE?
        BEQ     LKOUT           ;JUMP,IF SO
UNPACK: BIC     #170000,(R0)    ;12-BIT DATA
        ASL     (R0)            ;UNPACK DATA INTO
        ASL     (R0)            ;TWO6-BIT BYTES
        ASRB    (R0)            ;LEAST SIG. BIT IS
        ASRB    (R0)            ;TRANSFERRED FIRST
        BICB    #300,(R0)       ;CLEAR OFF SIGN BIT
        BIC     #140000,(R0)+   ;CLEAR OFF SIGN BIT
        BIC     #140000,(R0)+
        DEC      R1
        BNE      UNPACK         ;BRANCH, IF NOT FINISHED
        BISB    #LWD,-1(R0)     ;SET UP LAST BYTE
        MOV     (R5),R0         ;RESTORE PARAMETERS
        MOV     @2(R5),R1       ;TO REGISTERS R0 AND R1
LKOUT:  MOV     PSW,-(SP)       ;LOCK OUT SYSTEM
        MOV     #P7,PSW
        BIT     #FOEN,@#MTCSR   ;DECK STILL ON-LINE?
        BNE     2$
        JMP     ERROFF          ;FATAL ERROR, IF NOT
2$:     MOVB    (R0)+,@#MTOUT   ;1ST. DATA WORD
        BPL     8$
        MOV     (SP)+,PSW
        MESS    </1ST BYTE NEGATIVE!/>
        BR      6$
8$:     MTOP    WRT             ;START BLOCK WRITE
        BIT     #ILLCOM,@#MTIN  ;TEST FOR ILLEGAL CMD
        ENE     3$
        JMP     ILL
4$:     MOVB    (R0)+,@#MTOUT
        BMI     5$              ;END OF WRITE
3$:     TST     @#MTCSR         ;WAIT  FOR  DATA IN STROBE
        BPL     3$
        BR      4$
5$:     TSTB    @#MTIN          ;F.U. STILL BUSY
        BPL     5$
        MOV     (SP)+,PSW       ;UNLOCK SYSTEM
        BIT     #PARITY,@#MTIN  ;PARITY ERROR?
        BNE     6$
        MESS    </MT WRITE ERROR/>
6$:     RTS     PC

MTRD:   CMP     (R5)+,#2        ;CHECK FOR LEGAL NO.
        BEQ     1$              ;OF PARAMETERS
        RTS     PC              ;RETURN, IF NOT
1$:     MOV     (R5),R0         ;BUFFER ARRAY POINTER TO R0
        MOV     @2(R5),R1       ;NO. OF 'SAMPLES' TO R1
        CMP     #ID,R0          ;LABEL READ?
        BEQ     7$
        ASL     R1              ; BYTES TO R1
```

```
7$:     MOV     PSW,-(SP)           ;LOCK OUT SYSTEM
        MOV     #P7,PSW             ;RT-11 OFF
        BIT     #FOEN,@ MTCSR       ;DECK STILL ONLINE?
        BNE     2$
        JMP     ERROFF              ;FATAL ERROR, IF NOT
2$:     MTOP    RD                  ;START BLOCK READ
        BIT     #ILLCOM,@#MTIN      ;ILLEGAL COMMAND?
        BNE     3$
        JMP     ILL
3$:     TSTB    @ MTCSR             ;WAIT FOR DATA OUT STROBE
        BPL     3$
        MOVB    @#MTIN,(R0)         ;READ DATA
        BICB    #300,(R0)+          ;CLEAR OFF NOISE
        DEC     R1
        BNE     3$                  ;END OF READ
5$:     TSTB    @#MTIN              ;F.U. STILL BUSY?
        BPL     5$
        MOV     (SP)+,PSW           ;UNLOCK SYSTEM
        BIT     #PARITY,@#MTIN      ;READ PARITY ERROR?
        BNE     8$
        MESS    </MT READ ERROR/>
8$:     BIT     #FLMARK,@#MTIN      ;FILEMARK DETECTED?
        BNE     6$
        MESS    </FILEMARK DETECTED/>
6$:     MOV     (R5),R0             ;RESTORE DATA
        MOV     @2(R5),R1           ;PARAMETERS
        CMP     #ID,R0              ;LABEL READ?
        BNE     PACK
        RTS     PC                  ;RETURN,IF SO
PACK:   ASLB    (R0)                ;TWO 6-BIT BYTES ARE PACKED
        ASLB    (R0)                ;AND ONE
        ASR     (R0)                ;12-BIT DATA
        ASR     (R0)                ;NUMBER IS FORMED
        BIC     #170000,(R0)+
        DEC     R1
        BNE     PACK
        RTS     PC

MTEOF:  MTOP    WFLMK               ;WRITE FILEMARK TO TAPE
        RTS     PC

CLOMT:  MTOP    WFLMK               ;WRITE TILEMARKS TO TAPE
        MTOP    WFLMK               ;TAPE MUST BE CLOSED BY
        REWIND                      ;2 EOF MARKS (EVEN PARITY)
        RTS     PC

UNPLAB: CMP     (R5)+,#2            ;CHECK FOR LEGAL NO.
        BEQ     1$                  ;OF PARAMETERS
        RTS     PC                  ;RETURN, IF NOT
1$:     MOV     (R5),R0             ;INPUT ARRAY POINTER TO R0
        MOV     @2(R5),R1           ;NO. OF LABEL CHARS TO R1
        MOV     (R5),R4             ;OUTPUT ARRAY BUFFER TO R4
2$:     MOV     (R0)+,R3            ;CHARACTER TO R3
        BIC     #177700,R3          ;GET L.S. 6-BITS
        MOVB    R3,(R4)+            ;WRITE AWAY
        DEC     R1                  ;COUNT ON NO. OF CHARS.
        BNE     2$
        BISB    #LWD,-1(R4)         ;SET UP LAST BYTE
        RTS     PC
```

```
PACLAB: CMP     (R5)+,#3        ;CHECK FOR LEGAL
        BEQ     1$              ;OF PARAMETERS
        RTS     PC              ;RETURN, IF NOT
1$:     MOV     (R5),R0         ;INPUT ARRAY POINTER TO R0
        MOV     @2(R5),R1       ;NO. OF LABEL CHARS TO R1
        MOV     4(R5),R4        ;OUTPUT ARRAY POINTER TO R4
3$:     CLRB    (R4)            ;CLEAR LOWER BYTE
        CMPB    #40,(R0)        ;DIGIT?
        BLE     2$              ;BRANCH, IF SO
        BISB    #100,(R0)       ;ADD BIT 7 BACK
2$:     MOVB    (R0)+,R4)+      ;MOVE INTO LOWER BYTE
        CLRB    (R4)+           ;CLEAR UPPER BYTE
        DEC     R1              ;COUNT ON LABEL CHARS
        BNE     3$              ;GET NEXT CHARACTER
        RTS     PC

ERRNRD: MESS    </MT ERROR--DICK NOT READY/>
        .EXIT

ERROFF: MESS    </MT ERROR--DECK OFF-LINE/>
        .EXIT

ILL:    MESS    </ILLEGAL COMMAND/>
        REWIND
        .EXIT

        .CSECT  BUFF

ID:     .BLKW   11
ID2:    .BLKW   20
IBUFF:  .BLKW   6
IBUFF1: .BLKW   6
IBUFF2: .BLKW   200
```

Magnetic Tape Interface

Three registers on the unibus function in much the same way as the DR11C interface.

(i) MTCSR: magnetic tape control and status register.

(ii) MTIN: a 16 bit input register providing read/write etc. status indications.

(iii) MTOUT: a 16 bit output register, the upper byte of which is used for issuing commands to the tape unit.

The requisite address locations are as follows:

MTCSR = 164000

MTIN = 164002

MTOUT = 164004

MTCSR

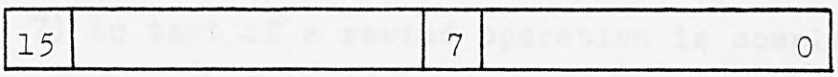

REQB REQB Enable tape formater unit

REQA - read;

REQB - write.

MTIN

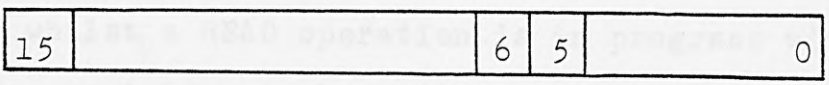

Data

inverted, i.e. 0 when giving indication

normal sense (ie not inverted)

BITS 0-5 6 bit data

Status Indicators:

Bit 6 - transport file protected (file write protected)

7 - DFU busy (DFU busy for all operations except rewind); useful to see if previous command is finished.

8 - parity error; check after reading/writing a block.

9 - illegal command state; check after issueing a command.

10 - file mark detected (set after a read operation has found a file mark

11 - BOT (beginning of tape)

12 - data busy (not found useful)

13 - rewind in progress; use this instead of DFU (bit 7) to test if a rewind operation is complete.

14 - transport ready (says that tape is loaded and door shut, etc.).

15 - EOT (end of tape).

N.B. None of these status indications can be tested successfully whilst a READ operation is in progress without losing or risking to lose data. Checking a status indication causes a DT pulse to be transmitted, resetting the REQA latch.

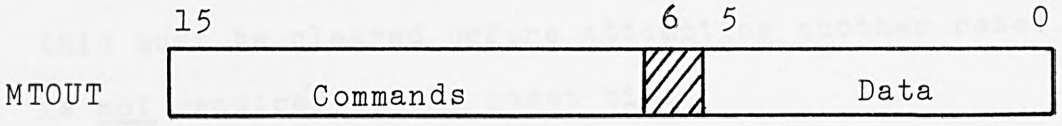

BITS 0-5 6 bit data

BIT 6 not used

Commands

BIT 7 - last byte indication (see below)

8 - erase*

9 - write file mark*

10 - edit; same as write bit but does not generate a full inter-block gap. Used when overwriting a block with new data, but the block must be of the same length as the one overwritten.

11 - reverse

12 - rewind (rewinds to BOT)

13 - write (write a block forwards)

14 - go (start the command set up by bits 8-13)

15 - reset or INIT - CLR; reset DFU abort current command

*Must be set together with write bit. Write bit permits all write operations.

Either read or write depending on state of the bit.

Read a block forwards is Go bit on its own.

To issue a command set the appropriate bits (excluding the GO bit). No bits are set for a read forward operation. Command will commence operation when go bit is set. Clear go bit before attempting to issue another command. Any command can be aborted by setting tape reset bit. Again this must be cleared before attempting another reset. Go is <u>not</u> required by the reset bit.

Read and write request (REQA, REQB) are set by data strobe pulses (transfer data from/to DFU) and are not requests (from DFU) for data to be transferred. The implications of this are that when writing a block the first data byte must be in the data register before issuing the write command.

Write operations (except file mark) cease when the last byte bit is set with the last byte. No more strobe pulses occur after this and the DFU busy bit must be tested to determine when another command can be given. The request lines are set by the strobe pulses and are cleared when either more data is placed in the output register (NDR pulse) or data is read (DT pulse).

If two strobe pulses occur without a response from the computer a 'led' on the back of the tap drive is latched on to indicate data lost. There are two indicators, one for read data lost, one for write data lost. The indicators remain on until the next reset pulse.

When a read is in progress it is necessary to know in advance how many bytes are in the block. After the expected number of bytes have been received a check is made for DFU busy to indicate when another command can be issued.

If a block is shorter than expected most programs will "hang-up" waiting for a REQA interrupt or status indication that will never be given. Blocks longer than expected cause no special problems except that data is lost after the expected quantity.

Always issue a reset instruction at the start of operations. BIT 0 of the MTCSR sets the DFU "on-line". The tape drive will not respond to computer instructions if this bit is not set; manual operations can only be performed if it is unset (clear).

The read routine exits on encountering a filemark. Successive read calls CALL MTRD(,), read successive data blocks from tape.

Subroutine MTWRT writes data to magnetic tape. Register 5 passes over the data array buffer pointer from control program MTMAP.FOR. The subroutine also includes a tape edit facility for modifying (updating) the count of the number of parallel traces held in a magnetic tape file.

Each call to MTWRT writes over a data set as a separate block with a preceding inter-block gap (unless the Edit modification is being employed).

The macros of MTCRE.MAC are self-explanatory. .MACRO MTOP A moves a command bit to the MTOUT upper byte of the register, etc. These macros, together with the set up of command and test bits, need no further description given the magnetic tape interface document supplied as part of this appendix.

MTREAD.MAC is the assembler routine used in conjuction with MAPMT.FOR. Since this only involves reading from tape, the write operations of MTCRE.MAC have been omitted. In all other respects the program commentary for MTCRE.MAC is sufficient for MTREAD.MAC.

MTCRE.MAC Program Commentary

Subroutine INITMT initialises the magnetic tape unit at commencement of operations.

MTEOF and CLOMT are routines to write a filemark to tape and to close the magnetic tape with 2 filemarks respectively. N.B. The 2 closure filemarks are requested by the ULCC computer facility when reading magnetic tapes.

PACLAB and UNPLAB are routines for packing and unpacking the identifier label ∇SPN∇M(I1)T(I1)N(I1) post to read and prior to write tape operations respectively. N.B. (i) The last data byte to be transferred to any write operation is flagged as follows:

```
BISB #LWD, - 1(R4)
```

i.e. the last word bit is set in the last byte; here register 4 holds the output array buffer pointer. (ii) Only the least significant 6 bits are written over PACLAB adds back the necessary bit 7 of the ASC 11 code for non-digit characters.

DATPRP and DATPK prepare data for an MTWRT operation and pack data following an MTRD operation respectively.

DATPRP unpacks a 12-bit words into 2 6-bit bytes the M.S. part is transferred first. Register 5 passes over the data buffer array pointer together with the number of words in the data transfer. Again the LWD bit is automatically set. DATPK's function is merely to reconstitute a pair of 6-bit bytes into a single 12-bit word when data is read over from magnetic tape.

MTRD reads a data block from tape. The correct number of words to be read is passed over. The system remains locked out if the block size is smaller than that stated by the number of bytes parameter of the read routine.

APPENDIX 5B

Mapping Program Documentation

This appendix provides hard copy listings of all programs concerned with the various aspects of mapping and recording operations. The fortran programs are virtually self-explanatory, however, the interactive features of these programs are again elucidated in the form of operations manuals of the surface mapping procedures.

Program directory

(a) profile data gathering:

SRRMPP.FOR

Operations manual for SRRMPP.FOR

TALY.MAC

TALY.MAC program commentary

(b) transfer (write) to magnetic tape;

MTMAP.FOR

Operations manual for MTMAP.FOR

(c) perspective plots and magnetic tape (read:

MAP.MT.FOR

Operations manual for MAP.MT.FOR

PROGRAM

FILENAME: SRRMPP.FOR

ASSOCIATED FILE(S) (1) TALY.MAC

DESCRIPTION

The program allows for the automatic mapping of surface by a Talysurf-10 machine. The output signal from the Talysurf is electronically recorded into core and displayed on the tektronix panel. Valid data may be subsequently transferred to a floppy disc file. Operator interaction allows for several traces (assumed parallel) to be taken and recorded.

SRRMPP.FOR Operations Manual

Stage	Operation or Display	Action
1	Run program	.RU SRRMPP
2	'IDENTIFIER LABEL'	Type in M,T,N identifier tags (3I1)
3	'NUMBER OF PARALLEL TRACES'	Type in no. of traces (I4)
4	'NUMBER OF SAMPLES PER TRACE'	Type in no. of samples (I4)
5	'LENGTH OF TRACE'	Type in range (mm) (F3.1)
6	'HORIZONTAL MAGNIFICATIONS'	Type in V_H setting of Talysurf
7	'CLOCK PULSE FREQUENCY='HZ	Set up pulse generator with the display frequency setting
8	'SEPARATION OF PARALLEL TRACES'	Type in inter-trace gap (H2) (F6.4)
9	'MAGNIFICATION FACTOR'	Type in graphics display ← → magnification factor
10	'FIRST TRACE'	(Information only)
11	'SET TALYSURF-10 AND GO'	Set up talysurf run and press start button
12	'LOOK AT DATA TABLE' 'FIRST TRACE COMPLETED'	Type return (Information only)
13	'SECOND TRACE'	Type Y → reset talysurf and gather second trace
	Q('SECOND TRACE OPTION?')	Type return → continue
14	Q('ACCEPT DATA?')	Type Y → data to disc Type return → stage 11
15	'STEP TEST-PIECE BY H2 IF DATA ACCEPTED'	Advance specimen by inter trace gap (H2)
16	'END OF MAP?'	Program counts on no. of traces. Goes to stage 10 if mapping continuing
	STOP	

```
NLIST  BEX,SEQ

TITLE  TALYSURF MAP DATA GATHER

GLOBL  GETDAT

MCALL  REGDEF

REGDEF

DRCSR=164020
DROUT=DRCSR+2
DRIN=DROUT+2

PSW=177776
P7=340

GETDAT:  CMP    (R5)+,#3          ;CHECK FOR LEGAL NO. OF
                                  ;PARAMETERS
         BEQ    1$                ;RETURN IF ILLEGAL NO.
         RTS    PC                ;OF PARAMETERS

1$:      MOV    (R5),R0           ;ARRAY POINTER TO R0
         MOV    @2(R5),R1         ;NO. OF SAMPLES TO R1

         MOV    PSW,-(SP)
         MOV    #P7,PSW

REST:    TSTB   @#DRCSR           ;WAIT FOR FIRST CLOCK PULSE
         BPL    REST              ;TALYSURF RUNNING?
         JMP    GO                :YES!

LOOP:    TSTB   @#DRCSR           ;NEW DATA REQUEST?
         BPL    LOOP              ;NO

GO:      MOV    @4(R5),@#DROUT    ;START ADC CYCLE

LOOP1:   TST    @#DRCSR           ;CONVERSION COMPLETE?
         BPL    LOOP1             ;NO

         MOV    @#DRIN,(R0)       ;RESULT INTO ISCAN ARRAY
         BIC    #170000,(R0)+     ;CLEAR OFF NOISE

         DEC    R1                ;DECREMENT COUNTER
         BNE    LOOP              ;BRANCH IF NOT FINISHED

         CLR    @#DRCSR
         MOV    (SP)+,PSW

         RTS    PC

         END    GETDAT
```

TALY.MAC program commentary

Register five passes over parameters from SRRMPP.FOR control program: subroutine call is

CALL GETDAT(ISCAN,ISPLES,3)

Here, ISCAN is the matrix to hold profile data samples, ISPLES is the number of samples to be gathered during the trace, whilst 3 refers to channel 3 input at ADC board.

The RT-11 system is locked out during the data gathering process this is achieved by moving priority 7 to the processor status word (PSW).

The clock pulse is linked, together with the talysurf-10 interface circuit, to request A (REQA) line of DRCSR.

When talysurf is activated the circuit logic allows the data request pulses to select REQA.

```
TSTB  @#DRCSR
```

ADC is started whenever DROUT low order byte is addressed

```
MOV  @4(R5),@#DROUT  starts ADC conversion cycle

TST  @#DRCSR  recall ADC sets REQB line when data
              conversion is complete
```

DRIN buffer holds 12 bit data word which is passed to ISCAN array

```
MOV  @#DRIN,(R0)
```

When data gathering is complete the RT-11 control system is restored.

PROGRAM

FILENAME : MTMAP.FOR

ASSOCIATED FILE(S) (1) MTMAP.MAC

DESCRIPTION

The program transfers surface data acquired via the Talysurf-10 and recorded on floppy discs to magnetic tape. Existing mag. tape files can be read and checked or merely bypassed before transferring more data. The last file can be augmented with further profile scans if desired.

Stage	Operation or Display	Action
1	Run program	.RU MTMAP
2	Q('MT FILE EXTEND?')	Type Y → add further scans to an existing mag. tape file.
3	Q('BYPASS EXISTING FILES?')	Type Y → to read existing files. Type return → initialise new tape ready for recording scan data. Type in new filename, format as given in 5.
4	Q('DISPLAY EXISTING FILE(S)?')	Type Y → read mag. tape file and display data. Type return → read to end of recorded mag. tape data.
5	Q('MODIFY LABEL?')	Type Y → Type in ∇SPN∇M(I1)T(I1)N(I1) i.e. new file name.
6	Q('TRANSFER LABEL?')	Type Y → Label written to tape.
7	Q('DISPLAY TRANS.FILES?')	Type Y for data to be displayed.
8	Q('OPEN ANOTHER DISCFILE?')	Type Y for further files to be transferred from floppy disc, or Type return → stage 10.
9	Q('WRITE FLMK TO CLOSE MTFILE?')	Type Y to close mag. tape file.
10	Q('MT FILE EXTEND?')	Type Y to augment current mag. tape file. Type return → end.
11	Q('MODIFY ITRACE?')	Type Y to update number of traces in mag. tape file. Type in update trace count.
12	Q('READ TO END OF RILE?')	Type Y to read file and forego data display option. Go to stage 14. Type return → display mag. tape file information.
13	Q('CONTINUE READ CHECK?')	Type return → end.

Stage	Operation or Display	Action
14	Q('READ/WRITE ANOTHER FILE?')	Type Y → continue file transfers. Go to stage 4. Otherwise, type return → end.
15	STOP	

PROGRAM

FILENAME: MAPMT.FOR

ASSOCIATED FILE(S) (1) MTREAD.MAC

DESCRIPTION

The program transfers successive profile traces from magnetic tape into core to be graphed as an isometric surface projection on the tektronix screen.

MAPMT.FOR OPERATIONS MANUAL

Stage	Operation or Display	Action
1	Run program	.RU MAPMT
2	'MAGNIFICATION FACTOR'	Type in profile trace display magnification.
3	'NO. OF PARALLEL TRACES'	Type in number of parallel traces constituting the perspective plot.
4	Q('REQUIRED FILE?')	Type Y is displayed file name is the required file. Go to stage 6.
5	Q('LAST FILE?')	Type Y to abort. Type return and re-enter stage 4.
6	'PRINT/GRAPH OUT FIRST TRACE'	Type return (information only).
7	Q('END OF MAP?')	Type Y → mapping complete. Type return → go to stage 4 to search for further profile data plots to augment perspective plot.
	STOP	

CHAPTER 6

DATA PRESENTATION AND STATISTICAL ANALYSIS

Abstract

Following the discussion of the data acquisition methods of Chapter 5, the initial data processing routines are described, and typical examples of graphical and statistical output are provided.

Williamson [1968] first achieved a three-dimensional map of a surface. His initial work has been extended by Thomas [1975], Sayles and Thomas [1976], Sayles and Thomas et al [1977], contemporary with our own work, whereby the data gathering procedure has been automated and controlled by a minicomputer, in a manner similar to that described in the previous chapter. The topicality of this research is further evidenced by the recent papers by Teague et al [1982], and George and Radcliffe [1982], presented recently at the International Conference on "Metrology and Properties of Engineering Surfaces".

Attention is given to certain metrological problems, particularly with those associated with the accepted routines for computing the statistics of surface slopes.

The relationship between the derived statistics of surface roughness and beam scatter collated and presented here, forms part of the treatment of Chapter 7, where the 'cause and effect' of surface roughness/laser beam interaction is investigated fully.

6.1 Graphical Presentation of Intensity Data

6.1.1. Two and Three Dimensional Polar Diagrams

The natural form of graphical presentation of intensity data is the polar diagram. This best provides

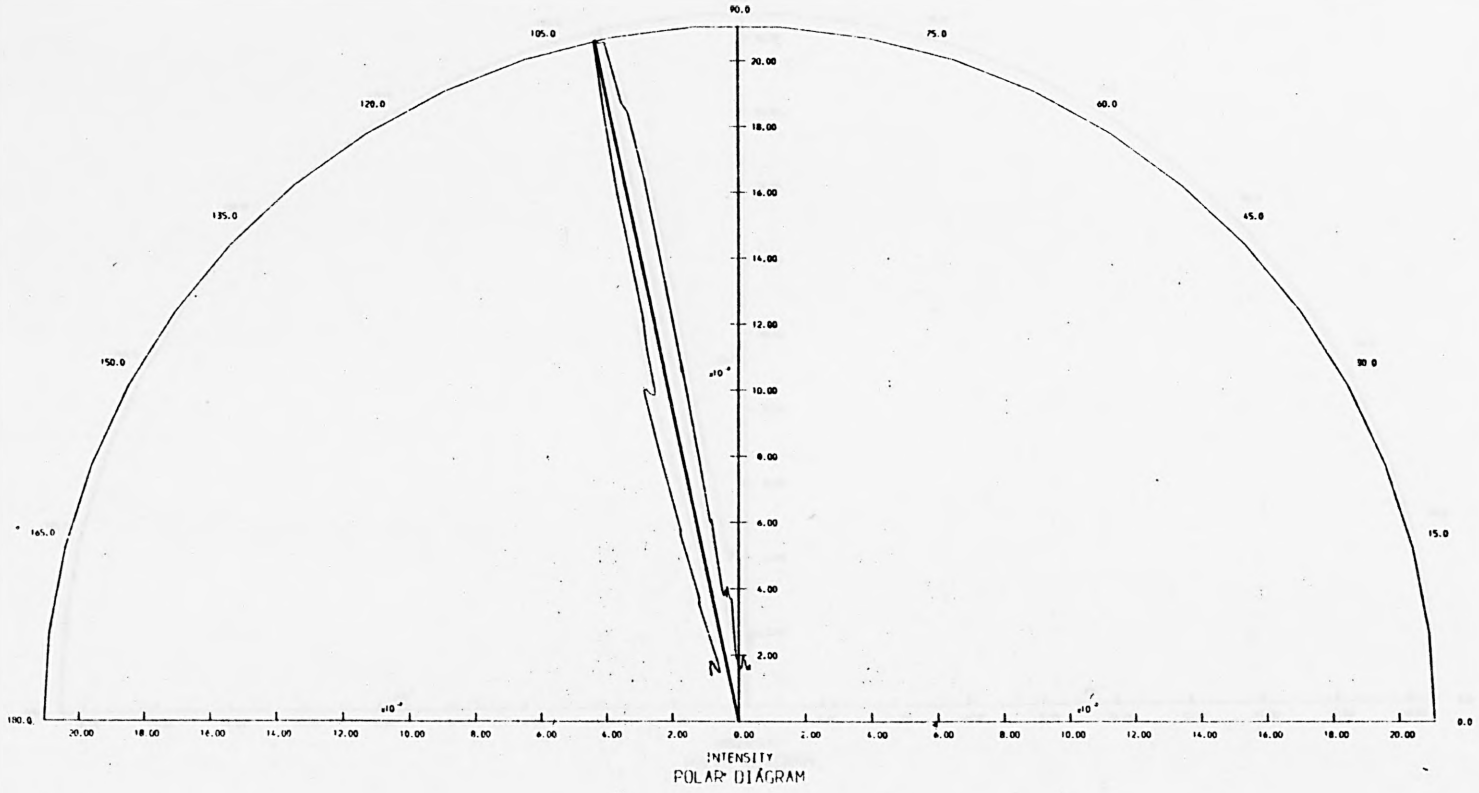

FIG. 6.1.1. Polar plot of intensity: defect specimen M1T4 scan 180°.

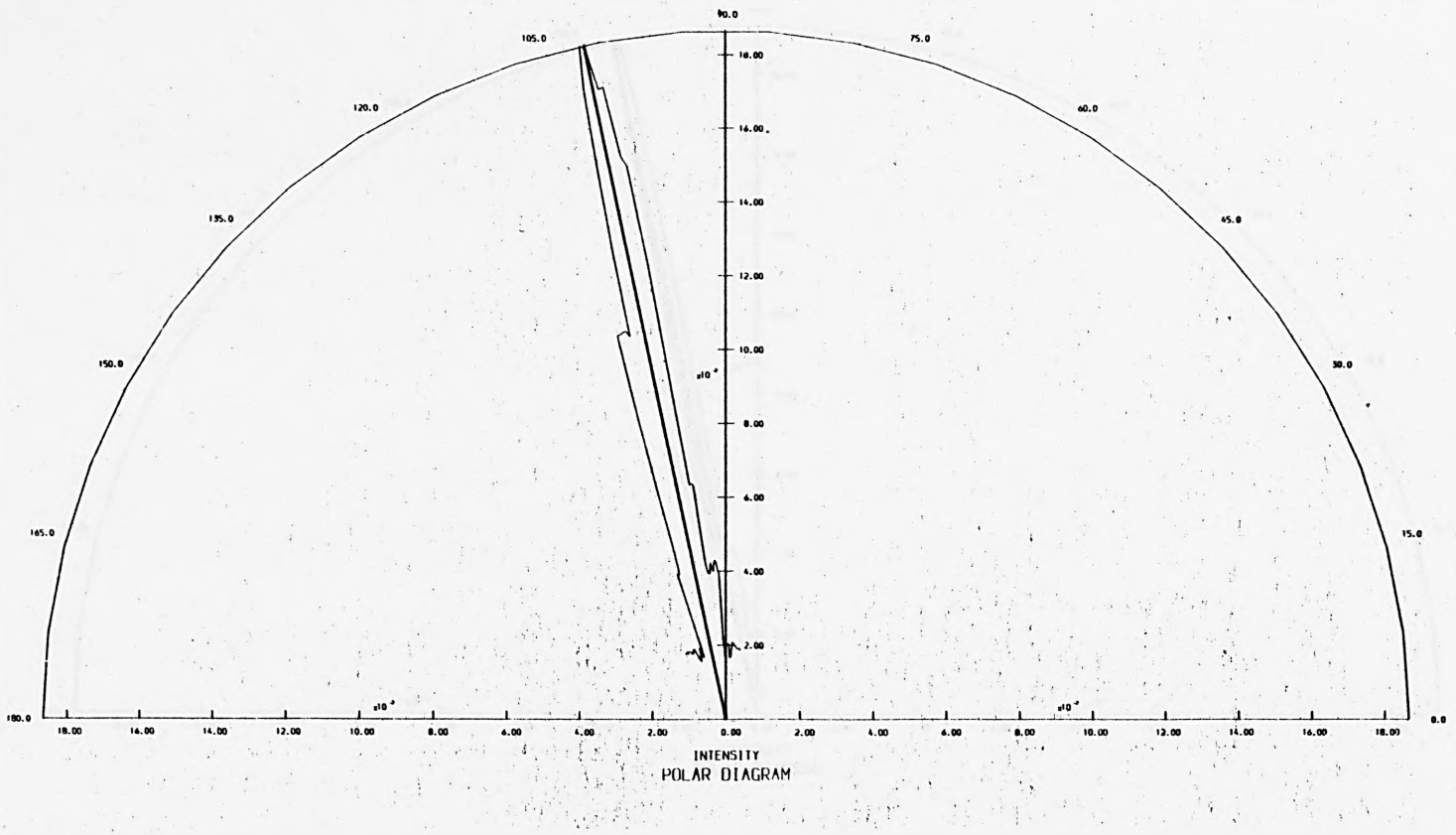

FIG. 6.1.2. Polar plot of intensity: defect specimen M1T4 scan 190°

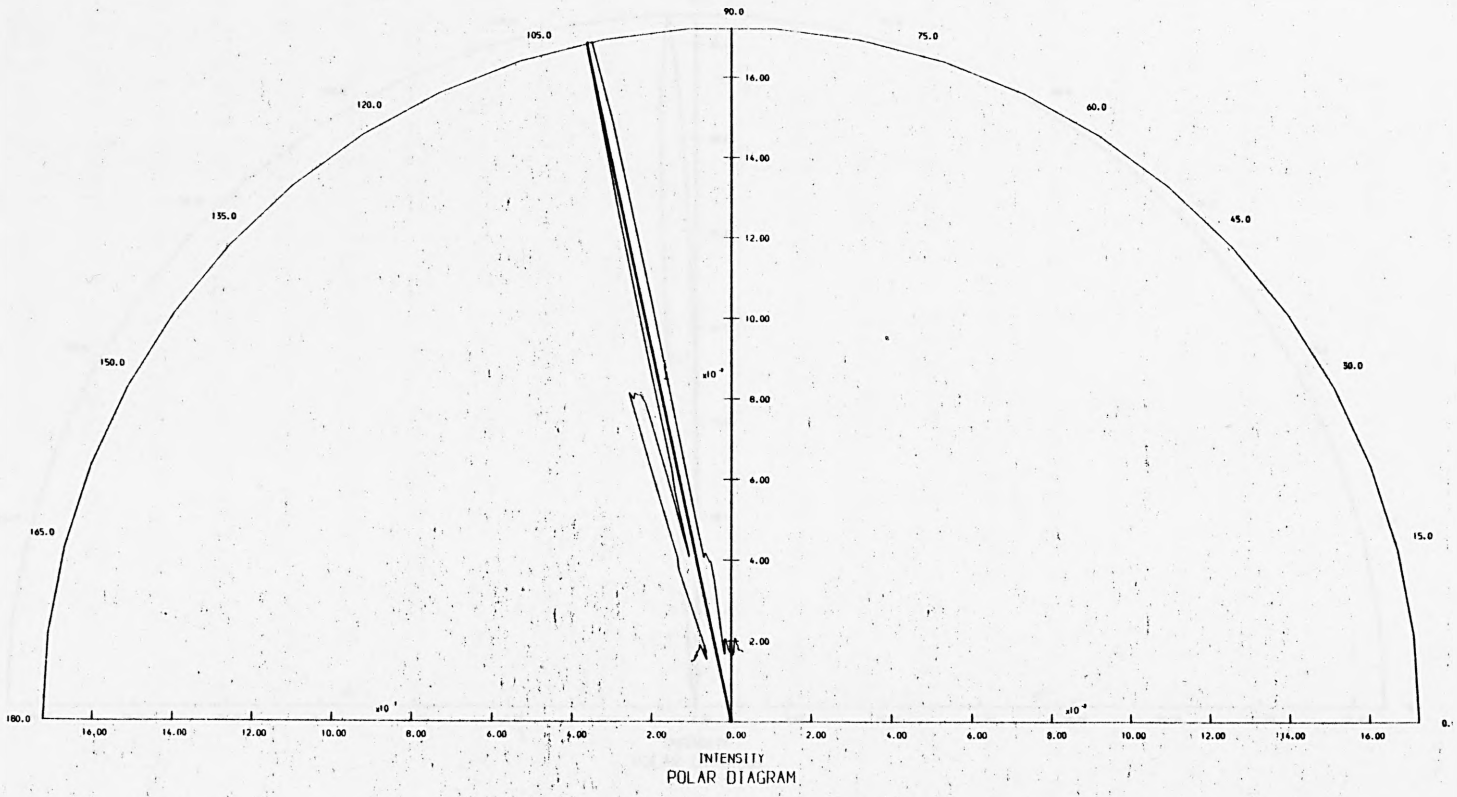

FIG. 6.1.3. Polar plot of intensity: defect specimen M1T4 scan 200°

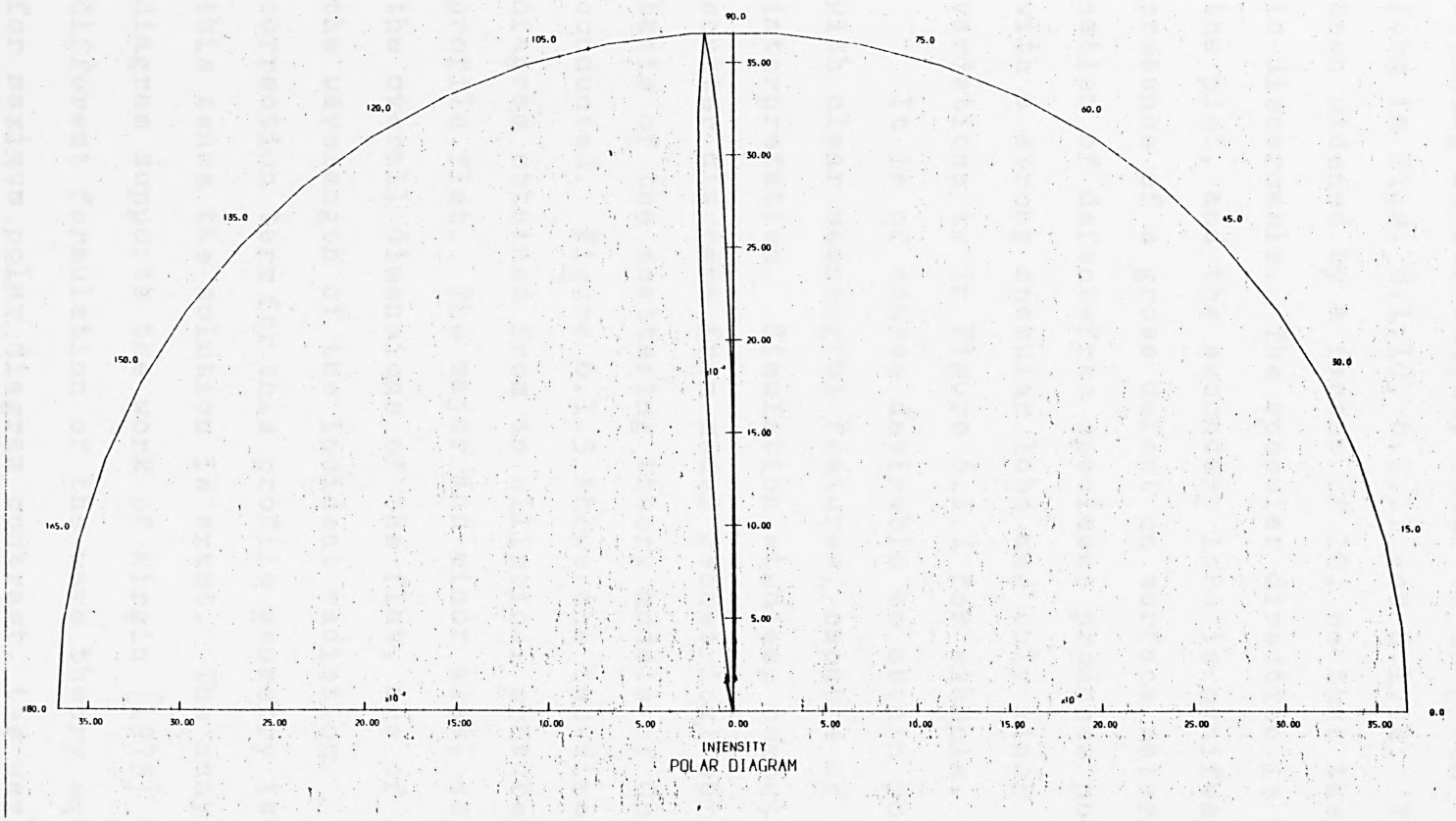

FIG. 6.1.4. Plot of intensity: non-defect specimen

the directional description of the scattered radiation. Figures 6.1.1, 6.1.2 and 6.1.3 are polar plots of the scanning sensor output, later to be given cartesian form in Figs. 6.1.10, 6.1.11 and 6.1.12. They have been widened by a factor of 10, so that the fine detail is discernable. The specular direction is indicated on the plot, and the secondary lobe is manifested by the presence of a gross defect on surface material. Examination of defect-free specimens produces polar diagrams with a strong specular lobe and only minor fine detail variations as in Figure 6.1.4 for example.

It is of course desirable to obtain polar diagrams with clear meaningful features, capable of unambiguous interpretation. Simulation studies, computing polar scatter diagrams from model geometrical surfaces on the basis of the scattering theory models of Chapter 4, were conducted. Figure 6.1.5 shows the two-dimensional polar diagram obtained from an elliptical protuberance on a profile flat. The major and minor axes, as well as the overall dimensions of the flat, are of the order of the wavelength of the incident radiation. The end-correction term for this profile geometry is zero and in this sense the solution is exact. The many-lobed polar diagram supports the work of Wirgin [1975] using a different formulation of the wave theory equation: that for maximum polar diagram contrast, the wavelength of the incident light should be of the same order as the size of the defect protuberances. He terms this a so-called 'resonance' effect. We shall take up this point again in Chapter 9.1 when discussing instrument design.

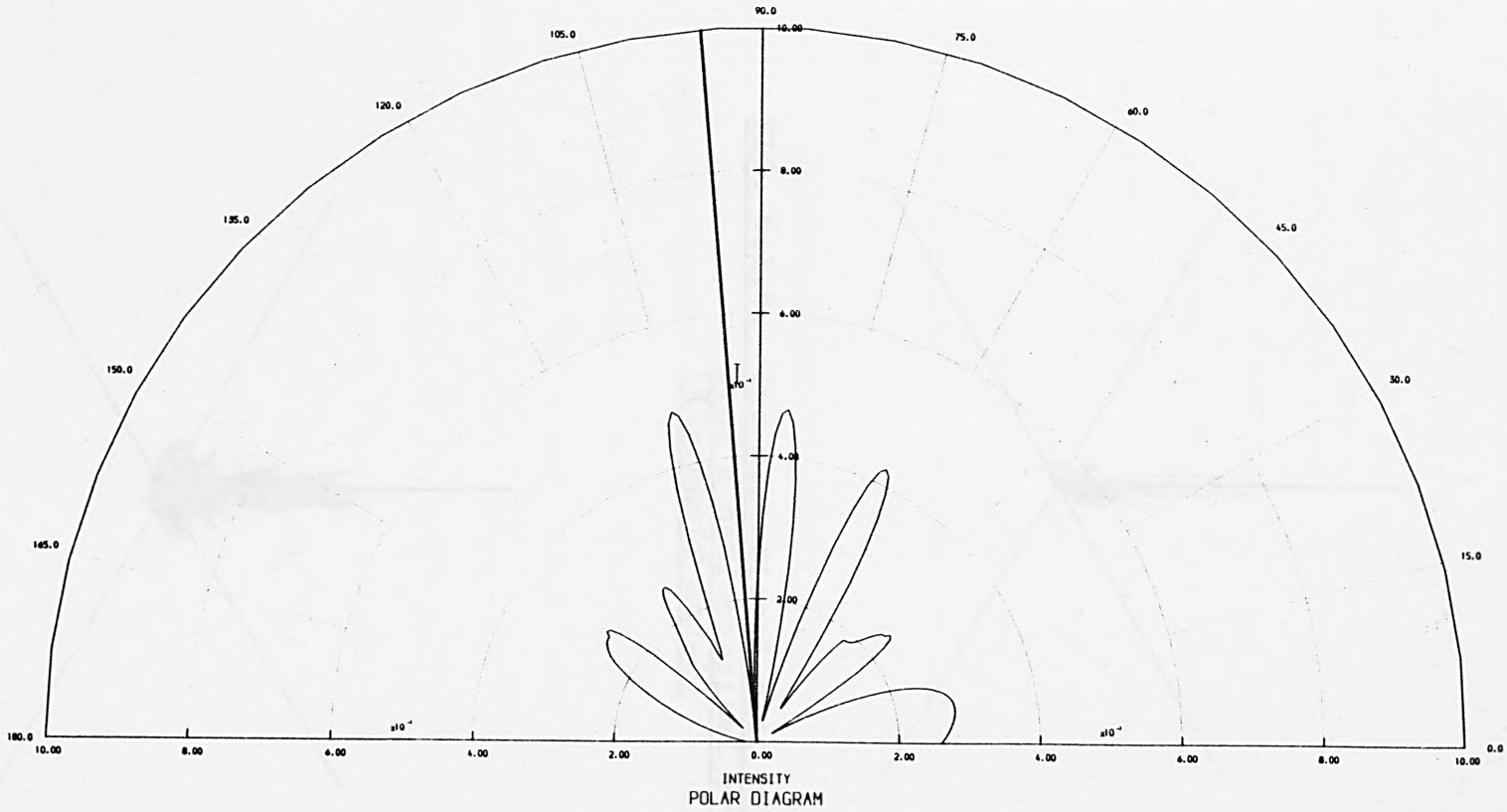

FIG. 6.1.5. Two-dimensional polar plot of scattering from an elliptical protuberance (Kirchhoff model)

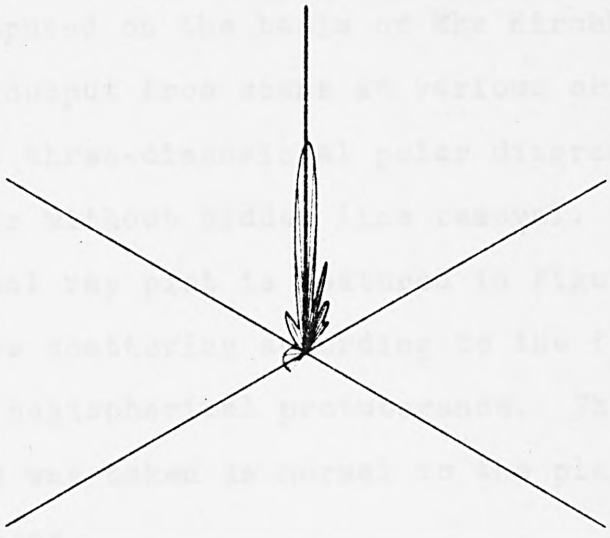

FIG. 6.1.6. Two-dimensional plot of scattering from a hemispherical protuberance (Kirchhoff model)

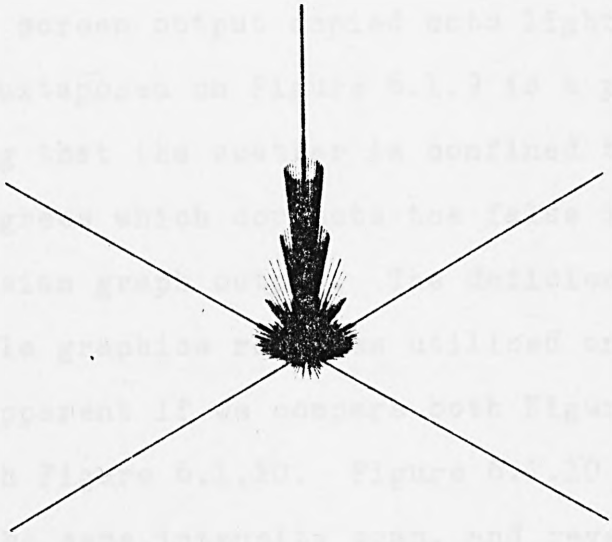

FIG. 6.1.7. Three-dimensional ray plot of scattering from a hemispherical protuberance (facet model)

Again Figure 6.1.6 shows the scattering from a hemispherical protuberance on a flat plane from a 2-D scan, computed on the basis of the Kirchhoff model. Computed output from scans at various orientations, enables a three-dimensional polar diagram to be built up with or without hidden line removal. A three-dimensional ray plot is featured in Figure 6.1.7, which shows rays scattering according to the facet model from the same hemispherical protuberance. The angle of incidence was taken as normal to the plane in both computations.

6.1.2. Intensity Versus Angle Plots

Cartesian plots of intensity versus angle are frequently exploited, although their visual impact is enhanced or dimished when distorted by changes of scale. Figures 6.1.8 and 6.1.9 were produced from the tektronix screen output copied onto light sensitive paper. Juxtaposed on Figure 6.1.9 is a polar plot indicating that the scatter is confined to at most one or two degrees which corrects the false impression of the cartesian graph output. The deficiencies of the over-simple graphics routines utilised on the PDP are readily apparent if we compare both Figures 6.1.8 and 6.1.9 with Figure 6.1.10. Figure 6.1.10 is a microfilm plot of the same intensity scan, and reveals just how much of the fine detail was suppressed.

The scan was from a metal specimen bearing a scratch defect. We also include a sequence of three plots from the same specimen, featured earlier as a sequence of polar diagrams (Figures 6.1.1-6.1.3), and we observe the bimodal nature of the plot at certain

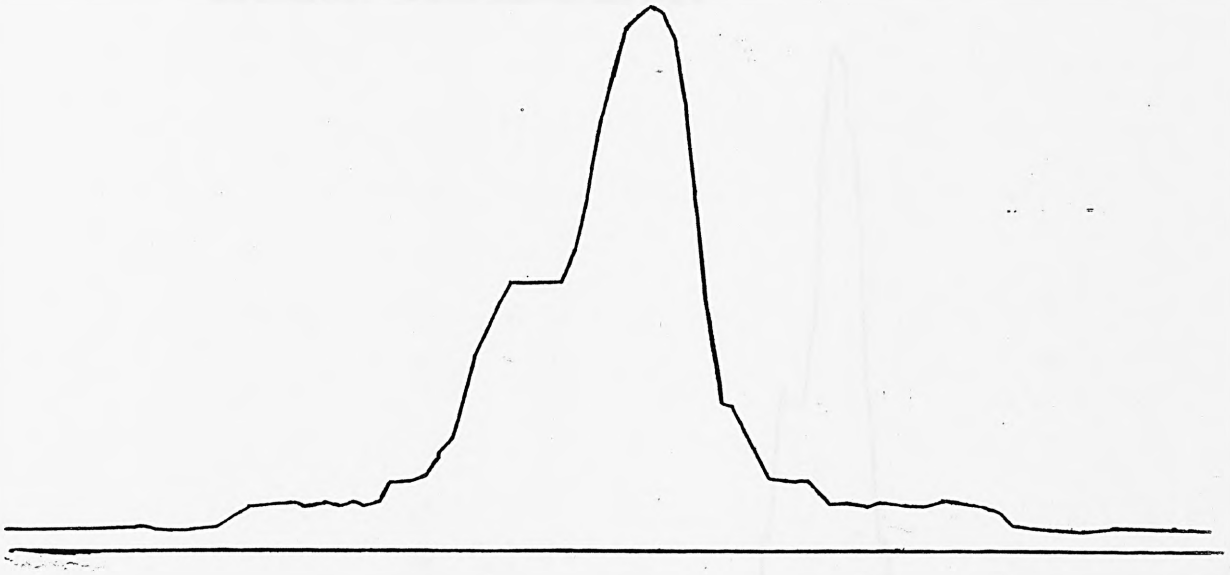

FIG. 6.1.8. Cartesian plot of intensity versus angle obtainable on Tektronix screen

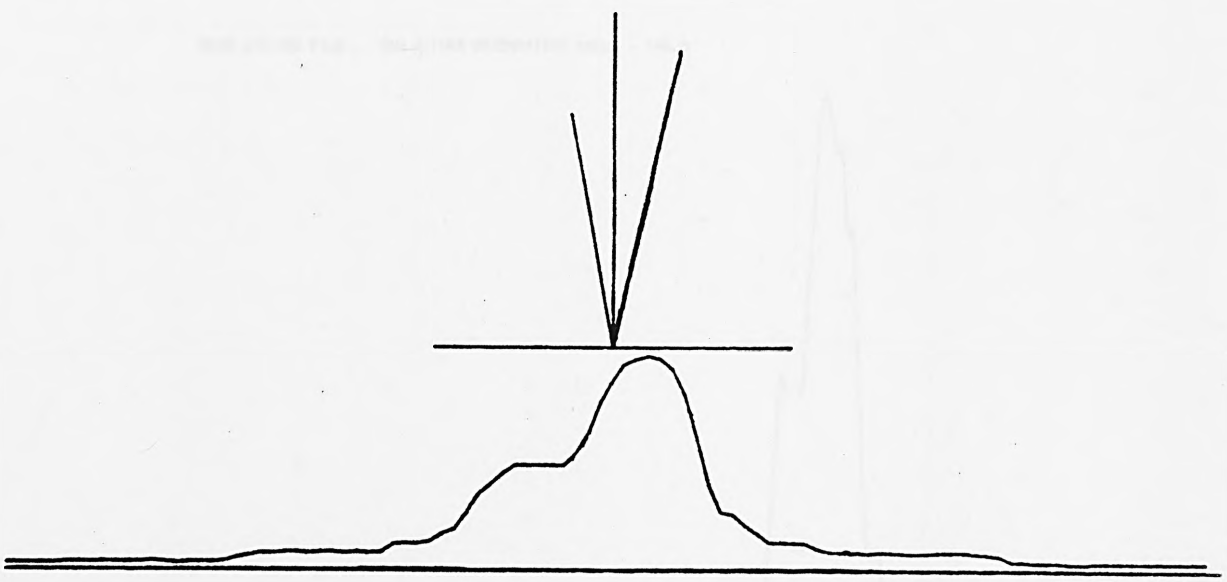

FIG. 6.1.9. Polar diagram and cartesian plot of intensity scatter (Tektronix screen output)

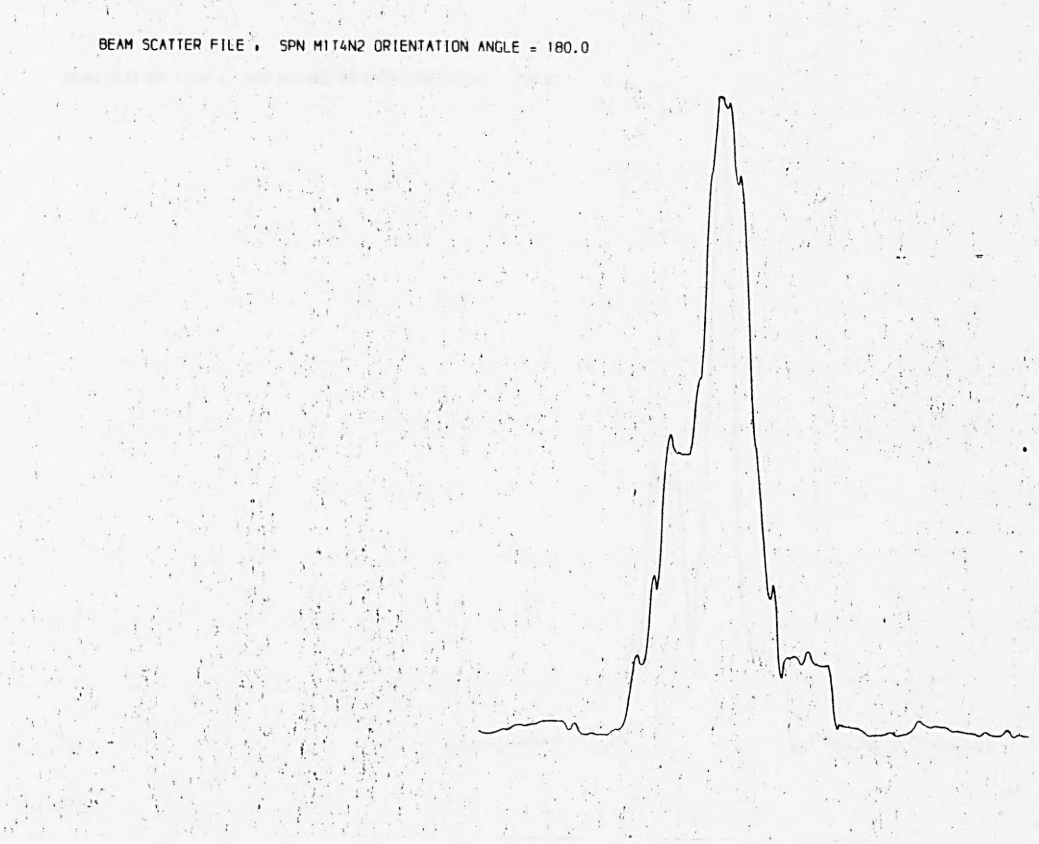

FIG. 6.1.10. Cartesian plot of intensity: defect specimen M1T4 scan 180°

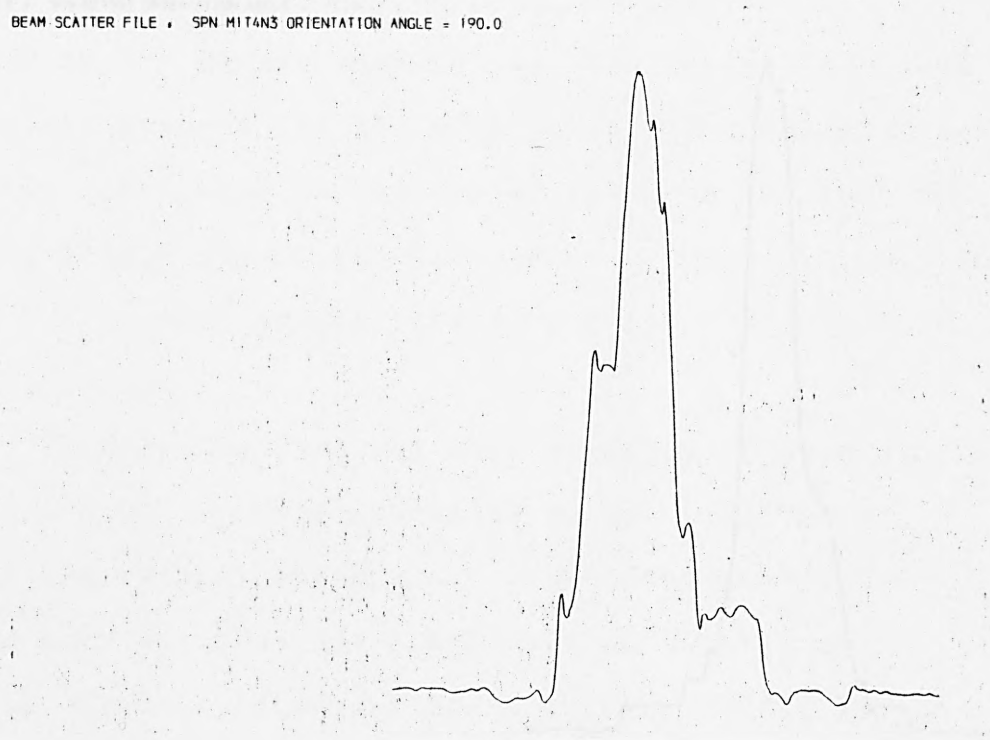

FIG. 6.1.11. Cartesian plot of intensity: defect specimen M1T4 scan 190°

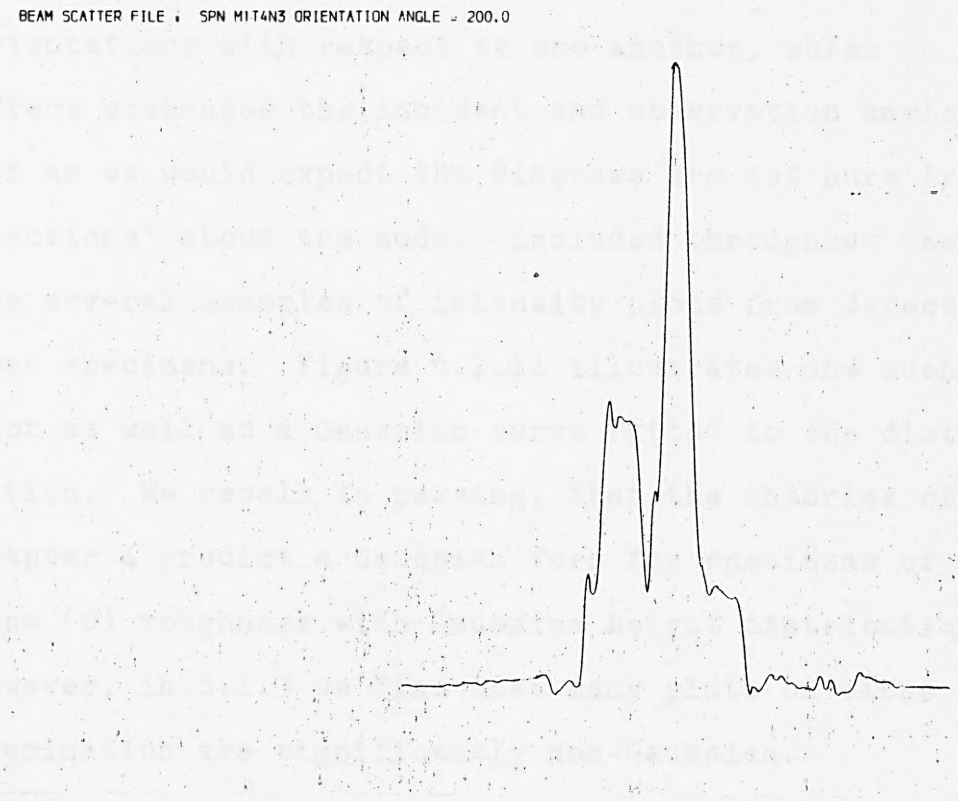

FIG. 6.1.12. Cartesian plot of intensity: defect specimen M1T4 scan 200°

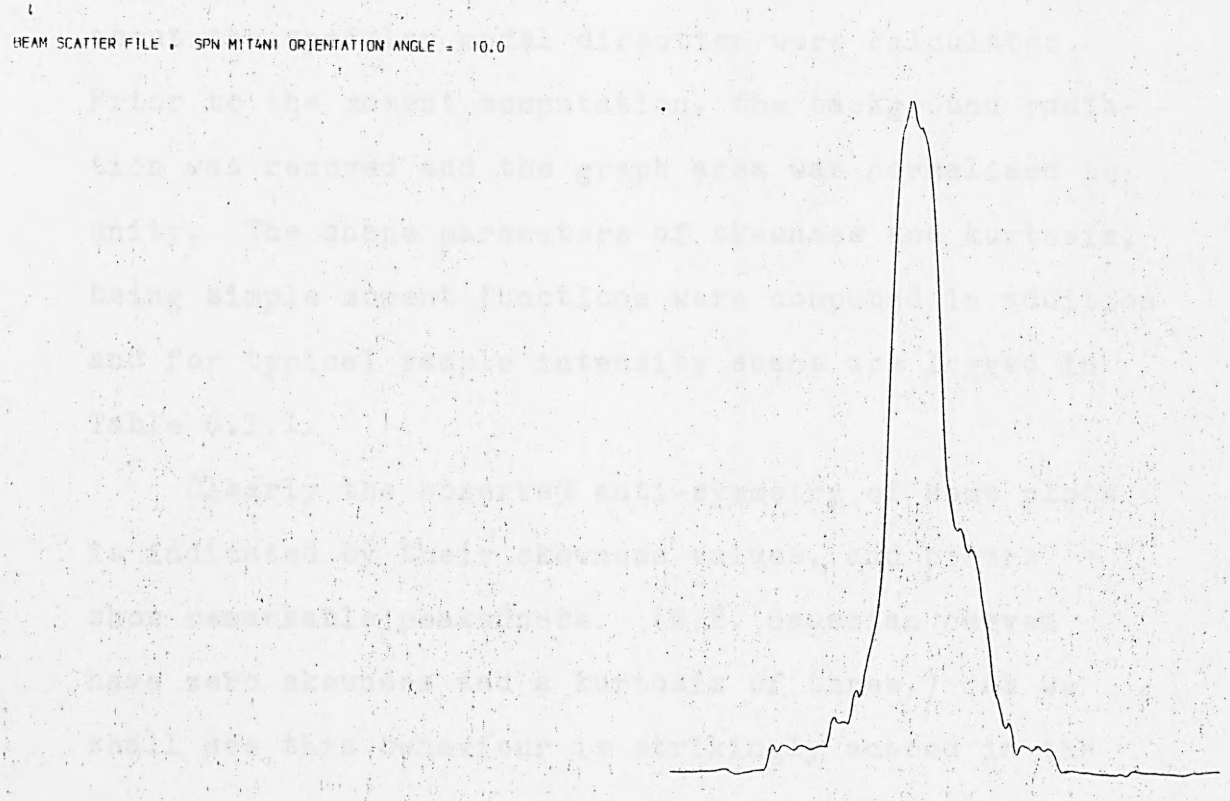

FIG. 6.1.13. Cartesian plot of intensity: defect specimen M1T4 scan 10°

orientations. Figures 6.1.11 and 6.1.13 are 180° orientations with respect to one another, which in effect exchanges the incident and observation angles, but as we would expect the diagrams are not pure 'reflections' about the mode. Included throughout the text are several examples of intensity plots from defect free specimens. Figure 6.1.14 illustrates one such plot as well as a Gaussian curve fitted to the distribution. We recall in passing, that the theories of Chapter 4 predict a Gaussian form for specimens of Type (C) roughness with Gaussian height distributions. However, in 6.1.3 we find that many plots on close examination are significantly non-Gaussian.

6.1.3. Moment Description of Intensity Distributions

To quantify an intensity plot, albeit in a rather limited manner, the low order moments of the intensity about the specular modal direction were calculated. Prior to the moment computation, the background radiation was removed and the graph area was normalised to unity. The shape parameters of skewness and kurtosis, being simple moment functions were computed in addition and for typical sample intensity scans are logged in Table 6.1.1.

Clearly the observed anti-symmetry of some plots is indicated by their skewness values, and others show remarkable peakedness. (N.B. Gaussian curves have zero skewness and a kurtosis of three.) As we shall see this behaviour is strikingly echoed in the skewness and kurtosis of the distribution of height slopes of the particular specimens.

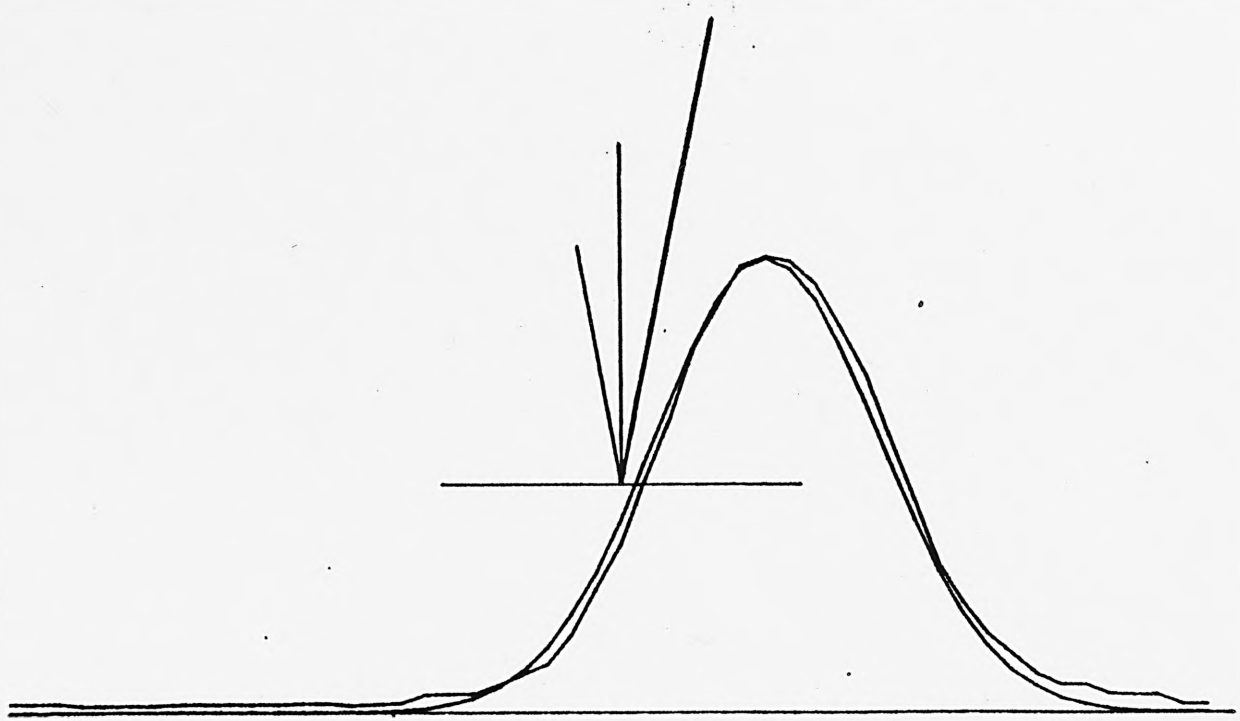

FIG. 6.1.14. Cartesian Plot of Intensity: non-defect specimen M1T2 with fitted Gaussian frequency curve

Specimen Labels	Specimen Description	Summary Statistics of Intensity Plots
M0T2	Stainless Steel Rolled	Scan 190 Scan 270 SD* 0.18 SD 0.20 SK -0.53 SK -2.53 KU 5.94 KU 15.71
M0T3	Stainless Steel Rolled	Scan 10 Scan 40 SD 0.46 SD 0.58 SK -1.06 SK -1.89 KU 3.74 KU 4.06
M1T1	Steel Ground	Scan 180 Scan 90 SD 0.21 SD 0.20 SK 1.01 SK 0.60 KU 12.51 KU 9.8
M1T2	Steel Ground	Scan 180 Scan 90 SD 0.20 SD 0.24 SK -0.23 SK -2.00 KU 4.14 KU 12.99
M3T1	Brass Ground	Scan 160 Scan 270 SD 0.22 SD 0.19 SK 0.42 SK 0.60 KU 5.37 KU 8.08
M3T2	Brass Ground	Scan 0.0 Scan 90 SD 0.21 SD 0.30 SK 0.31 SK 1.8 KU 6.99 KU 8.50
M2T4	Copper Ground	SD 0.58 SD 0.34 SK 1.58 SK -0.94 KU 3.11 KU 8.07
M2T2	Copper Ground	SD 0.23 SD 0.25 SK -0.80 SK 1.40 KU 12.27 KU 18.66

*SD = standard deviation
SK = skewness
KU = kurtosis

TABLE 6.1.1. Description of Intensity Plot in terms of Moments

6.1.4. Fitting a Pearson Type VII Frequency Function

Pearson [1914] developed a system for fitting frequency curves. He defined seven different types each determined by specified ranges of skewness and kurtosis. For the Sheffield samples of stainless steel for instance: the specimen MOT3 yielded plots which were more adequately Gaussian, with or across the rolling direction, which contrasted markedly with specimen MOT2, for which the plots are either Pearson type IV, if we treat the skewness as significant, or else are modelled according to the symmetric Pearson type VII.

It was deemed more appropriate to fit Pearson VII curves as the skewness was likely to be attributable in part to sampling variations of the surface roughness, and to surface defect effects, rather than according to a systematic effect of real interest. This latter interpretation however demands its retention as an information statistic.

The type VII Pearson curve is of the form:-

$y = yo(1 + x^2/c^2)^{-m}$, containing two parameters m and c. This family includes the well known Cauchy and t-distributions of statistical theory. Relationships between the moments of the Pearson VII are phrased in terms of gamma functions and we may deduce (c.f. Appendix 6).

$$\sigma^2 = \frac{c^2}{2m - 3} \qquad \ldots.(1)$$

$$\beta_2 = \frac{6m - 9}{(2m - 5)} \qquad \ldots.(2)$$

The parameter m is stated entirely in terms of the kurtosis via (2), whilst the parameter c clearly influences the spread of the distribution. For those intensity distributions with high peakedness the Pearson VII provided an adequate fit.

Specimen M0T2 - scan 270

St. dev. of intensity scatter = 0.199 degrees
Skewness of intensity scatter = -2.54
Kurtosis of intensity scatter = 15.72

Pearson VII parameters m = 2.736
c^2 = 0.980

Observed Intensity	Pearson VII Fitted Frequency
0.0013	0.0084
0.0030	0.0118
0.0240	0.0167
0.0236	0.0234
0.0469	0.0334
0.0589	0.0463
0.0754	0.0626
0.1070	0.0812
0.1159	0.0994
0.1181	0.1131
0.1182	0.1182
0.1163	0.1131
0.1158	0.0994
0.0930	0.0812
0.0820	0.0626
0.0696	0.0463
0.0470	0.0334
0.0240	0.0237
0.0240	0.0167
0.0012	0.0117
0.0006	0.0008

Sum of Squared errors = 0.0034

TABLE 6.1.2. Pearson VII fit to highly Kurtosed intensity curve

6.2 Graphical Presentation and Statistical Analysis of Surface Topography Data

6.2.1 Perspective and Contour Plots

A perspective plot, namely an oblique projection of the data base, is a powerful visual display of the surface topography. The resolution bias, lent by the manner of the data acquisition (c.f. Chapter 5), can be removed by sampling ten times less often, along a particular trace, before invoking the graphical procedures.

The refinement of removing hidden lines is available. Maintaining an up-to-date view of the horizon as each profile is sketched, is virtually the only additional complication afforded to the program software. Such an image, whereby what is graphed is what is seen, is more consistent with our usual conception of reality. However, as a representation of the surface the full information might be of more value. Another representation, would be to graph out those portions of a profile trace, hidden on a particular perspective plot, at reduced intensity.

Examples of perspective plots are reproduced in Figures 6.2.1 to 6.2.4. Figure 6.2.1 and 6.2.2 show plots of a ground steel specimen, with and without hidden line removal. Surface defects are plainly visible. Figure 6.2.3 shows another steel specimen ground to a less smooth finish. Deliberate parallel scratches were made on the specimen illustrated in Figure 6.2.4; the material has been literally gouged out and forms a rim on either side of each scratch.

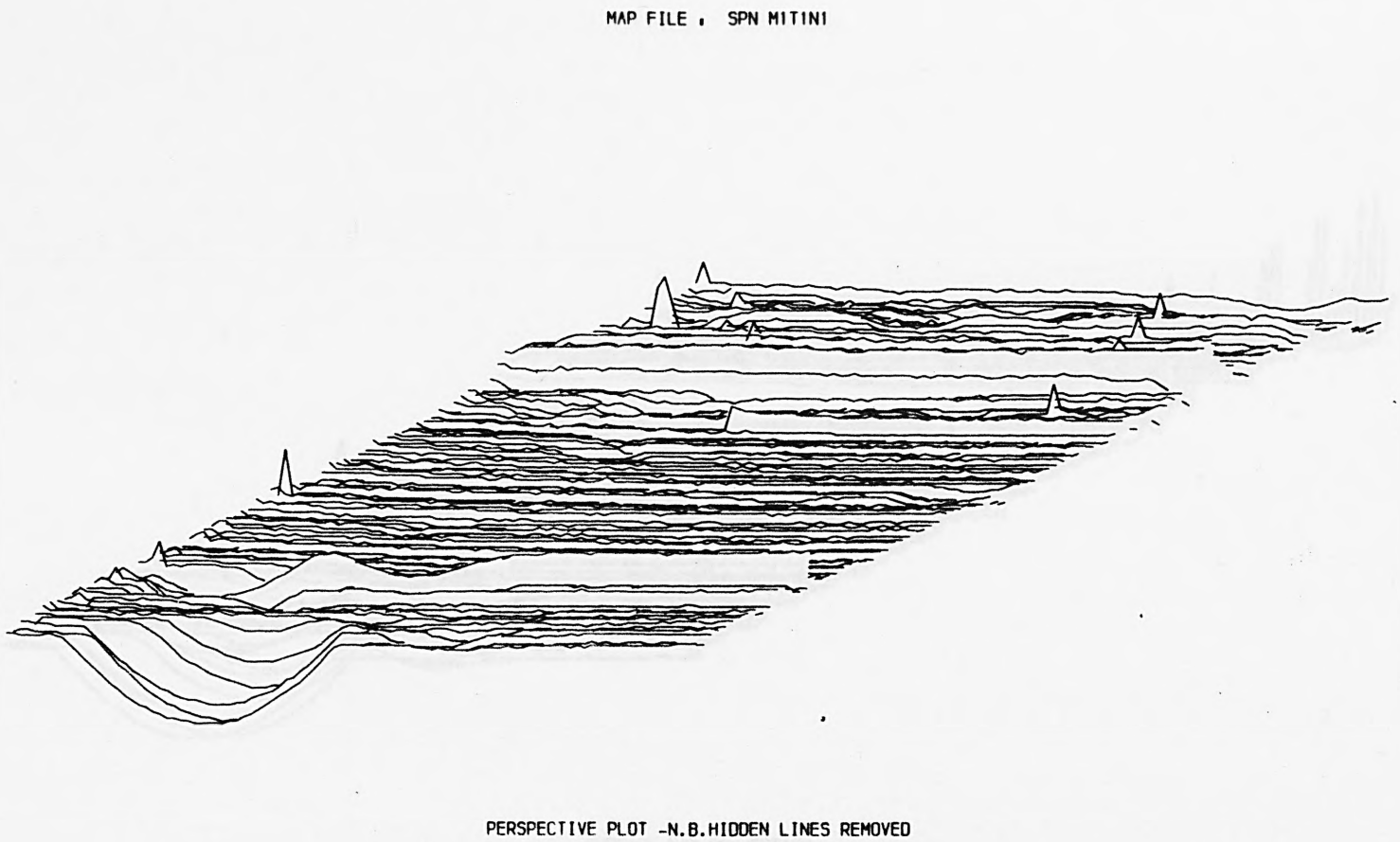

FIG. 6.2.1. Perspective plot of specimen M1T1 with hidden line removal

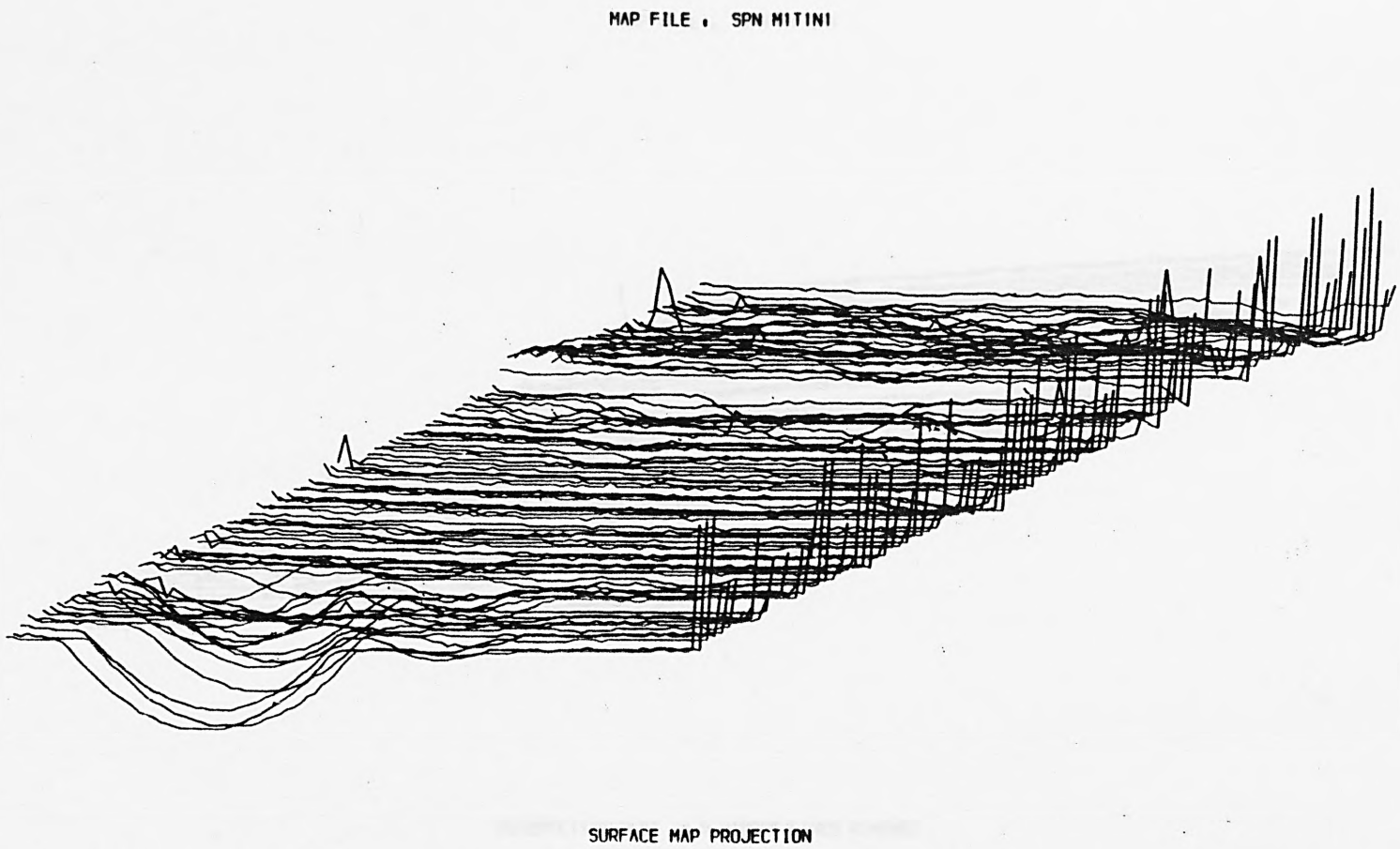

FIG. 6.2.2. Perspective plot of specimen M1T1 without hidden line removal

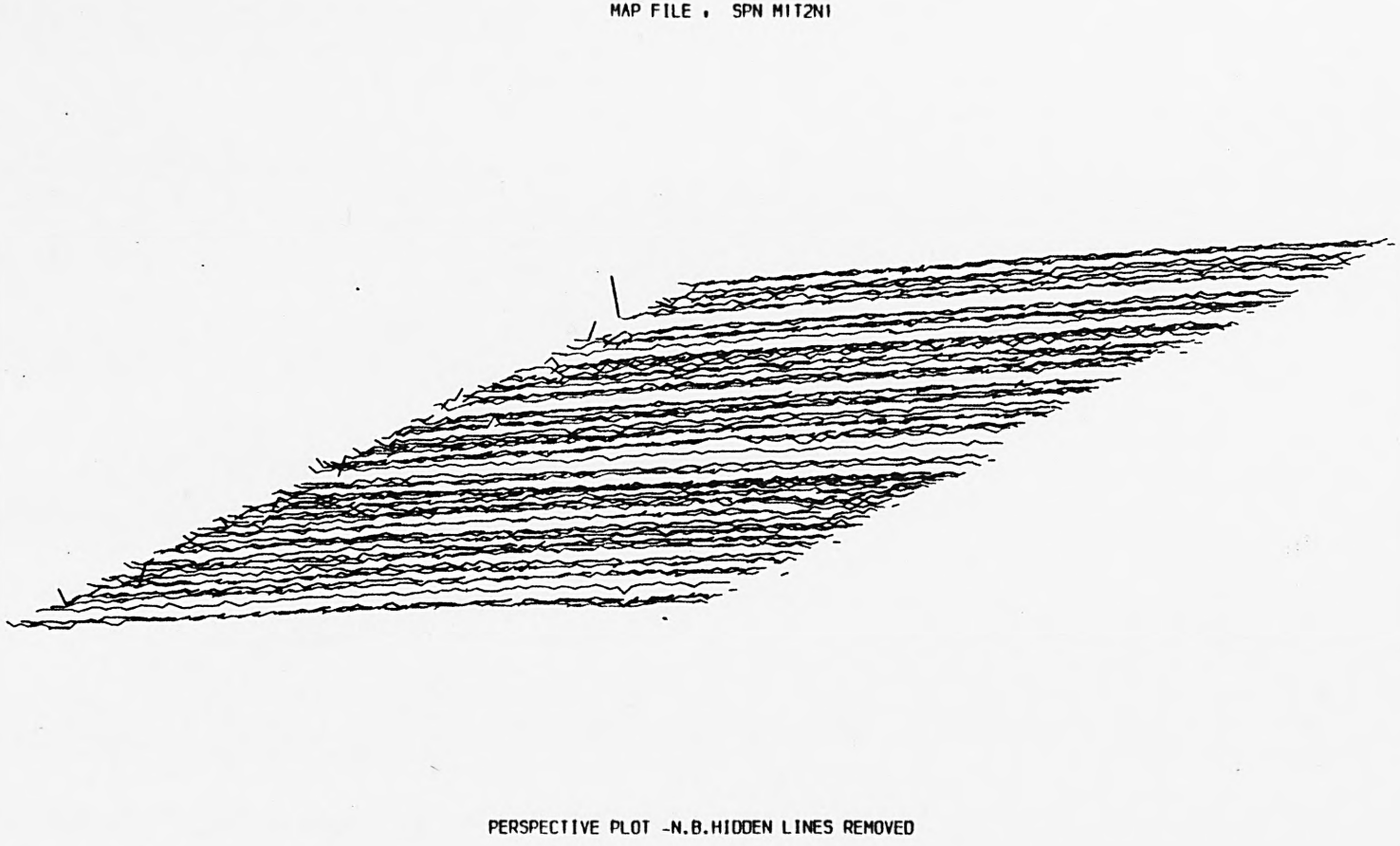

FIG. 6.2.3. Perspective plot of specimen M1T2 with hidden line removal

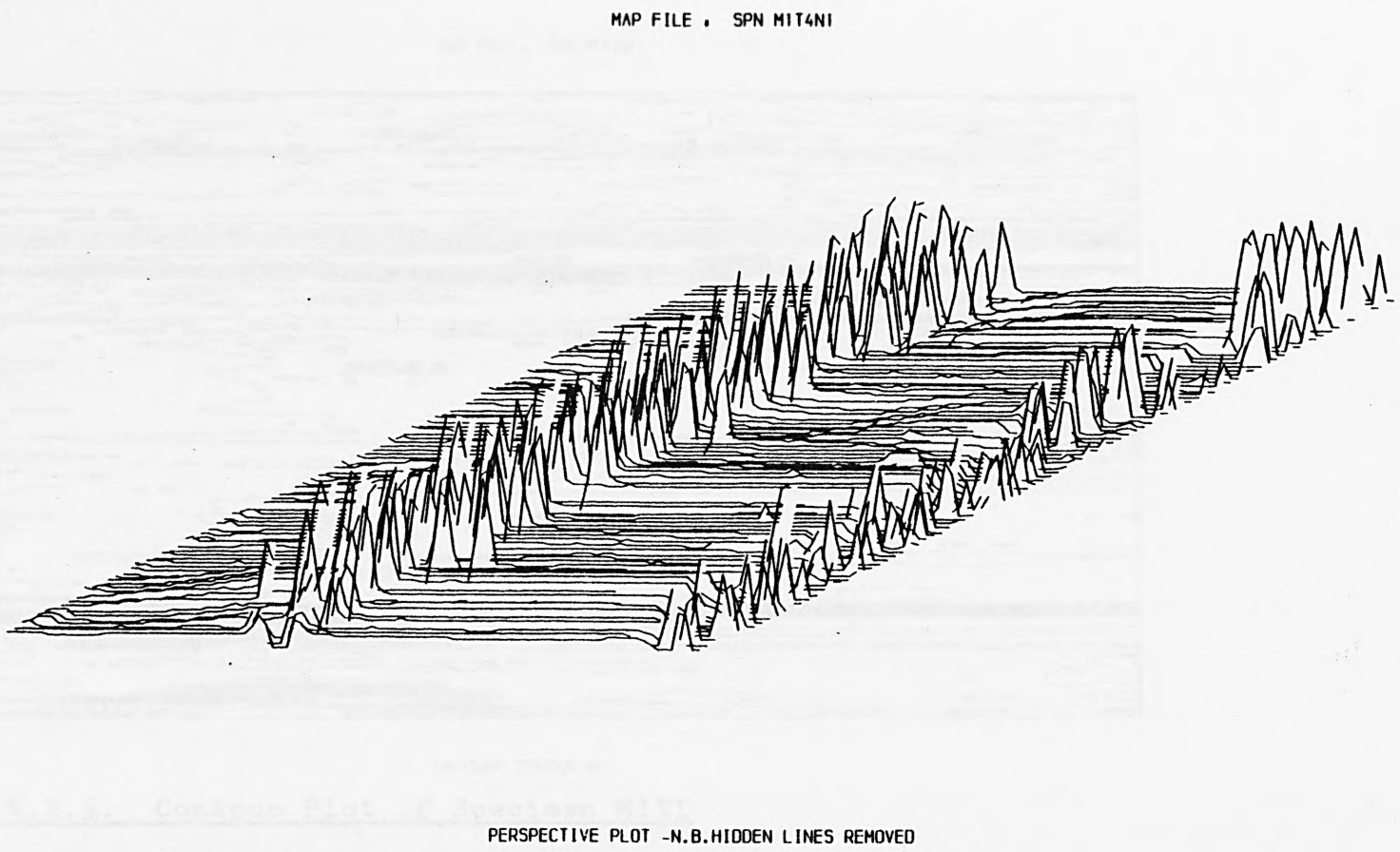

FIG. 6.2.4. Perspective plot of defect specimen M1T4

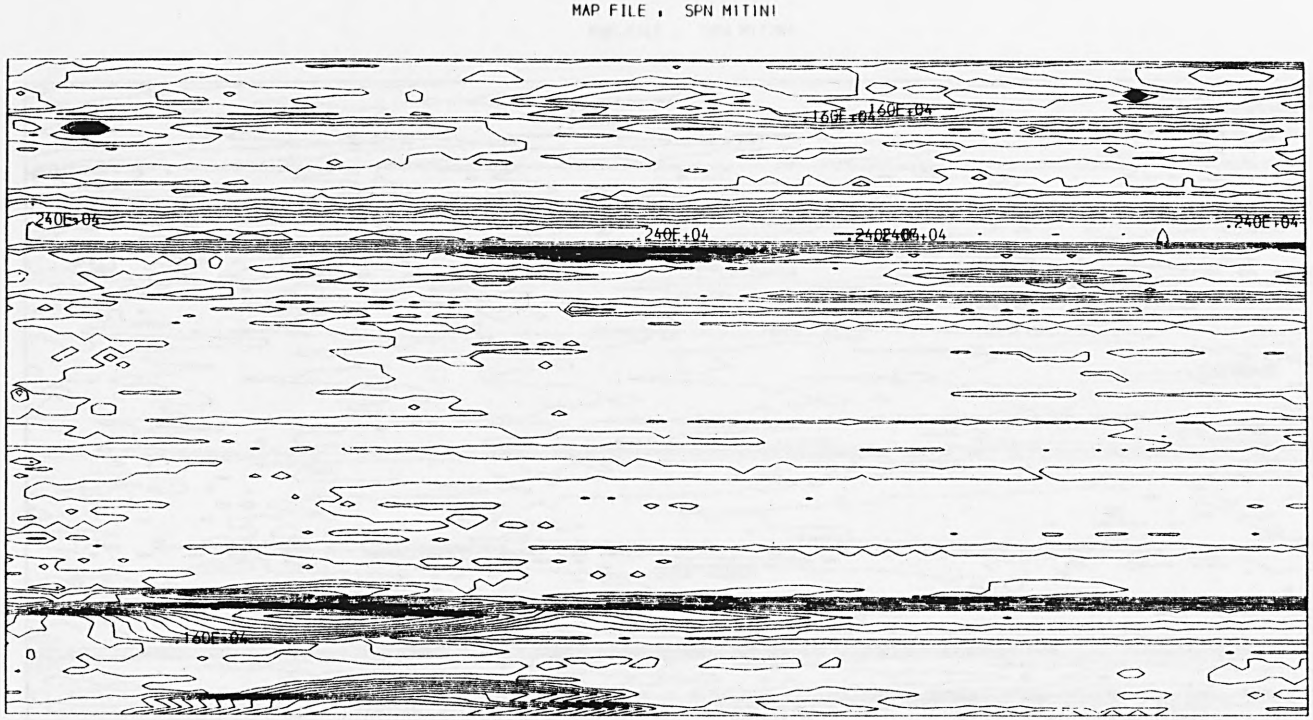

FIG. 6.2.5. Contour Plot of Specimen M1T1

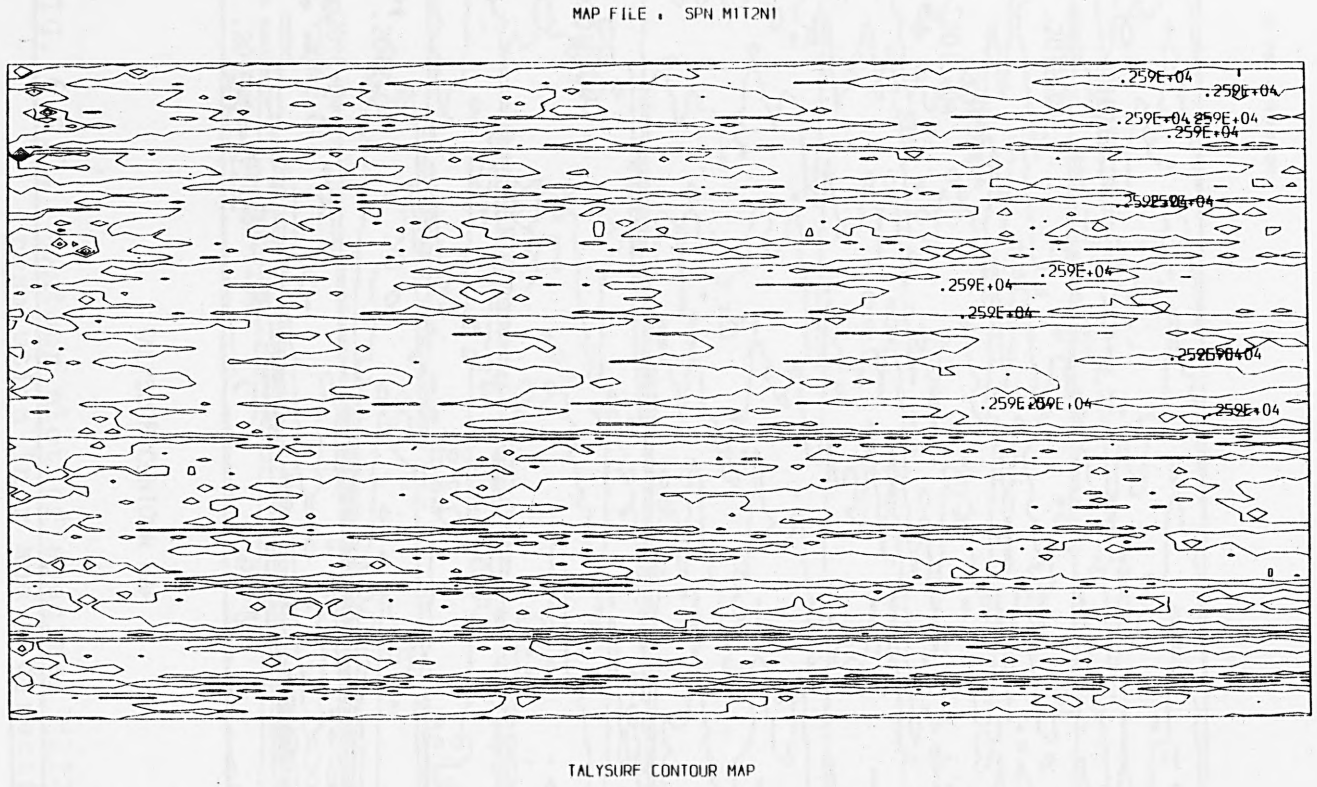

FIG. 6.2.6. Contour Plot of Specimen M1T2

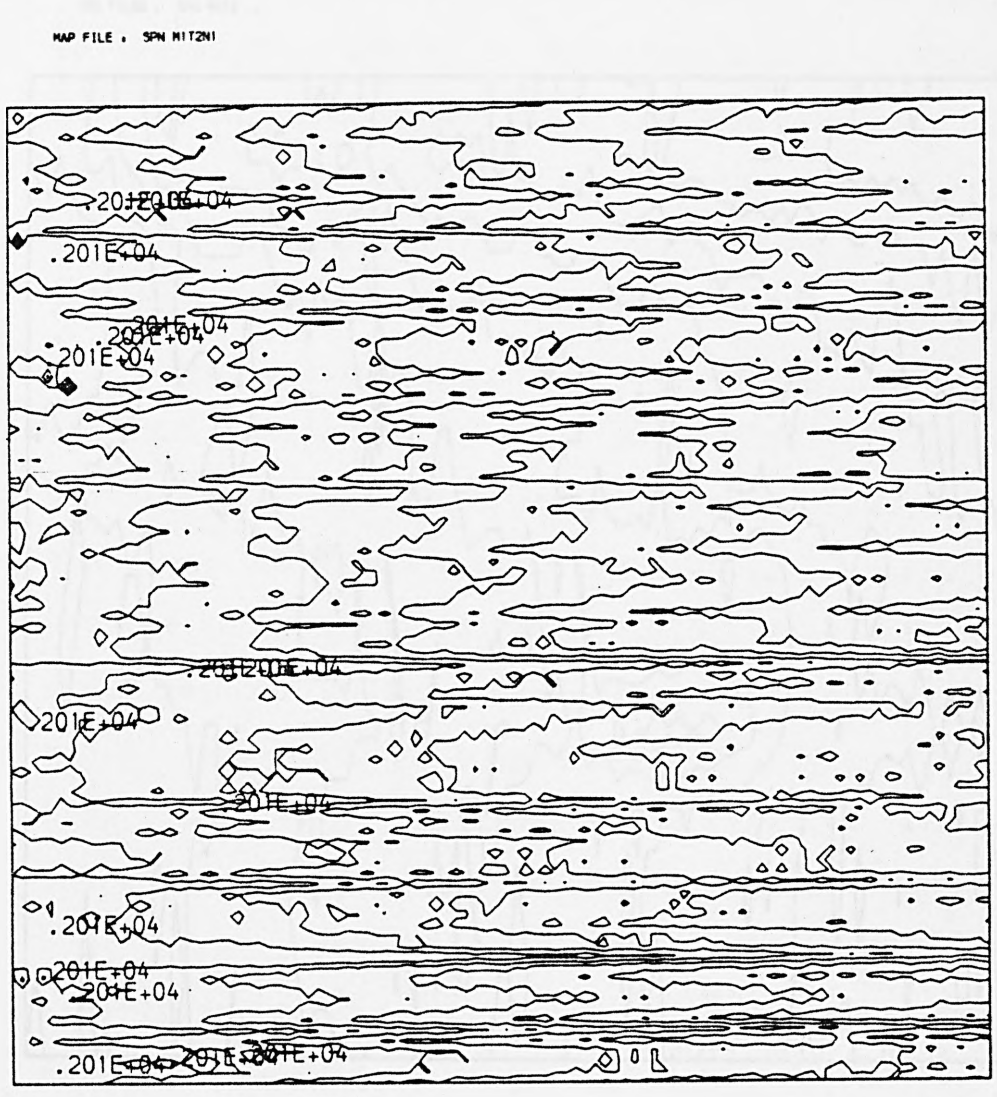

FIG. 6.2.7. Contour plot of specimen M1T2 (equal resolution in x and y directions)

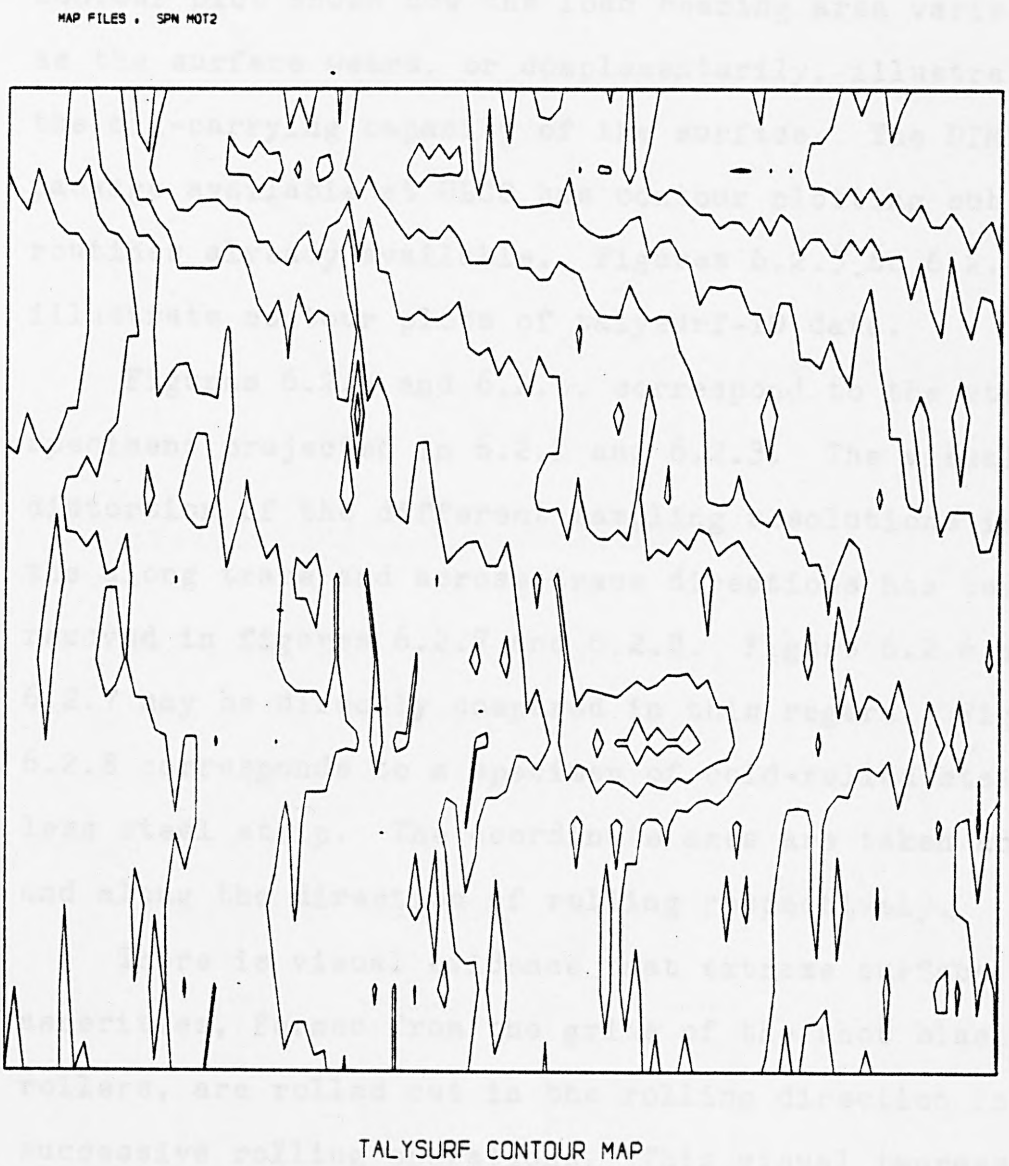

FIG. 6.2.8. Contour plot of cold-rolled stainless steel specimen MOT2

An alternative image to the perspective plot, much used by the cartographer, is a contour map. This form of representation would be of interest to the tribologist concerned with problems of wear. The contour plot shows how the load bearing area varies as the surface wears, or complementarily, illustrates the oil-carrying capacity of the surface. The DIMFILM package available at ULCC has contour plotting sub-routines already available. Figures 6.2.5 to 6.2.8 illustrate contour plots of talysurf-10 data.

Figures 6.2.5 and 6.2.6. correspond to the steel specimens projected in 6.2.1 and 6.2.3. The visual distortion of the different sampling resolutions in the along trace and across trace directions has been removed in figures 6.2.7 and 6.2.8. Figure 6.2.6 and 6.2.7 may be directly compared in this regard. Figure 6.2.8 corresponds to a specimen of cold-rolled stainless steel strip. The coordinate axes are taken across and along the direction of rolling respectively.

There is visual evidence that extreme surface asperities, formed from the grits of the shot blasted rollers, are rolled out in the rolling direction in successive rolling operations. This visual impression of anisotropy is borne out later in the chapter, by autocorrelations computed along and across the trace directions, as well as by intensity plots taken in these directions.

6.2.2. Fitting a Mean Plane to 3-D Topography Data

Firstly, to remove possible trends etc., a mean plane: $z = \alpha + \beta x + \gamma y$ is fitted to the data.

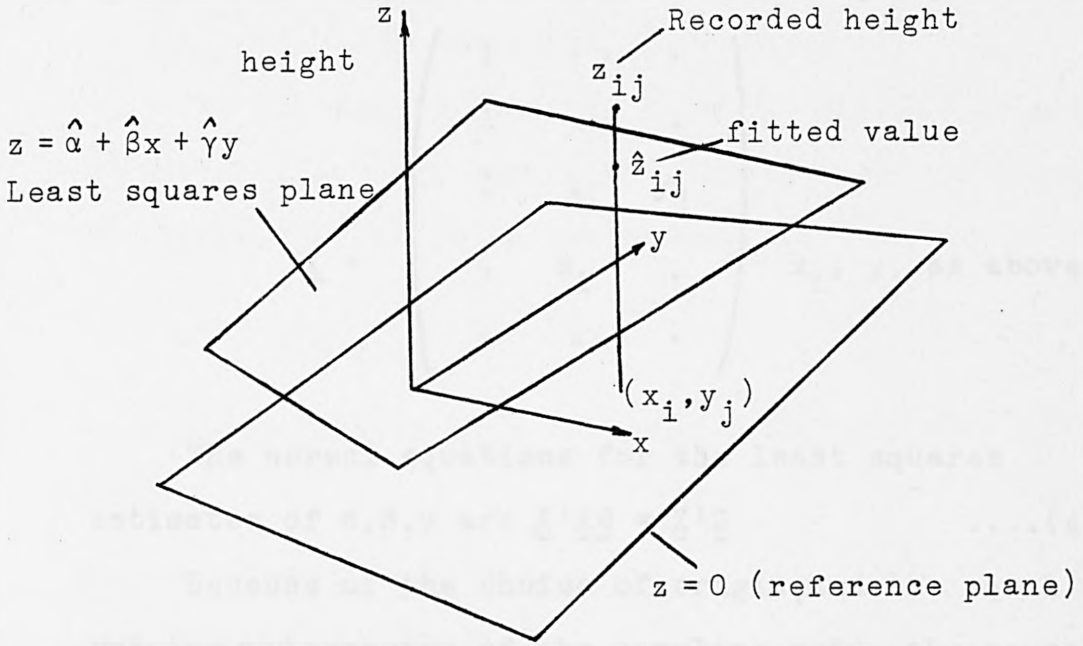

FIG. 6.2.9. Least Squares Plane

The model $E(z_{ij}) = \alpha + \beta x_i + \gamma y_j \quad \forall i,j$ is proposed. In vector form, $E(\underline{z}) = \underline{X}\,\underline{\theta}$ ....(3) where the parameter vector $\underline{\theta}' = (\alpha, \beta, \gamma)$ and $\underline{X}$ is the so-called design matrix.

The grid of sampling points is as follows:

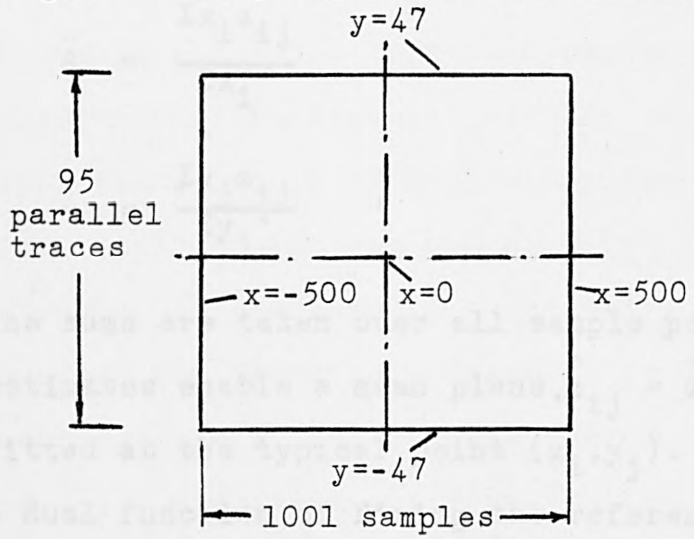

FIG. 6.2.10 Sampling Grid

Thus, $x_i = 0, \pm 1, \pm 2, \ldots \pm 500$

$y_j = 0, \pm 1, \pm 2, \ldots \pm 47$

With the origin chosen as shown:

$$\underline{X} = \begin{pmatrix} 1 & \cdot & \cdot \\ 1 & \cdot & \cdot \\ 1 & \cdot & y_j \\ \cdot & x_i & \cdot \\ \cdot & \cdot & \cdot \end{pmatrix} \quad x_i,\ y_j \text{ as above}$$

The normal equations for the least squares estimates of α, β, γ are $\underline{X}'\underline{X}\underline{\theta} = \underline{X}'\underline{Z}$ ....(4)

Because of the choice of origin, and the equal spacing and symmetry of the sampling grid, the normal equations read,

$$\begin{pmatrix} n & o & o \\ o & \Sigma x_i^2 & o \\ o & o & \Sigma y_j^2 \end{pmatrix} \begin{pmatrix} \hat{\alpha} \\ \hat{\beta} \\ \hat{\gamma} \end{pmatrix} = \begin{pmatrix} \Sigma z_{ij} \\ \Sigma x_i z_{ij} \\ \Sigma y_j z_{ij} \end{pmatrix} \qquad ....(5)$$

and $n = 95 \times 1001$, the total number of samples.

Solving
$$\hat{\alpha} = \frac{\Sigma z i_{ij}}{n} \quad ;$$

$$\hat{\beta} = \frac{\Sigma x_i z_{ij}}{\Sigma x_i^2} \quad ; \qquad ....(6)$$

$$\hat{\gamma} = \frac{\Sigma y_j z_{ij}}{\Sigma y_j^2} \quad ,$$

where the sums are taken over all sample points. The above estimates enable a mean plane, $\hat{z}_{ij} = \hat{\alpha} + \hat{\beta}x_i + \hat{\gamma}y_j$, to be fitted at the typical point (x_i, y_j). This plane has the dual function of fixing the reference surface height at zero, as well as removing any trends in the data, due to the surface of the metal specimen not being held flat during the data gathering operations.

$z_{ij} - \hat{z}_{ij}$ = profile height - fitted value

= surface height residual

The residuals, obtained from the profile height variation about the mean plane, enable the variance of surface height to be estimated, viz

$$\hat{\sigma}^2 = \frac{1}{n-3} \sum_{i,j} (z_{ij} - \hat{z}_{ij})^2 \qquad \ldots.(7)$$

or, computationally much simpler, from the ANOVA table below.

Source of variation	S. of Sqs	d.f.
Regression (fitting of plane)	$\hat{\alpha}(\Sigma z_{ij}) + \hat{\beta}(\Sigma x_i z_{ij}) + \hat{\gamma}(\Sigma y_j z_{ij})$	3
Residual	By difference	n-3
Total	Σz_{ij}^2	n

whence, $\hat{\sigma}^2 = \frac{1}{n-3}$ x Residual Sum of Squares.

In performing the above we have restricted the linear model such that:

$$= \alpha + \beta x_i + \gamma y_j + e_{ij}$$

with the errors e_{ij} taken to be independent with constant variance σ^2. Subsequent residual analysis could investigate the validity of such assumptions. Such a statistical model would seem appropriate if the surface were isotropic, in the case of a specially prepared ground surface for instance. However, it could be quite inappropriate if the surface texture had a preferred lay. Specimens cut from a piece of rolled steel do have different height distributions along and across the rolling direction.

If we consider the i^{th} scan only we could fit the

model $E(z_{ij}) = \alpha + \beta x_j + e_{ij}$ where the e_{ij} are taken as zero mean, independent with var $(e_{ij}) = \sigma_x^2$, the variance of heights taken in the x- direction. Expanding to the full quota of m(=95) scans say, the ANOVA table would read:

Source of Variation	S of Sqs	d.f.	Mean Sq
Regression (fitting β term)	$\hat{\beta}(\Sigma x_i z_{ij})$	1	
Residual	By difference	n-2	$\hat{\sigma}_x^2$
Total	$\Sigma zy^2 - G^2/n$	n-1	

where G, the grand total = Σz_{ij}. Alternatively, we could consider the fitting of the 'across scans' with the model $E(z_{ij}) = \alpha + \gamma y_j + e_{ij}$ with $var(e_{ij}) = \sigma_y^2$, the variance of heights in the y-direction. Comparing the three situations, we have, remembering the orthogonality of the design:

	S of Sqs	M Sq	S of Sqs	M Sq	S of Sqs	M Sq
Regression (linear)	$\hat{\beta}\Sigma x_i z_{ij}$		$\hat{\gamma}\Sigma y_j z_{ij}$		$\hat{\beta}\Sigma x_i z_{ij} + \hat{\gamma}\Sigma y_j z_{ij}$	
Residual		$\hat{\sigma}_x^2$		$\hat{\sigma}_y^2$		$\hat{\sigma}^2$
Total	$\Sigma z^2_{ij} - G^2/n$		$\Sigma z^2_{ij} - G^2/n$		$\Sigma z^2_{ij} - G^2/n$	

From which we can deduce $2\hat{\sigma}^2 < \hat{\sigma}_x^2 + \hat{\sigma}_y^2$. ....(8)

However the usual practice is to estimate σ_x^2 and σ_y^2 from single traces taken in their respective directions, after fitting a least squares datum to the output profile records. This must inevitably lead to very much reduced estimates of σ_x^2 and σ_y^2. The model for σ^2 fitted an overall regression plane to the entire 3-dimensional surface topography data. For an individual trace σ_x^2 to be comparable with $\hat{\sigma}_x^2$ we effectively

hypothesise that the overall regression plane fits all scans, and given the large number of degrees of freedom involved the statistical test reduces to comparison with $F_{1,\infty}$

Brownlee [1965] Chapter 11 discusses the analogous statistical problem.

From tables we find $F_{1,\infty}$ (5%) = 3.84 and $F_{1,\infty}$ (1%) = 6.63. The interpretation is that the overall plane model may be taken as an adequate fit to all the individual profiles if $\sigma^2/\sigma_x^2 < 3.84$, and even a variance ratio of 6, would be observable 1 time in 100.

6.2.3. Profile Height and Slope Analysis

Surface Heights

As a check on the fidelity of the talysurf-10 measurements, and on certain of the derived statistical papameters, advantage was taken on the surface metrology routines developed initially at Leicester Polytechnic, by Stout, King and Spedding, and currently being exploited at Lanchester Polytechnic. Figures 6.2.9-6.2.14 pages are outputs from their graph plotter which economically depict a variety of computed surface distributions and surface roughness measures. The data was obtained by a Talysurf-5 stylus instrument and processed by a Data General minicomputer.

The most commonly quoted measure of surface roughness, certainly by industrial users, is the CLA or R_A value of roughness heights. This measure in statistical parlance is the MAD (mean absolute deviation) and for the normal distribution is related to the variance σ^2 (or standard deviation σ) by $\sigma^2 = \pi/2(CLA)^2$.

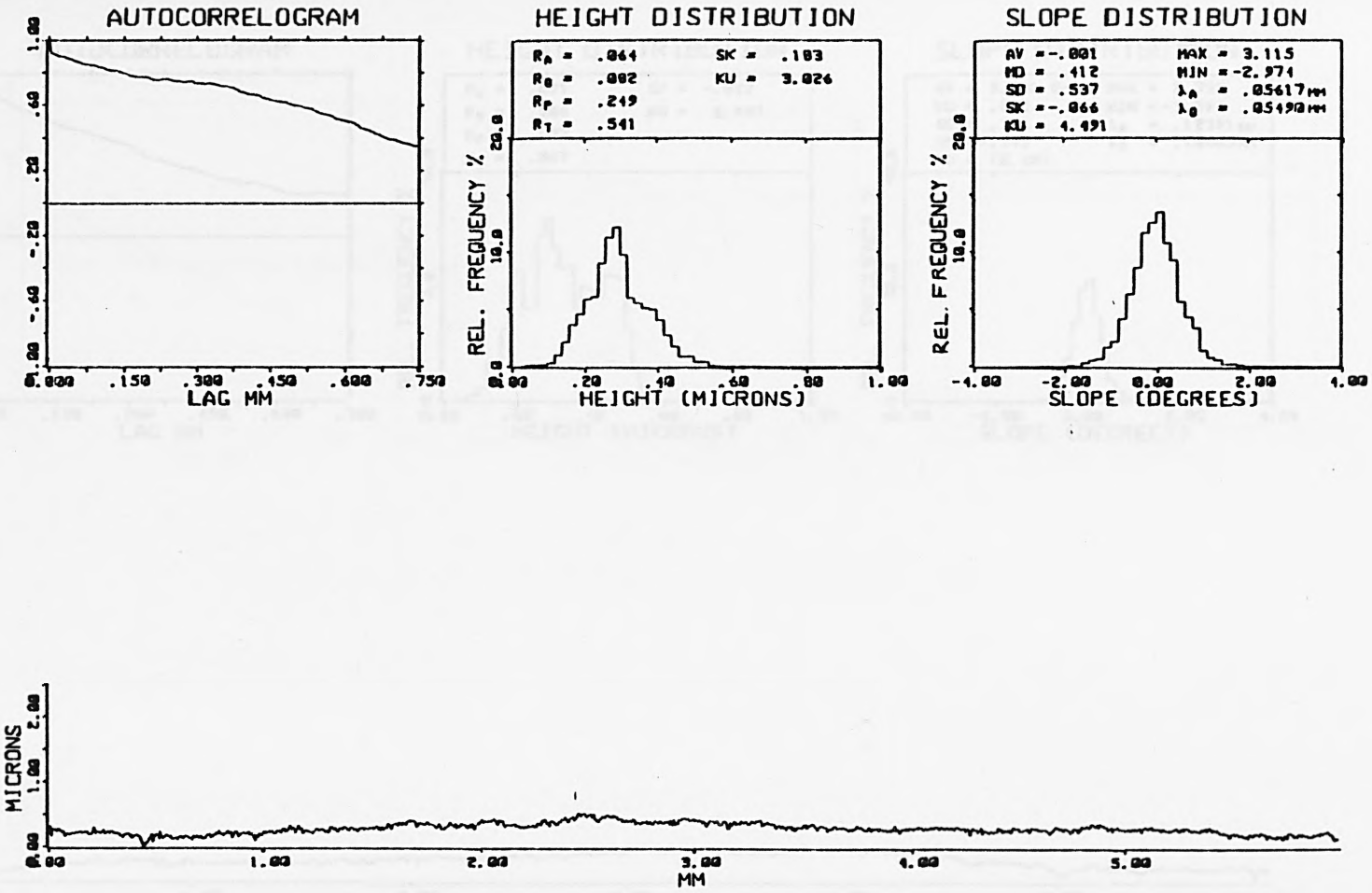

FIG. 6.2.9. Statistical functions of surface height: M1T2

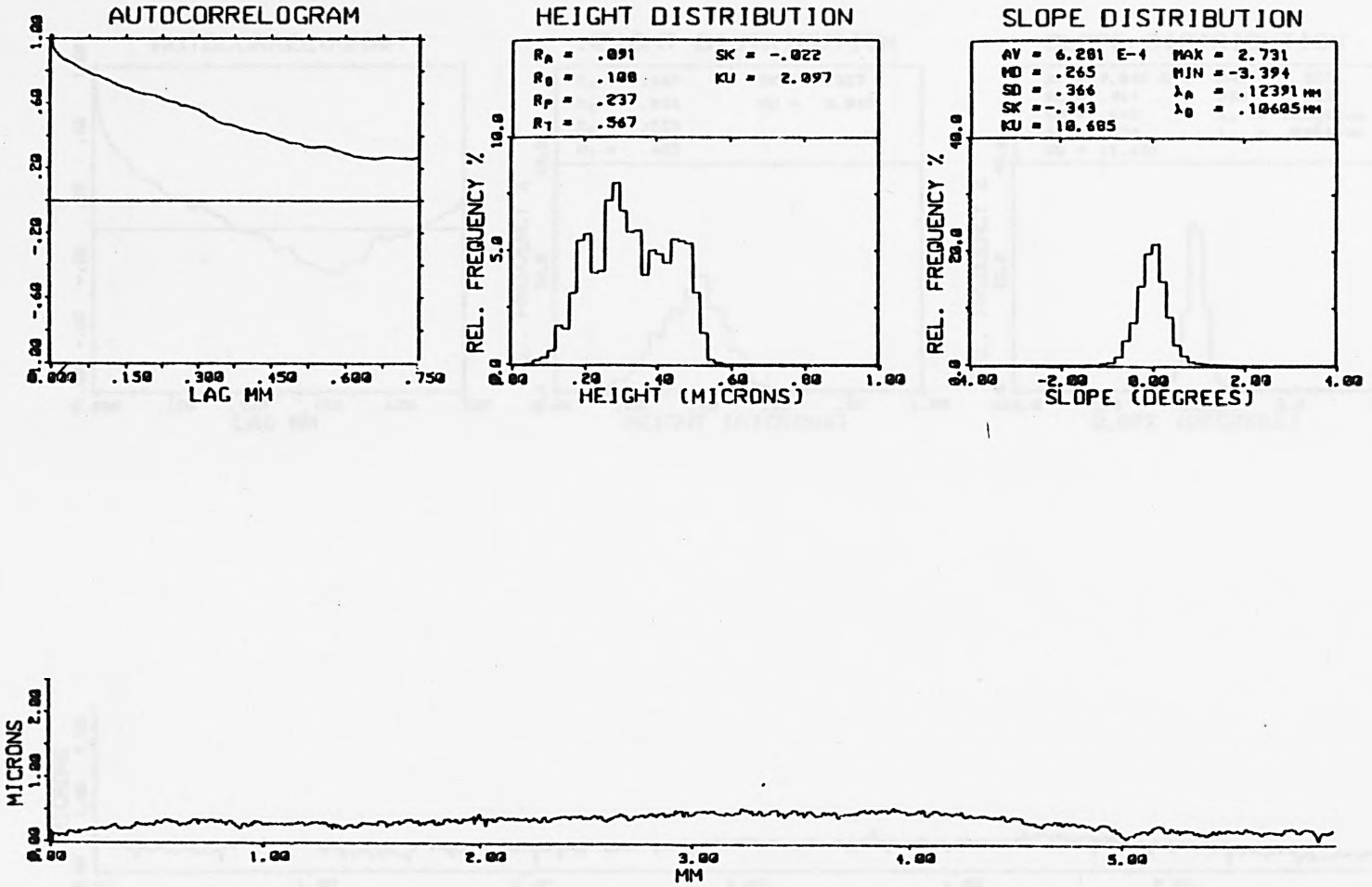

FIG. 6.2.10. Statistical functions of surface heights: M1T2 (perpendicular trace)

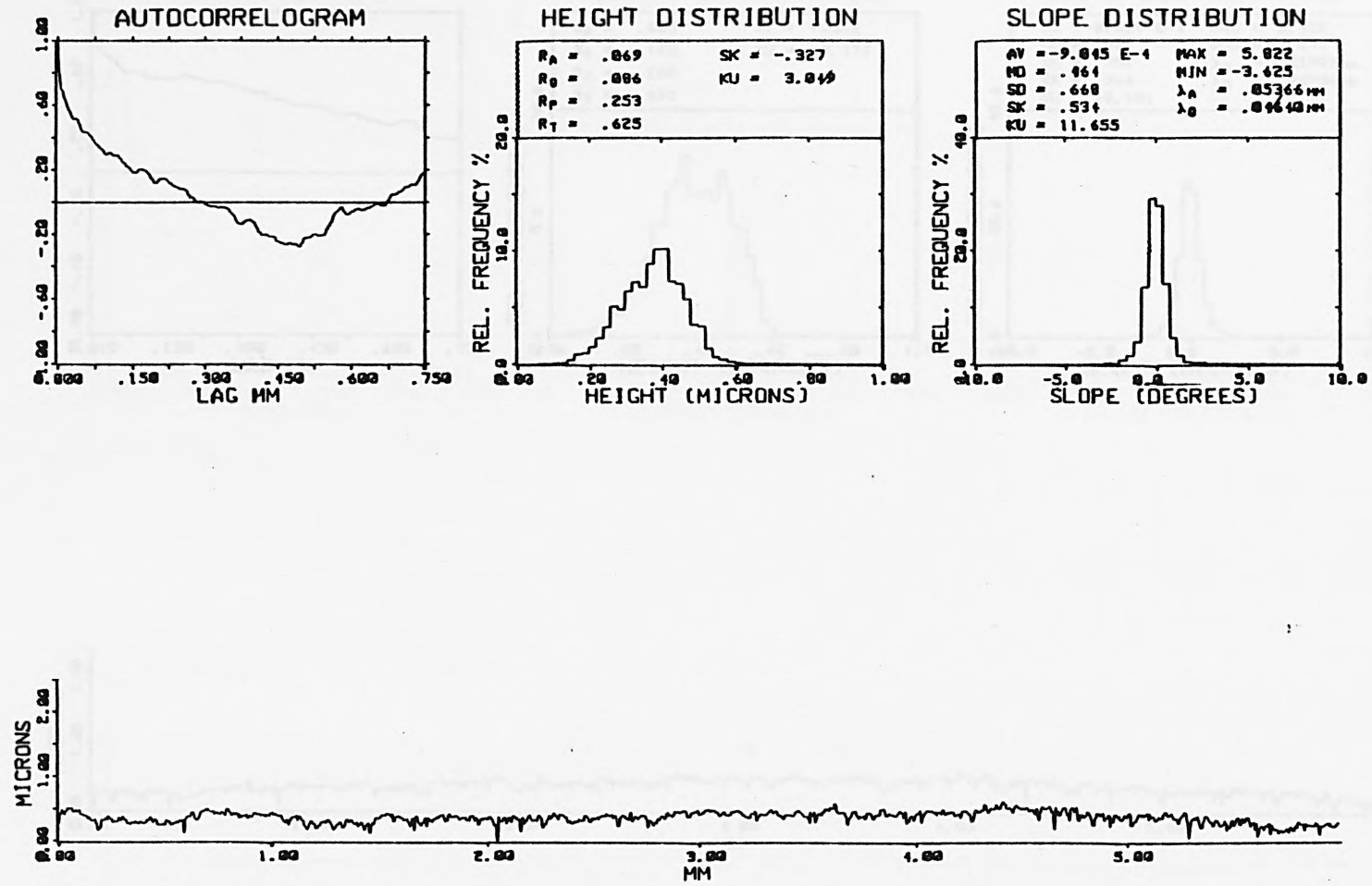

FIG. 6.2.11. Statistical functions of surface heights: M3T2

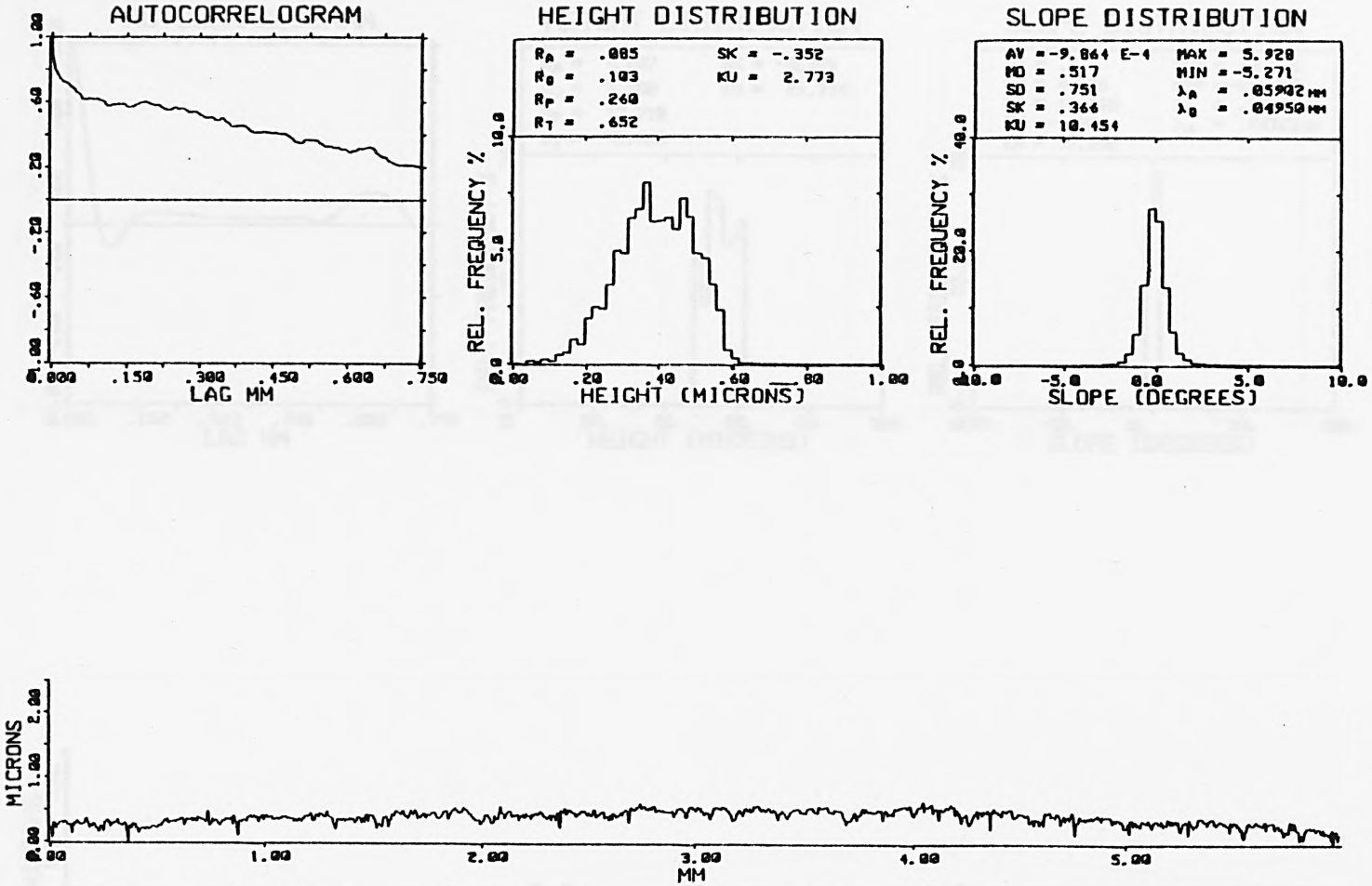

FIG. 6.2.12. Statistical functions of surface height: M3T2 (perpendicular trace)

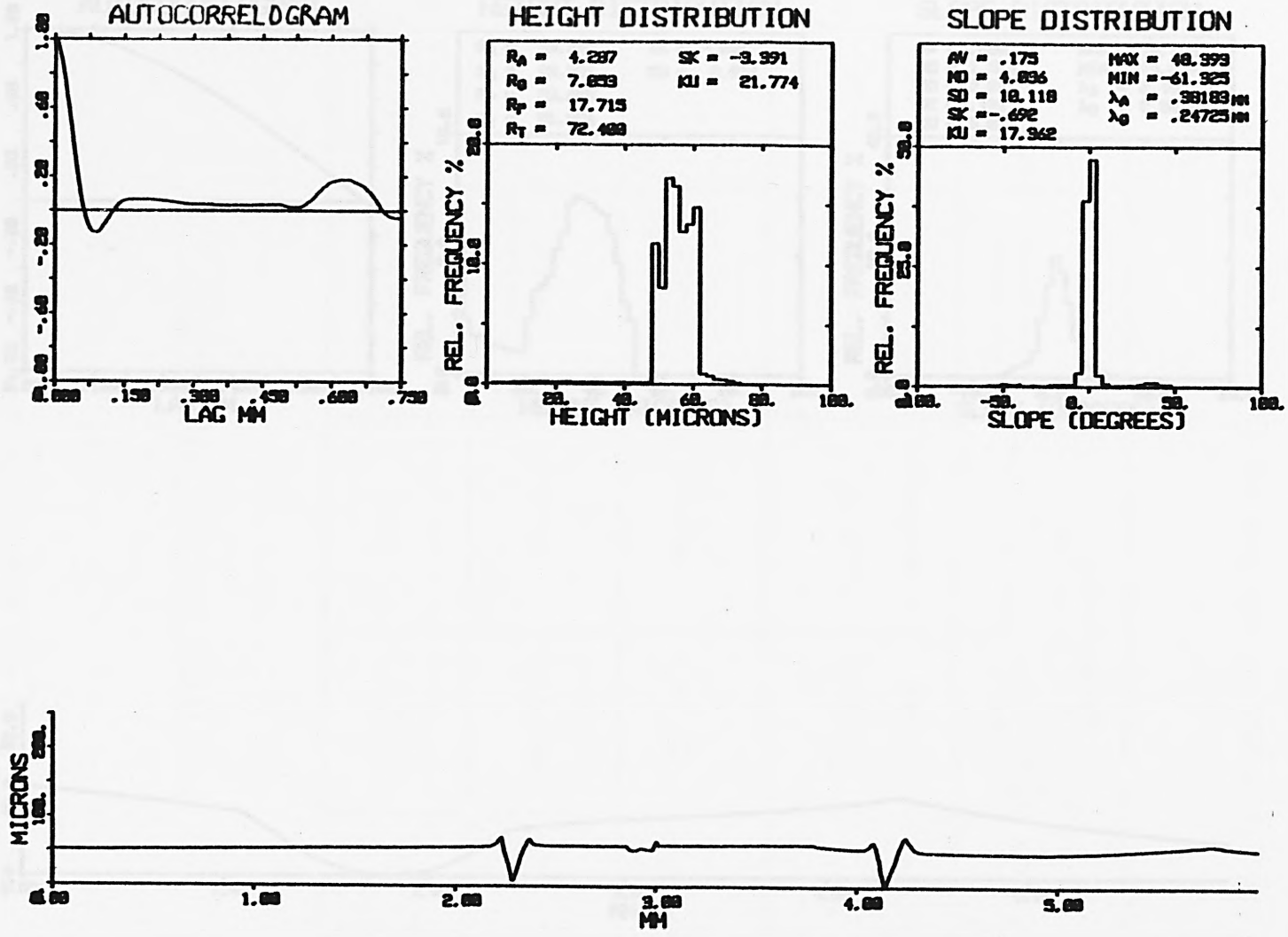

FIG. 6.2.13. Statistical functions of surface height: M3T5 (parallel scratches defect)

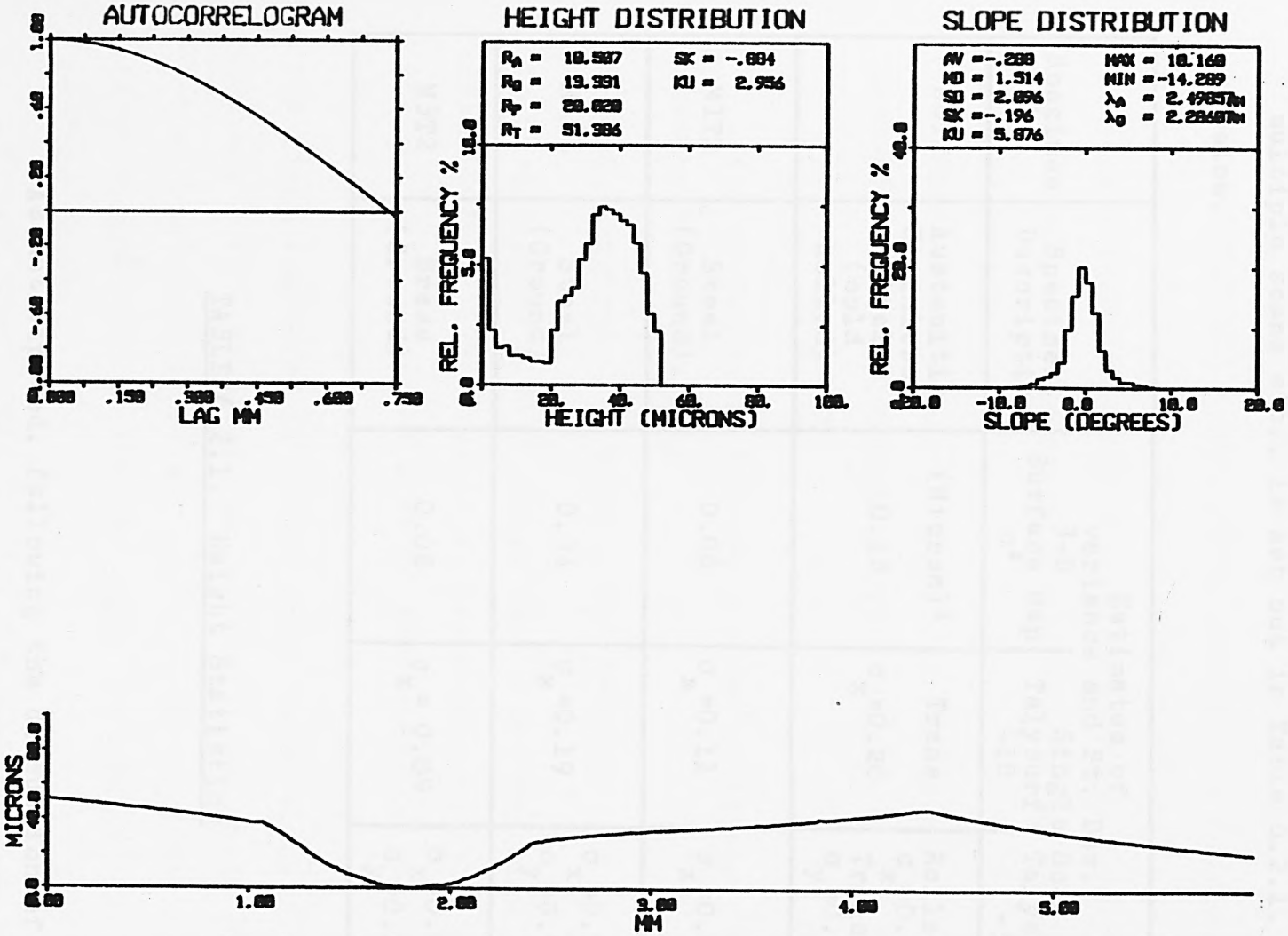

FIG. 6.2.14. Statistical functions of surface height: M2T3 (indentation defect)

The variance of surface heights obtained from a variety of metal specimens, measured by various instruments and computed on the basis of single or multiple scans etc., is set out in Table 6.2.1. below.

Specimen Label	Specimen Description	Estimates of variance and St. Dev. 3-D Surface Map σ^2	Single Scan Talysurf -10	Single Scan Talysurf -5
M0T2	Austenitic Stainless Steel (cold Rolled)	$(\text{Micron})^2$ 0.18	Trans σ_x=0.20	Rolled σ_x=0.12 Trans σ_y=0.18
M1T2	Steel (Ground)	0.06	σ_x=0.11	σ_x=0.08
M1T1	Steel (Ground)	0.34	σ_x=0.19	σ_x=0.11 σ_y=0.08
M3T2	Brass (Ground)	0.08	σ_x= 0.09	σ_x=0.09 σ_y=0.10

TABLE 6.2.1. Height Statistics

As anticipated, following the discussion of 6.2.2, $\sigma^2 > \sigma_x^2$ but the variance ratios of the specimens M0T2, M1T2 and M3T2 are such that a mean plane is tolerably fitted to these data bases and thus σ^2 gives the variance of heights for an AREA. This is perhaps a more meaningful statistic than the more restrictive

R_A (= CLA) or R_q (= σ) values of a single scan. Considering the steel specimens M1T1 and M1T2, M1T1 although ground to a finer finish than M1T2 the presence of defects, clearly visible in the perspective plots of Figures 6.2.1 and 6.2.2, gives rise to the much enhanced σ^2 value of 0.34. The single scan σ_x^2 values 0.04 0.01 of talysurfs 10 and 5 respectively vouch for the super smooth microgeometry of the underlying texture.

Surface Slopes

The surface slope at any point is described in terms of the two principal profile slopes:

$$\zeta' = (\zeta_x'^2 + \zeta_y'^2)^{\frac{1}{2}} \qquad \ldots.(9)$$

For an isotropic surface a slope parameter η may be further defined, namely

$$\eta = \frac{\zeta'}{(2\sigma_s^2)^{\frac{1}{2}}} \qquad \text{where} \quad \sigma_s^2 = -C''(0).$$

Longuet-Higgins [1957] showed that η was Rayleigh distributed. (This result is important, as it is consistent with the facet view of scattering if we link this result to the amplitude distribution of the reflected field scattered by a very rough surface, (c.f. Chapter 8.1). Moreover, we can easily see that, since for an isotropic surface $\zeta' = \sqrt{2}\,\zeta_x'$, the variance of facet slopes over an AREA is twice the variance of a profile slope.

For an anisotropic surface the distribution of slopes is Hoyt distributed. (The Rayleigh and Hoyt distributions are discussed in detail in Appendices 8A-8D).

However, as has been pointed out by Whitehouse and

Archard [1970], and reiterated by Thomas and Sayles [1978], not all calculated parameters should be taken at their face value. Estimates of the slope parameter, a parameter of crucial interest to this study, can yield widely different numerical values depending on the sampling interval (c.f. Thomas and Sayles [1978]).

In the first instance which formula should we use to compute a numerical value of slope? We can view the problem as one of numerical analysis and base a formula on a Taylor expansion at the point of interest t, say

$$\hat{\zeta}' = \frac{1}{2\tau}\left[z_{t+\tau} - z_{t-\tau}\right] \qquad \ldots.(10)$$

$$\simeq \zeta'(t) + O(\tau^3)$$

$$\text{or} \quad \hat{\zeta}' = \frac{1}{60\tau}\left[z_{t+3\tau} - 9z_{t+2\tau} + 45z_{t+\tau} - 45z_{t-\tau} + 9z_{t-2\tau} - z_{t-3\tau}\right] \qquad \ldots.(11)$$

$\simeq \zeta'(t) + O(\tau^7)$, where the weights are so designed that the 'error' term is of the order τ^4 and τ^7 respectively.

The slope histograms and slope moments routines of Watson [1979], and presented in Figures 6.2.9-6.2.14, employed the second formula for $\zeta'(t)$ above, which is referenced in Whitehouse [1974]. Whitehouse expresses a preference for (11) and states that (10) can lead to large or small angles which are not physically realistic. Alternatively (10) and (11) are obtained if we fit:

(i) a quadratic polynomial to the points $z_{t-\tau}$, z_t and $z_{t+\tau}$,

(ii) a polynomial of degree 6 through the 7 points $z_{t-3\tau}$, $z_{t-2\tau}$, z_{t-z}, z_t, $z_{t+\tau}$, z_{t+2t}, $z_{t+3\tau}$,

and evaluate the polynomial derivative at the point in question t.

If we view the problem in statistical terms, regarding a single profile as one realisation of a stochastic process ensemble, we might consider

$$\zeta' = \frac{z_{t+\tau} - z_t}{\tau} \qquad \ldots.(12)$$

The above could be regarded as a representative value in the interval $(t,t+\tau)$ since at some point § the profile slope takes the value $\hat{\zeta}'$ by the mean value theorem.

In terms of expected values,

$$E[\hat{\zeta}'] = \frac{1}{\tau} E[z_{t+\tau} - z_t] = 0$$

$$E[(\hat{\zeta}')^2] = \frac{1}{\tau^2} E[(z_{t+\tau} - z_t)^2] = \frac{1}{\tau^2} S(\tau) \qquad \ldots.(13)$$

for a stationary process, where $S(\tau)$ is the so-called structure function i.e.

$$V[\zeta'] = \frac{1}{\tau^2} S(\tau).$$

Or, in terms of the auto-correlation function, $C(\tau)$

$$V[\hat{\zeta}'] = \frac{1}{\tau^2} 2\sigma^2[1 - C(\tau)] \qquad \ldots.(14)$$

whichever approach is adopted, the formal estimator is a linear combination of sample heights. Thus, if we consider a Gaussian surface, the estimators above all give rise to sample values which are normally distributed with zero mean. For the simple chord estimator, Whitehouse and Archard's [1970] theory has been used to investigate the variation of mean absolute slope and peak radius of curvature for a negative exponential autocorrelation function.

$$V[\hat{\zeta}'] = 2\sigma^2/\tau^2 \ (1 - e^{-\tau/T}) \qquad \ldots.(15)$$

$$\sim (2\sigma^2/\tau^2)\tau/T \qquad \text{for small } \tau \text{ and is}$$

meaningless as $\tau \to 0$ (c.f. Chapter 8.3).

For the autocorrelation function postulated in equation (19) of 8.2 :

$$V[\hat{\zeta}'] = \begin{cases} \frac{2\sigma^2}{\tau^2}\left(1-e^{-(\tau/T)^{\left[2-\{(\tau-\ell)/\ell\}^m\right]^{\frac{1}{m}}}}\right), & \tau \leqslant \ell \\ \frac{2\sigma^2}{\tau^2}\left(1-e^{-\tau/T}\right), & \tau > \ell \end{cases} \quad \ldots.(16)$$

For the Gaussian autocorrelation function:

$$V[\hat{\zeta}'] = 2\sigma^2/\tau^2(1-e^{-\tau^2/T^2})$$

$$= 2\sigma^2/\tau^2(\tau^2/T^2 - \frac{\tau^4/T^4}{2!} + \ldots)$$

$$\to 2\sigma^2/T^2 \text{ as } \tau \to 0$$

In this instance we can regard $\hat{\zeta}'$ as a consistent estimator in the statistical sense, since $\hat{\zeta}' \to$ true theoretical value as the sampling interval is reduced.

For the composite autocorrelation function with

we have: $$\frac{\text{theoretical value}}{\text{expected value}} \sim \frac{2\sigma^2/T^2}{2\sigma^2/\tau T} = \frac{\tau}{T} \quad \ldots.(17)$$

Thus for typical τ = 2μm, T = 200μm, theoretical value is $\frac{1}{100}$ x measured value. That is the standard deviation of slopes is estimated ten times too high!

For the 7-point estimator of (11)

$$V[\hat{\zeta}'] = \frac{1}{60^2\tau^2} E\left[z_{t+3\tau} - 9z_{t+2t} + 45z_{t+\tau} - 45z_{t-\tau} + 9z_{t-2t} - z_{t-3\tau}\right]^2$$

Writing out the variances and covariance terms:

$$\begin{pmatrix} 1 - 9C(\tau) + 45C(2\tau) - 45C(4\tau) + 9C(5\tau) - C(6\tau) & & & & \\ & 9^2 - 9.45C(\tau) + 9.45C(3\tau) - 81C(4\tau) + 9C(5\tau) & & & \\ & & 45^2 - 45^2C(2\tau) + 45.9C(3\tau) - 45C(4\tau) & & \\ & & & 45^2 - 45.9C(\tau) + 45C(2\tau) & \\ & & & & 9^2 - 9C(\tau) \\ & & & & & 1 \end{pmatrix} \sigma^2,$$

which leads to

$$V[\hat{\zeta}'] = \frac{\sigma^2}{60^2\tau^2}\{2(1+9^2+45^2) - 4(9+9.45)C(\tau) + 2(2.45-45^2)C(2\tau) + 4(9.45)C(3\tau) + 2(-2.45-81)C(4\tau) + 2(2.9)C(5\tau) - 2C(6\tau)\}$$

For a Gaussian autocorrelation function we have:

$$V[\hat{\zeta}'] = \frac{\sigma^2}{60^2\tau^2} \cdot \frac{\tau^2}{T^2}\{ + 4.9 + 4.9.45 - 8(2.45 - 45^2) - 36.9.45 - 32(-2.45 - 81) - 25.4.9 + 2.36\} + O(\tau^2)$$

$= 2\sigma^2/T^2 + O(\tau^2)$, which is again consistent. In fact $V[\zeta'] \sim 2\sigma^2/T^2 + O(\tau^4)$.

The simple chord estimator has a slight negative bias and is asympototically less efficient than the 7-point estimator.

The following tables, compiled on the basis of both types of slope estimator with various underlying surface autocorrelations, illustrate these and other points. We can see, for example, that when the autocorrelation is pure negative exponential, the variance the simple chord estimate is approximately 5/4 times the variance of the 7-point estimate.

Theoretically, we have

chord estimate: $V[\hat{\zeta}'] = \frac{2\sigma^2}{\tau T} - \frac{2\sigma^2}{T^2} + O(\tau)$

seven-pt estimate: $V[\hat{\zeta}'] = \frac{\sigma^2}{\tau T}\left(1 + \frac{89}{150}\right) - \frac{2\sigma^2}{T^2} + O(\tau)$

For the composite autocorrelation the simple chord estimate provides a superior estimate of the true slope variance, since the longer lags involved in the 7-point estimate sense the misleading negative exponential portion of the autocorrelation function. Table 6.2.3. details computed slope statistics in a similar manner to the

Surface Parameters:

RMS Surface heights, σ: 0.2μm

Correlation length, T: 50μm

⇒ true theoretical slope variance:

3.2×10^{-5}

Autocorrelation function	Sample spacing	Estimate of slope variance Chord	7-point
Gaussian	0.5	3.1998×10^{-5}	3.2000×10^{-5}
	1.0	3.1994×10^{-5}	3.2000×10^{-5}
	1.5	3.1986×10^{-5}	3.2000×10^{-5}
	2.0	3.1974×10^{-5}	3.2000×10^{-5}
	2.5	3.1960×10^{-5}	3.2000×10^{-5}
	3.0	3.1942×10^{-5}	3.2000×10^{-5}
	3.5	3.1922×10^{-5}	3.2000×10^{-5}
Negative Exponential	0.5	3.184×10^{-3}	2.533×10^{-3}
	1.0	1.584×10^{-3}	1.259×10^{-3}
	1.5	1.051×10^{-3}	8.339×10^{-4}
	2.0	7.842×10^{-4}	6.215×10^{-4}
	2.5	6.242×10^{-4}	4.941×10^{-4}
	3.0	5.176×10^{-4}	4.092×10^{-4}
	3.5	4.415×10^{-4}	3.485×10^{-5}
Composite model $\ell = 5$ $m = 2$ (c.f. Chapter 8)	0.5	2.381×10^{-4}	2.518×10^{-4}
	1.0	3.339×10^{-4}	3.795×10^{-4}
	1.5	3.893×10^{-4}	4.622×10^{-4}
	2.0	4.159×10^{-4}	4.972×10^{-4}
	2.5	4.213×10^{-4}	4.474×10^{-4}
	3.0	4.118×10^{-4}	3.849×10^{-4}
	3.5	3.922×10^{-4}	3.372×10^{-4}

TABLE 6.2.2. Chord and 7-pt estimates of slope variance for various autocorrelation functions of surface height

height statistics portrayed in Table 6.2.1. Both chord and 7-point estimators have been employed on actual surface profile data. The chord variance exceeds that of the 7-point estimate in much the same proportion as suggested by the negative exponential autocorrelation model. Corresponding autocorrelation plots, some of which are presented below, do exhibit exponential decay.

		Estimates of Slope Variance		
Specimen Label	Specimen Description	3-D Surface Map	Single Scan Talysurf-10	Talysurf 5
M0T2	Stainless Steel Cold Rolled	0.0074	Chd. 0.0064 7-pt 0.0036	Chd 0.0070 7pt 0.0048
M1T2	Steel Ground	0.00046	Chd. 0.00040 7-pt 0.00032	Chd 0.00016 7pt 0.00009
M1T1	Steel Ground	0.00050	Chd. 0.00025 7-pt 0.00020	Chd 0.00011 7pt 0.00004
M3T2	Brass Ground	0.00064	Chd. 0.00057 7-pt 0.00013	Chd 0.00028 7pt 0.00017

TABLE 6.2.3. Slope Statistics

6.2.4. Autocorrelations of Surface and Profile Heights

Autocorrelation plots of single scans obtained by a talysurf-5 were included within the complex of statistical functions shown in Figures 6.2.9-6.2.14. Autocorrelation plots based on parallel profile scans, thereby further smoothing out surface noise are shown in Figures 6.2.15-6.2.18. The plots reflect the same information and are broadly described by negative exponential functions. Figure 6.2.16 shows some evidence of underlying periodicity. The anisotropy of M0T2, the cold rolled steel strip specimen, is plainly evident whichever processing is utilised.

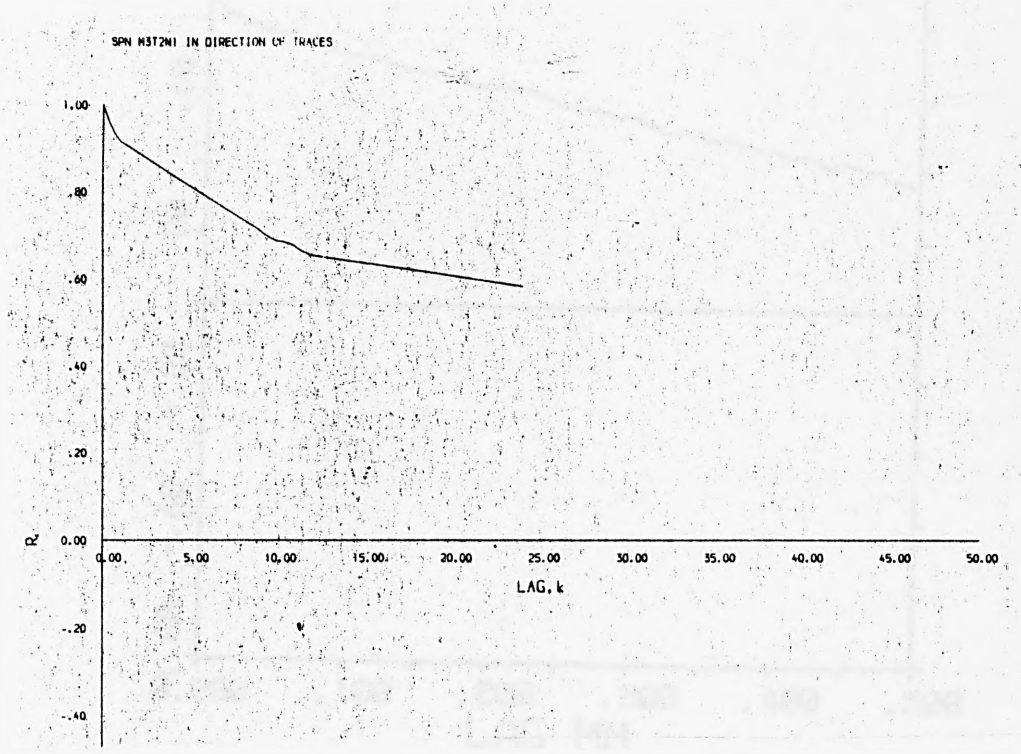

FIG. 6.2.15. Autocorrelation function of surface height: M3T2

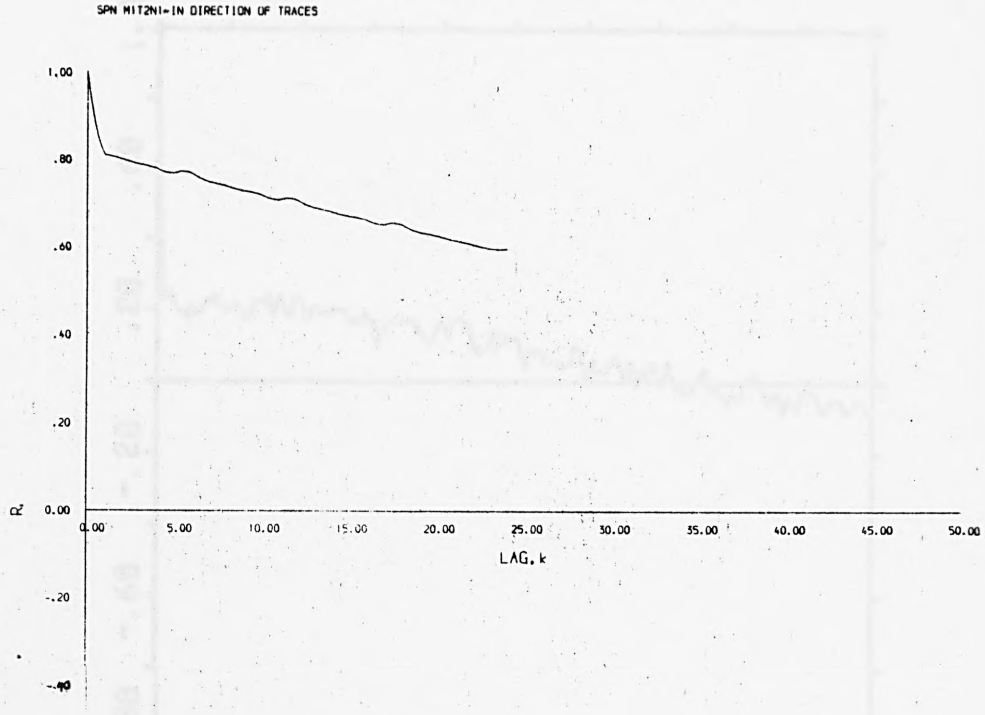

FIG. 6.2.16. Autocorrelation function of surface height: M1T2

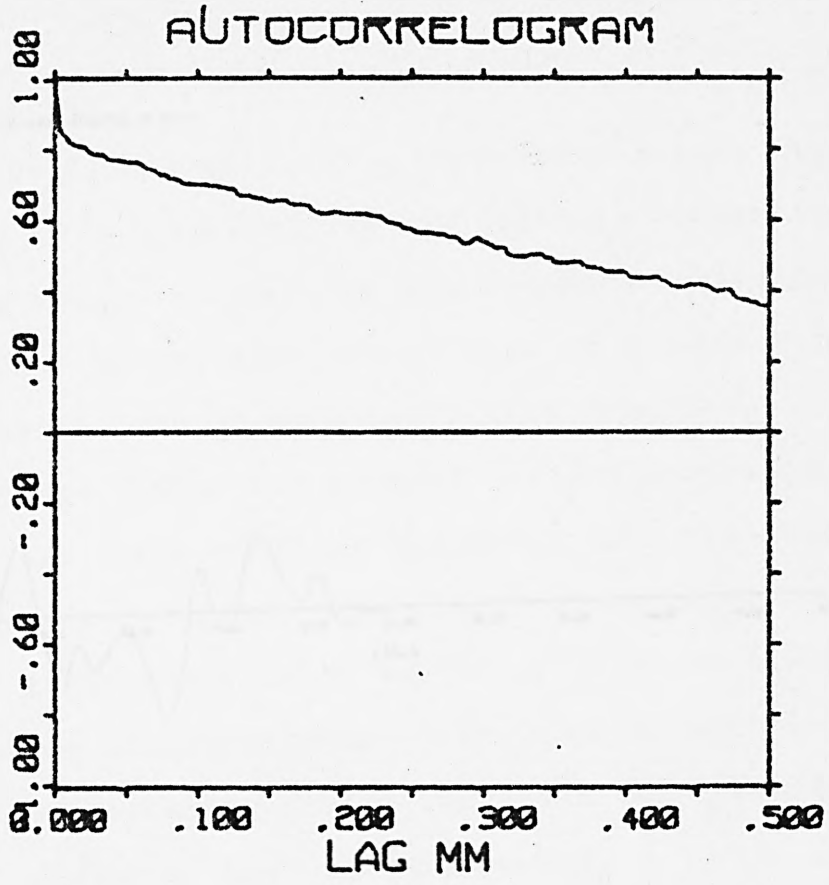

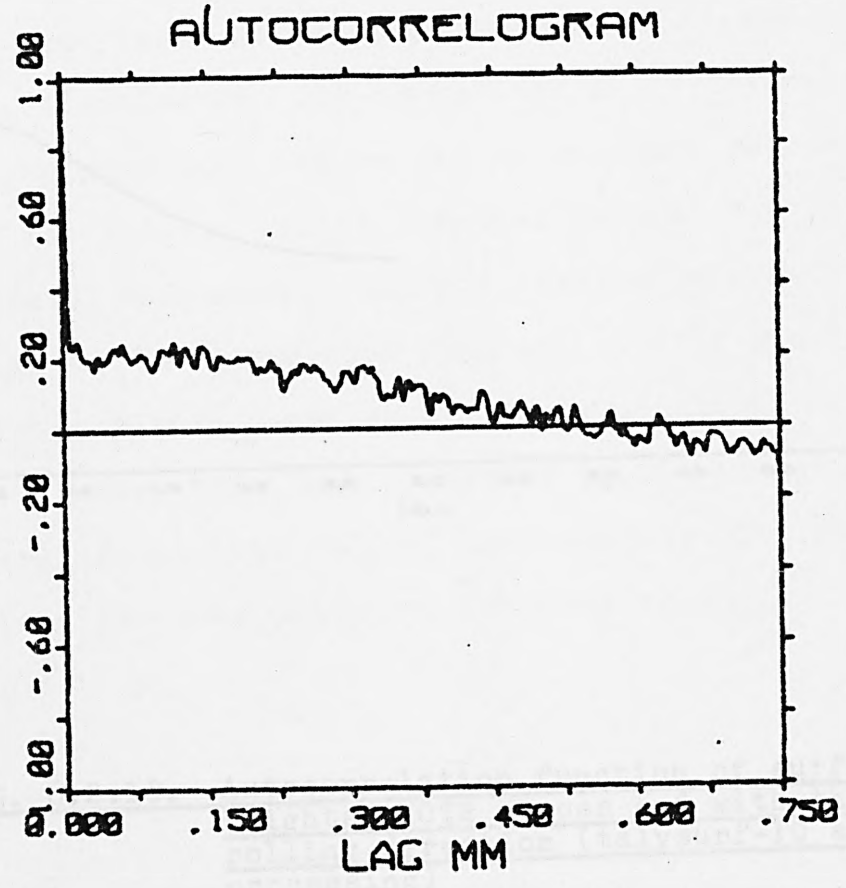

FIG. 6.2.17. Autocorrelation function of surface heights: MOT2 with and across the rolling direction (Talysurf-5 system)

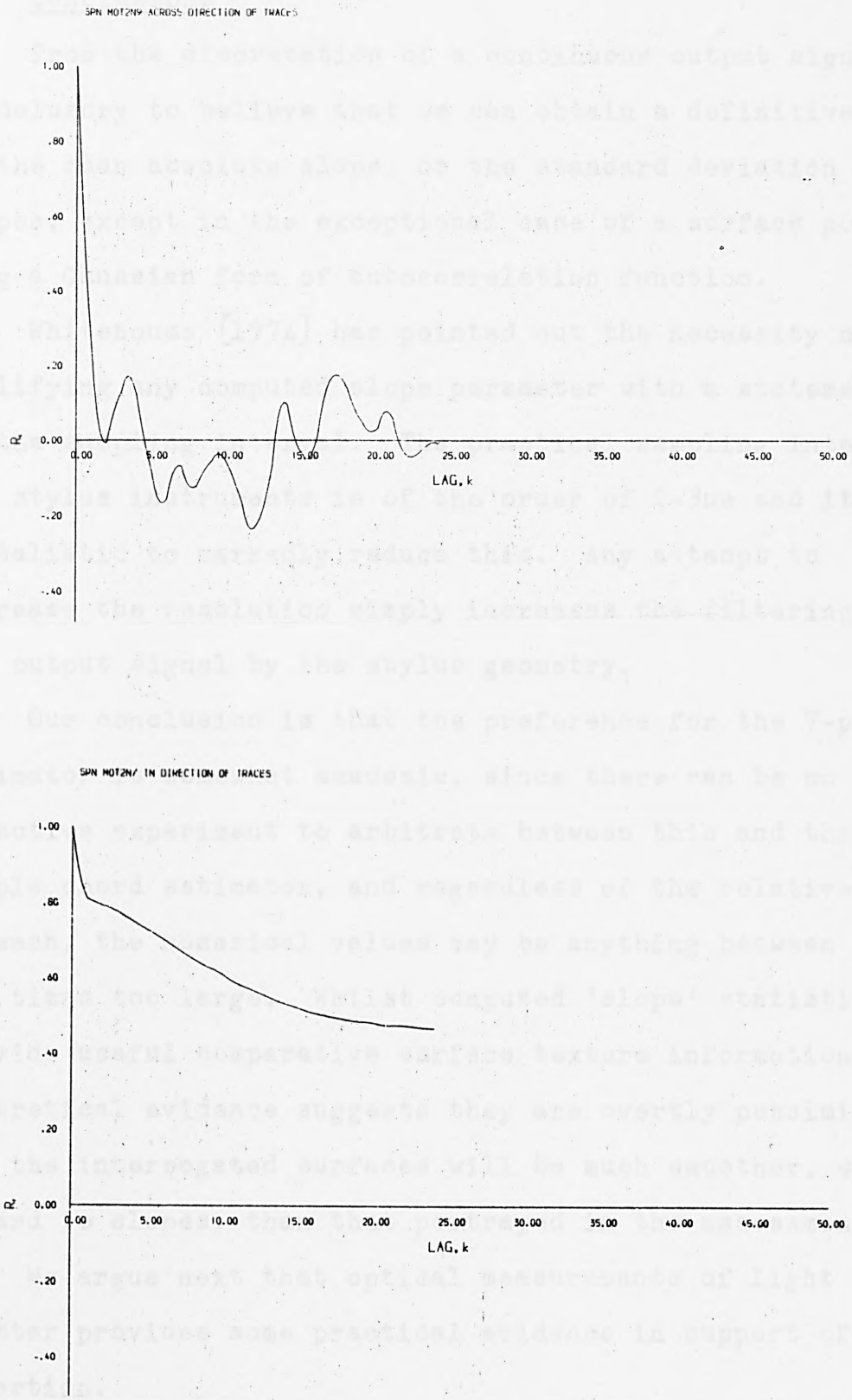

FIG. 6.2.18. Autocorrelation function of surface heights: MOT2 across and with the rolling direction (talysurf-10 area processing)

6.3 Conclusions

From the discretation of a continuous output signal it is delusory to believe that we can obtain a definitive value of the mean absolute slope, or the standard deviation of slopes, except in the exceptional case of a surface possessing a Gaussian form of autocorrelation function.

Whitehouse [1974] has pointed out the necessity of qualifying any computed slope parameter with a statement of the sampling interval. The practical sampling interval for stylus instruments is of the order of 2-3μm and it is unrealistic to markedly reduce this. Any attempt to increase the resolution simply increases the filtering of the output signal by the stylus geometry.

Our conclusion is that the preference for the 7-point estimator is somewhat academic, since there can be no objective experiment to arbitrate between this and the simple chord estimator, and regardless of the relative merits of each, the numerical values may be anything between 4 and 100 times too large. Whilst computed 'slope' statistics provide useful comparative surface texture information, the theoretical evidence suggests they are overtly pessimistic and the interrogated surfaces will be much smoother, with regard to slopes, than that portrayed in the assessment.

We argue next that optical measurements of light scatter provides some practical evidence in support of this assertion.

APPENDIX 6A

A normalised Pearson VII curve is synonoymous with the t-distribution. We take therefore:

$$f(x) = \frac{\Gamma(m)}{c\sqrt{\pi}\Gamma(m-\frac{1}{2})} \left(1 + \frac{x^2}{c^2} \right)^{-m}$$

The second moment, $\int x^2 f(x)dx$

$$= \frac{\Gamma(m)\, c^2}{c\sqrt{\pi}\Gamma(m-\frac{1}{2})} \int_{-\infty}^{\infty} \frac{1 + x^2/c^2 - 1}{(1 + x^2/c^2)^m} dx$$

$$= \frac{c^2\Gamma(m)}{c\sqrt{\pi}\Gamma(m - \frac{1}{2})} \left\{ \int \frac{1}{(1 + x^2/c^2)^{m-1}} dx - \int \frac{1}{(1 + x^2/c^2)^m} dx \right\}$$

$$= \frac{c^2\Gamma(m)}{\Gamma(m-\frac{1}{2})} \quad \frac{\Gamma(m-3/2)}{\Gamma(m-1)} - c^2$$

$$= \frac{c^2(m-1)}{m-3/2} - c^2$$

$$= \frac{c^2(2m-2)}{2m-3} - c^2$$

$$\sigma^2 = \frac{c^2}{2m-3} \qquad \ldots.(1)$$

Also we have the identity :

$$x^4 \equiv c^4(1 + x^2/c^2)^2 - c^4 - 2x^2c^2$$

$$c^4(1 + x^2/c^2)^2 - 2c^4(1 + x^2/c^2) + c^4.$$

$\therefore$ Therefore the fourth moment, μ_4

$$= \frac{c^4\Gamma(m)\Gamma(m-5/2)}{\Gamma(m-1/2)\Gamma(m-2)} - \frac{2c^4\Gamma(m)\Gamma(m-3/2)}{\Gamma(m-1/2)\Gamma(m-1)} + c^4$$

$$= c^4\frac{(m-1)(m-2)}{(m-3/2)(m-5/2)} - 2c^4\frac{m-1}{m-3/2} + c^4$$

$$\frac{\mu_4}{c^4} = \frac{(m-1)}{(2m-3)(2m-5)} \{ 4(m-2) - 4(2m-5) \} + 1$$

$$= \frac{4(m-1)(3-m)}{(2m-3)(2m-5)} + 1$$

$$= \frac{3}{(2m-3)(2m-5)}$$

$$\therefore \quad \frac{\mu_4}{(\sigma^2)^2} = \beta_2 = \frac{3(2m-3)}{2m-5}$$

$$\text{i.e.} \quad \beta_2 = \frac{6m-9}{2m-5}$$

$$\therefore \quad m = \frac{(5\beta_2 - 9)}{2(\beta_2 - 3)} \qquad \ldots\ldots(2)$$

CHAPTER 7

VALIDATION OF LIGHT SCATTERING MODELS

Abstract

Theory suggests that the back scattering of light from very rough surfaces is geometric. At first sight actual intensity plots support this, in so far as the skewness of the distribution is reversed, and indeed the distribution as a whole transposes, if the incident and specular directions are interchanged.

A Kirchhoff scattering model, for Gaussian surfaces, is derived and investigated to anticipate the extent to which a geometric view of scattering is upheld, for the specimen material investigated.

The facet model and Kirchhoff theory model predictions are compared with intensity scatter data to resolve the issue objectively.

7.1 Modelling Intensity Scatter Distributions

Chapter 8 discusses scattering from various forms of non-Gaussian surfaces. Here we assume a Gaussian surface and attempt to model the intensity for known σ and $C(\tau)$. The modelling is performed for two reasons. Firstly, the reverse procedure in effect is to estimate surface roughness parameters, and secondly to provide useful comment on the formal model validations of sections 7.2.1 and 7.2.2.

We postulate an autocorrelation function

$$C(\tau) = \begin{cases} e^{-\tau^2/T_3^2} & o<\tau<k_1, \\ A_1 e^{-\tau/T_1} & k_1<\tau<k_2, \\ A_2 e^{-\tau/T_2} & \tau>k_2, \end{cases} \qquad \ldots.(1)$$

where the constants A_1 and A_2 preserve the continuity of

the function at lags k_1 and k_2 respectively (continuity of the derivative cannot however be maintained at these points). Such a function reasonably models observed autcorrelation data, and leads to tractable mathematics, although may not strictly possess all the requirements of being a semi-definite function (c.f. Chapter 8 for full discussion of properties of ACF's in general). We view the function for the time being as an improper autocorrelation function and proceed regardless. Diagrammatically we distort the lag-scale to illustrate $C(\tau)$ in the figure, and model the characteristics of many measured autocorrelation functions by two negative exponential functions - one appertaining to small lags (micro-structure) and the other to large lags (macro-structure).

The terms 'micro-structure' and 'macro structure' refer to the structure of the autocorrelation function, and not to the mechanical profile structure, and will do so throughout 7.1. Whatever the separation lag τ, however small, profile heights $\zeta(x+\tau)$ and $\zeta(x)$ are a composite of macro and micro mechanical components: only by appropriate filtering could they be separated.

As $\tau \to 0$ the ratio $\frac{\zeta(x+\tau) - \zeta(x)}{\tau}$ approaches the facet slope in which the macro component is dominant.

The micro-structure itself is conceived as having a two part structure: a 'mini-micro' component which allows for the mathematical cusp to be erroded to a form $e^{-\tau^2/T_3^2}$ (to allow for realistic scattering behaviour for very rough surfaces) and a 'maxi-micro' component $A_1 e^{-\tau/T_1}$. Here k_1 and k_2 are small $k_1 \sim 0.5\mu m$ and $k_2 \sim 0.6\mu m$.

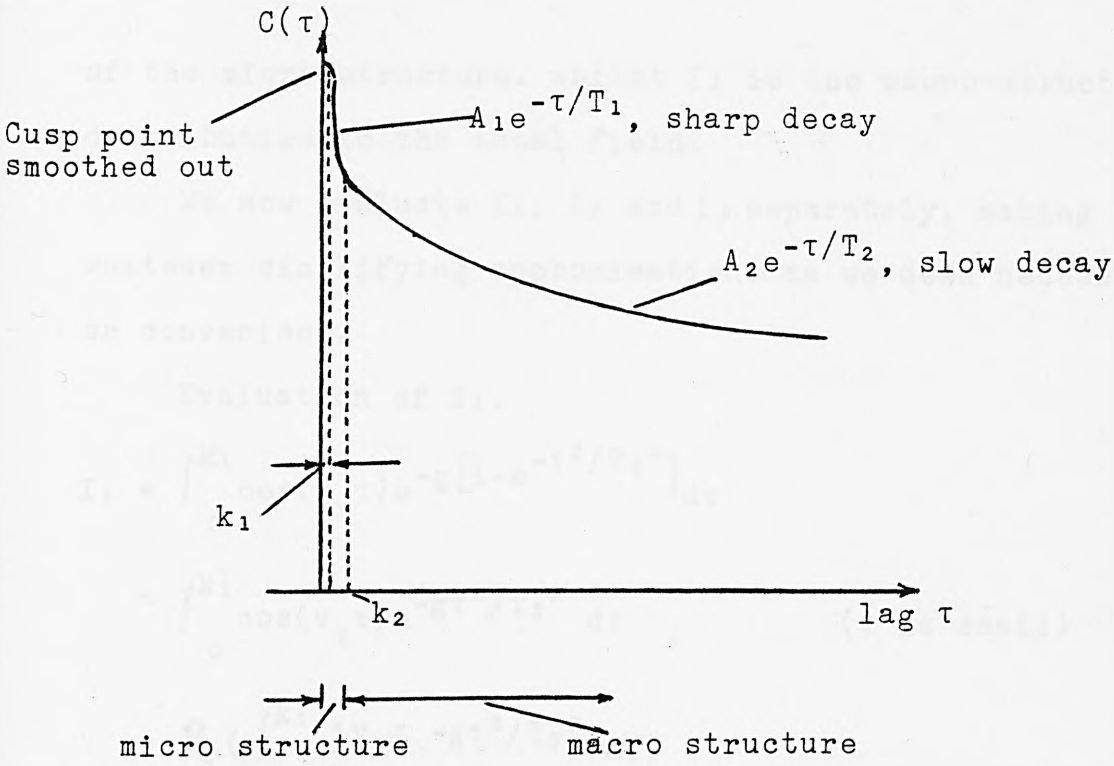

FIG. 7.1.1. Model Autocorrelation Function

The intensity of the reflected field from a surface having such a C(τ) function is proportional to

$$\int_{-L}^{L} e^{iv_x\tau}\, e^{-g[1-C(\tau)]}\, d\tau \qquad \ldots.(2)$$

$$= 2\int_{o}^{L} \cos(v_x\tau)\, e^{-g[1-C(\tau)]}\, d\tau$$

$$= 2\{ \int_{o}^{o}{}^{k_1} \cos(v_x\tau)\, e^{-g\left[1-e^{-\tau^2/T_3{}^2}\right]}\, d\tau$$

$$+ \int_{k_1}^{k_2} \cos(v_x\tau)\, e^{-g[1-A_1e^{-\tau/T_1}]}\, d\tau$$

$$+ \int_{k_2}^{L} \cos(v_x\tau)\, e^{-g\left[1-A_2e^{-\tau/T_2}\right]}\, d\tau \;\} \qquad \ldots.(3)$$

$= 2\{ I_1 + I_2 + I_3 \}$ say, provided g is sufficiently large (if not there is an additional term $e^{-g}\sin(cv_xL)$ to consider). The integrals I_1 and I_2 represent the individual contributions of the mini-micro and maxi-micro components

of the micro-structure, whilst I_3 is the macro-structure contribution to the total field.

We now evaluate I_1, I_2 and I_3 separately, making whatever simplifying approximations as we deem necessary or convenient.

Evaluation of I_1.

$$I_1 = \int_0^{k_1} \cos(v_x\tau) e^{-g\left[1-e^{-\tau^2/T_3^2}\right]} d\tau$$

$$\sim \int_0^{k_1} \cos(v_x\tau) e^{-g\tau^2/T_3^2}\, d\tau \qquad (\tau \text{ is small})$$

$$= \mathcal{R}\left(\int_0^{k_1} e^{iv_x\tau - g\tau^2/T_3^2}\, d\tau \right)$$

$$= \mathcal{R}\left(\int_0^{k_1} e^{-g/T_3^2(\tau - iv_x/2/g/T_3^2)} \cdot e^{-T_3^2/4gv_x^2}\, d\tau \right)$$

$$= e^{-T_3^2/4g/v_x^2}\, \mathcal{R}\left(\int_0^{k_1} e^{-g/T_3^2(\tau - iv_x/2g/T_3^2)^2} d\tau \right)$$

$$= e^{-T_3^2 v_x^2/4g}\, \sqrt{2\pi}\, \frac{T_3}{\sqrt{2g}}\, \mathcal{R}\left(\int_0^{k_1} \frac{1}{\sqrt{2\pi}/\frac{T_3^2}{\sqrt{2g}}} e^{-g/T_3^2\left(\tau - iv_x \frac{T_3^2}{2g}\right)^2} d\tau \right)$$

$$= e^{-T_3^2 v_x^2/4g}\, \sqrt{\pi}\, \frac{T_3}{\sqrt{g}}\, \mathcal{R}\left(\int_b^a \frac{1}{\sqrt{2\pi}} e^{-z^2/2} dz \right), \qquad \ldots.(4)$$

on writing $z = \dfrac{-iv_x T^2/2g}{T_3/\sqrt{2g}}$ and

$$a = \frac{-iv_x T_3^2/2g}{T_3/\sqrt{2g}} = \frac{-iv_x T_3}{\sqrt{2g}} \text{ and}$$

$$b = k_1\sqrt{2g}/T_3 + a.$$

The integral has a Gaussian form but has a complex argument and is evaluated between complex limits. Taking the real part however, ensures that

$$I_1 = e^{-T_3^2 v_x^2/4g} . \sqrt{\pi} . \frac{T_3}{\sqrt{g}} \left(\Phi(\sqrt{2g}k_1/T_3) - 0.5\right) \qquad \ldots.(5)$$

where Φ is the cumulative distribution function for the normal. As a check on our calculations if $g \to \infty$ (surface becoming very rough),

$$I_1 \to e^{-T_3^2 v_x^2/4g} \sqrt{\pi}\, T_3/\sqrt{g} \cdot \tfrac{1}{2} \qquad \ldots.(6)$$

In particular for $v_x = 0$ (specular direction).

$$I_1 = \sqrt{\pi}\, T_3/\sqrt{g}\ (\Phi(\sqrt{2g}k_1/T_3) - 0.5). \qquad \ldots.(7)$$

Evaluation of I_2

$$I_2 = \int_{k_1}^{k_2} \cos(v_x\tau) e^{-g\left[1-A_1 e^{-\tau/T_1}\right]} d\tau \text{ with } A_1 e^{-k_1/T_1} = e^{-k_1^2/T_3^2}$$

$$\sim \int_{k_1}^{k_2} \cos(v_x\tau) e^{-g\left[1-A_1+A_1\tau/T_1\right]} d\tau, \text{ again } \tau \text{ small}$$

$$= e^{-g_1} \int_{k_1}^{k_2} \cos(v_x\tau) e^{-gA_1\tau/T_1} d\tau \text{ with } g_1 = g(1-A_1)$$

$$= e^{-g_1}\, \mathcal{R}\left(\int_{k_1}^{k_2} e^{(iv_x - gA_1T_1)\tau} d\tau\right)$$

$$= e^{-g_1}\, \mathcal{R}\left(\frac{1}{iv_x - gA_1/T_1}\left[e^{(iv_x - gA_1/T_1)\tau}\right]_{k_1}^{k_2}\right)$$

$$= e^{-g_1}\, \mathcal{R}\left(\frac{-iv_x - gA_1/T_1}{v_x^2 + g^2A_1^2/T_1^2}\left[e^{iv_x - gA_1/T_1)k_2} - e^{(iv_x - gA_1/T_1)k_1}\right]\right)$$

$$= e^{-g_1} \frac{1}{g^2A_1^2/T_1^2 + v_x^2}\, \mathcal{R}\left((iv_x + gA_1/T_1)\left[e^{iv_x k_1} e^{-(gA_1/T_1)k_1} - e^{iv_x k_2} e^{-(gA_1/T_1)k_2}\right]\right),$$

$$= e^{-g_1} \frac{1}{1 + v_x^2 T_1^2/g^2A_1^2}\left\{\frac{T_1}{gA_1} \cdot \left(e^{-gA_1k_1/T_1}\cos(k_1v_x) - e^{-gA_1k_2/T_1} \cdot \cos(k_2v_x)\right)\right.$$

$$\left. - \frac{T_1^2}{g^2A_1^2} v_x \left(e^{-gA_1k_1/T_1}\sin(v_xk_1) - e^{-gA_1k_2/T_1} \cdot \sin(v_xk_2)\right)\right\} \qquad \ldots.(8)$$

In particular $v_x = 0$ (specular direction)

$$I_2 = e^{-g_1}\{ T_1/gA_1(e^{-gA_1k_1/T_1} - e^{-gA_1k_2/T_1}) \}$$

$$\sim e^{-g_1}\{ \frac{T_1}{gA_1}\left(\frac{gA_1k_2}{T_1} - \frac{gA_1k_1}{T_1}\right) \}$$

$$= e^{-g_1}\,(k_2 - k_1)$$

with $k_1 = 0$ $I_2 \to k_2$.

Evaluation of I_3.

The evaluation of I_3 is very similar to that of I_2 and so much of the detailed working is omitted.

$$I_3 = \int_{k_2}^{L} \cos(v_x\tau)e^{-g\left[1-A_2e^{-\tau/T_2}\right]}d\tau$$

$$\sim \int_{k_2}^{L} \cos(v_x\tau)e^{-g\left[1-A_2+A_2\tau/T_2\right]}d\tau \qquad \text{and here}$$

$A_2e^{-k_2/T_2} = A_1e^{-k_1/T_1}$. The approximation is still acceptable and relies on large g values but this is not over critical as T_2 is large (slow decay phase). We shall return to this point later for the sake of completeness in developing a more general theory.

$$I_3 = e^{-g_2}\,\mathcal{R}\left(\int_{k_2}^{L} e^{(iv_x - gA_2/T_2)\tau}d\tau\right) \qquad g_2 = g(1-A_2)$$

$$= e^{-g_2}\,\frac{1}{1+T_2^2v_x^2/g^2A_2^2}\left\{\frac{T_2}{gA_2}\left(e^{-(gA_2/T_2)k_2}\cos(k_2v_x) - e^{-\frac{gA_2L}{T_2}}\cos(v_xL)\right)\right.$$

$$\left. -\frac{T_2^2}{g^2A_2^2}v_x\left(e^{-(gA_2/T_2)k_2}\sin(k_2v_x) - e^{-\frac{gA_2L}{T_2}}\sin(v_xL)\right)\right\} \qquad \ldots.(9)$$

Again, in the specular direction,

$I_3 = e^{-g_2}\,T_2/gA_2\,(e^{-(gA_2/T_2)k_2} - e^{-(gA_2/T_2)L})$ and with k_2 small and L very large,

$I_3 \sim e^{-g_2}(T_2/gA_2).e^{-gA_2k_2/T_2}$.

The intensity amplitudes in the specular direction namely:

$$\frac{\sqrt{\pi}\,T_3}{\sqrt{g}}\left(\Phi(\sqrt{2g}k_1/T_3) - 0.5\right);$$

$$e^{-g_1 T_1/gA_1}\left(e^{-gA_1k_1/T_1} - e^{-gA_1k_2/T_1}\right); \qquad \ldots.(10)$$

$$e^{-g_2 T_2/gA_2}\left(e^{-gA_2k_2/T_2} - e^{-gA_2L/T_2}\right)$$

give the relative contributions of the individual structure components to the total field.

We shall explore these amplitudes a little before interpreting the total field.

(1) $\frac{\sqrt{\pi}T_3}{\sqrt{g}}\left(\Phi(\sqrt{2g}k_1/T_3 - 0.5\right)$, for small k_1 and moderately large, T_3 (for $\sqrt{2g}k_1/T_2 < 0.05$), the function $\Phi(\sqrt{2g}k_1/T_3 - 0.5)$ is linear and we may write

$$\frac{\sqrt{\pi}T_3}{\sqrt{g}}\left(\Phi(\sqrt{2g}k_1/T_3) - 0.5\right) = \frac{\sqrt{\pi}T_3}{\sqrt{g}} \cdot \frac{\sqrt{2g}k_1}{T_3} \cdot \frac{0.0200}{0.05}$$

(the last fraction is taken from tables of the Normal distribution) $= \sqrt{2\pi}.\ \frac{2}{5}\ k_1.$ $\qquad \ldots.(11)$

(2) $e^{-g_1}\ \frac{T_1}{gA_1}\left(e^{-gA_1k_1/T_1} - e^{-gA_1k_2/T_2}\right)$

$$= \frac{T_1}{gA_1}\ e^{-g\left[1-A_1+A_1k_1/T_1\right]} - e^{-g\left[1-A_1+A_1k_2/T_1\right]}$$

Let us write $k_2 = k_1+d$, then we have

$$(2) = T_1 gA_1\ e^{-g\left[1-A_1+A_1k_1/T_1\right]}\left\{1-e^{-gA_1d/T_1}\right\}$$

in general and for small d

$$= \frac{T_1}{gA_1}\ e^{-g\left[1-A_1+A_1k_1/T_1\right]}\left\{1-1+gA_1d/T_1\right\}$$

$$= e^{-g\left[1-A_1+A_1k_1/T_1\right]}.d\ ,\ \text{in either event} \to 0 \text{ as } g\to\infty.$$

(3) $e^{-g_2}\cdot\frac{T_2}{gA_2}\left(e^{-gA_2k_2/T_2}-e^{-gA_2L/T_2}\right)$

$$=\frac{T_2}{gA_2}\left\{e^{-g\left[1-A_2+A_2k_2/T_2\right]}-e^{-g\left[1-A_2+A_2L/T\right]}\right\}$$

$$\sim\frac{T_2}{gA_2}\,e^{-g\left[1-A_2+A_2k_2/T_2\right]}$$ for large L which again $\to 0$ as $g\to\infty$.

Depending on the magnitudes of the parameters g, k_1, k_2, T_1, T_2, T_3 either of (1), (2) or (3) could dominate.

Before discussing the fit of such a three part scattering model to actual scatter data, we review the computation of I_3 when g and T_2 are not especially large, and the approximation of $e^{-\tau/T_2}$ by $1 - \tau/T_2$ may not be justified.

Recomputation of I_3,

$$I_3 = \int_{k_2}^{L}\cos(v_x\tau)e^{-g\left[1-A_2e^{-\tau/T_2}\right]}d\tau$$

$$=\int_{k_2}^{L}\cos(v_x\tau)e^{-g}\,e^{gA_2e^{-\tau/T^2}}d\tau$$

$$=e^{-g}\int_{k_2}^{L}\cos(v_x\tau)\sum_{m=0}^{\infty}\frac{(gA_2)^m}{m!}\,e^{-m\tau/T_2}d\tau$$

$$=e^{-g}\sum_{m=0}^{\infty}\frac{(gA_2)^m}{m!}\int_{k_2}^{L}\cos(v_x\tau)\,e^{-m\tau/T_2}d\tau, \qquad \ldots.(12)$$

switching the order of integration and summation

$$I_3 = e^{-g}\sum_{m=0}^{\infty}\frac{(gA_2)^m}{m!}\,\mathcal{R}\left(\int_{k_2}^{L}e^{(iv_x-m/T_2)\tau}d\tau\right).$$

Reworking in full,

$$I_3 = e^{-g}\sum_{m=0}^{\infty}\frac{(gA^2)^m}{m!}\,\mathcal{R}\left\{\left[\frac{1}{iv_x-m/T_2}\,e^{(iv_x-m/T_2)\tau}\right]_{k_2}^{L}\right\}$$

$$\mathcal{R}(.) = \mathcal{R}\left\{\frac{-iv_x-m/T_2}{v_x^{\,2}+m^2/T_2^{\,2}}\left(e^{(iv_x-m/T_2)L}-e^{(iv_x-m/T_2)k_2}\right)\right\}$$

$$= \frac{1}{v_x^2+m^2/T_2^2}\left\{\frac{m}{T_2}\left(e^{-mk_2/T_2}\cos(v_xk_2)-e^{-mL/T_2}\cos(v_xL)\right)\right.$$

$$\left.-v_x\left(e^{-mk_2/T_2}\sin(v_xk_2)-e^{-mL/T_2}\sin(v_xL)\right)\right\}$$

$$= \frac{1}{1+v_x^2T_2^2/m^2}\left\{\frac{T_2}{m}\left(e^{-mk_2/T_2}\cos(v_xk_2)-e^{-mL/T_2}\cos(v_xL)\right)\right.$$

$$\left.-(T_2^2/m^2)v_x\left(e^{-mk_2/T_2}\sin(v_xk_2)-e^{-mL/T_2}\sin(v_xL)\right)\right\}$$

....(13)

Recombining,

$$I_3 = e^{-g}\sum_{m=1}^{\infty}\frac{(gA_2)^m}{m!}\frac{1}{1+v_x^2T_2^2/m^2}\{.\} + e^{-g}\operatorname{sinc}v_xL \quad ....(14)$$

For a modestly rough surface $g\sim 10$ say the series is rapidly convergent. In particular in the specular direction ($v_x = 0$) and if we allow $L \to \infty$,

$$I_3(\text{spec}) = e^{-g}\sum_{m=1}^{\infty}\frac{(gA_2)^m}{m!}\frac{T_2}{m}e^{-mk_2/T_2}$$

$$= e^{-g}T_2\sum_{m=1}^{\infty}\left\{\frac{gA_2e^{-k_2/T_2}}{m!\,m}\right\}^m, \text{ which is of the}$$

form,

$$= e^{-g}T_2\sum_{m=1}^{\infty}\frac{x^m}{mm!} \quad ....(15)$$

(The series $\sum_{m=1}^{\infty}\frac{x^m}{mm!}$ cannot be obtained in closed form and can only be expressed in terms of the exponential integral $E_i(x) = \int_{-\infty}^{x}\frac{e^t}{t}\,dt$, where explicitly $E_i(x) = \gamma + \sum_{m=1}^{\infty}\frac{x^m}{mm!}$ and γ is Euler's constant. This however, although mathematically precise, is not particularly useful and the series itself provides a means of numerically evaluating $E_i(x)$).

But $I_3(\text{spec}) < e^{-g}T_2\sum_{m=1}^{\infty}\frac{(gA_2)^m}{m!}$

$= e^{-g}T_2\{e^{gA_2}-1\}$ by comparison with the exponential series.

Alternatively,

$$I_3(\text{spec}) > e^{-gT_2} \sum_{m=1}^{\infty} \frac{\{gA_2 e^{-k_2/T_2}\}^m}{m!(m+1)}$$

$$= e^{-gT_2} \frac{1}{\{gA_2 e^{-k_2/T_2}\}} \sum_{m=1}^{\infty} \frac{(gA_2 e^{-k_2/T_2})^{m+1}}{(m+1)!}$$

$$= e^{-gT_2} \frac{1}{gA_2 e^{-k_2/T_2}} (e^{gA_2 e^{-k_2/T_2}} - 1 - gA_2 e^{-k_2/T_2}) \quad \ldots.(16)$$

We thus have bounds on $I_3(\text{spec})$.

Returning to 7.1.12 we see that I_3 is basically built up by a sequence of $\frac{1}{1+v_x^2 T_2^2/m^2}$ curves where this 'mth harmonic' is weighted by $(\frac{gA_2 e^{-k_2/T_2}}{m!\, m})^m T_2$.

We now discuss the fitting of the 3-part intensity model to real life data.

For large scale roughness both facet and wave theory scattering models converge upon a Gaussian-form of intensity distribution, and we would require of our model that this is permitted to happen. In short the facet theory explains the scatter entirely in terms of the autocorrelation micro structure. The necessary prerequisites are that (i) $C''(0)$ is finite (accommodated by $e^{-\tau^2/T_3^2}$), (ii) k_1 is sufficiently large (fitting a range of scatter distributions arising from a variety of rough surfaces suggests that $k \sim 0.5\mu m$).

Autocorrelation functions obtained mechanically plainly demonstrate that $k_1 << 2\mu$. Furthermore, the exceedingly rapid transition in all cases to the slow decay $A_2 e^{-\tau/T_2}$ phase implies that T_1 is small, possibly as low as $0.6\mu m$ in some cases, and in consequence I_2 is a near constant uniform distribution, of low magnitude. Diagnostic checking of the model fit suggests that with k_1 relatively large k_2 can

only be slightly larger. To summarise $k_1 \sim 0.5\mu m$, $k_2 \sim 0.6\mu m$ seem to be universally acceptable values. Thus our model is effectively almost reduced to (1) and (3), (2) provides about 1% of the scatter.

For large and moderate roughness, the following composite patterns of the scatter distribution are drawn, together with some explanation.

(A) Large scale surface roughness - large g

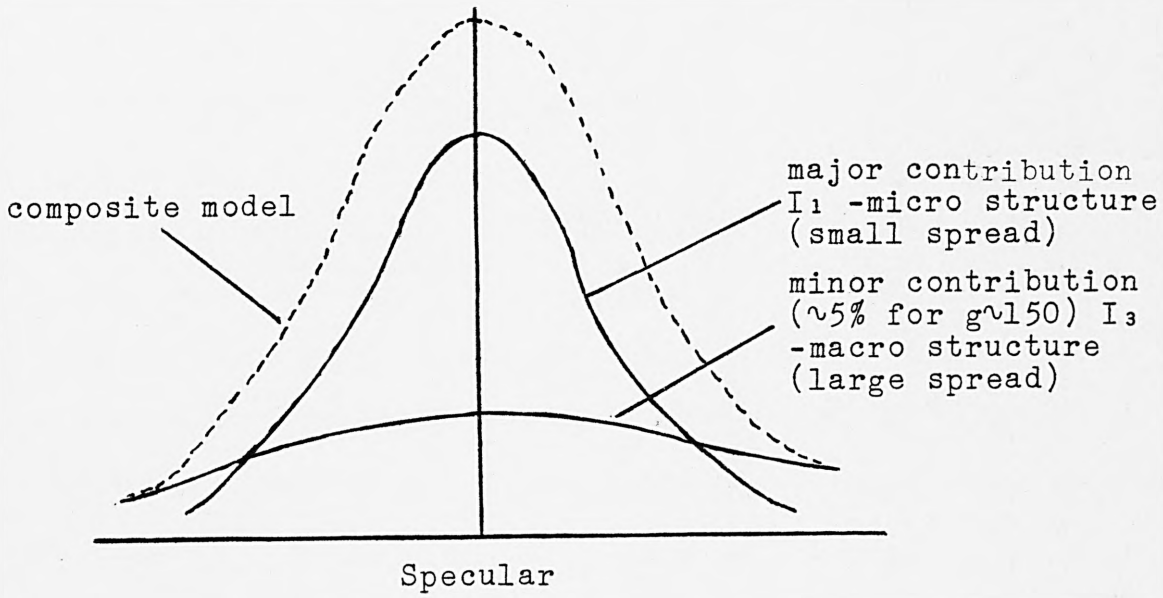

FIG. 7.1.2. Components of Scatter from very rough surface

As described previously, the micro-structure component dominates, and is the major contributor to the near specular scatter but a minor, though significant rôle is played by the macro structure which contributes a disperse scatter distribution of small amplitude. For the micro structure alone, unless the surface is exceedingly rough, cannot by itself explain the scatter to fit the tail intensity distributions. Unrealistically large values of T_3 would be required, resulting in a marked lack of fit in the

neighbourhood of the specular direction.

(B) Moderate surface roughness (e.g. g∿20)

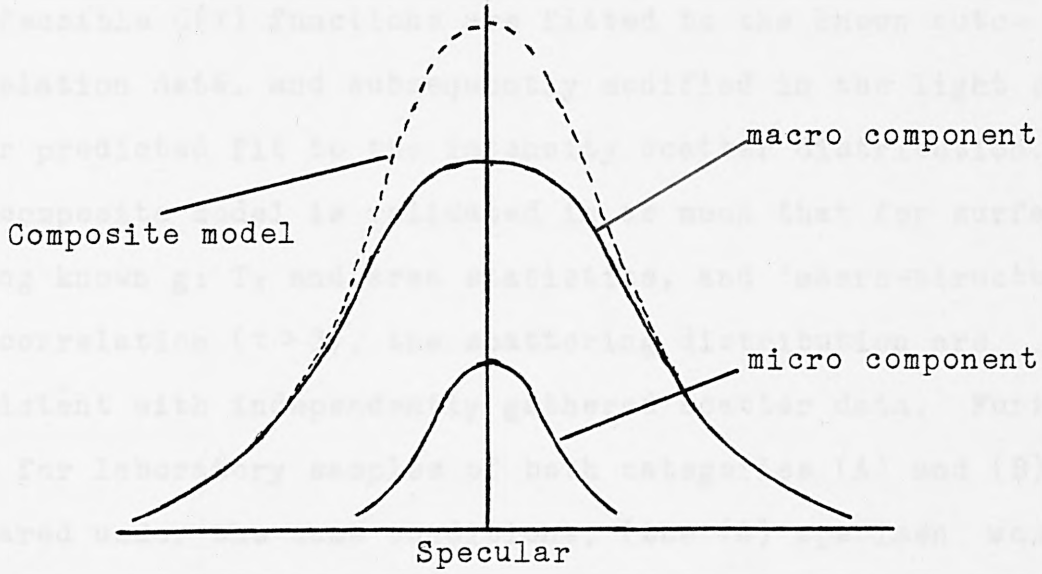

FIG. 7.1.3. Scattering components for a moderately rough surface

With decreasing roughness g↘, the relative influence of the structure components changes - the micro-structure effect gives way to the macro-structure effect as shown in (A) and (B).

Summary

At the outset a model of typically observed auto-correlation functions was proposed. Later certain ranges of the parameters were deduced as necessary concomitants of understood scattering phenomena, remembering that any derived scattering model should be flexible to the extent that, on ranging the magnitudes of the surface roughness parameters, the scatter model should freely adapt and smoothly conform to model the current governing scatter distribution.

The precise nature of the micro-structure cannot be confirmed by stylus instruments, as they are not capable of the resolution required, but is in part conjecture, based

on physical scattering phenomena. Values of k_1 and k_2 cannot be uniquely determined from auto-correlation plots, and feasible $C(\tau)$ functions are fitted to the known auto-correlation data, and subsequently modified in the light of their predicted fit to the intensity scatter distribution. The composite model is validated in as much that for surfaces having known g_1 T_2 and area statistics, and 'macro-structure autocorrelation ($\tau > 3$), the scattering distribution are consistent with independently gathered scatter data. Furthermore for laboratory samples of both categories (A) and (B) prepared under the same conditions, (the (A) specimen was ground and polished to a smoother condition), the structure boundaries k_1 and k_2 could be taken as invariant, with the scatter model predicting a satisfactory explanation of each observed scatter distribution.

However for many specimens the micro-structure component was not as dominant as anticipated. The reason for this was the non-Gaussian nature of the specimen surfaces. Theory for a negative exponential surface for instance would be modified by replacing (2) by

$$\int_{-L}^{L} e^{iv_x\tau} \frac{1}{\{1+g[1-C(\tau)]\}} \, d\tau$$

and proceeding as before. The theme of non-normality is now taken up in 7.2.

7.2. Model Prediction of Intensity Scatter

The metal specimens interrogated, whether of the laboratory prepared ground variety or specimens of commercial cold-rolled stainless steel, were mainly of the Type (C) very rough category, according to the order of the g parameter. (Provided the incidence of the illumination was not oblique.)

In consequence, the facet and Kirchhoff predictions for such specimens ought to be in close agreement (c.f. Chapter 4), and the information on slopes is likely to be paramount:

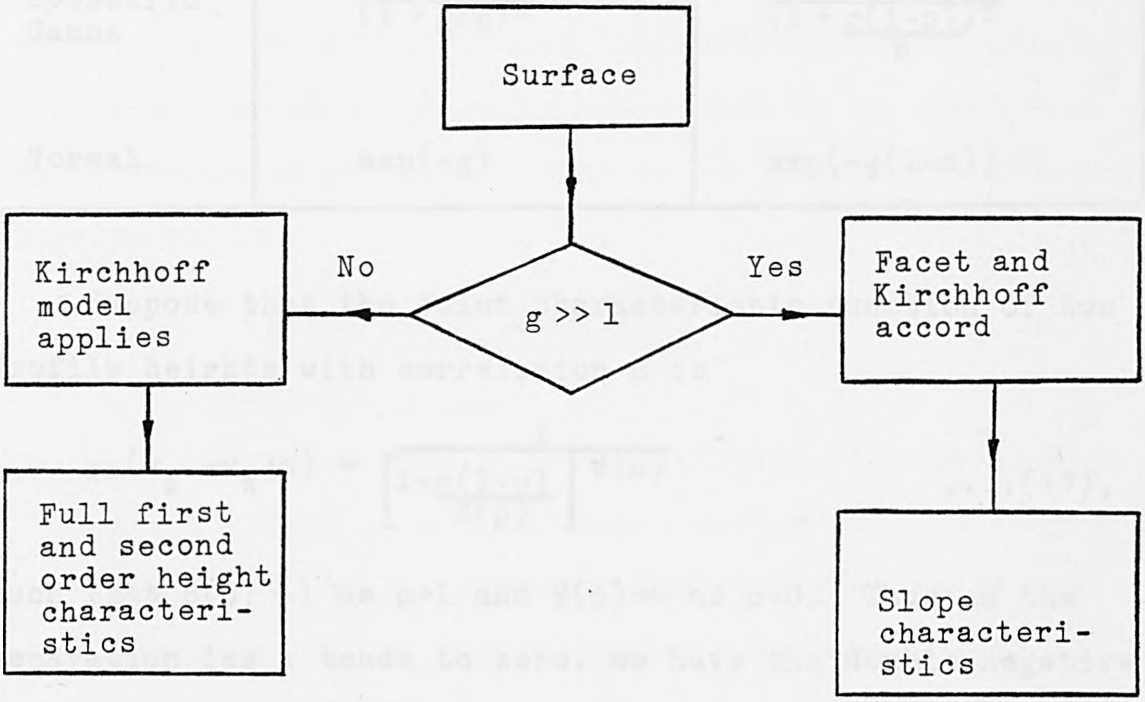

FIG. 7.2.1. Scattering theory appropriate to the value of g

A striking feature of the statistical analyse of surface profiles discussed in the previous chapter, was the marked difference in the histograms of surface heights and surface slopes of some specimens (c.f. Fig. 6.2.10. etc.) Since a surface of Gaussian heights would generate Gaussian slopes, this phenomenon requires some investigation:

Quoting some results derived in the next chapter, we propose the following mechanism:

Distribution	Joint Characteristic Function of independent variables	Joint Characteristic Function of dependent variables
Laplace	$\frac{1}{1+g}$	$\frac{1}{1+g(1-\rho)}$
Symmetric Gamma	$\frac{1}{(1+g/\beta)^{\beta}}$	$\frac{1}{(1+\frac{g(1-\rho)}{\beta})^{\beta}}$
Normal	$\exp(-g)$	$\exp(-g(1-\rho))$

Suppose that the joint characteristic function of two profile heights with correlation ρ is

$$\chi_2(v_z,-v_z;\rho) = \frac{1}{\left[1+\frac{g(1-\rho)}{\beta(\rho)}\right]^{\beta(\rho)}} \qquad \ldots.(17),$$

such that $\beta(\rho) \to 1$ as $\rho \to 1$ and $\beta(\rho) \to \infty$ as $\rho \to 0$. Thus as the separation lag τ tends to zero, we have the double negative exponential (Laplace) distribution of slopes. As τ tends to infinity on the other hand, the heights are independent samples, and we have a Gaussian charactersitic function so that the height distribution appears normal. That is, treating the sample heights as independent random variables, we obtain an apparent normal distribution. For chords of fixed lag τ, the characteristic function is the intermediate case, and the distribution of chord slopes is characterised by the difference of two identical gamma variates.

A simple function would be say,

$$\chi_2(v_z,-v_z;\rho) = \frac{1}{\{1+g(1-\rho)\rho\}^{1/\rho}} . \qquad \ldots.(18)$$

If we further take $\rho(\tau) = e^{-\tau/T}$, then for a rough surface and τ small, the characteristic function virtually becomes

$$\frac{1}{\{1 + g\tau/T\}^{1+\tau/T}} \quad .$$

Thus the distribution of chord samples is symmetric, with zero odd moments and with even moments defined by the gamma density function. Hence, under these hypotheses, the shape of the chord distribution closely approximates the actual distribution of slopes. Although no great reliance can be placed upon the numerical values of variance estimates, descaled parameters such as kurtosis might be reasonably valid.

7.2.1. One-Dimensional Models
Facet Model Prediction

Feature Fitting

Although mostly of Type (C), the specimens were nevertheless weak scatterers, and as we have seen in Chapter 6, by far the most dominant feature of the intensity plots is a strong specular lobe. However, on closer examination, there are small details which disturb the apparent lobe symmetry at the peak and the foot of the lobe. The facet model slope prediction may be compared in Figures 7.2.2.-7.2.4. There are obvious difficulties of interpretation, since we are trying to compare a bar-chart of profile slopes with a continuous 5 degree polynomial fit to intensity data, compounded with distortions of scale. Despite the subjectivity of the exercise, the significant lobe features of the intensity plots can be matched with bar chart features of profile slope diagrams. This is true of the ground steel specimens M1T1 and M1T2, portrayed in Figures 7.2.2. and 7.2.3. as well as the defect specimen M2T4. The magnitude of the defect was

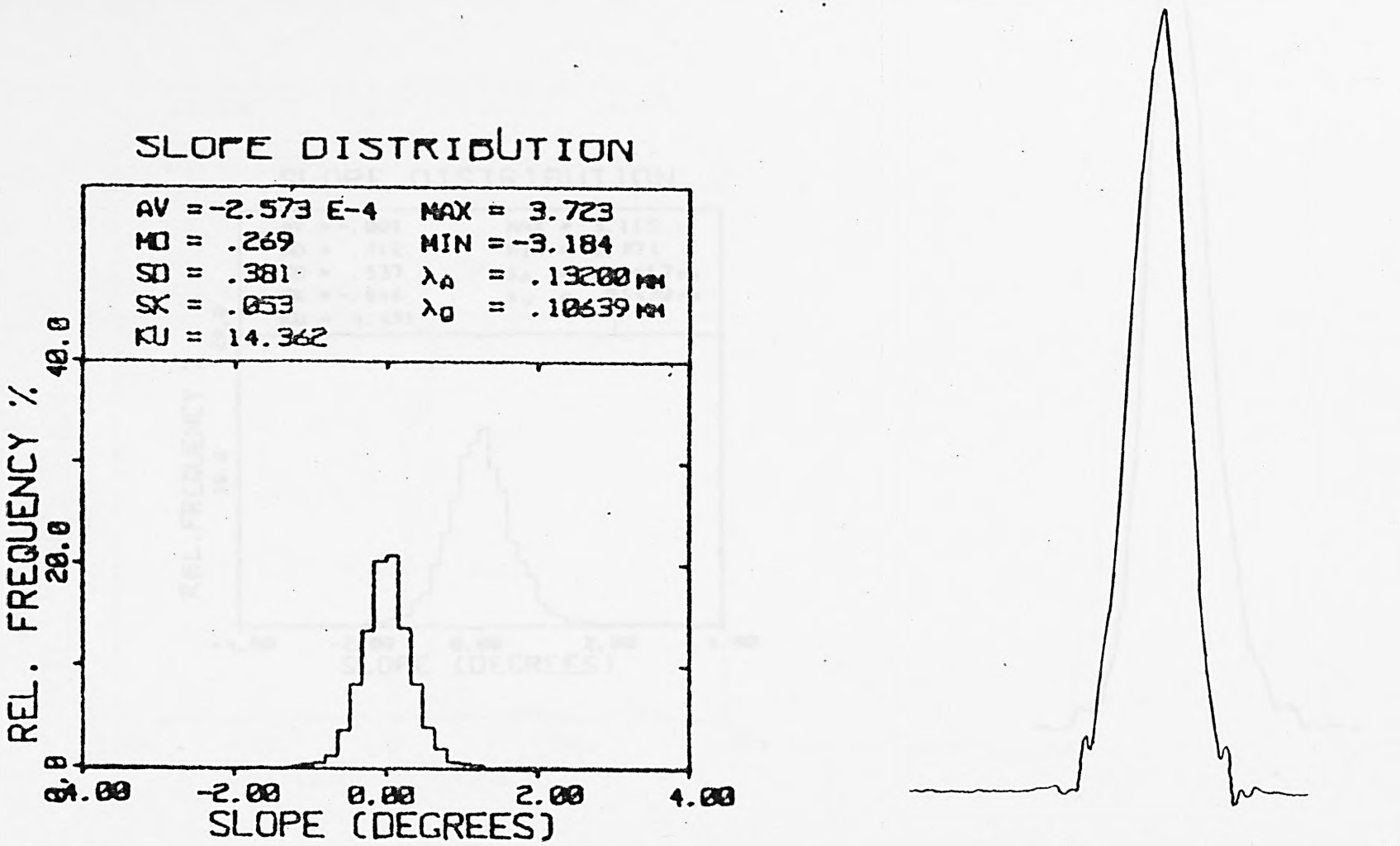

FIG. 7.2.2. Intensity scatter with corresponding slope distribution (Specimen M1T1)

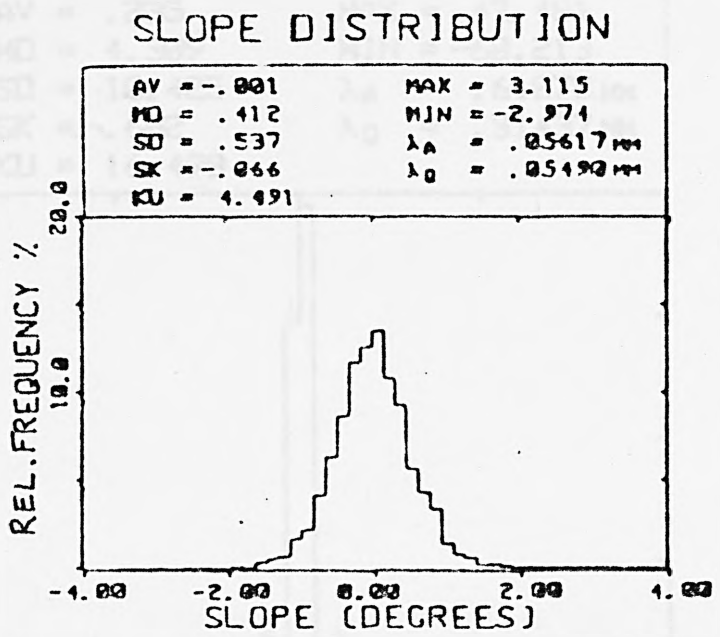

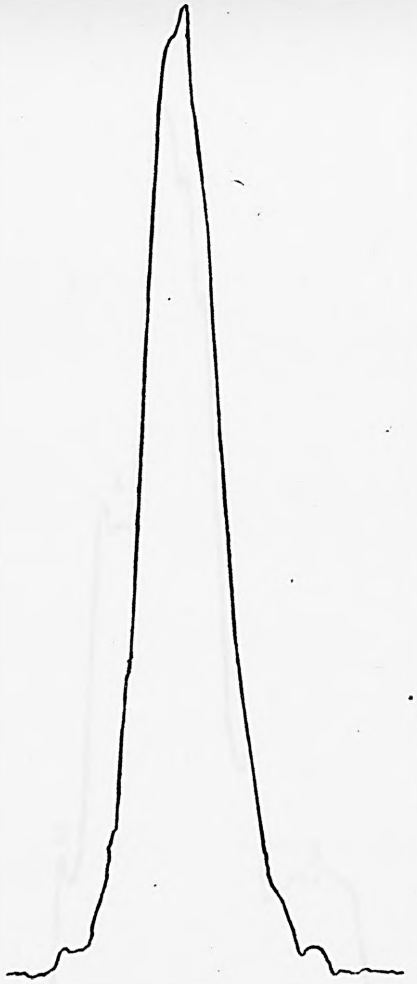

FIG. 7.2.3. Intensity scatter with corresponding slope distribution (specimen M1T2)

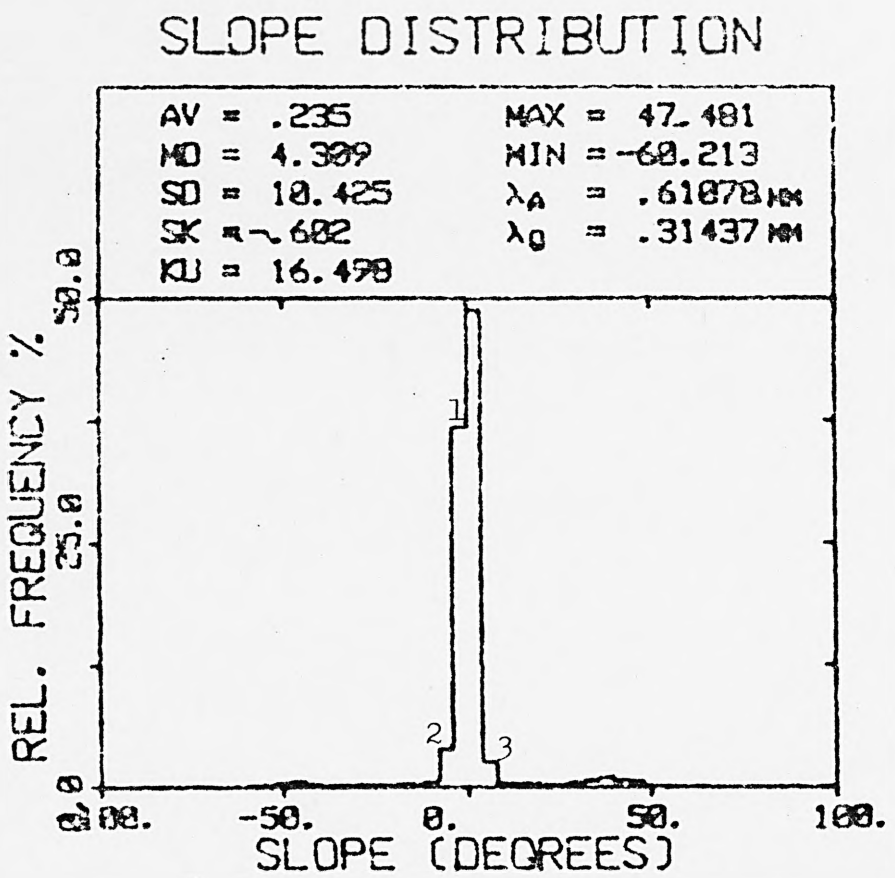

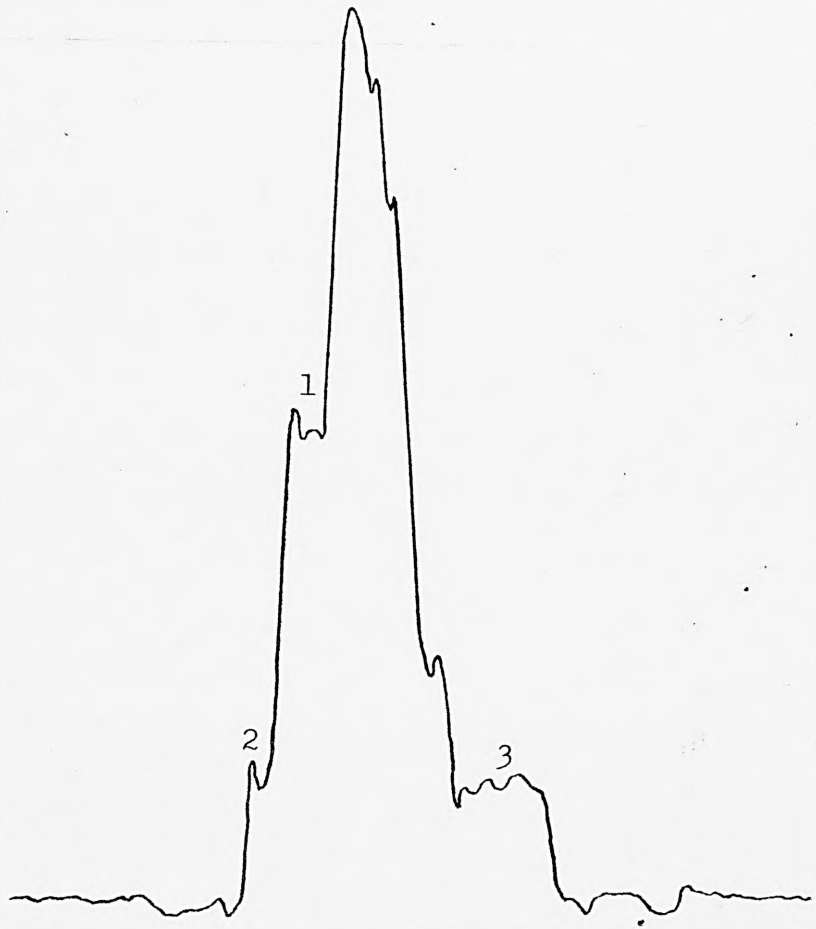

FIG. 7.2.4. Intensity Scatter with corresponding slope statistics (M1T4 scratch defect)

such that talysurf lost much of its sensitivity and could only record gross variations. These gross variations are seen without difficulty on the accompanying intensity graph.

This visual agreement is supported quantitatively, if we collate and compare the moment statistics of allied diagrams. The standard deviation, skewness and kurtosis measures are given in the following Table 7.2.1. Scatter diagrams of the same are presented in Figures 7.2.5.-7.2.7.

For a valid model the points should lie close to the line passing through the origin of unit slope for each separate scatter diagram. In each case correlation coefficients have been calculated and show that some 45% of the variation is explained. This low figure reflects the disperse distribution of the scatter about their respective regression lines.

Specimen		Slope Statistics	Intensity Statistics	Comment
M1T2	SCAN 180	SD 0.54 Degrees SK -0.66 KU 4.49	SD 0.20 Degrees SK -0.23 KU 4.14	For perp. scans wide difference in kurtosis is picked up
	SCAN 90	SD 0.36 Degrees SK -0.34 KU 10.69	SD 0.25 Degrees SK -1.98 KU 12.99	
M1T1	SCAN 180	SD 0.38 Degrees SK 0.053 KU 14.36	SD 0.21 Degrees SK 1.01 KU 12.51	Very smooth underlying surface texture but large defect pits present
	SCAN 90	SD 0.38 Degrees SK -0.21 KU 13.82	SD 0.21 Degrees SK -1.78 KU 13.94	
M3T2	SCAN 0	SD 0.46 Degrees SK 0.534 KU 11.66	SD 0.21 Degrees SK 0.31 KU 6.99	
	SCAN 90	SD 0.75 Degrees SK 0.37 KU 10.45	SD 0.30 Degrees SK 1.8 KU 8.50	
M3T1	SCAN 190	SD 0.215 Degrees SK -0.045 KU 4.30	SD 0.19 Degrees SK -1.15 KU 8.47	This specimen is particularly smooth and of Type (B) roughness
	SCAN 270	SD 0.22 Degrees SK 0.42 KU 5.37	SD 0.19 Degrees SK 0.60 KU 8.08	
M2T2	SCAN 90	SD 0.75 Degrees SK -0.56 KU 6.61	SD 0.23 Degrees SK -0.80 KU 4.32	For perp. scans wide difference in kurtosis is picked up
	SCAN 0	SD 0.53 Degrees SK -0.48 KU 16.56	SD 0.59 Degrees SK -3.62 KU 16.07	

TABLE 7.2.1. Moments of Slopes and Intensity Plots for corresponding specimens

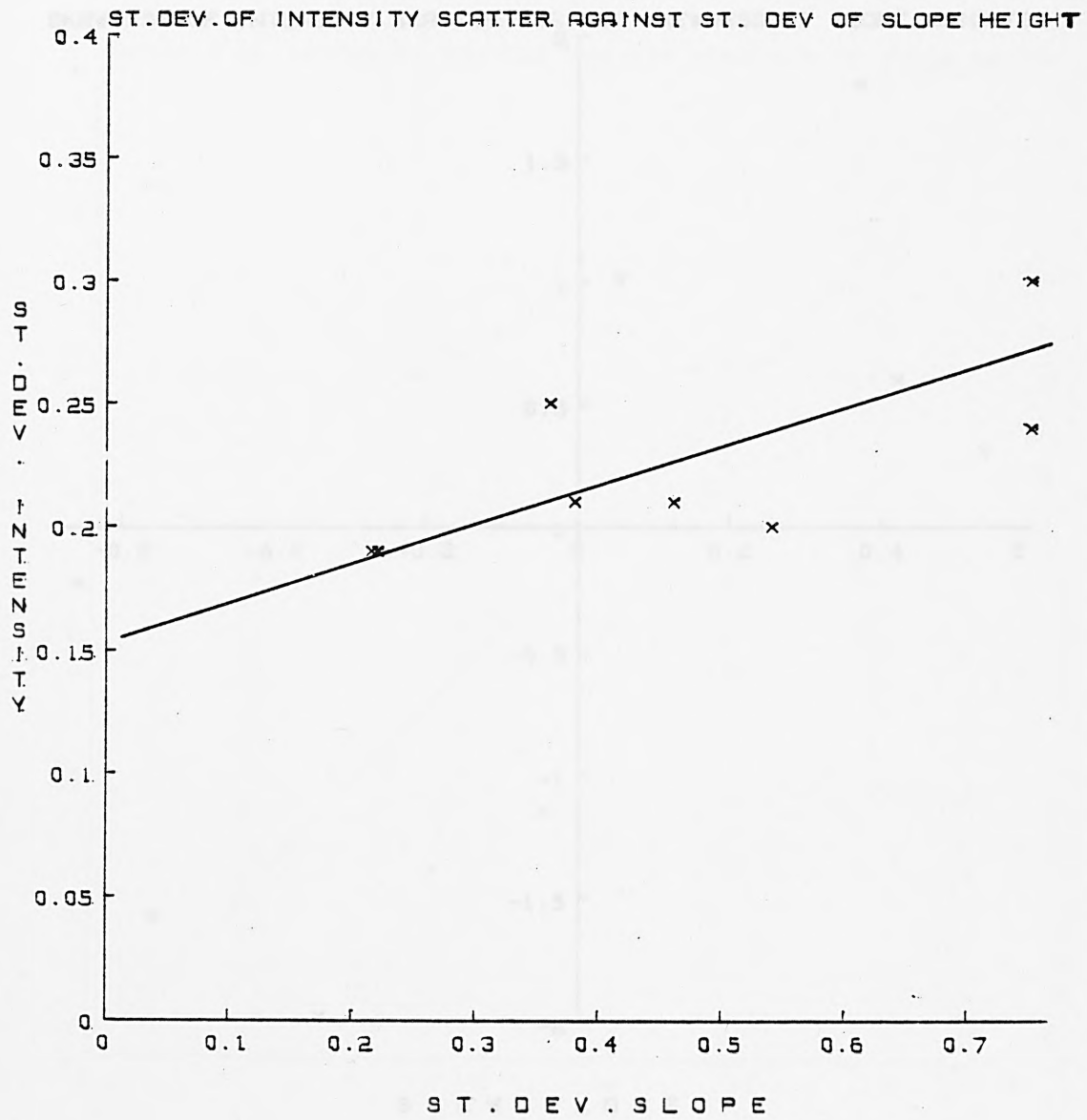

FIG. 7.2.5. Scatter diagram of st. dev. of intensity and st. dev. of surface profile slopes

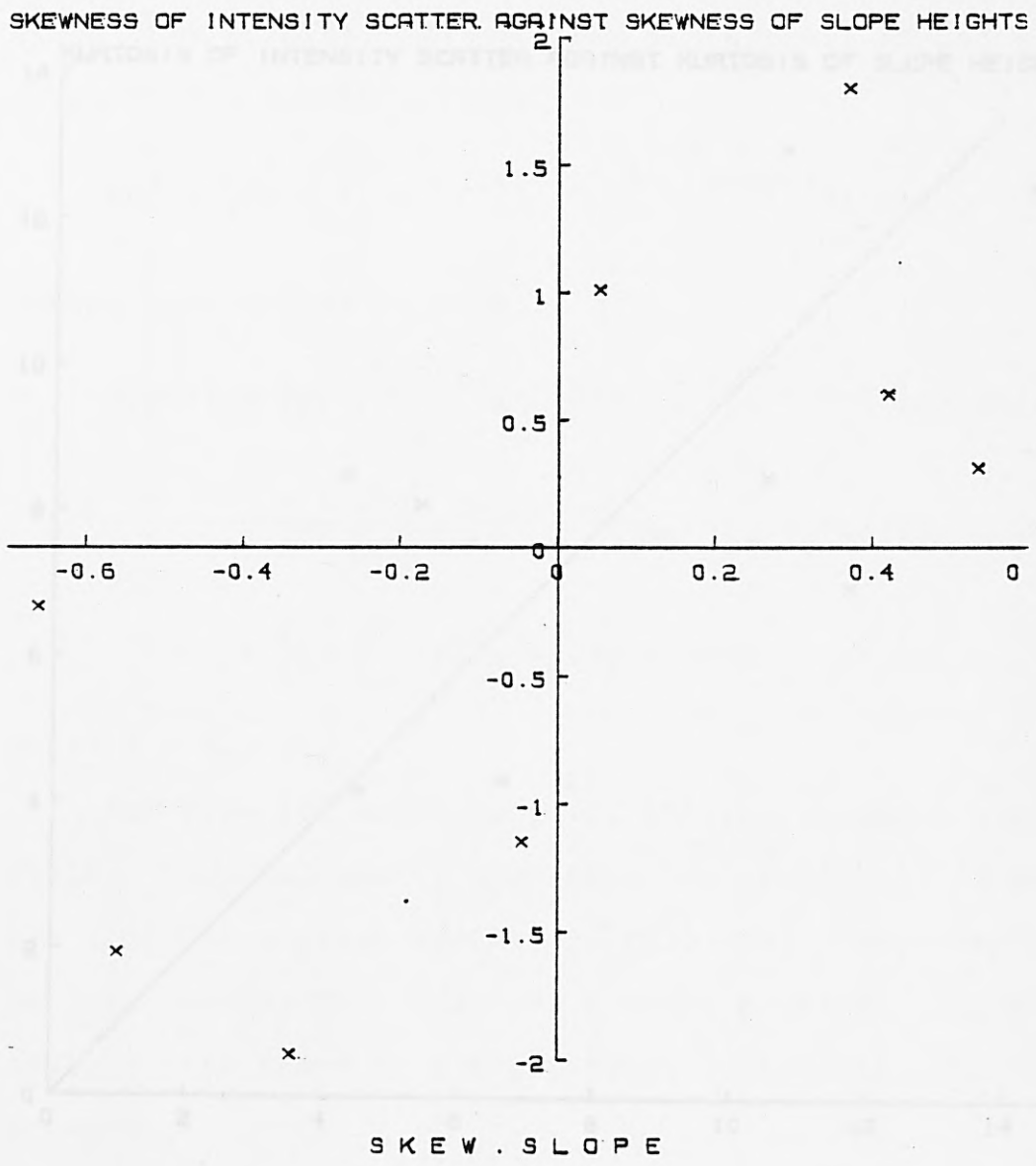

FIG. 7.2.6. Scatter diagram of skewness of intensity distribution and skewness of surface profile slopes

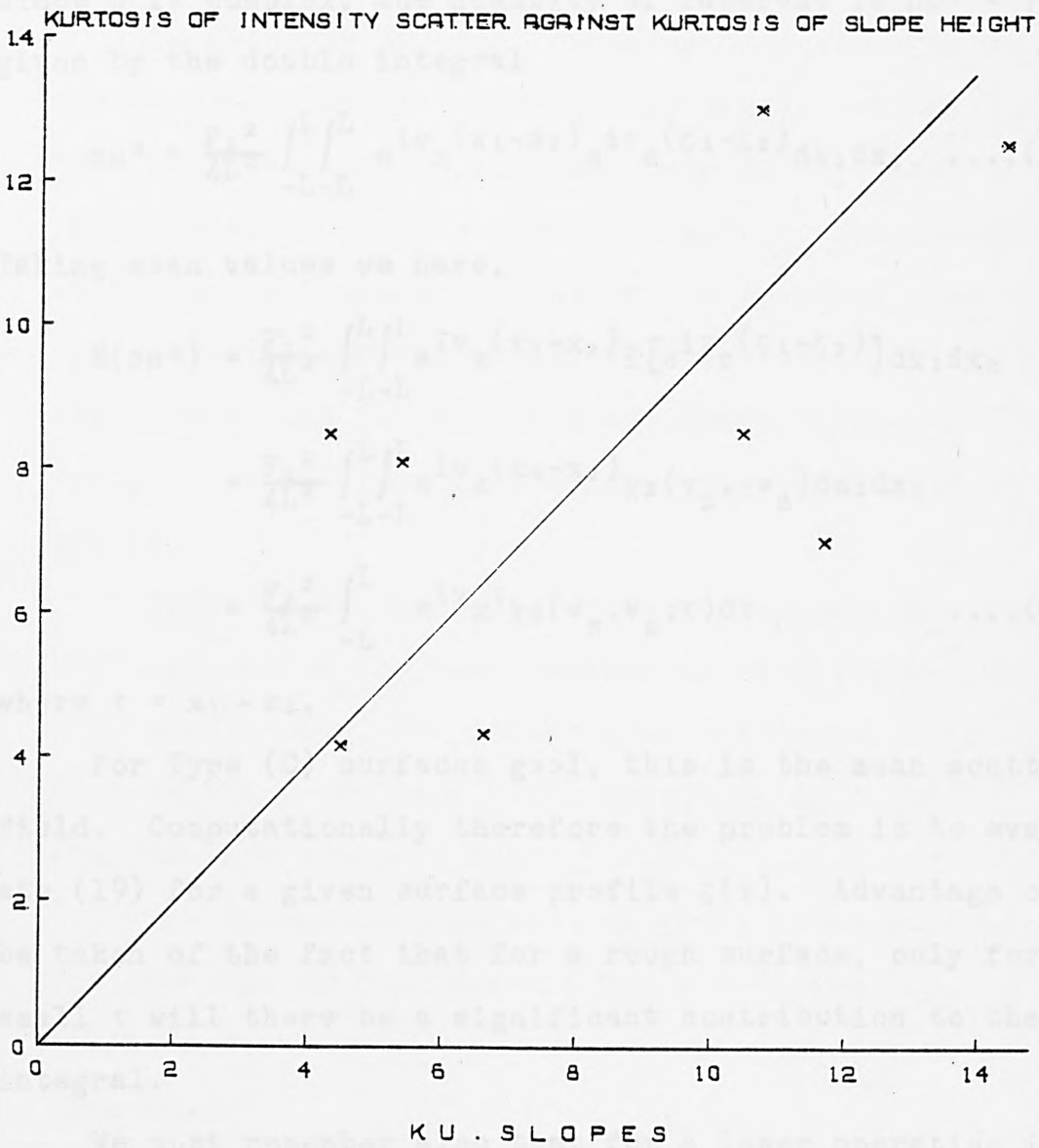

FIG. 7.2.7. Scatter diagram of kurtosis of intensity distribution and kurtosis of surface profile slopes

Wave Theory Model Prediction

We recall the solution for a perfectly conducting one-dimensionally rough surface:-

$$\rho(\theta_2) = \frac{F^2}{2L}\int_{-L}^{L} e^{i\underline{v}\cdot\underline{r}}\,dx \qquad \text{(c.f. (14) of Chapter 4)}$$

Since ρ is complex, the quantity of interest is $\rho\rho^* = |\rho|^2$, given by the double integral

$$\rho\rho^* = \frac{F_2{}^2}{4L^2}\int_{-L}^{L}\int_{-L}^{L} e^{iv_x(x_1-x_2)}e^{iv_z(\zeta_1-\zeta_2)}dx_1dx_2 \qquad \ldots.(19)$$

Taking mean values we have,

$$E(\rho\rho^*) = \frac{F_2{}^2}{4L^2}\int_{-L}^{L}\int_{-L}^{L} e^{iv_x(x_1-x_2)}E\left[e^{iv_z(\zeta_1-\zeta_2)}\right]dx_1dx_2$$

$$= \frac{F_2{}^2}{4L^2}\int_{-L}^{L}\int_{-L}^{L} e^{iv_x(x_1-x_2)}\chi_2(v_z,-v_z)dx_1dx_2$$

$$= \frac{F_2{}^2}{4L^2}\int_{-L}^{L} e^{iv_x\tau}\chi_2(v_z,v_z;\tau)d\tau \qquad \ldots.(20)$$

where $\tau = x_1 - x_2$.

For Type (C) surfaces $g>>1$, this is the mean scattered field. Computationally therefore the problem is to evaluate (19) for a given surface profile $\zeta(x)$. Advantage can be taken of the fact that for a rough surface, only for small τ will there be a significant contribution to the integral.

We must remember also that for a laser operating in TM00 mode, the energy characteristics of a Gaussian beam distant r from the axis are,

$A(r) = A_o\exp(-r^2/w^2)$

$I(r) = I_o\exp(-2r^2/w^2)$, where w is the point where the power energy falls to e^{-2} of its axial value.

(Koechner [1976] provides a valuable reference of laser characteristics.) Assuming a Gaussian fall-off across the 2mm laser spot, the following intensity distributions Figs. 7.2.8.-7.2.9. were derived on the basis of measured profiles.

Feature Fitting

In matching physical features of scanned intensity distributions and Kirchoff theory prediction intensity distributions, we confront the same difficulties of interpretation as with the facet model. For instance, whilst the antisymmetric tip of the specular lobe is indisputably captured by the Kirchhoff model (c.f. Fig. 7.2.2. and 7.2.8.), the secondary diffraction features at the foot of the lobe are not matched so easily.

Table 7.2.2. presents, standard deviation, skewness and kurtosis of the one-dimensional wave theory intensity predictions, for defect free specimens, with those of intensity scan data. The accompanying scatter diagrams are shown in Figs. 7.2.10.-7.2.12.

One dimensional models are likely to be more successful when the surface texture has a definite lay, or when a linear-type defect such as a scratch or groove is present.

Scratch defects were examined at 10 degree and 30 degree incidence. With the scratch aligned at right angles to the incident laser beam two prominant lobes were present. If the scratch were parallel to the scratch on the other hand, a single central lobe was present with minor side lobes.

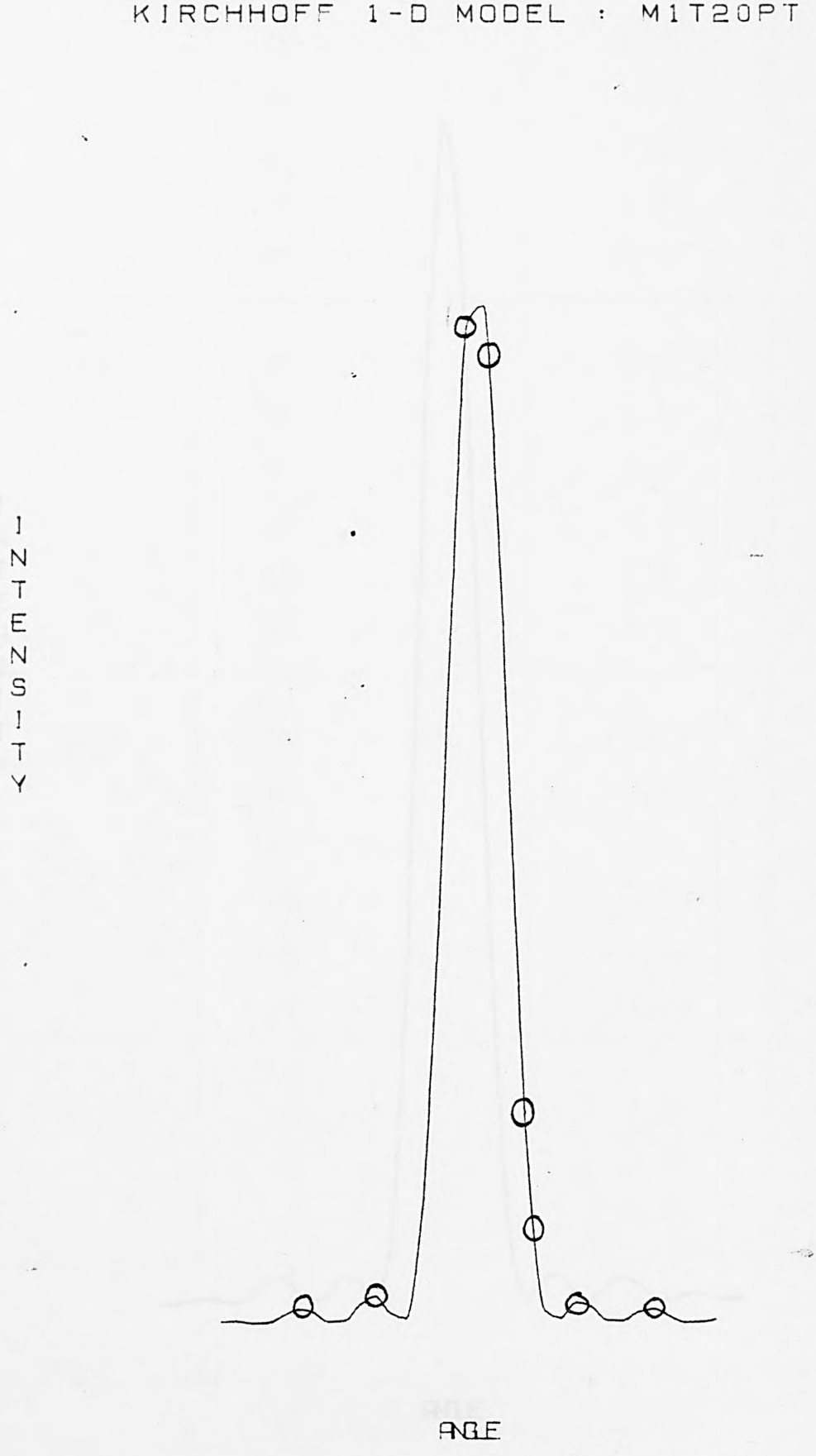

FIG. 7.2.8. Kirchhoff one-dimensional prediction model for specimen M1T2

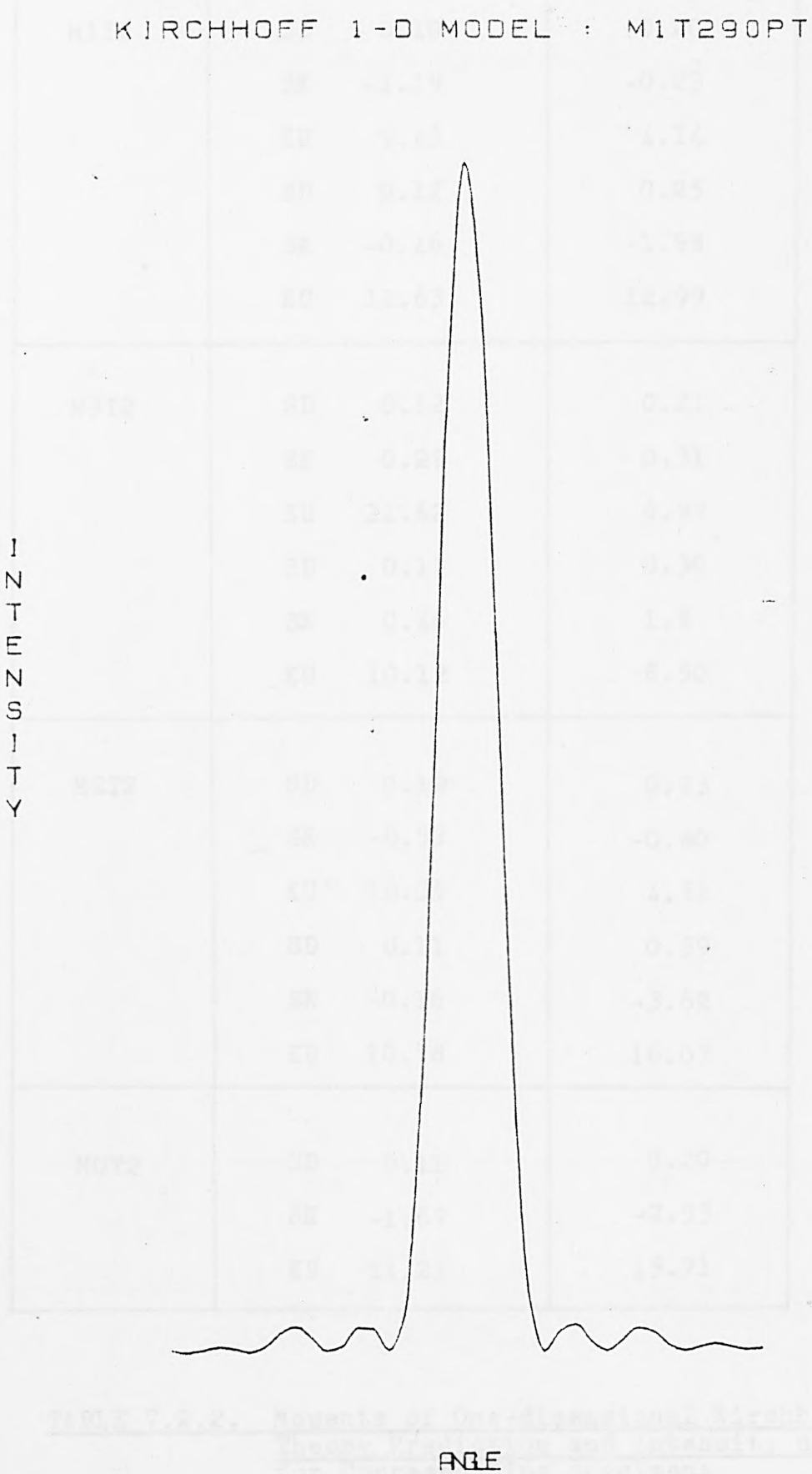

FIG. 7.2.9. Kirchhoff one-dimensional prediction model for specimen M1T2

Specimen	One Dimensional Kirchhoff Pred.		Intensity Statistics
M1T2	SD	0.10	0.20
	SK	-1.19	-0.23
	KU	9.45	4.14
	SD	0.12	0.25
	SK	-0.46	-1.98
	KU	12.63	12.99
M3T2	SD	0.12	0.21
	SK	0.29	0.31
	KU	11.62	6.99
	SD	0.13	0.30
	SK	0.46	1.8
	KU	10.12	8.50
M2T2	SD	0.10	0.23
	SK	-0.53	-0.80
	KU	10.35	4.32
	SD	0.11	0.59
	SK	-0.16	-3.62
	KU	10.78	16.07
M0T2	SD	0.11	0.20
	SK	-1.69	-2.53
	KU	11.23	15.71

TABLE 7.2.2. Moments of One-dimensional Kirchhoff Theory Prediction and Intensity plots, for Corresponding Specimens

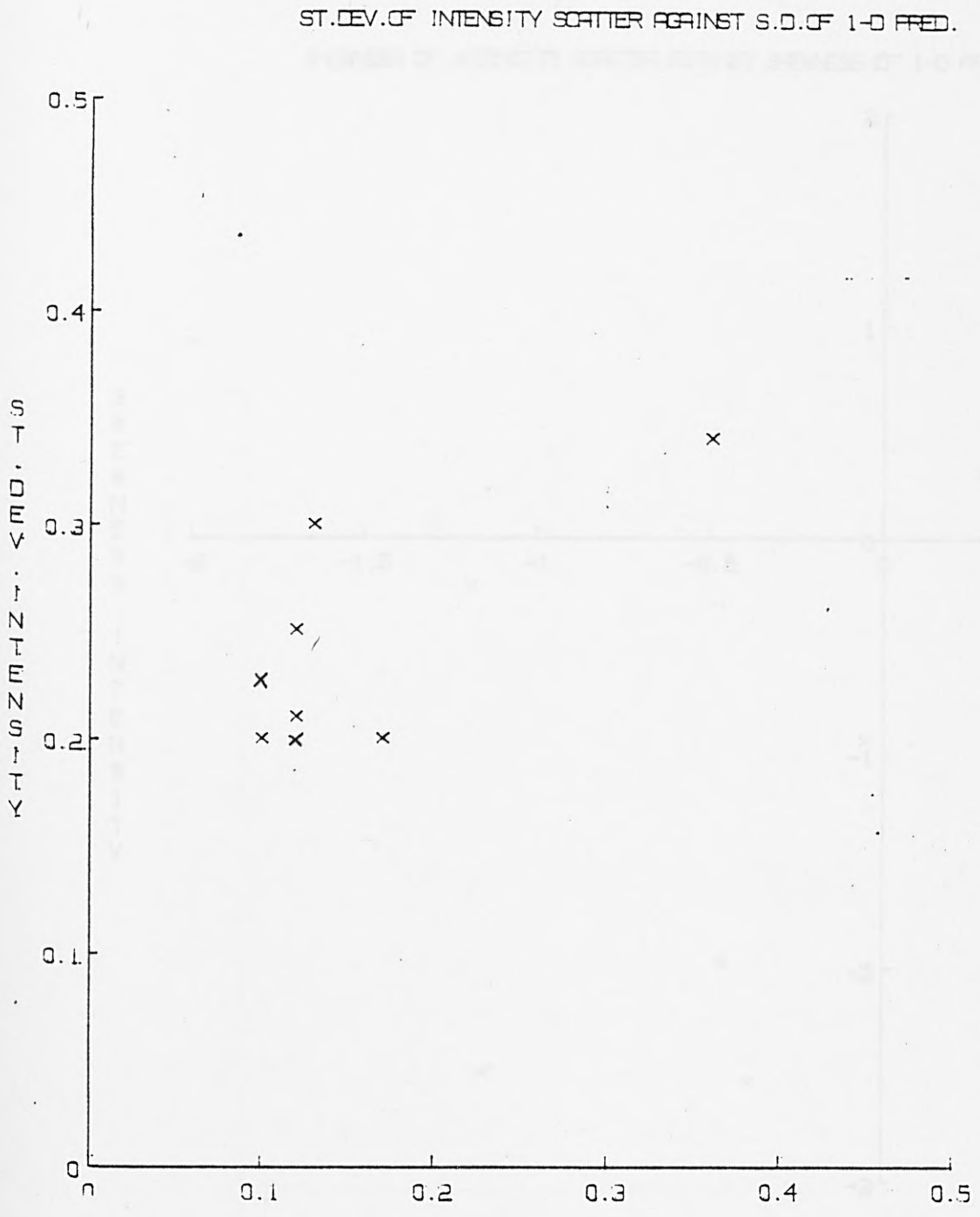

FIG. 7.2.10. Scatter diagram of st. dev. of intensity against st. dev. of Kirchhoff one-dimensional prediction model

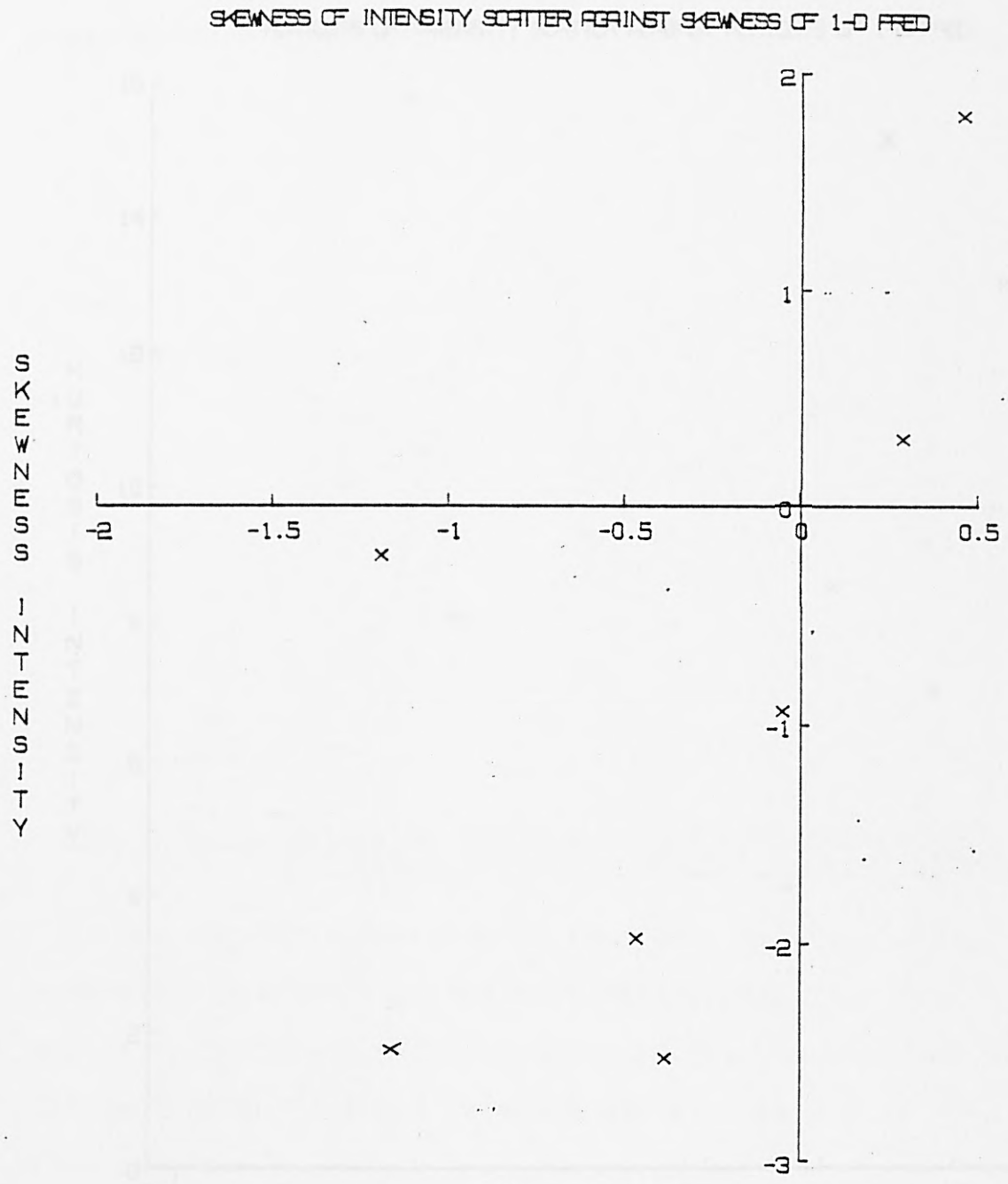

FIG. 7.2.11. Scatter diagram of skewness of intensity against skewness of Kirchhoff one-dimensional prediction model

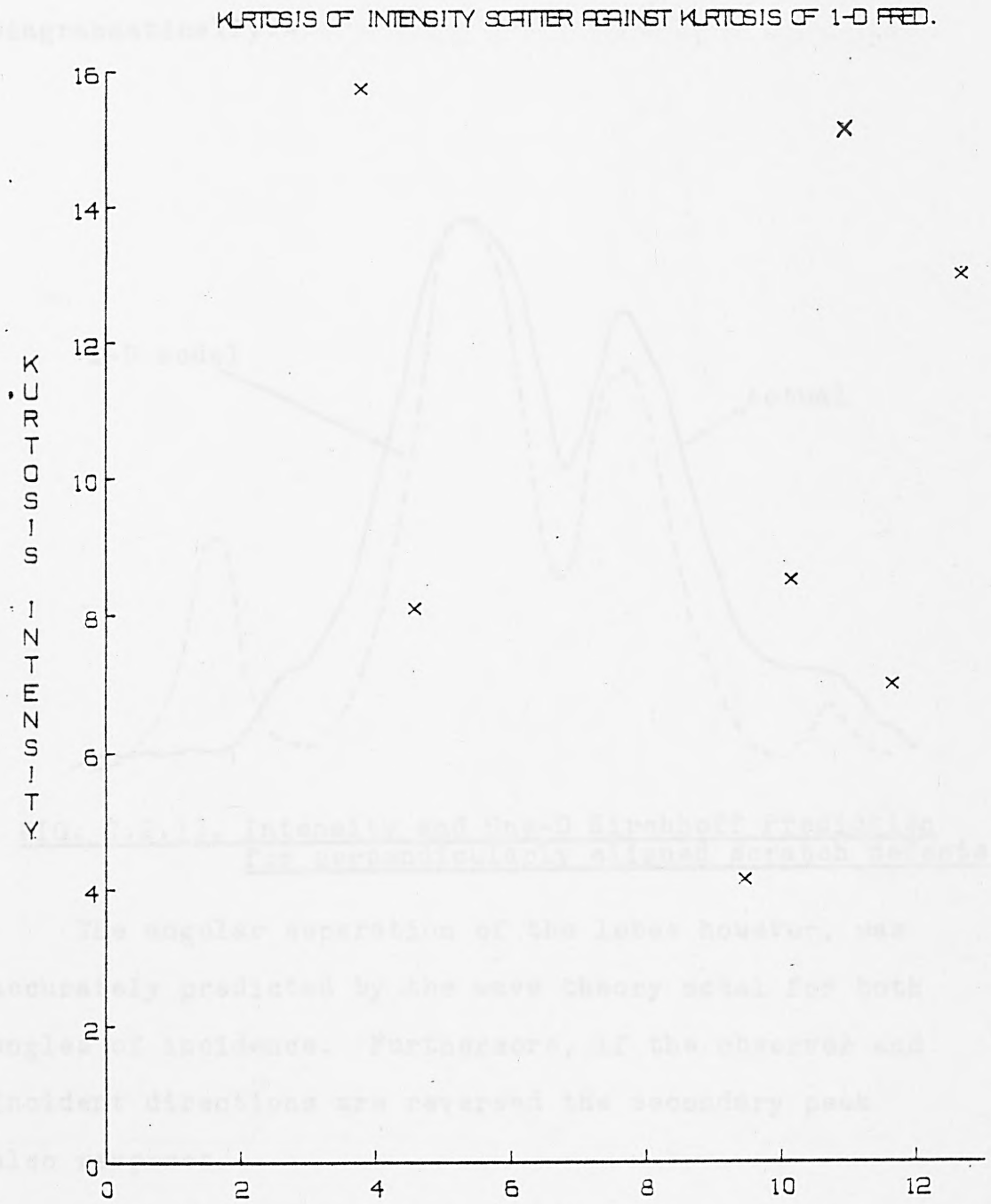

FIG. 7.2.12. Scatter diagram of kurtosis of intensity against kurtosis of Kirchhoff one-dimensional prediction model

In the case of the perpendicular alignment, the wave theory model predicted three major lobes, one central with two symmetrically placed off-central lobes. Diagrammatically:-

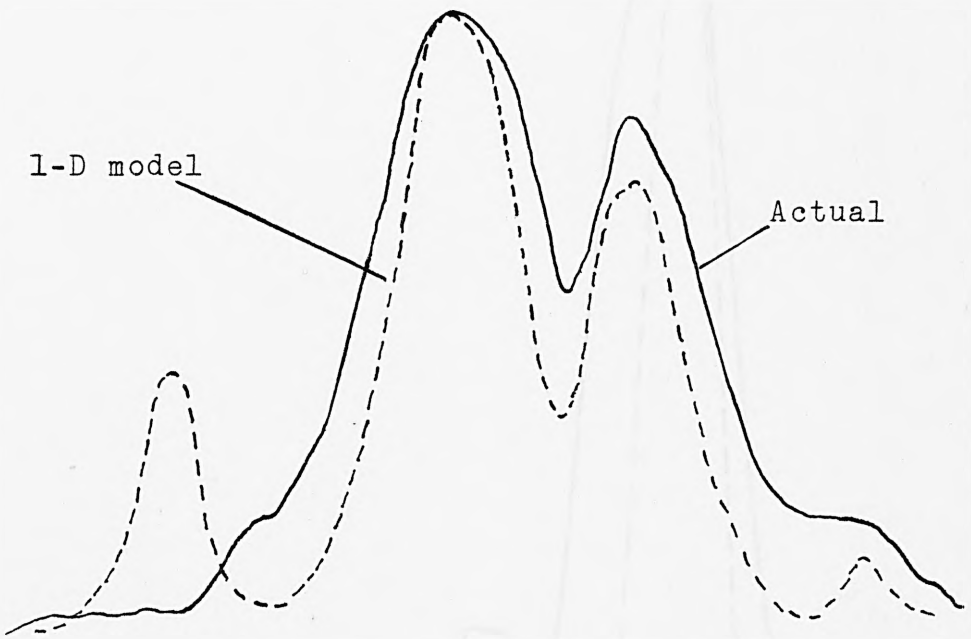

FIG. 7.2.13. Intensity and One-D Kirchhoff Prediction for perpendicularly aligned scratch defects

The angular separation of the lobes however, was accurately predicted by the wave theory model for both angles of incidence. Furthermore, if the observer and incident directions are reversed the secondary peak also reverses.

The model assumes that shadowing and secondary reflections do not occur, whereas in practice, particularly in the case of a severe scratch they do, and in consequence a major side lobe is suppressed.

For parallel alignment, the Kirchhoff wave theory model accurately predicted the angular separation of asymmetrically positioned secondary lobes.

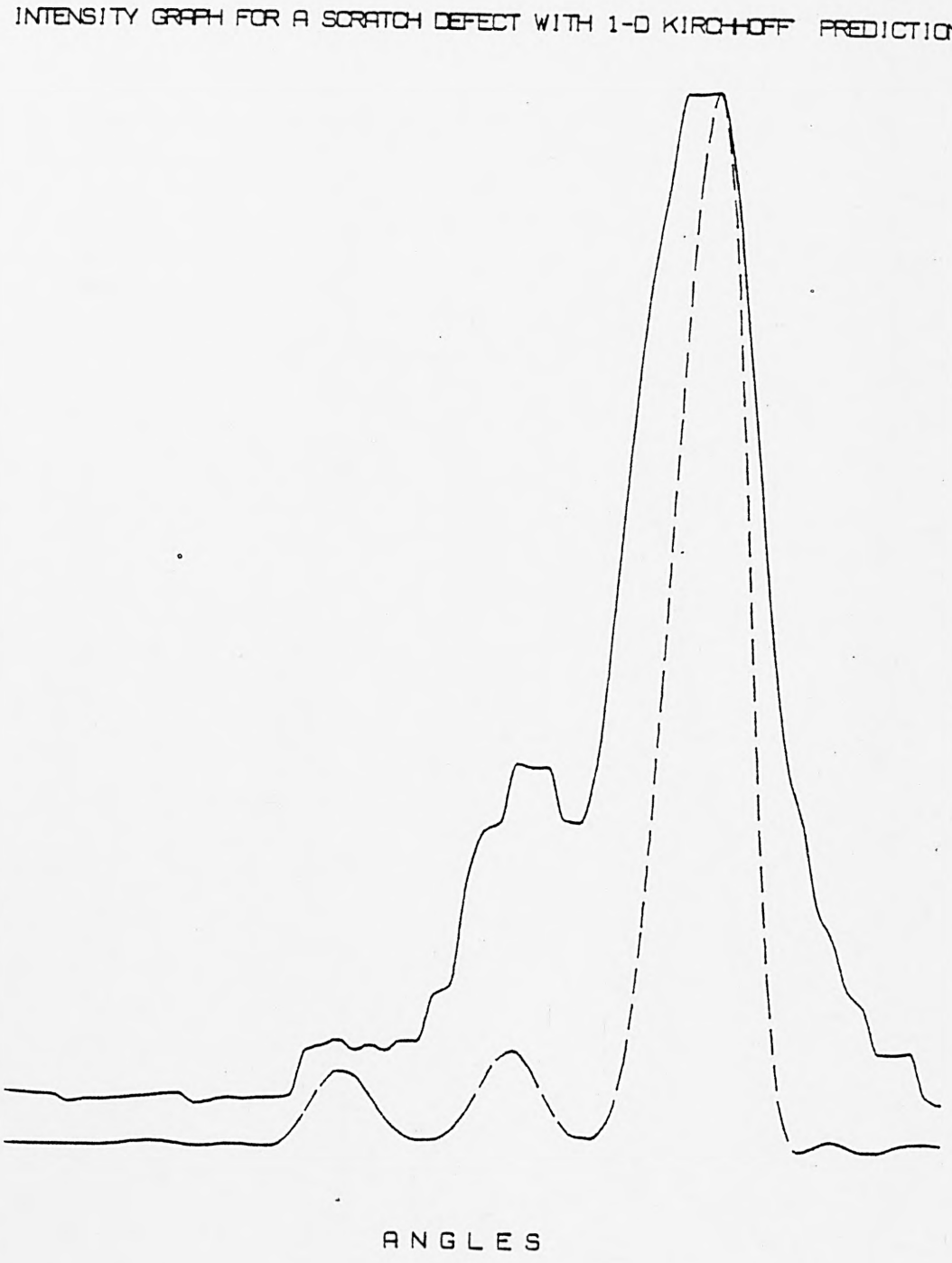

FIG. 7.2.14. Scratch defect specimen M2T4 scan 270°: Angle of incidence 30° (perpendicular alignment)

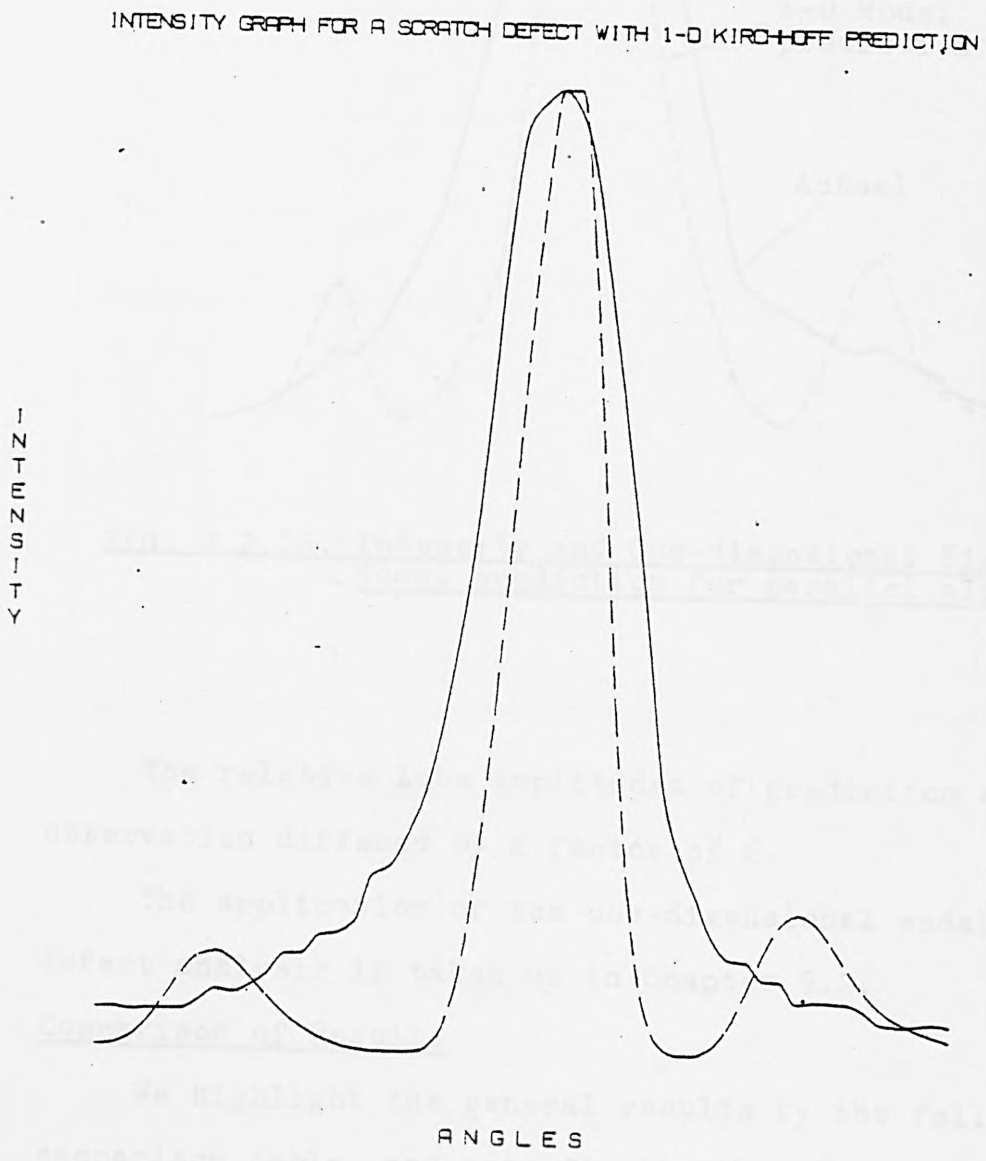

FIG. 7.2.15. Scratch defect specimen M2T4 scan 180°: angle of incidence 30° (parallel alignment)

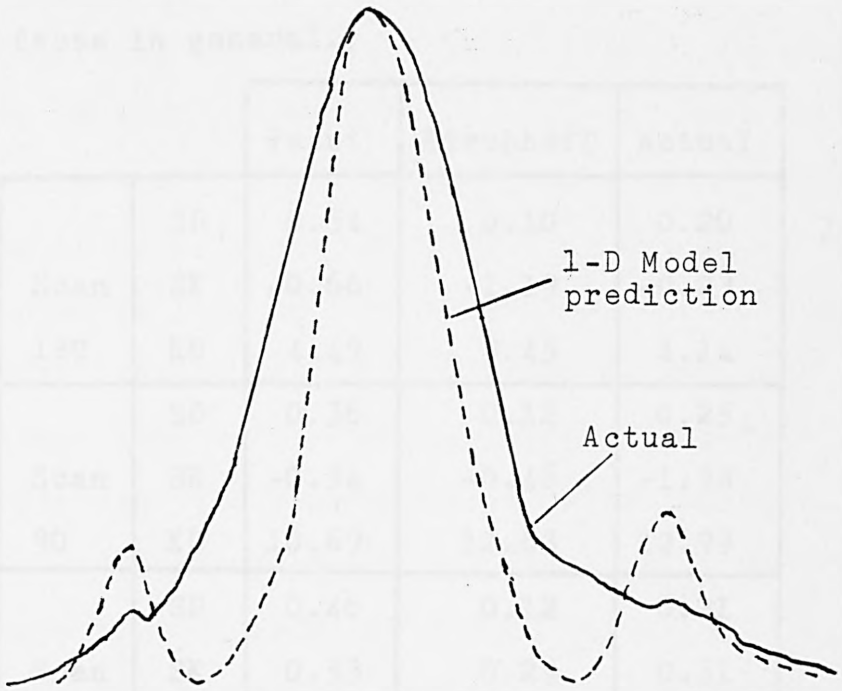

FIG. 7.2.16. Intensity and One-dimensional Kirchhoff Model prediction for parallel alignment

The relative lobe amplitudes of prediction and observation differed by a factor of 2.

The application of the one-dimensional model to defect analysis is taken up in Chapter 9.2.

Comparison of Results

We highlight the general results by the following comparison table, and note firstly that the two theoretical models are in close agreement with regard to skewness and kurtosis, which incidently supports the surmise of 7.2. With regard to the standard deviation however, the facet model predicts a scatter dispersion four times larger than that of the wave theory prediction. The observed scattering is in fact mid-way between the two predictions. (The slopes of

the regression lines of Figs. 7.2.5. and 7.2.10. testify to these facts in general.)

			Facet	Kirchhoff	Actual
M1T2	Scan 180	SD	0.54	0.10	0.20
		SK	-0.66	-1.19	-0.23
		KU	4.49	9.45	4.14
	Scan 90	SD	0.36	0.12	0.25
		SK	-0.34	-0.46	-1.98
		KU	10.69	12.63	12.99
M3T2	Scan 0	SD	0.46	0.12	0.21
		SK	0.53	0.29	0.31
		KU	11.66	11.62	6.99
	Scan 90	SD	0.75	0.13	0.30
		SK	0.37	0.46	1.8
		KU	10.45	10.12	8.50

TABLE 7.2.3. Comparison of Moment Statistics for Prediction Models and Data Scans

Comment has been made at length about the difficulties of slope measurement and the apparent failure of the facet model is primarily a failure of metrology.

The wave theory model is based on an analysis of a single profile, which presupposes that the surface has a two-dimensional roughness only. In the Longuet-Higgins model (c.f. Chapter 6) $\zeta' = \sqrt{\zeta'^2_x + \zeta'^2_y}$; this is equivalent to setting $\zeta'_y \equiv 0$ and we see at once that a two-dimensional analysis must underestimate the slope variance. Treating ζ'_x and ζ'_y as identical but independent random variables, the slope variance would double,

but for highly correlated ζ'_x and ζ'_y, the variance would quadruple and so would agree with observation. From the intensity modelling of 7.1, and from further work of Chapter 8, for a rough surface the intensity variance is proportional to g or σ^2. But σ_x^2 for a single scan is four to five times less than σ^2 based on an AREA measurement (c.f. Chapter 6) and thus three-dimensional surface topography scattering models may be entertained with some prospect of realising an adequate fit. Returning to the facet model and considering a typical scan (M1T2 scan 180 degrees); if scattering is geometrical and the facet and wave theory model are in accord.

$$\frac{\text{Predicted intensity variance by facet model}}{\text{Predicted intensity variance of Kirchhoff model}} = 1$$

Then $\dfrac{\text{Theoretical variance of slopes}}{\text{(Predicted intensity variance)}} = \dfrac{1}{4}$

But, $\dfrac{\text{Estimated variance of slopes}}{\text{(Predicted intensity variance)}} = 16$

$$\frac{\text{Estimated variance of slopes}}{\text{(True slope variance)}} = 64$$

$$\frac{\text{Estimated chord variance}}{\text{(True slope variance)}} = 100$$

Then $\dfrac{2\sigma_x^2\,[1 - C(2)]}{4} = 2\sigma_x^2\,\dfrac{0.024}{4}$

$= 100 \times 8\sigma_x^2/T_3^2$

$> T_3^2\ 2 \times 0.006 = 100 \times 8$

$> T_3 \sim 250\mu m$ which is the same order of magnitude as the T_3 values which emerged in 7.1 in the course of intensity modelling.

Prediction of the scattered field by an enhanced one-dimensional Kirchhoff wave theory model, which took into account the electrical properties of different materials was also carried out. The moments of the scatter distribution were virtually the same (within 1%) as those computed under the assumption of perfect conductability. This was so regardless of the surface material whether copper, brass or steel. The additional subroutine, determining the local reflectance etc. increased the computer processing time by a factor of 10 and could now be happily discarded. Our conclusion concurs with the generally held view, that the roughness of a surface modifies the scattered field to a much greater extent than does its electrical properties.

7.2.2. Two Dimensional Models

For a perfectly conducting two-dimensionally rough surface,

$$\rho(\theta_2) = \frac{F_3}{A} \iint_A e^{i\underline{v}\cdot\underline{r}}\, dx\, dy \qquad \ldots.(21)$$

From which we obtain

$$\rho\rho^* = \frac{F_3^2}{A^2} \iiiint_A e^{iv_x(x_1-x_2) + iv_y(y_1-y_2) + iv_z(\zeta_1-\zeta_2)} dx_1 dx_2 dy_1 dy_2 \qquad \ldots.(22)$$

Taking mean values we have

$$E(\rho\rho^*) = \frac{F_3^2}{A^2} \iiiint_A e^{iv_x(x_1-x_2) + iv_y(y_1-y_2)} E\left[e^{iv_z(\zeta_1-\zeta_2)}\right] dx_1 dx_2 dy_1 dy_2$$

$$= \frac{F_3^2}{A^2} \iiiint_A e^{iv_x(x_1-x_2) + iv_y(y_1-y_2)} \chi_2(v_z, -v_z) dx_1 dx_2 dy_1 dy_2 \qquad \ldots.(23)$$

For Type (C) surfaces the mean scattered field is given by the fourth order integral of (22) above.

Again, only for near neighbours (x_1, y_1), (x_2, y_2), separated by a small distance τ, will there be a significant contribution; a fact which brought the computer processing time to within a tolerable limit. The Gaussian beam characteristics were again included.

An adequate fit for Type (C) surfaces was obtained, even on the basis of only two adjacent parallel traces. This is significant since the height variance had remained constant over the two traces. Thus the underlying cause of the inadequacy of one-dimensional models, was not the enlarged global variances of surface heights, and we must look beyond the first order surface statistics. The extra 'degree of freedom' of a three-dimensional surface introduced a greater degree of variation in surface slopes and modification in the second order surface statistics. Two adjacent traces represented a 1/50th sample of the illuminated area A.

The model fit is close enough for a point-by-point comparison to be made. For illustration, the two-dimensional Kirchhoff model prediction data on two parallel profiles for the rolled steel specimen MOT2, together with actual scan data from the same specimen, are presented in Table 7.2.4. Comparisons can be drawn with the corresponding prediction, based on full area information, contained in the same table. Area predictions for Type (C) specimens and actual intensity data are further tabled in Appendix 7, together with their accompanying graphs. The prediction and scan data are taken with the rolling direction. The surfaces illu-

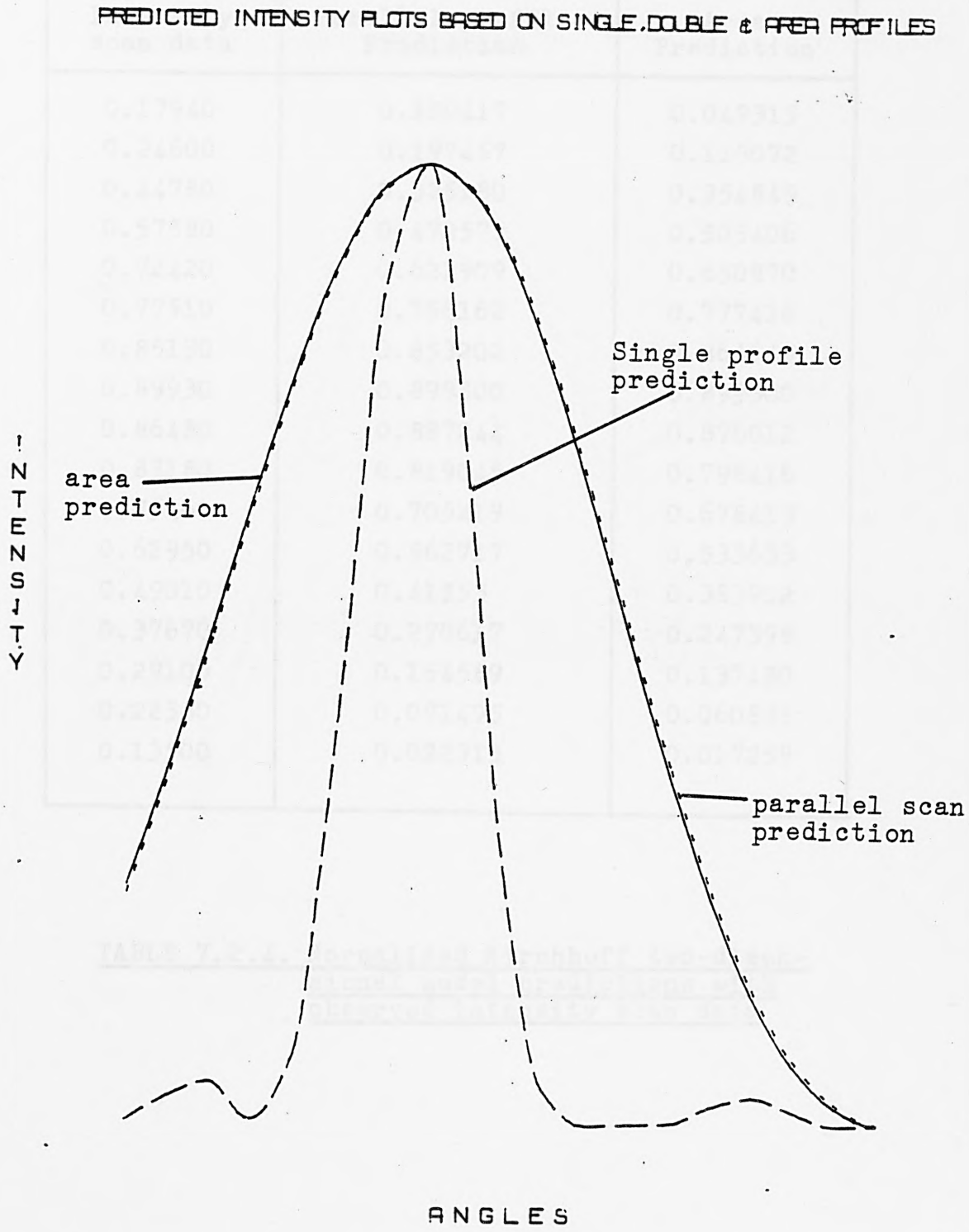

FIG. 7.2.17. Predicted intensity plots, based on single and double profiles, and area information (specimen MOT2)

SPECIMEN MOT2

Intensity scan data	Parallel profile Prediction	Area Prediction
0.17940	0.100417	0.049315
.0.24600	0.197457	0.119072
0.44780	0.325180	0.354849
0.57580	0.472577	0.503406
0.72420	0.622909	0.650870
0.77510	0.756162	0.777416
0.85130	0.853202	0.864645
0.89930	0.899300	0.899300
0.86480	0.887244	0.876012
0.83180	0.819045	0.798416
0.73460	0.705219	0.678413
0.62950	0.562717	0.533633
0.49010	0.41553	0.383902
0.37670	0.270617	0.247398
0.29100	0.154589	0.137480
0.22380	0.071495	0.060835
0.13500	0.022315	0.017259

TABLE 7.2.4. Normalised Kirchhoff two-dimensional model predictions with observed intensity scan data

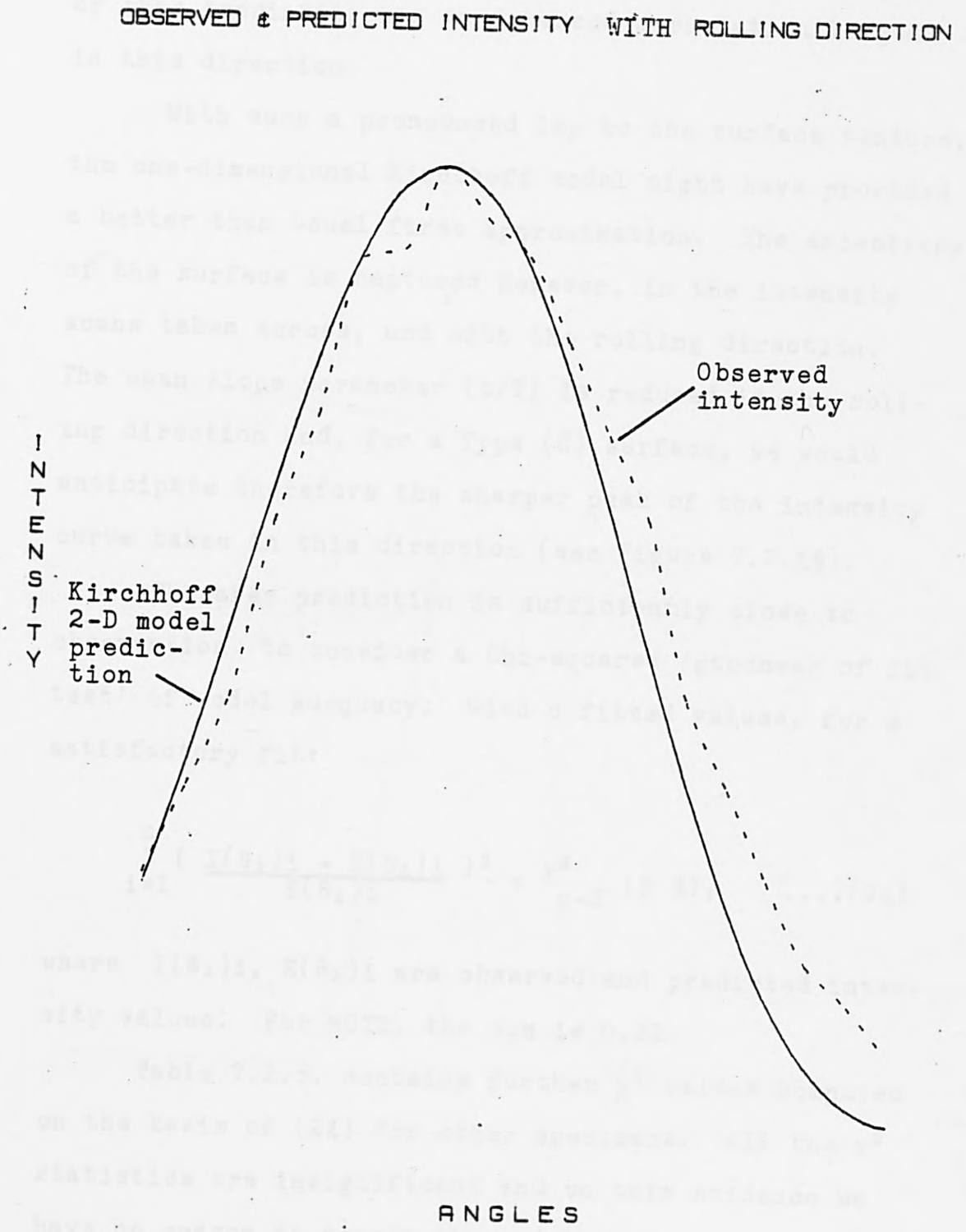

FIG. 7.2.18. Observed and predicted intensity graph for specimen MOT2 taken in the rolling direction

strated in Chapter 6 (Figs. 6.2.8. and 6.2.17.), was strongly anisotropic, with the roller surface texture imprinted along the direction of rolling. An effect of this imprinting was an enhanced correlation length in this direction.

With such a pronounced lay to the surface texture, the one-dimensional Kirchhoff model might have provided a better than usual first approximation. The anisotropy of the surface is captured however, in the intensity scans taken across, and with the rolling direction. The mean slope parameter (σ/T) is reduced in the rolling direction and, for a Type (C) surface, we would anticipate therefore the sharper peak of the intensity curve taken in this direction (see Figure 7.2.19).

The area prediction is sufficiently close to observation to consider a Chi-squared 'goodness of fit test' of model adequacy. With n fitted values, for a satisfactory fit:

$$\sum_{i=1}^{n} \left\{ \frac{I(\theta_2)i - E(\theta_2)i}{E(\theta_2)i} \right\}^2 < \chi^2_{n-2} \ (5\ \%), \qquad \ldots.(24)$$

where $I(\theta_2)i$, $E(\theta_2)i$ are observed and predicted intensity values. For MOT2, the sum is 0.22.

Table 7.2.5. contains further χ^2 values computed on the basis of (24) for other specimens. All the χ^2 statistics are insignificant and on this evidence we have no reason to reject the model.

N.B. The χ^2 values cannot be interpreted in the usual way since the test is formally calculated on <u>frequency</u> count data based on <u>independent</u> samples.

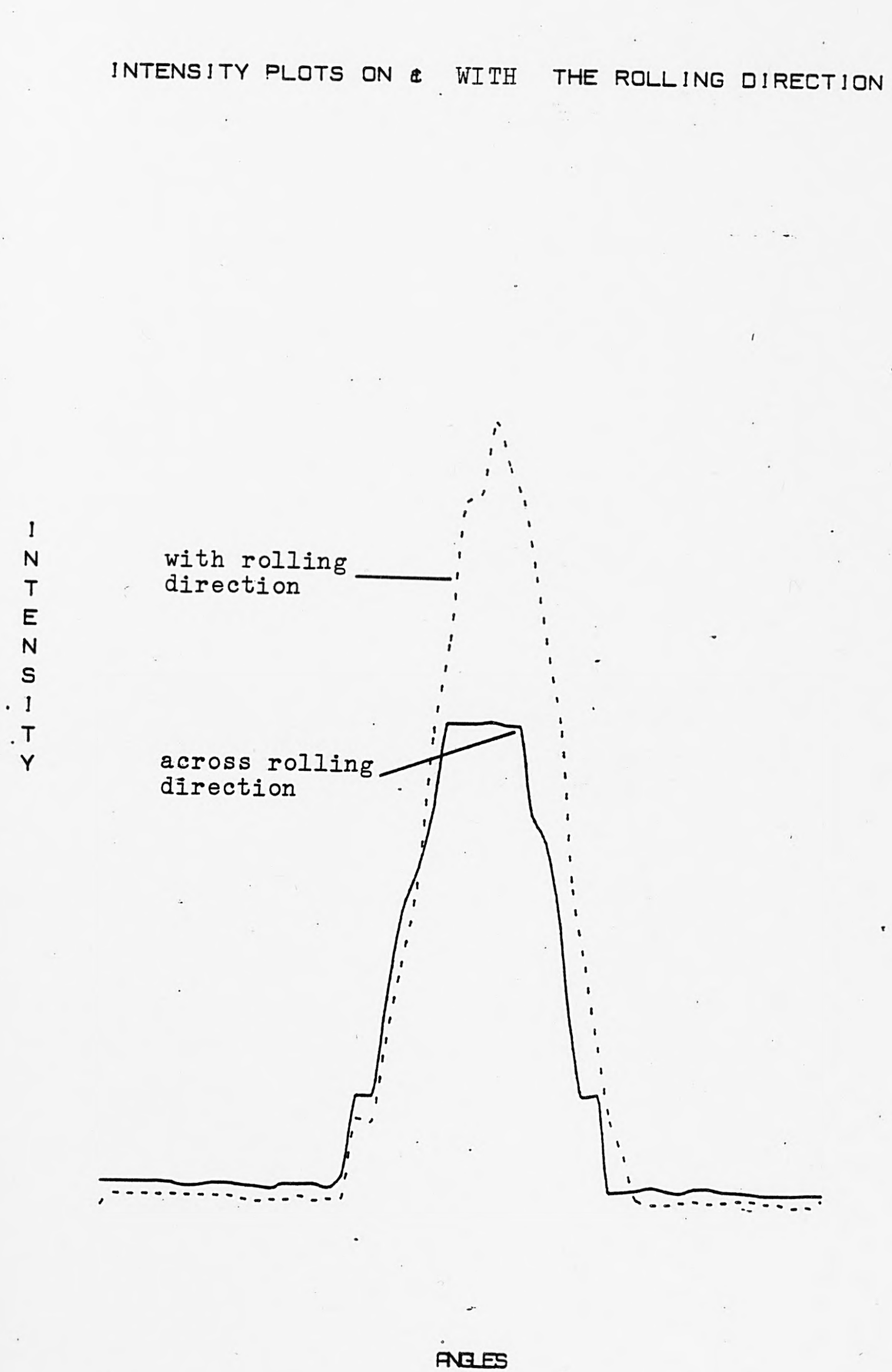

FIG. 7.2.19. Intensity plots across and with the rolling direction, for cold rolled specimen M0T2

Milana and Rasello [1981] compute 'χ^2' values as a measure of support for appropriate autocorrelation models, but do not give details of the computations.

Specimen	χ^2	No. of points
M0T2	0.22	17
M1T2	0.02	18
M3T2	0.08	21
M1T1	0.10	22

TABLE 7.2.5. Chi-squared values for closeness of fit of area predictions

7.3 Conclusions

Qualitatively, slope distributions and intensity curves do match, demonstrating that the scattering mechanism is predominantly geometric. Moreover, quantitatively, there is close agreement with regard to the overall shape. The degree of peakedness, measured by the kurtosis of the slope profiles is mirrored in the intensity plots, moreover deviations in the lobe symmetry (given by the direction and magnitude of the skewness) is attributable in large measure to skewness in the slope distribution. Where there is marked disagreement, is in the degree scattering.

For the facet model, the problem is partly one of any numerical technique for the process of differentiation. In contrast the integral formulation of the Kirchhoff model enjoys the inherent stability of an integration process.

The predictive power of the Kirchhoff wave theory model is remarkable, not least in view of the restrictive nature of the approximations imposed in its formulation, (the surface should contain no sharp edges, multiple scattering is ignored, etc.), but also because of the coarseness of the sampling grid, and that the predicted intensity distribution is for the far field , Fraunhofer zone of diffraction. The prediction applies to a particular viewing direction and not to the field captured by a finite aperture. The scanning diode surveyed the scattered field at a distance of 12 cms from the surface, which had the merit of stable intensity readings, but was of the order of ten times too close to sense the far field. (Strictly speaking we should calculate the intensity at a point, not in a direction, on the basis of spherical scattered waves

and not plane ones.) For the Fraunhofer linear approximation to hold, we require that $d >> \frac{D^2}{4\lambda}$ ....(25) with d, D, λ as defined below. Equation (25) is adapted from (33) p.384 Born and Wolf [1965].

Since speckle has the characteristics of a 0/1 binary phenomenon, it is desirable to capture several speckles within the viewing aperture, in order to smooth out intensity variations. The Rayleigh criterion:

$$Rsp = \frac{0.61\lambda d}{D}, \qquad ....(26)$$

gives the speckle radius, Rsp, where λ and D are the wavelength and diameter of the laser beam, and d is the distance of the detector from the surface, when no imaging system is used (c.f. Goodmann [1975]). Formula (26) is modified for a Gaussian profile laser operating in TM00 mode to

$$Rsp = \frac{0.61\lambda d}{D_e} \qquad ....(27)$$

D_e is the diameter of laser beam at 1/e points.

(c.f. Dainty [1976]).

For our rig d = 12 cms, D = 1 mm, λ = 628^{o}A, which implies Rsp $\sim 5 \times 10^{-2}$ mm. Thus the scanning transducer output is an average over some 400 speckles. For scratch defects the one-dimensional theory provided partial, but nevertheless useful, information.

If we base a wave theory prediction on area information, albeit only on two parallel profiles, there is immediately an adequate fit with observed intensity scans. The standard deviation increases by a factor of 2 from the one-dimensional model and agrees with observation. Over two traces the height variance is not appreciably different from estimates of height variances taken on the individual profiles. This suggests that the overall variation of

heights is important in determining the absolute value of intensity, but that the individual facet slopes determine the scatter dispersion for strong scatters, and, moreover, that a single profile is an inadequate determinant of slope statistics. The rough surfaces examined ought to be viewed as two-dimensional stochastic processes for purposes of signal processing.

APPENDIX 7

Kirchhoff Prediction and Intensity Scan Data: Tables and Graphs

Intensity scan data	Double profile prediction	Area Prediction
0.04060	0.049350	0.047769
0.06020	0.074964	0.073238
0.08030	0.103764	0.101989
0.12020	0.133200	0.131477
0.14400	0.160282	0.158814
0.17970	0.182036	0.180944
0.18160	0.195925	0.195319
0.20030	0.200300	0.200300
0.18840	0.194631	0.195263
0.18010	0.179621	0.180887
0.16060	0.157043	0.158814
0.14000	0.129522	0.131703
0.11600	0.100048	0.102442
0.08050	0.071558	0.073917
0.06070	0.046512	0.048674
0.04020	0.026575	0.028412
0.02140	0.012489	0.013810
0.01250	0.004087	0.004867

TABLE 7.A.1. Prediction and observed intensity data for specimen M1T2

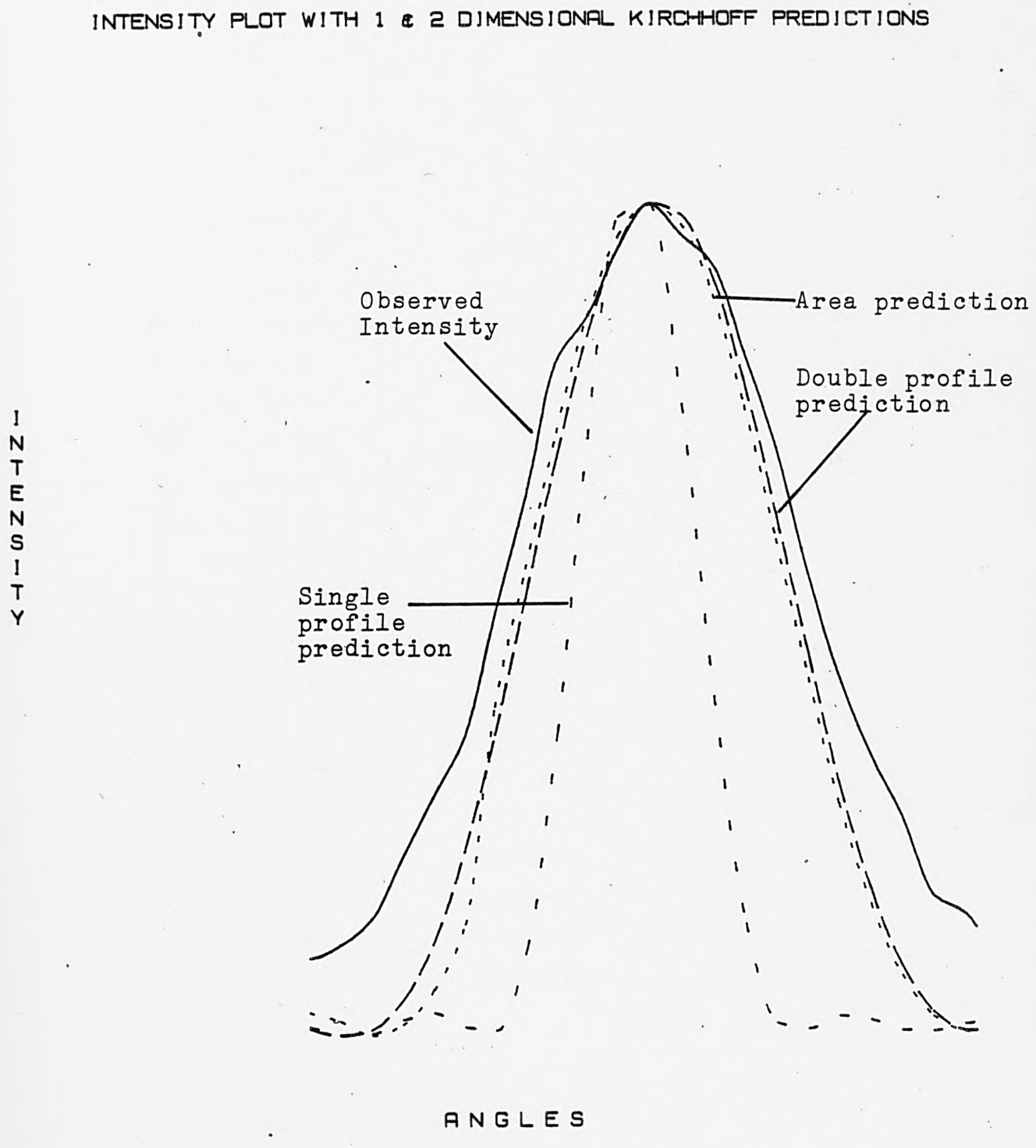

FIG. 7.A.1. Plots of observed intensity scan with Kirchhoff predictions: specimen M1T2

Intensity scan data	Kirchhoff area prediction
0.10280	0.02128
0.13360	0.06750
0.18380	0.09204
0.27010	0.25934
0.39030	0.40280
0.56210	0.56754
0.72950	0.73973
0.89440	0.90269
1.00790	1.03884
1.12500	1.13274
1.17360	1.17360
1.12470	1.15643
1.11610	1.08358
1.03660	0.96358
0.91320	0.81049
0.73570	0.64094
0.56410	0.47231
0.42620	0.31938
0.32440	0.19332
0.22370	0.09988
0.14300	0.03969

TABLE 7.A.2. Kirchhoff area prediction and observed intensity data for specimen M3T2

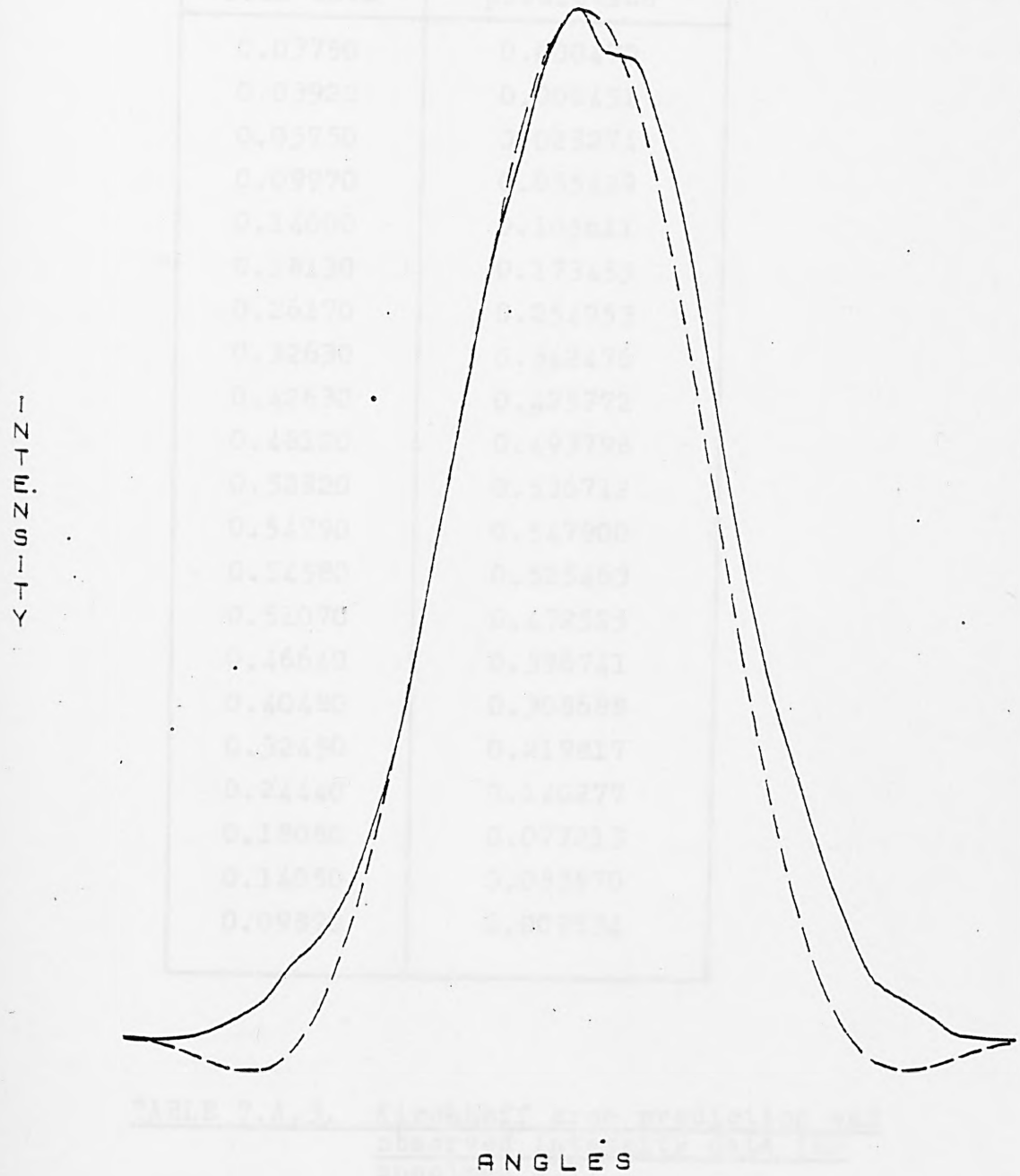

FIG. 7.A.2. Plot of observed intensity scan with Kirchhoff area prediction: specimen M3T2

Intensity scan data	Kirchhoff area prediction
0.03750	0.000470
0.03920	0.006451
0.05750	0.023274
0.09970	0.055429
0.14000	0.105611
0.18130	0.173453
0.26170	0.254953
0.32630	0.342476
0.42630	0.425772
0.48120	0.493798
0.52820	0.536712
0.54790	0.547900
0.54580	0.525463
0.51070	0.472525
0.46640	0.396741
0.40480	0.308688
0.32450	0.219817
0.24440	0.140277
0.18080	0.077213
0.14050	0.033870
0.09870	0.009534

TABLE 7.A.3. Kirchhoff area prediction and observed intensity data for specimen M1T1

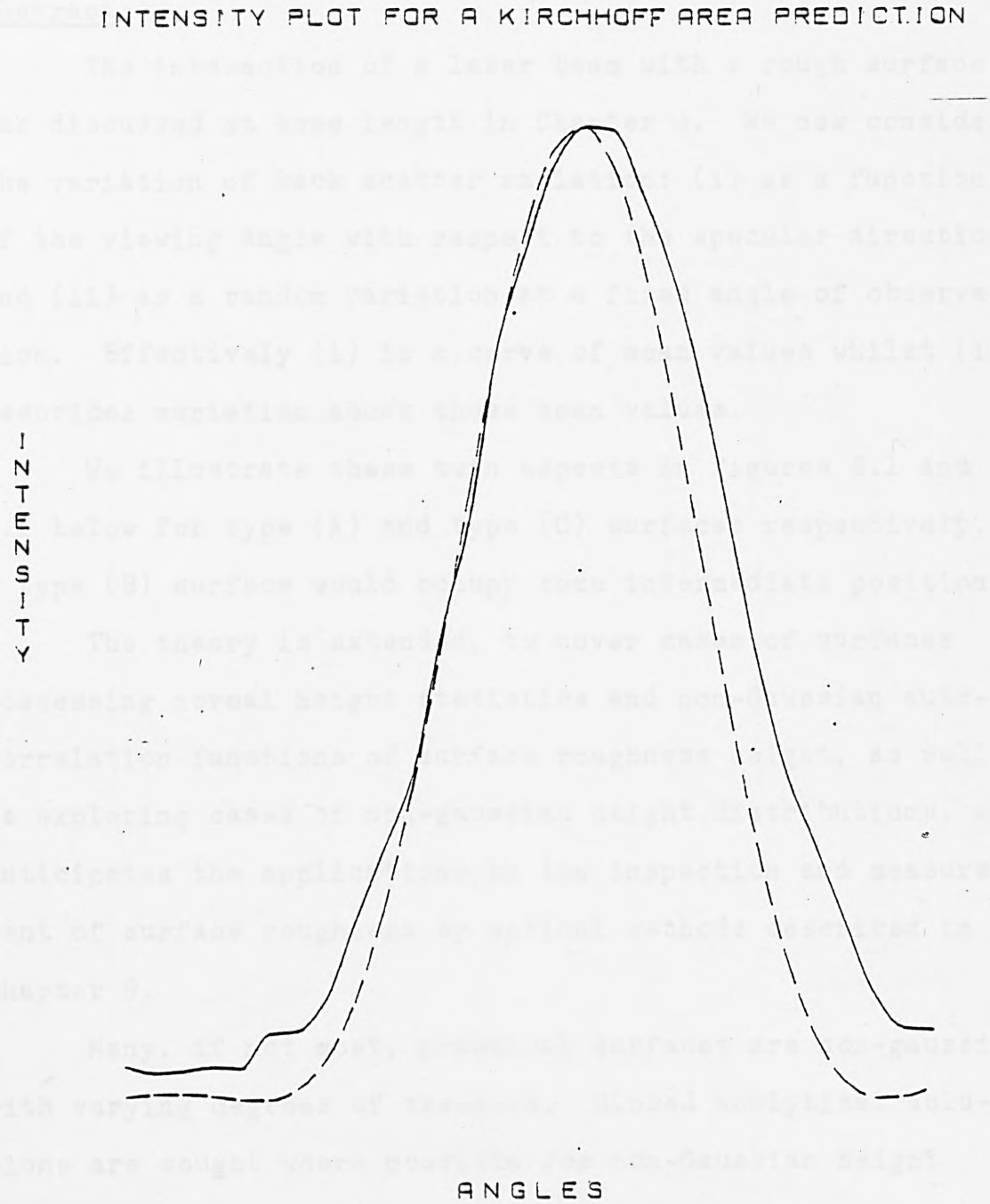

FIG. 7.A.3. Plot of observed intensity scan with Kirchhoff area prediction: specimen M1T1

CHAPTER 8

INTENSITY SCATTER DISTRIBUTIONS: SOME COMPARISONS WITH THEORY AND EXPERIMENT

Abstract

The interaction of a laser beam with a rough surface was discussed at some length in Chapter 4. We now consider the variation of back scatter radiation: (i) as a function of the viewing angle with respect to the specular direction, and (ii) as a random variation at a fixed angle of observation. Effectively (i) is a curve of mean values whilst (ii) describes variation about those mean values.

We illustrate these twin aspects in figures 8.1 and 8.2 below for type (A) and type (C) surfaces respectively. A type (B) surface would occupy some intermediate position.

The theory is extended, to cover cases of surfaces possessing normal height statistics and non-Gaussian auto-correlation functions of surface roughness height, as well as exploring cases of non-gaussian height distributions, and anticipates the applications to the inspection and measurement of surface roughness by optical methods described in Chapter 9.

Many, if not most, practical surfaces are non-gaussian with varying degrees of skewness. Closed analytical solutions are sought where possible for non-Gaussian height distributions, with a view to resolving the question of robustness of parameter estimates at a later stage.)

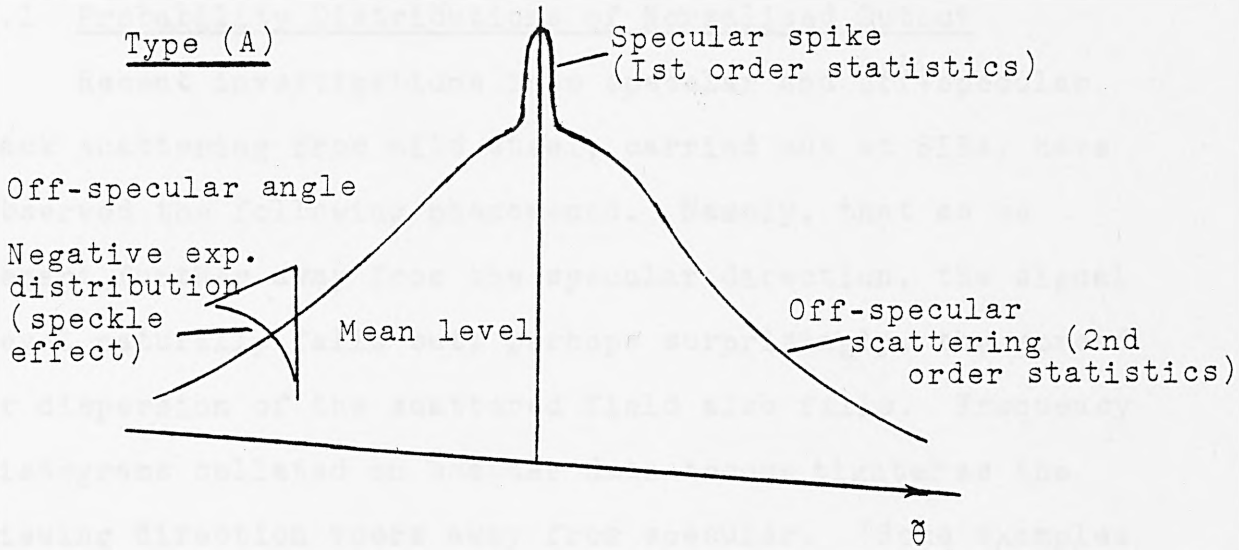

FIG. 8.1 Scattering from Type (A) very smooth surfaces

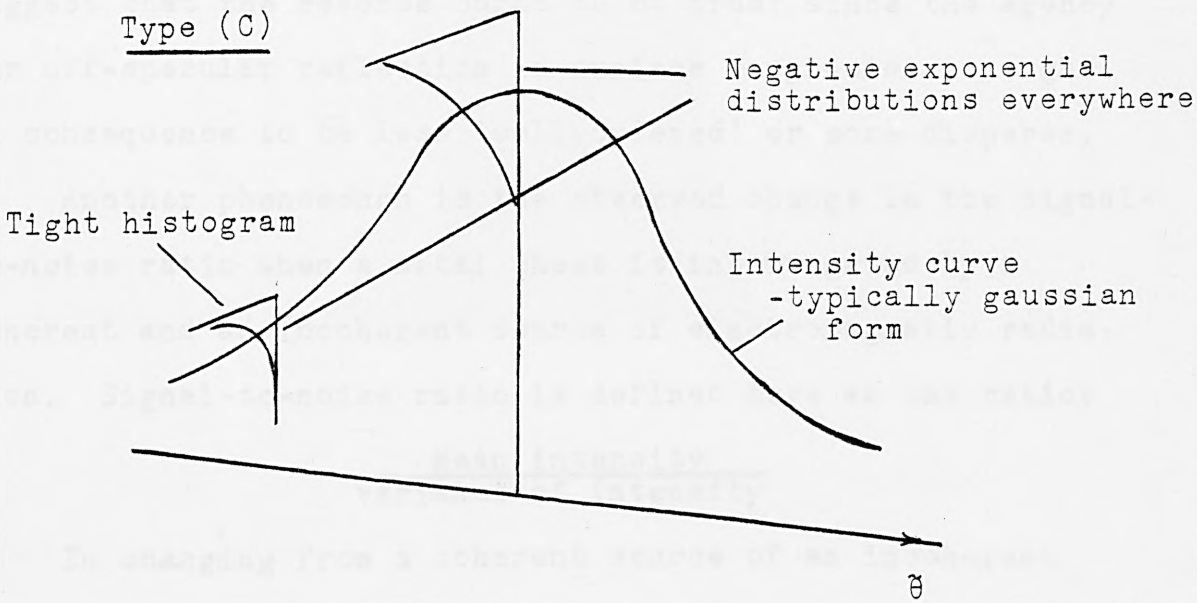

FIG. 8.2 Scattering from Type (C) very rough surfaces

8.1 Probability Distributions of Normalised Output

Recent investigations into specular and off-specular back scattering from mild steel, carried out at SIRA, have observed the following phenomenon. Namely, that as we depart further away from the specular direction, the signal level naturally falls but, perhaps surprisingly, the spread or dispersion of the scattered field also falls. Frequency histograms collated on scatter data become tighter as the viewing direction veers away from specular. (Some examples of which are reproduced in figures 8.1.1-8.1.3.) Indeed, the data has most variation at the specular angle when even bimodal distributions were encountered, although this feature was due to the fact that those particular test pieces were not flat. The observations are surprising to those unfamiliar with speckle theory since intuition might suggest that the reverse ought to be true: since the agency for off-specular reflection is surface roughness, it ought in consequence to be less 'well-ordered' or more disperse.

Another phenomenon is the observed change in the signal-to-noise ratio when a metal sheet is interrogated by a coherent and an incoherent source of electromagnetic radiation. Signal-to-noise ratio is defined here as the ratio:

$$\frac{\text{Mean intensity}}{\text{variance of intensity}}$$

In changing from a coherent source of an incoherent source, it is found that the signal-to-noise ratio of the back scattered radiation increases by a factor of 2 Norton-Wayne [1982].

An explanation of these phenomena is sought by the application of the beam scattering models of Chapter 4, adopting, where appropriate, the approach of Beckmann and

COLD ROLLED STEEL STRIP

HISTOGRAM OF SAMPLE LEVELS

MODAL LEVEL IS:- 154

MODE CELL CONTAINS 3732 SAMPLES.

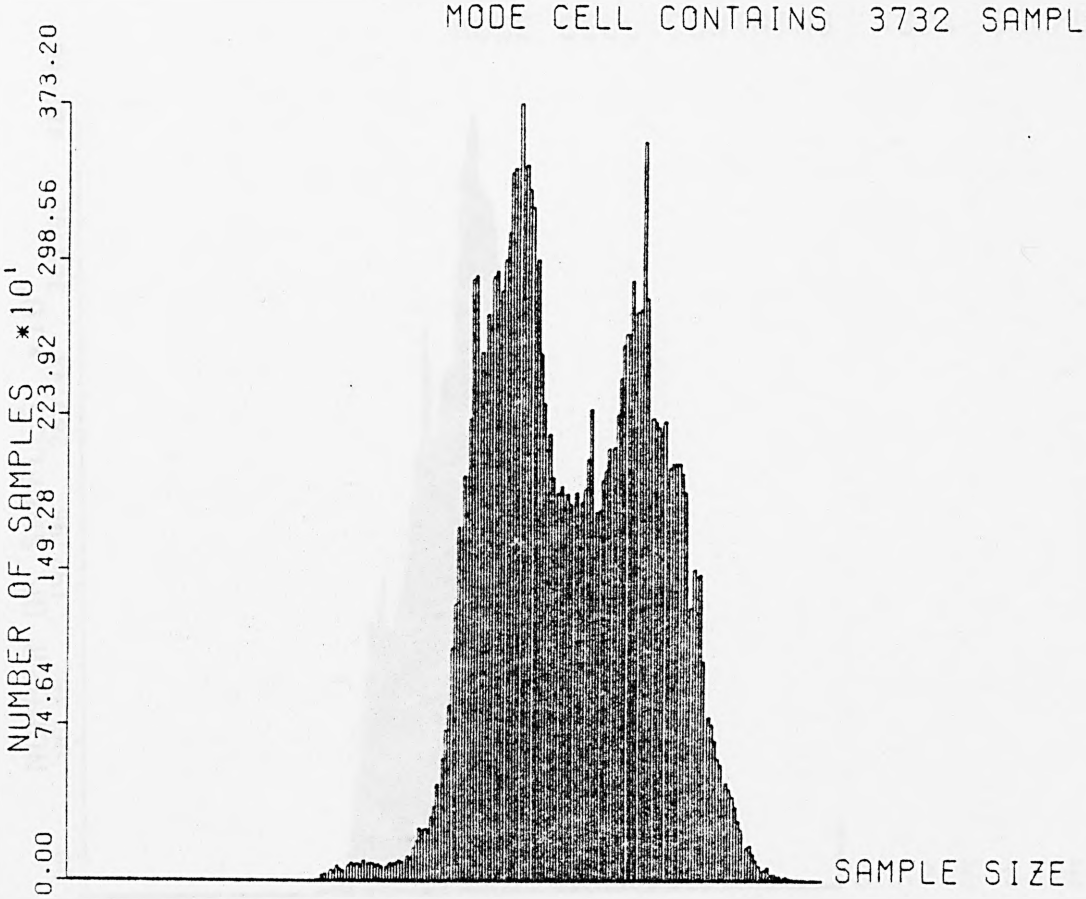

C16.08 DEFECT TYPE:- ROLL MARKS

PROCESSING:- NONE

DETECTOR:-SPECULAR

FIG. 8.1.1. Bimodal Scattering in the Specular Direction

COLD ROLLED STEEL STRIP

HISTOGRAM OF SAMPLE LEVELS

MODAL LEVEL IS:-134

MODE CELL CONTAINS 4824 SAMPLES.

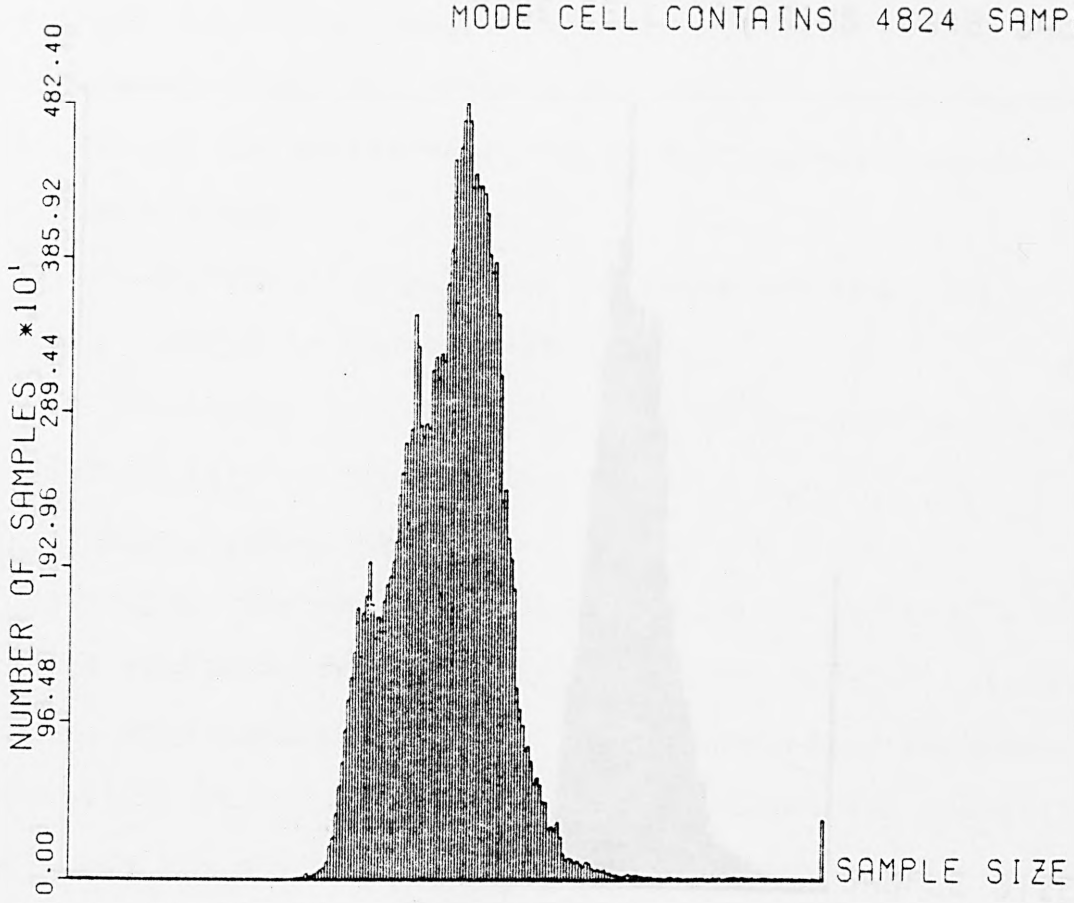

C16.08 DEFECT TYPE:- ROLL MARKS

PROCESSING:- NONE

DETECTOR:-5 DEG OFF-SPEC

FIG. 8.1.2. Off-Specular Scattering Tending Towards Negative Exponential

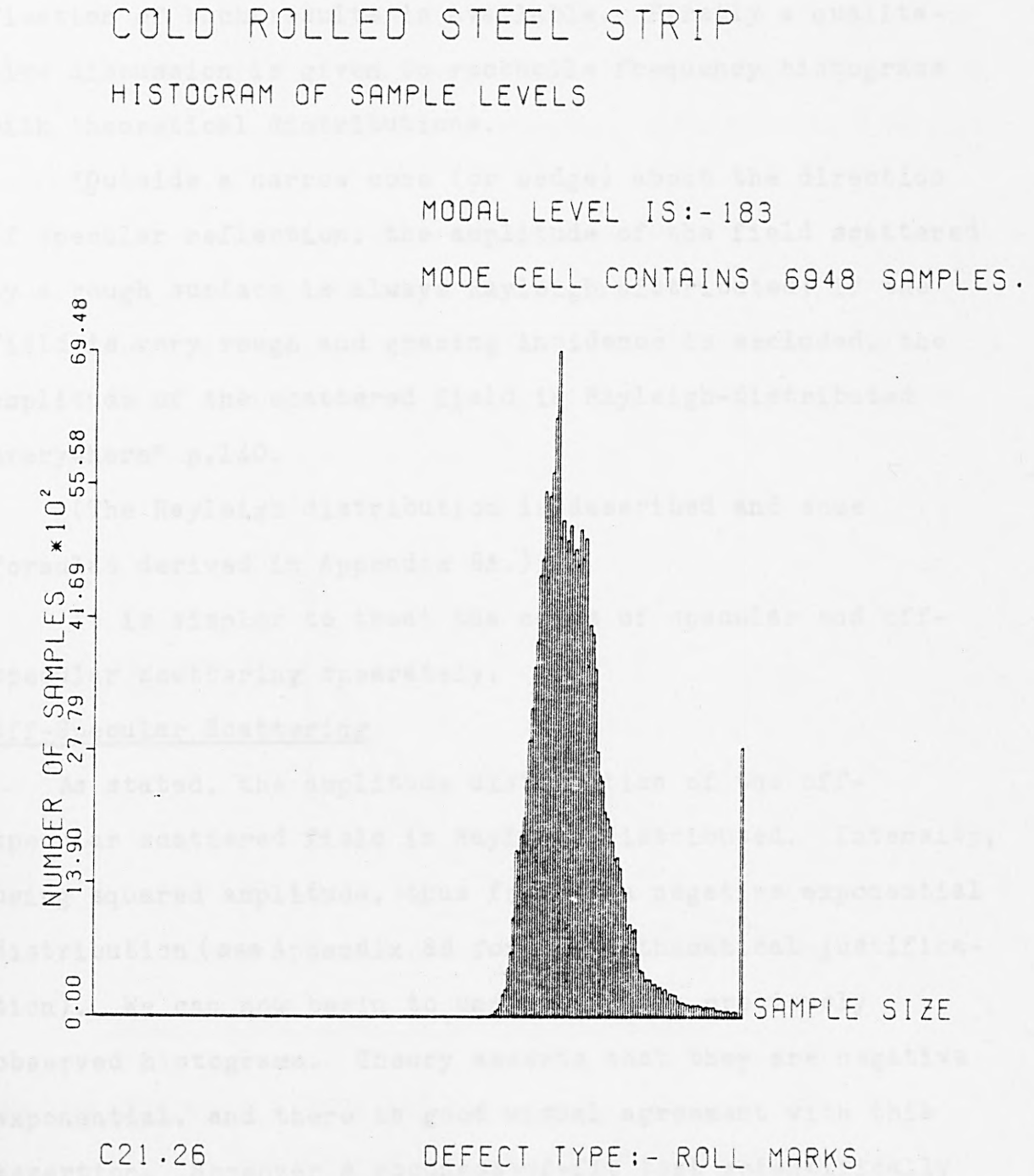

FIG. 8.1.3. Tight Negative Exponential Distribution of Off-Specular Scattering

Spizzichino [1963]. Page references are to their book where the quoted equations may be found and further justification of such results is available. Firstly a qualitative discussion is given to reconcile frequency histograms with theoretical distributions.

"Outside a narrow cone (or wedge) about the direction of specular reflection, the amplitude of the field scattered by a rough surface is always Rayleigh distributed; if the field is very rough and grazing incidence is excluded, the amplitude of the scattered field is Rayleigh-distributed everywhere" p.140.

(The Rayleigh distribution is described and some formulae derived in Appendix 8A.)

It is simpler to treat the cases of specular and off-specular scattering spearately.

Off-Specular Scattering

As stated, the amplitude distribution of the off-specular scattered field is Rayleigh-distributed. Intensity, being squared amplitude, thus follows a negative exponential distribution (see Appendix 8B for the mathematical justification). We can now begin to understand the previously observed histograms. Theory asserts that they are negative exponential, and there is good visual agreement with this assertion. Moreover a goodness-of-fit test scientifically supports this hypothesis. Also as we move further away from the specular direction, with an accompanying falling mean intensity level, the negative exponential distribution would impose an equal fall in intensity variance and so give rise to tighter and tighter histograms.

Specular Scattering

Very Rough Surfaces : Type (C)

As previously remarked, when the surface is very rough the amplitude of the scattered field is Rayleigh-distributed everywhere. Nevertheless the specular direction is preferred which,

⟹ larger mean signal level,

⟹ larger signal variance.

Thus the intensity distribution would be negative exponential with greatest spread in the specular direction. Diagrammatically:

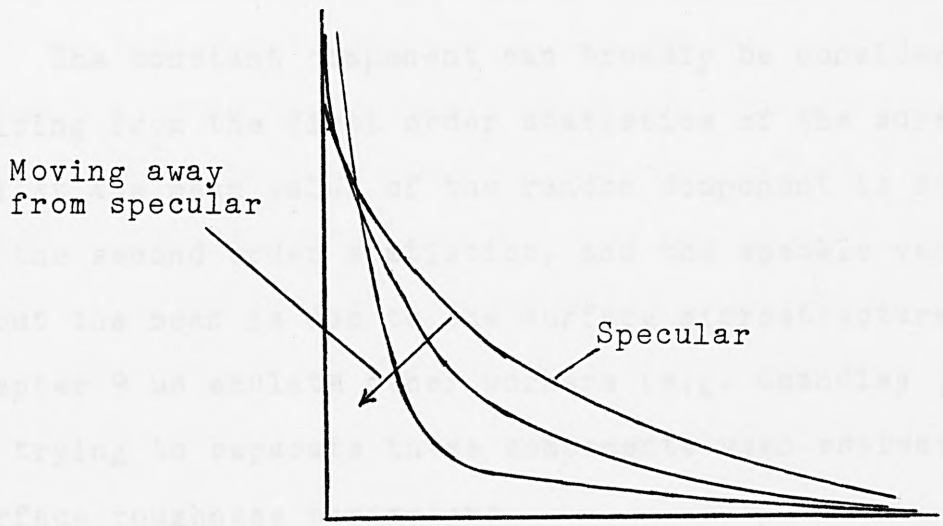

FIG. 8.1.4. Neg. Exponential Distribution

Smooth Surfaces : Type (A)

For weak scatterers the amplitude distribution of the scattered field in the specular direction will not be Rayleigh-distributed. In fact, for non-grazing incidence, "the amplitude of the field scattered in the specular direction has a constant coherent component and a random, Hoyt-distributed component". Beckmann [1959] and Appendix 8C). When the surface is very rough the latter component becomes incoherent (Rayleigh-distributed) and the former vanishes.

For this Type (C) situation: "In the non-specular directions the field (if any) is always incoherent." (Beckmann [1963] p.151.)

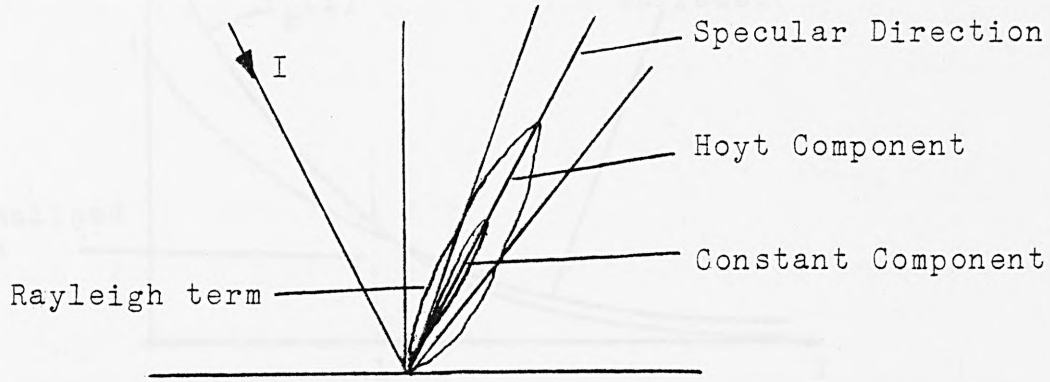

FIG. 8.1.5 Amplitude Distribution

The constant component can broadly be considered as arising from the first order statistics of the surface, whilst the mean value of the random component is attributable to the second order statistics, and the speckle variation about the mean is due to the surface microstructure. In Chapter 9 we emulate other workers (e.g. Chandley [1976] in trying to separate these components when estimating surface roughness parameters.

As roughness increases, the random component of the intensity distribution tends to the limiting case of the negative exponential distribution. The distributions are, for all grades of roughness, highly positively skewed. Figure 8.1.6. below illustrates these remarks.

The variance increases to a maximum as $k \searrow 1$ (see p for definition of k) in agreement with arguments applied by Beckmann [1963] (p.150)

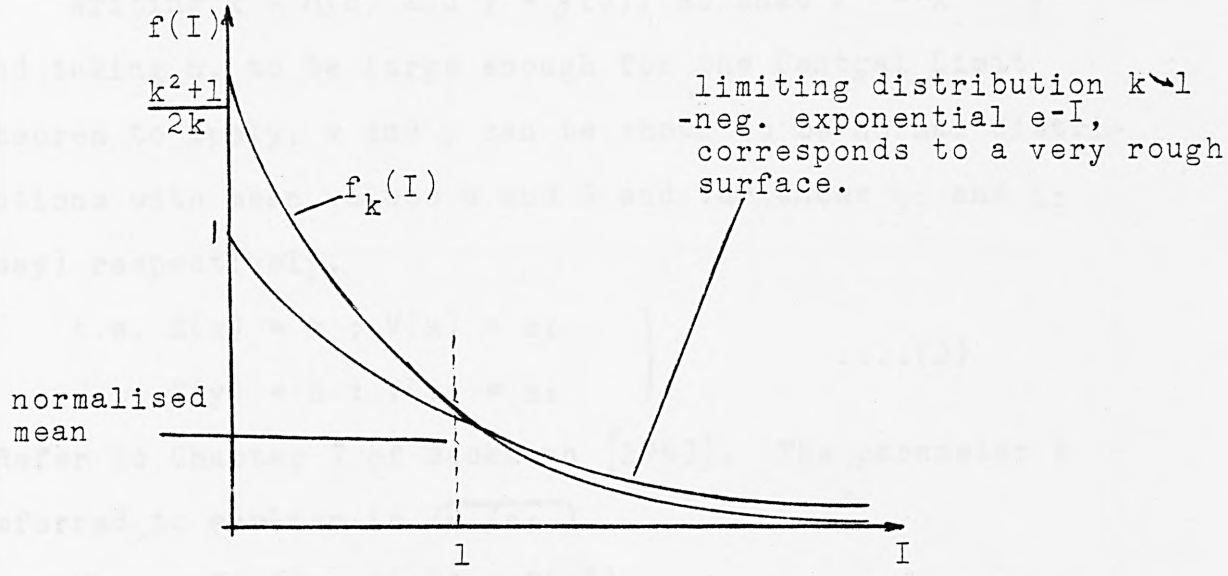

FIG. 8.1.6. Specular Intensity Random Component

We have explained that in the specular direction intensity variance increases as roughness increases, and that this variance exceeds all off-specular variance in the limit. The discussion above is now augmented by returning to first principles and re-examining mean values.

The total field scattered by a rough surface is necessarily the sum of mutually interferring elementary waves.

$$U = re^{i\psi} = \sum_{j=1}^{n} A_j e^{i\phi_j} \qquad \ldots.(1)\ (p.120)$$

where r, ψ are the resultant amplitude and phase of the scattered field and A_j, ϕ_j correspond to amplitude and phase of n elementary waves.

Writing $x = \mathcal{R}(U)$ and $y = \mathcal{J}(U)$, so that $r^2 = x^2 + y^2$ and taking n, to be large enough for the Central Limit Theorem to apply, x and y can be shown to be normal distributions with mean values α and β and variances ζ_1 and ζ_2 (say) respectively.

$$\left.\begin{aligned} \text{i.e. } E(x) &= \alpha \; ; \; V(x) = s_1 \\ E(y) &= \beta \; ; \; V(y) = s_2 \end{aligned}\right\} \qquad \ldots.(2)$$

(Refer to Chapter 7 of Beckmann [1963]. The parameter k referred to earlier is $\sqrt{s_2/s_1}$.)

Whence $E(r^2) = E(x^2) + E(y^2)$

$$= \alpha^2 + s_1 + \beta^2 + s_2 \qquad \ldots.(3)$$

Moreover, if the distribution of phases is symmetrical about zero (a reasonable assumption), then $\beta = 0$ and x and y are demonstrated to be uncorrelated, and being normal variables, independent.

In the specular direction each elementary wave has a randomly distributed phase according to

$$\phi = \frac{4\pi}{\lambda} \zeta(x) \cos\theta_1 \qquad \ldots.(4) \qquad \text{(p.150)}$$

Thus if z, the height distribution, is normal, then the phase distribution brought about by the surface variations is also normal.

Take, $z \sim N(0, \sigma_z^2)$ i.e. the height distribution is zero-mean normal with variance σ_z^2. If we take $\phi \sim N(0, \sigma_\phi^2)$ a relation between σ_z^2 and σ_ϕ^2 is easily established via (5), namely

$$\sigma_\phi^2 = \left(\frac{16\pi^2}{\lambda^2} \cos^2\theta_1\right) \sigma^2 \qquad \ldots.(5)$$

To ease the notation the suffix ϕ is dropped from σ_ϕ^2 from now on.

We now refer to Table 7.1. p.123 of Beckmann [1963] which lists expressions for α, s_1 and s_2 under the normal distribution for ϕ, viz

α	s_1	s_2
$n\, e^{-\frac{1}{2}\sigma^1}$	$\frac{n}{2}(1 - e^{-\sigma^2})^2$	$\frac{n}{2}(1 - e^{-2\sigma^2})$

Thus $E(r^2) = \alpha^2 + s_1 + s_2$

$$= n^2 e^{-\sigma^2} + n/2(1 - e^{-\sigma^2})^2 + \frac{n}{2}(1 - e^{-2\sigma^2})$$

$$= n^2 e^{-\sigma^2} + n/2(1 - 2e^{-\sigma^2} + e^{-2\sigma^2}) + \frac{n}{2}(1 - e^{-2\sigma^2})$$

$$= n^2 e^{-\sigma^2} + n(1 - e^{-\sigma^2} + e^{-2\sigma^2})$$

$$\to \begin{cases} n^2 & (\equiv \text{smooth surface}) \\ n & (\equiv \text{rough surface}) \end{cases} \qquad \ldots.(6)$$

Since, for a smooth surface $e^{-\sigma^2} \to 1$ whilst for a rough surface $e^{-\sigma^2} \to 0$.

Also $V(r^2) = 2(2\alpha^2 s_1 + s_1^2 + s_2^2)$ (c.f. Appendix 8E)

$$= 4n^2 e^{-\sigma^2}\frac{n}{2}(1 - e^{-\sigma^2})^2 + 2\frac{n^2}{4}(1 - e^{-\sigma^2})^4 + 2\frac{n^2}{4}(1 - e^{-2\sigma^2})^2$$

$$= (1 - e^{-\sigma^2})^2\{2n^3 e^{-\sigma^2} + n^2/2(1 - e^{-\sigma^2})^2 + \frac{n^2}{2}(1 + e^{-\sigma^2})^2\}$$

$$= (1 - e^{-\sigma^2})^2\{2n^3 e^{-\sigma^2} + n^2(1 + e^{-2\sigma^2})\}$$

$$\to \begin{cases} 2n^3 e^{-\sigma^2}(1 - e^{-\sigma^2})^2 \to o & (\equiv \text{smooth surface}) \\ n^2 & (\equiv \text{rough surface}) \end{cases} \qquad \ldots.(7)$$

The limit of $V(r^2)$ depends on the dominance of powers of n and the decay of $e^{-\sigma^2}$.

The case of a rough type (C) surface is easiest seen with $e^{-\sigma^2} \to o$ and $E(r^2) \to n$ and $V(r^2) \to n^2$.

N.B. $E(r^2) \to n$, $V(r^2) \to n^2$ is in agreement with the intensity (= amplitude squared = $x^2 + y^2$), behaving as a negative exponential distribution, or with the more fundamental result, that the amplitude distribution is Rayleigh:

$$f(r) = \frac{2r}{n} e^{-r^2/n} \qquad \ldots.(8)$$

Combining the above ideas, we see that theory substantiates that moving away from the specular direction has virtually the same effect as increasing the surface roughness, with regard to the intensity of the back scattered radiation: the variance falls in unison with the mean level.

8.1.1 Signal-to-Noise Ratio of Reflected Output from a Rough Surface

Expressing the signal-to-noise ratio, S/NR, ratio of the mean intensity to the variance of the reflected signal : $S/NR = \frac{E(r^2)}{V(r^2)}$, for a rough type (C) surface this measure approaches

$$\frac{E(r^2)}{V(r^2)} \rightarrow \frac{n}{n^2} = \frac{1}{n} \qquad \ldots.(9)$$

For a smoother type (B) surface,

$$\frac{E(r^2)}{V(r^2)} \rightarrow \frac{n^2 e^{-\sigma^2}}{2n\, e^{-\sigma^2}(1 - e^{-\sigma^2})^2} = \frac{1}{2n(1 - e^{-\sigma^2})^2}$$

$$\rightarrow \frac{1}{2n} \qquad \ldots.(10)$$

that is for a surface which is relatively smooth but nevertheless $e^{-\sigma^2}$ is small. Clearly for a super smooth surface, mathematically $V(r^2) \rightarrow 0$, with the surface noise tending to zero.

$$\frac{S/NR \text{ (smooth surface)}}{S/NR \text{ (rough surface)}} = \frac{1}{2(1 - e^{-\sigma^2})^2} > \frac{1}{2} \qquad \ldots.(11)$$

The practical implications of this result are discussed in the next chapter.

The arguments presented thus far concern the extreme changes in signal-to-noise ratio (S/NR), as defined, solely brought about by extreme changes of

surface roughness. The nature of the illumination was taken to be a coherent monochromatic source. For a type (C) surface: the surface roughness produces an incoherent scattered field from coherent illumination, the total scattered power from n facets is n and the intensity of the speckle pattern is negative exponential for all viewing angles.

Consider now the result of white light illumination. Such an incoherent source implies that the scattered field is summed algebraically and not vectorially so that scattering behaviour is described by the simple facet model. For n scattering facets, the total scattered power is again n. At a particular observation angle the mean intensity is directly proportional to the number of facets inclined at the appropriate angle. (A Poisson random variable with mean $\mu = np$ say.) The mean intensity μ is the same as for a coherent source of the same power output.

$$\frac{S/NR\ (coherent)}{S/NR\ (incoherent)} = {}^{1}\Big/\left(\mu/_{1}\right) = \frac{1}{\mu} = \frac{1}{np} \qquad ....(12)$$

Thus we have an improved S/NR consistent with the observations of Norton-Wayne. Formulated in terms of the speckle contrast, (SC say),

$$\frac{SC\ (coherent)}{SC\ (incoherent)} = {}^{1}\Big/\left(1/\sqrt{\mu}\right) = \sqrt{\mu} = \sqrt{np}$$

i.e. a reduction in the speckle contrast.

8.2. Modelling of Scatter from Rough Surfaces with Non-Gaussian Auto-correlation Functions

As in Chapter 4, formal scattering theories are based on the assumption that the autocovariance function of surface roughness height, $B(\tau)$, is of the form

$B(\tau) = \sigma^2 e^{-\tau^2/T^2}$ where T is the correlation length. In practice, however, it is doubtful that any real surface has such an autocovariance function. A negative exponential : $B(\tau) = \sigma^2 e^{-|\tau|/T}$ is commonly encountered. (c.f.,Chapter 6) although the curve has to be modified in the vicinity of $\tau = 0$), so that the distribution of slopes has finite moments. The nature of possible modifications is discussed so as to be compatable with both theory and experimental observation of scattering, as well as with mechanical profile considerations.

For a surface defined in terms of the following surface statistics:

surface roughness height, $Z \sim D(0,\sigma^2)$,

autocovariance function, $B(\tau) = \sigma^2 e^{-|\tau|/T}$,

the variance of z' (the random variable of surface gradients) is infinite (c.f. Appendix 8I). The facet theory of scattering described in Chapter 4 (which is based purely on z'), when applied to such a surface, would predict a wide dispersion in the reflected field, even when the surface is optically smooth (Type (A)). The singularity of the variance is due to the feature of the autocorrelation function of the origin. A slight smoothing of the autocorrelation function dramatically alters the position: the mathematical infinity can be removed and a finite slope variance can be achieved. [An analogeous situation is the infinite stress computed at the corner of a square window cut in a panel sheet. The introduction of a small curvature in the window design at the corners, reduced the stress and the concomitant metal fatigue.]

Such smoothing is achieved if, for example, the following autocorrelation function obtains:

$$C(\tau) = \begin{cases} 1 - \frac{|\tau|}{\ell}\left(1 - e^{-|\tau|/T}\right), & 0<|\tau|<\ell \\ Ae^{-B|\tau|} & |\tau|>\ell \end{cases} \quad \ldots.(14)$$

where $A = e^{e^{\ell/T}-1}$ and $B = \frac{1}{\ell}\left(e^{\ell/T}-1\right) + \frac{1}{T}$

and $\ell<<T$, the constants A and B being derived from continuity considerations.

The argument for such a model, is that the negative exponential portion fits actual computed autocorrelation functions of surface heights, whilst the local quadratic portion near $\tau = 0$, preserves the concord between the facet theory and wave theory of scattering, for those surfaces where geometrical optics would be expected to provide a sufficient explanation of observed scatter. To be meaningful however, the case for such a model must be made on mechanical grounds. Let us consider for the moment, how a surface is generated in say a grinding or rolling operation. The deepest grooves are cut by large random grits, with the displaced material being pushed to the rim of the grooves. The height variations for large lags retains the essential Poissonian nature of the cutting process, with the associated exponential decay curve, whilst the smoothed variation for small lags is explained in terms of metal flow.

The resolution of the sampling (a 2μ or 3μ sampling interval was employed) is not sufficient to determine autocorrelation behaviour at the truly micro-level. Indeed stylus geometry prohibits valid objec-

tive assessment of the model. A two-structure auto-correlation function is accepted as being more reasonable in concept, than to suppose that a simple global model exists.

Whitehouse and Phillips [1978], [1982] have proposed a variety of extremely complex mathematical functions which exhibit the above autocorrelation characteristics

viz $C(\tau) = \text{sech } \frac{\pi\tau}{2} A_2(\theta) \cos (2\pi\tau A_2(\theta))$

where $A_2(\theta)$

$$= \text{sech } (2\pi\theta) + 2\Sigma \frac{(-1)^r \theta}{2\pi\{\theta^2 + [\frac{1}{4}(2r+1)]^2 \text{sech}\left[\frac{\pi(2r+1)}{8\theta}\right]\}} \quad \ldots.(15)$$

Such functions have the virtue that the change of form is internally imposed by preset parameters, whereas for a two-part function the change is defined externally, and, moreover, at the interface there must be some discontinuity of higher derivatives. Against this, we advocate that the different mechanisms involved in producing the surface topography, support the notion of a two-structure function, provided essential auto-correlation properties are preserved.

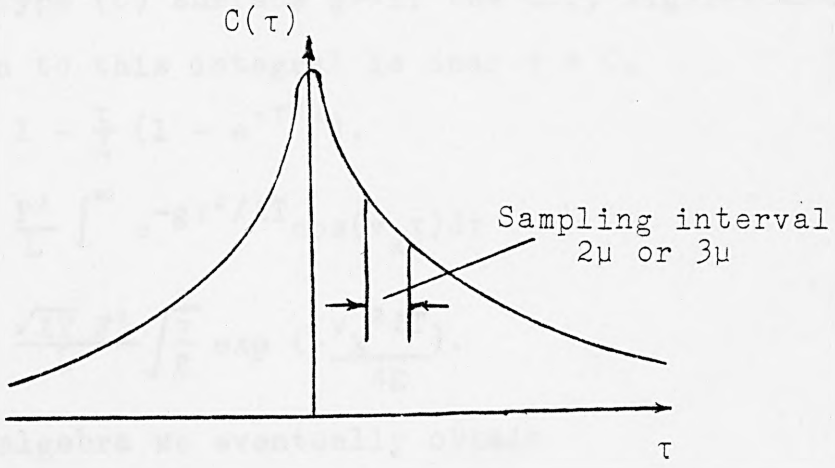

FIG. 8.2.1. Typical ACF

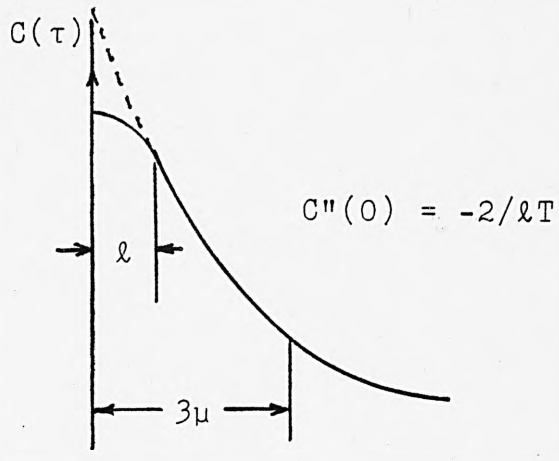

FIG. 8.2.2. ACF near $\tau = 0$

8.2.1. Rough Surfaces

For a surface with normal roughness heights, the distribution of derivatives is:

$$W(z') = \frac{1}{\sqrt{2\pi}} \frac{\sqrt{\ell T}}{\sqrt{2}\sigma} \exp\left(-\frac{1}{2} z'^2 \frac{\ell T}{2\sigma^2}\right), \text{ which}$$

leads to $\rho(\vartheta) = \frac{1}{\sqrt{\pi}} \frac{\sqrt{\ell T}}{2\sigma} \cdot 2 \exp\left(-\frac{1}{2} \frac{\ell T \vartheta^2}{8\sigma^2}\right)$, the information required by the facet scattering theory. The predicted scatter distribution about the specular direction is Gaussian with variance $8\sigma^2/\ell T$.

For the Kirchhoff wave theory we need to calculate:

$$\int_0^\infty e^{-g[1 - C(\tau)]} \cos(v_x \tau) d\tau$$

For a Type (C) surface $g >> 1$, the only significant contribution to this integral is near $\tau = 0$, when $C(\tau) = 1 - \frac{\tau}{\ell}(1 - e^{-\tau/T})$.

$$\text{then } I(\vartheta) = \frac{F^2}{L} \int^\infty e^{-g\tau^2/\ell T} \cos(v_x \tau) d\tau$$

$$= \frac{\sqrt{\ell T}\, F^2}{L} \sqrt{\frac{\pi}{g}} \exp\left(-\frac{v_x^2 \ell T}{4g}\right).$$

After some algebra we eventually obtain

$$I(\vartheta) \sim \frac{\sqrt{\pi}}{L \frac{4\pi}{\lambda} \cos\theta_1} \frac{\ell T}{\sigma} \exp\left(-\frac{\ell T \vartheta^2}{16\sigma^2}\right), \qquad \ldots.(16)$$

with the two theories compatible. With reference to Chapter 9.3) the geometrical surface roughness parameter convolved in the intensity formula has been modified to $\sigma/\sqrt{\ell T}$. The ratio $\sigma/\sqrt{\ell T}$ still has the dimensions of 'slope' but would require some re-interpretation.

Postulated Autocorrelation Functions

Essential and obvious properties of $C(\tau)$ are that:

$$\text{(i)} \quad C(-\tau) = C(\tau) ,$$

$$\text{(ii)} \quad C(0) = 1 ,$$

$$\text{(iii)} \quad C(\infty) = 0 ,$$

although these do not in themselves constitute a NS set of conditions for a function to be an autocorrelation function (we shall make reference to this remark later).

The following model autocorrelation function has been proposed:

$$C(\tau) = \begin{cases} 1 - \frac{\tau}{\ell}\left(1 - e^{-\tau/T}\right), & o < \tau < \ell \\ Ae^{-B\tau} & \tau > \ell, \ell << T \end{cases}$$

A and B >0 and for negative τ, $C(-\tau) = C(\tau)$. Near $\tau = 0$, $C(\tau)$ behaves as $1 - \tau^2/\ell T$, i.e. locally quadratic with $C(0) = 1$, $C'(0) = 0$ and $C''(0) = -2/\ell T$. For large τ, positive or negative, $C(\tau) \searrow 0$ brought about by the negative exponential decay. Thus properties (i), (ii) and (iii) are satisfied. The constants A and B are determined from elementary regularity restrictions, namely the continuity of $C(\tau)$ and $C'(\tau)$ at the point $\tau = \ell$.

Continuity of $C(\tau)$ implies

$$Ae^{-B\ell} = e^{-\ell/T}$$

whilst continuity of the derivative $C'(\tau)$ implies

$$-BAe^{-B\ell} = \frac{1}{\ell}\left(1 - e^{-\ell/T}\right) - \frac{1}{T}e^{-\ell/T}$$

$$Be^{-\ell/T} = \frac{1}{\ell}\left(1 - e^{-\ell/T}\right) + \frac{1}{T}e^{-\ell/T}$$

$$B = \frac{1}{\ell}\left(e^{\ell/T} - 1\right) + \frac{1}{T}$$

$$\sim \frac{2}{T} \quad \text{(correlation length} \sim T/2.\text{)}$$

Back substituting,

$$A = e^{B\ell} \cdot e^{-\ell/T}$$

$$= e^{\left(e^{\ell/T} - 1 + \ell/T\right)} \cdot e^{-\ell/T}$$

$$= e^{e^{\ell/T} - 1} \qquad *$$

$$\sim e^{\ell/T} \quad (\sim 1)$$

The precise function is therefore

$$C(\tau) = \begin{cases} 1 - \tau/\ell\left(1 - e^{-\tau/T}\right) & , \quad \tau \leqslant \ell \\ e^{\left(e^{\ell/T} - 1\right)} \cdot e^{-\tau/\ell\left(e^{\ell/T} - 1\right) - \tau/\ell} & , \quad \tau > \ell \,. \end{cases}$$

This function must also obey certain consistency relations in order to fulfil autocorrelation properties : a NSC that $C(\tau)$ is an autocorrelation function is that $C(0) = 1$ and $C(\tau)$ is a positive semi-definite function.

In particular the property

$C(2\tau) > -1 + 2\left[C(\tau)\right]^2$ is essential.

We now investigate the proposed function with regard to this restriction.

Case (i) $2\tau < \ell$

$$C(2\tau) + 1 - 2\left[C(\tau)\right]^2 = 1 - \frac{2\tau}{\ell}\left(1 - e^{-2\tau/T}\right) + 1 - 2\left[1 - \frac{\tau}{\ell}\left(1 - e^{-\tau/T}\right)\right]^2$$

$$= \cancel{1} - \frac{2\tau}{\ell}\left(1 - e^{-2\tau/T}\right) + \cancel{1} - \cancel{2} + \frac{4\tau}{\ell}\left(1 - e^{-\tau/T}\right) + \frac{2\tau^2}{\ell^2}\left(1 - e^{-\tau/T}\right)^2$$

$$= \frac{2\tau}{\ell}\left[-1 + e^{-2\tau/T} + 2 - 2e^{-\tau/T} - \tau/\ell + \frac{2\tau}{\ell} e^{-\tau/T} + \frac{\tau}{\ell} e^{-2\tau/T}\right]$$

$$= \frac{2\tau}{\ell}\left[1 + (1 - \tau/\ell)\, e^{-2\tau/T} - 2(1 - \tau/\ell)\, e^{-\tau/T} - \tau/\ell\right]$$

$$= \frac{2\tau}{\ell}(1 - \tau/\ell)\left[1 - 2e^{-\tau/T} + e^{-2\tau/T}\right]$$

$$= \frac{2\tau}{\ell}(1 - \tau/\ell)\left(1 - e^{-\tau/T}\right)^2$$

$$> 0 \quad (\tau < \ell)$$

Case (ii) $\tau > \ell$

$$C(2\tau) + 1 - 2\left[C(\tau)\right]^2 = Ae^{-2B\tau} + 1 - 2\left[Ae^{-B\tau}\right]^2$$

$$= -(2A^2 - A)\, e^{-2B\tau} + 1$$

$$> -(2A^2 - A)\, e^{-2B\ell} + 1 \text{ , taking } 2A^2 - A > 0$$

(otherwise result is trivial).

$$= -2e^{-2\ell/T} + A^{-1}e^{-2\ell/T} + 1 \quad \text{(appealing to (*))}$$

$$= -2e^{-2\ell/T} + e^{1-e^{\ell/T}} \times e^{-2\ell/T} + 1$$

$$= -2e^{-2\ell/T} + e^{1-(1 + \ell/T + \ell^2/T^2 2! + \ldots)} \times e^{-2\ell/T} + 1$$

$$= 1 + e^{-2\ell/T}\left(e^{-\ell/T} - \ell^2/T^2 2! - \cdots - 2\right)$$

$$= 1 + e^{-2\ell/T}\left(1 - \ell/T - \ldots - 2\right)$$

$$\sim 1 - (1 + \ell/T)(1 - 2\ell/T) \quad \text{small } \ell, \text{ large } T$$

$$= 1 - 1 - \ell/T + 2\ell/T + 2\ell^2/T^2$$

$$\sim \ell/T > 0$$

Case (iii) $2\tau > \ell > \tau$

$$C(2\tau) + 1 - 2\left[C(\tau)\right]^2 = Ae^{-2B\tau} + 1 - 2\left[1 - \frac{\tau}{\ell}\left(1 - e^{-\tau/T}\right)^2\right]$$

$$= Ae^{-2B\tau} + 1 - 2 + \frac{4\tau}{\ell}\left(1 - e^{-\tau/T}\right) - \frac{2\tau^2}{\ell^2}\left(1 - e^{-\tau/T}\right)^2$$

$$= e^{e^{k/T}-1} \times e^{\left[-2\tau/\ell\ (e^{\ell/T}-1) - 2\tau/T\right]} - 1 + \frac{4\tau}{\ell}\left(1 - e^{-\tau/T}\right)$$

$$- \frac{2\tau^2}{\ell^2}\left(1 - e^{-\tau/T}\right)^2$$

Using just order approximations,

$$\sim e^{\ell/T} \times e^{-2\tau/\ell \cdot \ell/T - 2\tau/T} - 1 + \frac{4\tau}{\ell}\frac{\tau}{T} - \frac{2\tau^2}{\ell^2}\frac{\tau^2}{T^2}$$

$$= e^{\ell/T}\, e^{-4\tau/T} - 1 + 4\tau^2/\ell T - 2\tau^4/\ell^2 T^2$$

$$\sim (1 + \ell/T)(1 - 4\tau/T) - 1 + 4\tau^2/\ell T$$

$$= 1 + \ell/T - 4\tau/T - 4\ell\tau/T^2 - 1 + 4\tau^2/\ell T$$

$$= \frac{1}{\ell T}\left(\ell^2 - 4\ell\tau + 4\tau^2\right)$$

$$= \frac{1}{\ell T}(\ell - 2\tau)^2 \geqslant 0$$

In summary, we may now confidently assert that the function $C(\tau)$ defined explicitly by (14) is an autocorrelation function. It is primarily negative exponential but the cusp at $\tau = 0$ has been smoothed off. This simple modification, effectively removes a singularity in the variance of the derivatives of the stochastic process, characterised by negative exponential autocorrelation functions.

We now crystallise the discussion in a search for a model autocorrelation function which satisfies the following properties and conditions:

(i) obvious end conditions

$C(0) = 1$; $C(\infty) = 0$

(ii) statistical consistency

$C(2\tau) > -1 + 2[C(\tau)]^2$

(iii) data characteristics

macro scale - negative exponential

(iv) permits compatibility of scattering models micro scale - local quadratic near $\tau = 0$.

(v) consistent with the dispersion of the scattered laser beam

$-C''(0) \sim 2/T^2$ (T = correlation length)

(For rough Type (C) surfaces, the dispersion of the scattered field is a function of the curvature at lag 0 of the autocorrelation curve c.f. Appendix 8I.

$\Longrightarrow$ robustness of the σ/T statistic estimated in Chapter 9.

This set of conditions, although imposing, is not sufficient for a unique model. Initially we look for a solution of the form : $C(\tau) = e^{-\gamma(\tau)}$ and using (1) - (v) try to find a suitable function γ.

Write $\gamma(\tau) = (\tau/T)^{\beta(\tau)}$. Then for (iii) and (iv) to be satisfied we require $\beta(\tau) \sim 1$ macro scale, and $\beta(\tau) \sim 2$ micro scale. Accordingly the two-scale model below is proposed.

$$C(\tau) = \begin{cases} e^{-(\tau/T)^{\beta(\tau)}}, & \text{for } \tau < \ell \\ e^{-\tau/T}, & \text{for } \tau > \ell \end{cases} \qquad \ldots.(18)$$

with $\beta(\ell) = 1$ to ensure continuity of $C(\tau)$ at $\tau = \ell$. The problem is in fact to find a $\beta(\tau)$ with <u>all</u> the desired properties.

Returning to the form $C(\tau) = e^{-\gamma(\tau)}$ and differentiating we obtain the expressions

$$C'(\tau) = -\gamma'(\tau)e^{-\gamma(\tau)}, \text{ and}$$

$$C''(\tau) = -\gamma''(\tau)e^{-\gamma(\tau)} + [\gamma'(\tau)]^2 e^{-\gamma(\tau)}$$

From (i) $\gamma(0) = 0$ and from (iv) $C'(0) = 0 \Rightarrow \gamma'(0) = 0$.

Further (v) $C''(0) = -\frac{2}{T^2} \Rightarrow \gamma''(0) = 2/T^2$.

For continuity of the derivative of $C(\tau)$ at $\tau = \ell$ we require $\gamma'(\ell) = \frac{1}{T}$.

With $\gamma(\tau) = (\tau/T)^{\beta(\tau)}$,

$$\log [\gamma(\tau)] = \beta(\tau) \log (\tau/T)$$

$$\frac{1}{\gamma(\tau)} \gamma'(t) = \beta'(\tau) \log (\tau/T) + \beta(\tau) \cdot \frac{1}{\tau}$$

$$\therefore \quad \gamma'(\tau) = \beta'(\tau) \left(\frac{\tau}{T}\right)^{\beta(\tau)} \log \left(\frac{\tau}{T}\right) + \beta(\tau)\frac{1}{T} \left(\frac{\tau}{T}\right)^{\beta(\tau)-1}$$

For $\gamma'(0) = 0$, $\beta(0)>1$ will suffice, whilst for the condition $\gamma'(\ell) = 1/T$, we have

$$\gamma'(\ell) = \beta'(\ell) \cdot \left(\frac{\ell}{T}\right)^{\beta(\ell)} \log \left(\frac{\ell}{T}\right) + \beta(\ell)\frac{1}{T}\left(\frac{\ell}{T}\right)^{\beta(\ell)-1} \text{ and}$$

therefore this condition is met by $\beta(\ell) = 1$ and $\beta'(\ell) = 0$.

Also $\gamma''(\tau) = \beta''(\tau) \left(\frac{\tau}{T}\right)^{\beta(\tau)} \log \left(\frac{\tau}{T}\right) + \beta'(\tau) \left(\frac{\tau}{T}\right)^{\beta(\tau)} \frac{1}{\tau} +$

$$\beta'(\tau)\gamma'(\tau) \log \left(\frac{\tau}{T}\right) + \beta'(\tau)\frac{1}{T} \left(\frac{\tau}{T}\right)^{\beta(\tau)-1} +$$

$$\beta(\tau)\frac{1}{T} \frac{d}{d\tau} \left(\frac{\tau}{T}\right)^{\beta(\tau)-1}$$

Last term $= \beta(\tau)\frac{1}{T}\{(\beta'(\tau) - 0) \log \left(\frac{\tau}{T}\right) + (\beta(\tau)-1) \cdot \frac{1}{\tau}\} \left(\frac{\tau}{T}\right)^{\beta(\tau)-1}$

There are several indeterminate terms on the R.H.S. for $\gamma''(0)$, but for $\tau \to 0$, positive powers of τ ensures zero limit values despite the presence of $\log \left(\frac{\tau}{T}\right)$ terms.

Then $\gamma''(0) = \beta(0) \frac{1}{T}\{\beta(0)-1\} \cdot \frac{1}{T} \cdot 1$ if $\beta(0) = 2$

$= 2/T^2$ (recall (v))

To date we have: $\beta(0) = 2$;

$\beta(\ell) = 1$;

$\beta'(\ell) = 0$

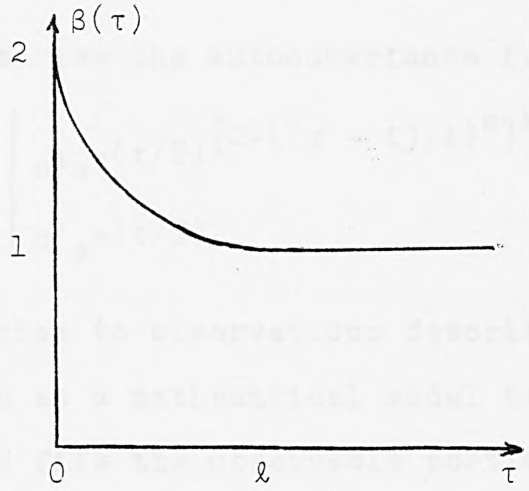

FIG. 8.2.3. Power Function $\beta(\tau)$

The simplest function which comes to mind is: $\beta(\tau) = 1 + \frac{(\tau - \ell)^2}{\ell^2}$, and this satisfies all the conditions except (ii). To satisfy this condition and to achieve the necessary autocorrelation property we require $\beta(\tau)$ to have fhe form shown below, i.e. $\beta(\tau)$ should decrease very rapidly near $\tau = 0$.

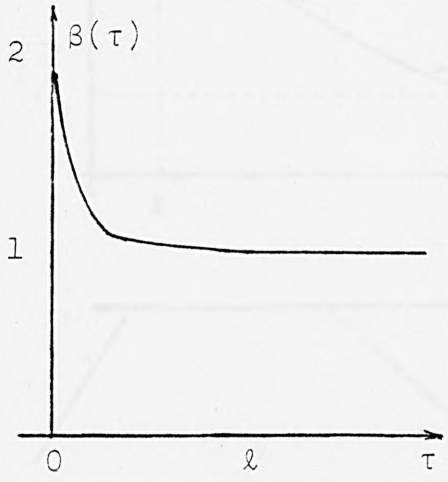

FIG. 8.2.4. Power Function $\beta(\tau)$

$\beta(\tau) = 2 - (1 - \frac{(\tau - \ell)^m}{\ell^m})^{1/m}$ for a sufficiently large m would work. (If we surmise $\ell \sim 1\mu m$, m may be taken as 10.)

To summarise the autocovariance function

$$B(\tau) = \begin{cases} \sigma^2 e^{-(\tau/T)} \left[2-\{(\tau - \ell)/\ell\}^m\right]^{1/m} & , \tau \leqslant \ell \\ \sigma^2 e^{-(\tau/T)} & , \tau > \ell \end{cases} \quad \ldots.(19)$$

could give rise to observations described in Chapter 6 and 7. $B(\tau)$ is seen as a mathematical model to a real-life function: it fits the observable portion of a real-life curve, whilst the unobservable, unsensed portion is modelled on the basis of purely deductive arguments.

FIG. 8.2.5. Model Autocorrelation Function

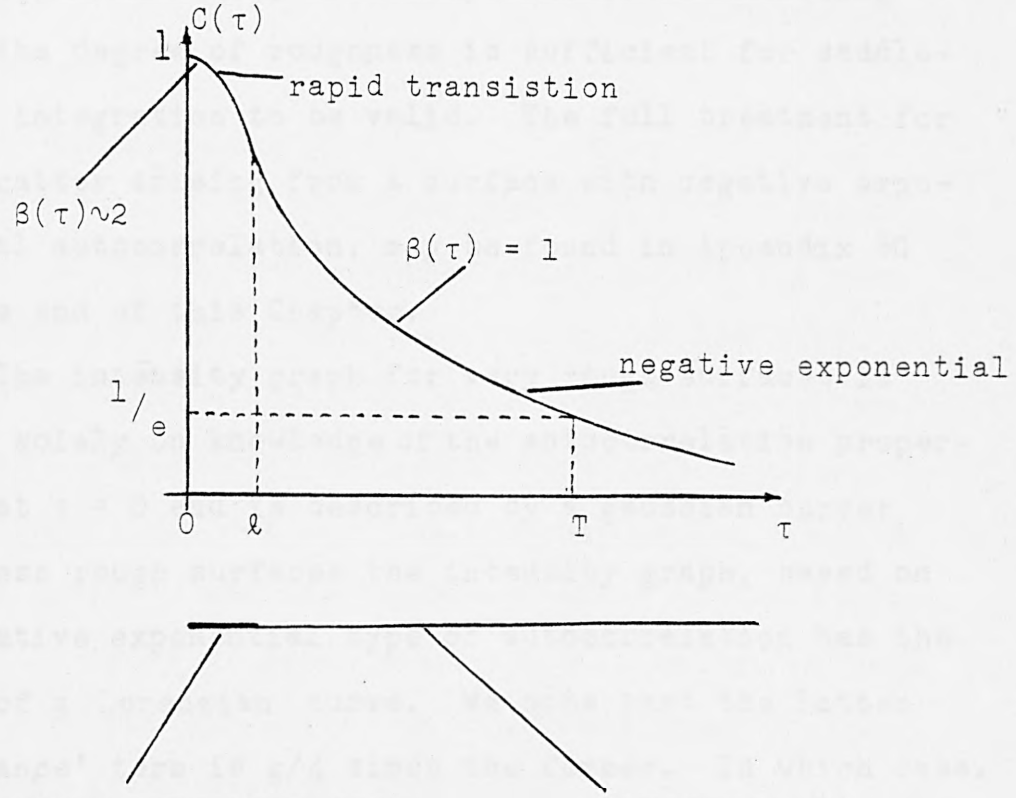

Influential zone for rough Type (C) surfaces. Facet and Kirchhoff theories converge.

$$I(\theta) \propto e^{\frac{-T^2 v_x^2}{4g}}$$

Influential zone of moderately rough Type (B) surfaces. Facet and Kirchhoff diverge.

$$I(\theta) \propto \frac{T/g}{1 + \frac{T^2 v_x^2}{g^2}}$$ (see over)

From the wave theory of scatter applied to surfaces with normal distribution of height, we may write

$$I(\theta) \propto \int_0^\infty e^{-g[1 - C(\tau)]} \cos(v_x \tau) d\tau \text{ for } g \gg 1 \quad \ldots.(20)$$

(for $g \simeq 10$ certainly.) For near specular angles (v_x small) and large T we may further approximate to:

$$I(\theta) \propto \int_0^\infty e^{-g\tau/T} \cos(v_x \tau) d\tau$$

$$= \frac{T/g}{1 + \frac{T^2}{g^2} v_x^2} \quad , \quad \ldots.(21)$$

treating the autocorrelation function as a pure negative exponential (ℓ, extremely small), and assuming that the degree of roughness is sufficient for saddle-point integration to be valid. The full treatment for the scatter arising from a surface with negative exponential autocorrelation, may be found in Appendix 8G at the end of this Chapter.

The intensity graph for very rough surfaces is based solely on knowledge of the autocorrelation properties at $\tau = 0$ and is described by a gaussian curve: for less rough surfaces the intensity graph, based on a negative exponential type of autocorrelation has the form of a Lorenzian curve. We note that the latter 'variance' term is $g/4$ times the former. In which case, we should expect to see the Kirchhoff model predicting scatter dispersion $\sqrt{g}/2$ times larger than that predicted on the basis of the facet theory.

This affords a possible explanation of apparent paradoxical scattering phenomena (c.f. Chapter 4), namely a smoother surface producing a wider scatter,

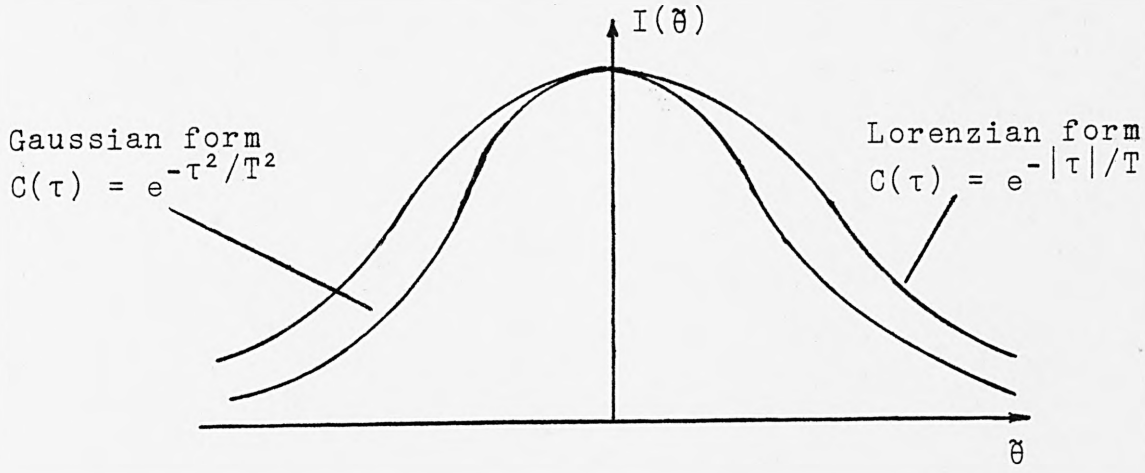

FIG. 8.2.6. Scattering from Rough Surfaces with C(τ) autocorrelation function

with the order of the increase in broad agreement with a $\sqrt{g}/2$ ratio.

8.2.2. Smooth Surfaces

The scatter distribution obtained when a laser beam is directed upon a ground glass mirror surface, at normal incidence, has been studied at the SIRA Institute by Dr L Cox. His work hopes to correlate scatter distribution characteristics with surface characteristics, such as the type of coating applied to the surface, and the surface texture of the surface layer, in terms of grain size and homogenity, as seen under a microscope. Certain empirical observations have been drawn from the experimental data. Does the Kirchhoff theory of electromagnetic scattering, (i) support these conclusions, or (ii) provide alternative models to fit the data?

The Experimental Scatter Distributions

A typical result is presented in figures 8.2.7, 8.2.8. Figure 8.2.7. is a plot (on log-linear paper) of the logarithm of intensity against observation angle.

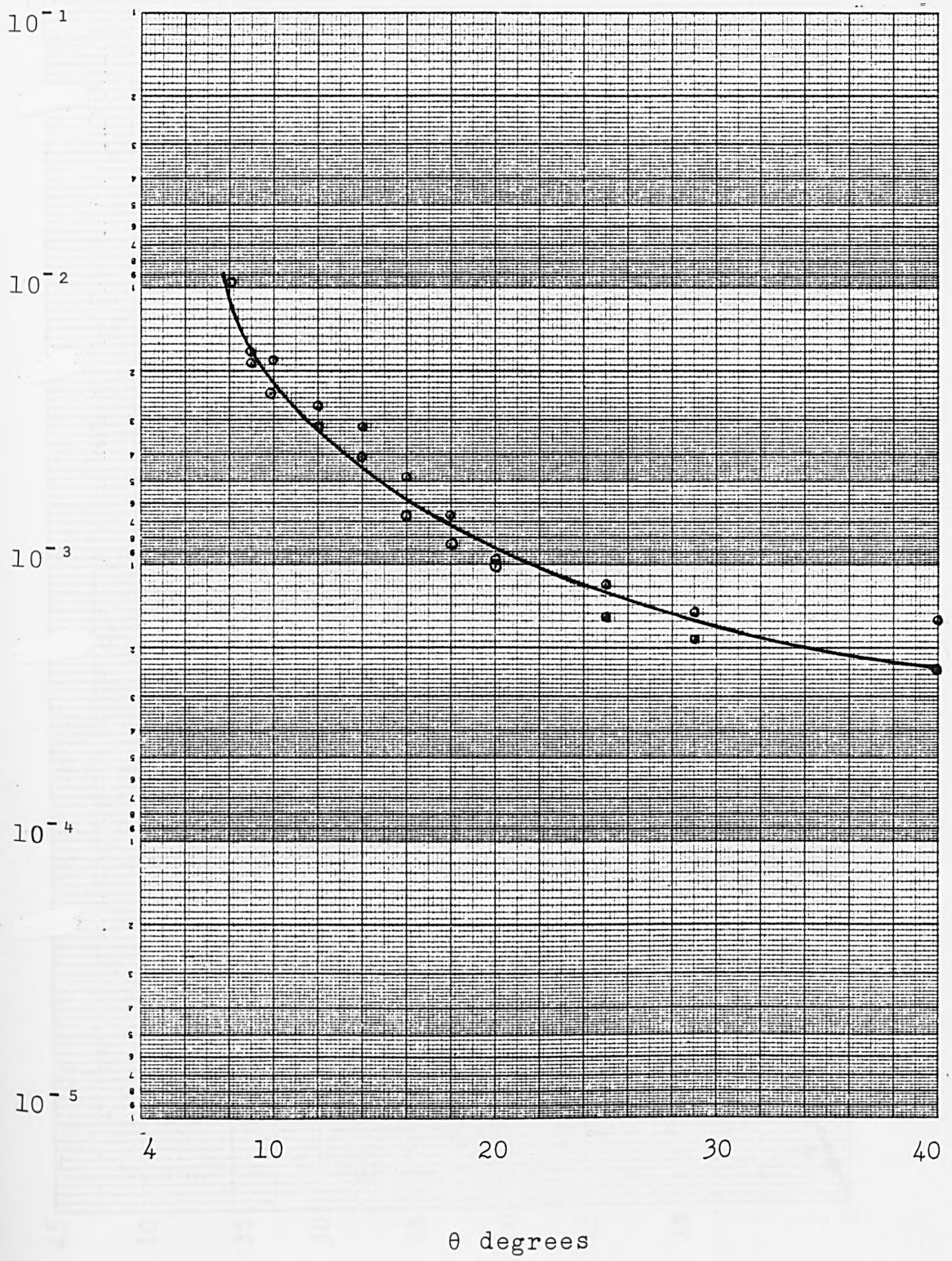

FIG. 8.2.7. Log (intensity) versus angle plot (off specular scattering)

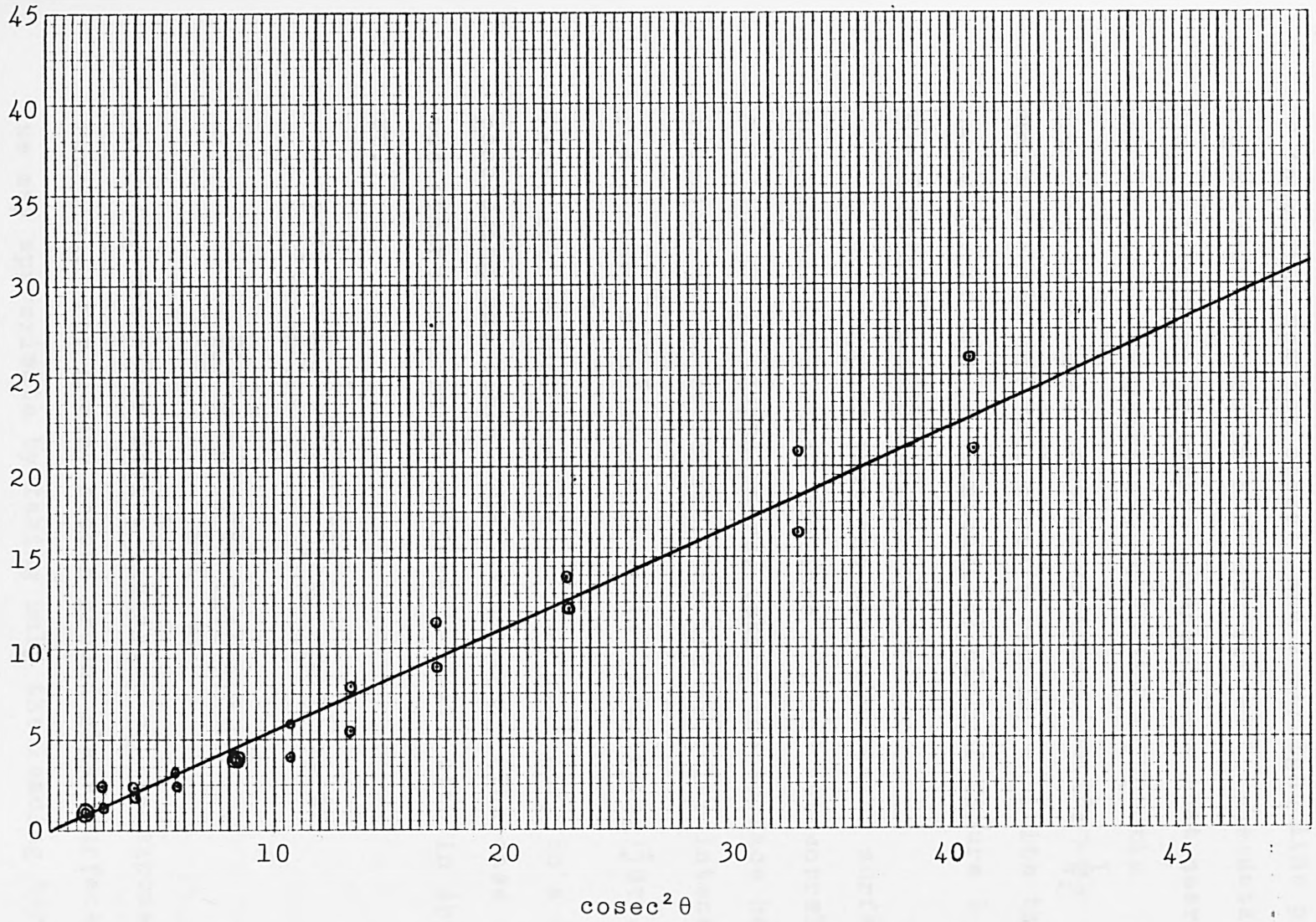

FIG. 8.2.8. Log (intensity) versus $\text{cosec}^2\theta$ plot with straight line fit

The angle of incidence $\theta_1 = 0^\circ$, whilst θ_2, the off-specular angle of scatter, varied as monitored between 5° and 40°. Figure 8.2.8. is a plot of the logarithm of intensity against $\text{cosec}^2\theta$ and a straight line passing through the origin has been fitted to the data. Simple intuitive arguments advanced, are that near the specular direction ($\theta_2 \to 0^\circ$), the asymptotic approach is as $\frac{1}{\theta_2{}^2}$. In this vicinity, $\cot^2\theta_2 \sim \frac{1}{\theta_2{}^2}$ But $1 + \cot^2\theta$ and thus $\text{cosec}^2\theta$ broadly exhibits the behaviour of the log (intensity) plot of figure 8.2.7.

The Theoretical Scatter Distribution

We now suppose that the distribution of surface heights has zero mean, variance σ^2, and autocorrelation function $C(\tau)$. Furthermore, taking the surface height distribution to be normal, the off-specular intensity

$$I(\theta_2) = \frac{F^2}{2L}\int_{-L}^{L} e^{iv_x\tau}\left[\exp\{-g(1 - C(\tau))\} - \exp(-g)\right]d\tau \quad ....(22)$$

(c.f. 4.41), applying the scattering theory to a surface possessing one-dimensional roughness. (The case of a two-dimensional rough surface is dealt with in Appendix 8H.)

$$I(\theta_2) = \frac{F^2}{2L}\int_{-L}^{L} e^{iv_x\tau}\, e^{-g}\left[\exp\{-gC(\tau)\}-1\right]d\tau$$

$$= \frac{F^2}{2L}\int_{-L}^{L} e^{iv_x\tau}\, e^{-g}\sum_{m=1}^{\infty}\frac{\{gC(\tau)\}^m}{m!}\,d\tau, \quad ....(23)$$

on using the power series expansion of the exponential function. For a very smooth ground glass surface $g<<1$, we may approximate by taking only the leading term. Therefore:

$$I(\theta_2) = \frac{F^2}{2L}e^{-g}g\int_{-L}^{L} e^{iv_x\tau}C(\tau)d\tau \quad ....(24)$$

In other circumstances, this provides a useful formula for estimating $C(\tau)$ from intensity data (c.f. Chapter 9). The Guassian function $C(\tau) = e^{-\tau^2/T^2}$ leads to a broadly quadratic log (intensity) graph which does not agree with observation. However, recalling our previous discussion, $C(\tau)$'s are typically of the form illustrated in Fig. 8.2.1. - a rapid fall within a lag of one micron, followed by a slow negative exponential decay, we formulate the mathematical model function shown:

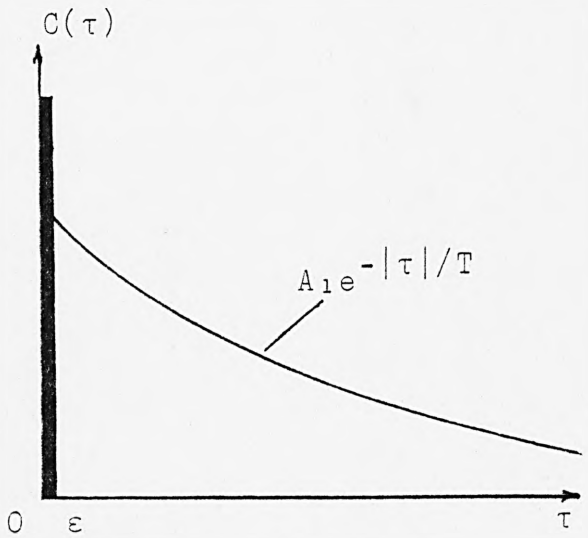

FIG. 8.2.9. Model Autocorrelation Function

The model function is the composite of an impulse at the origin, representing the micro component, and a negative exponential function of large correlation length representing the macro component.

Evaluating $I(\theta_2)$ we have,

$$I(\theta_2) = \frac{F^2}{2L}e^{-g}g\{\int_{-\varepsilon}^{\varepsilon} e^{iv_x\tau}\,d\tau + \int_{\varepsilon}^{L} A_1 e^{-\tau/T}d\tau + \int_{-L}^{-\varepsilon} A_1 e^{\tau/T}d\tau\},$$

remembering $C(-\tau) = C(\tau)$.

$$= \frac{F^2}{2L}e^{-g}g\{\left[\frac{1}{iv_x}e^{iv_x\tau}\right]_{-\varepsilon}^{\varepsilon} + A_1\int_{-\varepsilon}^{L} e^{(iv_x-\frac{1}{T})\tau}d\tau + A_1\int_{-L}^{-\varepsilon} e^{(iv_x+\frac{1}{T})\tau}d\tau\}$$

$$= \frac{F^2}{2L} e^{-g_g} \{ \frac{1}{iv_x} (e^{iv_x \varepsilon} - e^{-iv_x \varepsilon}) + A_1 \left[\frac{1}{iv_x - 1/T} e^{(iv_x - 1/T)\tau} \right]_{\varepsilon}^{L}$$

$$+ A_1 \left[\frac{1}{(iv_x + 1/T)} e^{(iv_x + 1/T)\tau} \right]_{-L}^{-\varepsilon} \}$$

$$= \frac{F^2}{2L} e^{-g_g} \{ \frac{2\sin(v_x \varepsilon)}{v_x} + A_1 . \frac{-(iv_x + i/T)}{v_x^2 + 1/T^2} (e^{(iv_x - 1/T)L} - e^{(iv_x - 1/T)\varepsilon})$$

$$+ A_1 \left[\frac{1}{(iv_x + i/T)} e^{(iv_x + 1/T)\tau} \right]_{-L}^{-\varepsilon} \}$$

$$= \frac{F^2}{2L} e^{-g_g} \{ \frac{2\sin(v_x \varepsilon)}{v_x} + A_1 . \frac{-(iv_x + 1/T)}{v_x^2 + 1/T^2} (e^{iv_x - 1/T)L} - e^{(iv_x - 1/T)\varepsilon})$$

$$+ A_1 \frac{(-iv_x + 1/T)}{v_x^2 + 1/T^2} (e^{-(iv_x + 1/T)\varepsilon} - e^{-(iv_x + 1/T)L}) \}$$

$$= \frac{F^2}{2L} e^{-g_g} \{ \frac{2\sin v_x \varepsilon}{v_x} + \frac{A_1}{v_x^2 + 1/T^2}$$

$$x \left(\frac{1}{T} \left[e^{-\varepsilon/T} 2\cos(v_x \varepsilon) - e^{-L/T} \cos(v_x \varepsilon) \right] \right.$$

$$\left. + v_x \left[e^{-L/T} 2\sin(v_x L) - e^{-\varepsilon/T} 2\sin(v_x \varepsilon) \right] \right) \}$$

For large L and ε small we may write:

$$I(\theta_2) = \frac{F^2}{2L} e^{-g_g} \{ \varepsilon + \frac{A_1}{v_x^2 + 1/T^2} (\frac{1}{T} - v_x^2 \varepsilon) \}$$

$$= \frac{F^2}{2L} e^{-g_g} g\varepsilon \{ 1 + \frac{A_1 (1/T\varepsilon - v_x^2)}{v_x^2 + 1/T^2} \}$$

$$= \frac{F^2}{2L} e^{-g_g} g\varepsilon \{ 1 - A_1 + \frac{1/T\varepsilon + 1/T^2}{v_x^2 + 1/T^2} \}$$

$$= \frac{F^2}{2L} e^{-g_g} g\varepsilon (1 - A_1) \left\{ 1 + \frac{B}{v_x^2 + 1/T^2} \right\}$$

Where $B = \frac{1}{1 - A_1} \left[\frac{1}{T\varepsilon} + \frac{1}{T^2} \right]$

Then $\log [I(\theta_2)] \simeq \text{Constant} - g + \log g + \frac{B}{v_x^2 + 1/T^2}$ ....(25)

Away from the specular angle, v_x is sufficiently dominant for the first order approximation to be valid. The variation of log (intensity) is governed by the behaviour of $\frac{B}{v_x^2+1/T^2} \simeq \frac{B}{v_x^2} = \frac{B}{4\pi^2/\lambda^2 \sin^2\theta_2}$

$$= \frac{\lambda^2 B}{4\pi^2} \operatorname{cosec}^2\theta_2$$

That is a near linear relationship with $\operatorname{cosec}^2\theta_2$.

8.3 Scattering from Rough Surfaces Possessing Non-Gaussian Distributions of Surface Profile Height

In addition to expounding the case of light scattering from rough surfaces, when the surface statistics are normal, Beckmann and Spizzichino [1963] formalised a procedure for dealing with the general case. However, on leaving the sanctuary of the normal distribution, the mathematics becomes more involved, and additional assumptions concerning the nature of high order moments and correlations, need to be made. A few simple cases, whereby the surface statistics are summarised by straightforward characteristic functions, or failing that, when the moments of the surface height distribution are readily compiled, are explored.

The following discussion is restricted to the case of surfaces possessing one-dimensional roughness. The governing equation for the intensity distribution is therefore,

$$I(\theta_2) = \rho_o \chi(v_z)\chi^*(v_z) + \frac{F^2}{2L}\int_{-L}^{L} e^{iv_x\tau}[\chi_2(v_z,v_z;\tau)-\chi(v_z)\chi^*(v_z)]d\tau \quad \ldots.(26)$$

(c.f. equation (36) p66)

Furthermore of prime interest, with regard to applications, are the very rough Type (C) surfaces with $g = \sigma^2 v_z^2 >> 1$, for which the leading term together with the second term in the integral are negligible. The methodology is to propose, if possible, a suitable $\chi_2(v_z,-v_z)$ for some specified height

distribution and to evaluate the subsequent integral by "saddle-point" integration, whereby the autocorrelation function is approximated by a local linear or quadratic curve in the neighbourhood of $\tau = 0$.

In simple cases the intensity graphs are sketched; others, involving advanced mathematical functions, would require numerical computation.

8.3.1. Surface Height Distribution : zero mean, negatively skewed, exponential

Height distributions, based on real data, are often negatively skewed (worn surfaces, plateau-honed surfaces, etc.), and so we transform the usual p.d.f. to accommodate this fact.

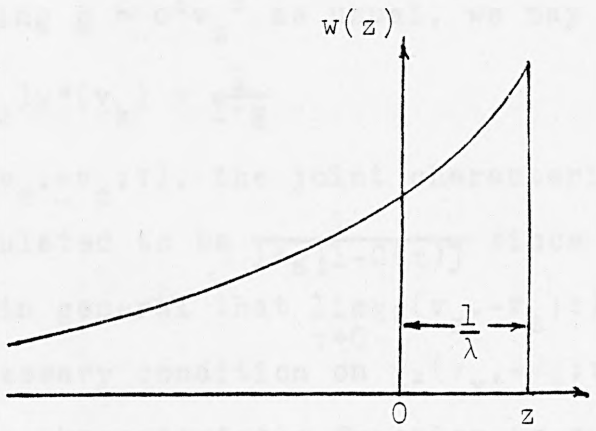

FIG. 8.3.1. Negative Exponential Distribution

$$w(z) = \begin{cases} \lambda e^{-(1-\lambda z)} & z < \frac{1}{\lambda}, \quad \lambda > 0 \\ 0 & , z \geq \frac{1}{\lambda}. \end{cases}$$

For this p.d.f., we have

$$\chi(v_z) = E[e^{iv_z z}]$$

$$= \int_{-\infty}^{1/\lambda} \lambda e^{-(1-\lambda z)} e^{iv_z z}\, dz$$

$$= \lambda e^{-1} \int_{-\infty}^{1/\lambda} e^{(\lambda+iv_z)z}\, dz$$

$$= \left[\frac{\lambda e^{-1}}{(\lambda+iv_z)} e^{(\lambda+iv_z)z} \right]_{-\infty}^{1/\lambda}$$

$$= \frac{\lambda}{\lambda+iv_z} e^{iv_z/\lambda}$$

$$\chi(v_z)\chi^*(v_z) = \frac{\lambda}{\lambda+iv_z} e^{iv_z/\lambda} \cdot \frac{\lambda}{\lambda-iv_z} e^{-iv_z/\lambda}$$

$$= \frac{\lambda^2}{\lambda^2+v_z^2}$$

$$= \frac{1}{1 + v_z^2/\lambda^2} \qquad \ldots.(27)$$

But $\frac{1}{\lambda^2}$ is the variance of the distribution $= \sigma^2$ and introducing $g = \sigma^2 v_z^2$ as usual, we may write

$$\chi(v_z)\chi^*(v_z) = \frac{1}{1+g} \qquad \ldots.(28)$$

$\chi_2(v_z, -v_z; \tau)$, the joint characteristic function was postulated to be $\frac{1}{1+g[1-C(\tau)]}$ since we certainly require in general that $\lim_{\tau \to 0} \chi_2(v_z, -v_z; \tau) = \chi(v_z)\chi^*(v_z)$ as a necessary condition on $\chi_2(v_x, -v_z; \tau)$. This form of bivariate characteristic function is substantiated in Johnson and Kotz [1972] p.260

$$f(x_1 x_2) = \frac{1}{\sigma_1 \sigma_2 (1-\rho)} \exp\left[-\frac{1}{1-\rho} \left(\frac{x_1}{\sigma_1} + \frac{x_2}{\sigma_2} \right) \right] \cdot I_0\left(\frac{2\sqrt{\rho}}{1-\rho} \sqrt{\frac{x_1 x_2}{\sigma_1 \sigma_2}} \right)$$

$\ldots.(29)$

is a bivariate distribution with negative exponential marginals and correlation ρ (c.f. Appendix 8F). (See also note on Moran's bivariate exponential distribution Johnson and Kotz [1972].

If $\sigma_1 = \sigma_2$

Then $\chi_2(v_z,-v_z;\tau) = \frac{1}{1+g[1-C(\tau)]}$ ....(30)

Then for Type (C) surfaces g>>1, we have

$$I(\theta_2) \sim \frac{F^2}{2L}\int_{-L}^{L} \left|\frac{e^{iv_x\tau}}{1 + g[1 - C(\tau)]}\right| d\tau \qquad ....(31)$$

We now proceed by taking $C(\tau) = e^{-\tau^2/T^2} \simeq 1 - \tau^2/T^2$ the Gaussian model form of autocorrelation much favoured in the past. Whence,

$$I(\theta_2) \simeq \frac{F^2}{2L}\int_{-\infty}^{\infty} \frac{\cos v_x\tau d\tau}{1+g\tau^2/T^2} \qquad ....(32)$$

$$= \begin{cases} \frac{\pi F^2 T}{4L\sqrt{g}} e^{-v_x T/\sqrt{g}} , & v_x>0 \\ \frac{\pi F^2 T}{4L\sqrt{g}} e^{v_x T/\sqrt{g}} , & v_x<0 \end{cases} \qquad ....(33)$$

(c.f. Gradshteyn and Ryzhik's tables of Integrals Series and Products 3.723(2) p.406)

$$= \begin{cases} \frac{\pi F^2 T}{4L\sqrt{g}} e^{-(T/\sigma)\tan\vartheta/2}, & \vartheta>0 \\ \frac{\pi F^2 T}{4L\sqrt{g}} e^{(T/\sigma)\tan\vartheta/2}, & \vartheta<0. \end{cases} \qquad ....(34)$$

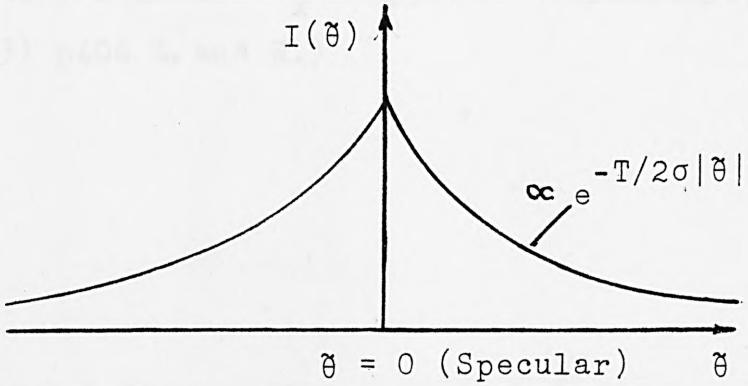

FIG. 8.3.2. Scattering from Type (C) Surface - Neg. Exponential Height Distribution

The intensity is a two-part function about the specular direction and has a cusp point in that direction. Clarke and Thomas [1979] show just such a cusp plot, obtained from a scanning instrument. The curve differs considerably from the Gaussian form:

$$I(\theta_2) = \frac{\sqrt{\pi}F^2T}{2L\sqrt{g}} \exp(-v_x{}^2T^2/4g) \qquad \ldots.(35)$$

when normal surface statistics are deemed appropriate. (c.f. case (6) Chapter 4.) In either situation the curves are completely specified by $\sqrt{g}/T$ or more appropriately by σ/T, a profile mean slope parameter, in keeping with the approximation to geometric scattering for rough Type (C) surfaces (c.f. Chapter 4). Measurements of half-widths of the intensity curves should correlate with this parameter (c.f. Chapter 9).

Again, in practice, autocorrelation functions are more often modelled by $C(\tau) = e^{-|\tau|/T}$ which would lead to

$$I(\theta_2) = \frac{F^2}{2L}\left\{\int_0^\infty \frac{\cos v_x\tau}{1+g\tau/T}\,d\tau + \int_{-\infty}^0 \frac{\cos v_x\tau}{1-g\tau/T}\,d\tau\right\}$$

$$= \frac{F^2}{L}\int_0^\infty \frac{\cos v_x\tau}{1+g\tau/T}\,d\tau$$

$$= \frac{F^2T}{Lg}\left[-\sin(v_xT/g)\,si(v_xT/g) - \cos(v_xT/g)\,ci(v_xT/g)\right], \qquad \ldots.(36) \quad v_x>0$$

($I(\theta_2)$ for negative v_x - appeal to symmetry.) (c.f. 3.722(3) p406 G. and R.)

8.3.3. Surface Height Distribution: zero mean, negatively skewed, gamma

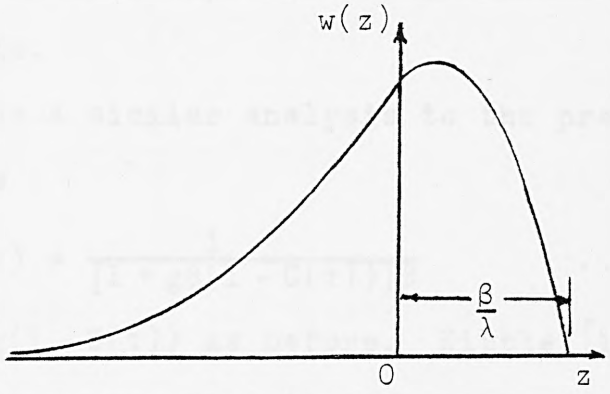

FIG. 8.3.3. Gamma Distribution

$$w(z) = \begin{cases} \lambda\left[\lambda(\beta/\lambda - z)\right]^{\beta-1} e^{-\lambda(\beta/\lambda - z)} / \Gamma(\beta) & , \ z<\beta/\lambda \\ 0 & , \ z>\beta/\lambda \end{cases}$$

[Check: $\int_{-\infty}^{\beta/\lambda} \lambda\left[\lambda(\beta/\lambda - z)\right]^{\beta-1} e^{-\lambda(\beta/\lambda - z)} dz = G$ say

Put $\frac{\beta}{A} - z = \S$

$- dz = d\S$

Then $G = \int_0^\infty \lambda\left[\lambda\S\right]^{\beta-1} e^{-\lambda\S} d\S = \Gamma(\beta)$ as required]

In this case $\chi(v_z) = \int_{-\infty}^{\frac{\beta}{\lambda}} \lambda\left[\lambda\left(\frac{\beta}{\lambda} - z\right)\right]^{\beta-1} e^{-\lambda(\beta/\lambda - z)} e^{iv_z z} dz$

$$= \int_0^\infty \frac{\lambda\left[\lambda\S\right]^{\beta-1} e^{-\lambda\S} e^{iv_z(\beta/\lambda - \S)} d\S}{\Gamma(\beta)}$$

$$= \frac{e^{iv_z\beta/\lambda}}{\Gamma(\beta)} \int_0^\infty \lambda(\lambda\S)^{\beta-1} e^{-(iv_z + \lambda)\S} d\S$$

$$= \frac{e^{iv_z\beta/\lambda}\,\lambda^\beta}{\Gamma(\beta)(iv_z + \lambda)^\beta} \int_0^\infty (iv_z + \lambda)\left[(iv_z + \lambda)\S\right]^{\beta-1} e^{-(iv_z+\lambda)\S} d\S$$

$$= \frac{\lambda^\beta e^{iv_z\beta/\lambda}}{\left[1 + iv_z/\lambda\right]^\beta \lambda^\beta}$$

$$\therefore \quad \chi(v_z)\chi^*(v_z) = \frac{1}{\left[1 + v_z^2/\lambda^2\right]^\beta}$$

$$= \frac{1}{\left[1 + g/\beta\right]^\beta} \qquad \ldots.(37)$$

The gamma distribution is less 'extreme' than the negative exponential and perhaps would provide a better fit to more modestly skewed real-life height distribution data.

If we pursue a similar analysis to the previous case, we suppose

$$\chi_2(v_z,-v_z;\tau) = \frac{1}{[1+g\beta(1-C(\tau))]\beta} \qquad ....(38)$$

replacing g by $g(1-C(\tau))$ as before. Kibble [1940] quotes a bivariate gamma distribution with gamma marginals of order p and correlation ρ, namely

$$f(x_1,x_2) = \frac{\rho^{-\frac{1}{2}(p-1)}(x_1x_2)^{\frac{1}{2}(p-1)}\exp\left[-\frac{(x_1+x_2)}{1-\rho}\right]}{\Gamma(p)(1-\rho)} \cdot I_{\rho-1}\left(\frac{2\sqrt{\rho}}{1-\rho}\sqrt{x_1x_2}\right)$$

which we can generalise to

$$f(x_1,x_2) = \frac{\rho^{-\frac{1}{2}(p-1)}[\lambda(x_1x_2)]^{\frac{1}{2}(p-1)}\exp\left[\frac{-\lambda(x_1+x_2)}{(1-\rho)}\right]}{\Gamma(p)(1-\rho)} \cdot I_{p-1}\left(\frac{2\chi\sqrt{\rho}}{1-\rho}\lambda\sqrt{x_1x_2}\right) \qquad ....(39)$$

The characteristic function, in this case is

$$\chi_2(v_z,-v_z;\rho) = \frac{1}{[1+v_z^2/\lambda^2(1-\rho)]^p} \qquad ....(40)$$

This could be deduced directly, following a precisely similar analysis to that portrayed in Appendix 8F, or by reference to the work of Moran [1969]. Working with the parameter g as usual, we have $\chi_2(v_z,-v_z;\tau) = \frac{1}{\{1+g\beta[1-C(\tau)]\}\beta}$ as postulated.

Then $I(\theta_2) = \frac{F^2}{2L}\int_{-L}^{L} \frac{e^{iv_z\tau}}{\{1 + g/\beta[1 - C(\tau)]\}^\beta} d\tau$

$$\simeq \frac{F^2}{2L}\int_{-L}^{L} \frac{e^{iv_x\tau}}{\{1 + g/\beta.\tau^2/T^2\}^\beta} d\tau$$

$$\simeq \frac{F}{L}\int_{o}^{\infty} \frac{\cos(v_x\tau)}{\{1 + g/\beta.\tau^2/T^2\}^\beta} d\tau \qquad \ldots.(41)$$

$(C(\tau) = e^{-\tau^2/T^2} \simeq 1 - \tau^2/T^2$ etc.)

Available from Gradshteyn and Ryzhik's tables of integrals are a number of special cases:

(i) $\beta = 3/2$ (c.f. p.472 3.876(5))

$$I(\theta_2) = F^2/L \int_{o}^{\infty} \frac{\cos(v_x\tau)}{\{1 + 2g\tau^2/3T^2\}^{3/2}} d\tau \qquad \ldots.(42)$$

$$\begin{cases} \frac{\pi F^2 3^{3/2} T^3}{L(2g)^{3/2}} e^{-v_x\sqrt{3}T/\sqrt{2g}}, & v_x > 0 \\ \frac{\pi F^2 3^{3/2} T^3}{L(2g)^{3/2}} e^{v_x\sqrt{3}T/\sqrt{2g}}, & v_x < 0, \end{cases} \qquad \ldots.(43)$$

which gives a similar output scatter diagram to the previous case.

(ii) $\beta = 2$ (c.f. p.410 3.729(i))

$$I(\theta_2) = \frac{F^2}{2L}\int_{-\infty}^{\infty} \frac{\cos v_x\tau}{\{1 + g\tau^2/2T^2\}^2} d\tau$$

$$\begin{cases} \frac{\pi F^2\sqrt{2}T}{8L\sqrt{g}} \left(1 + \frac{v_x\sqrt{2}T}{\sqrt{g}}\right) e^{-v_x\sqrt{2}T/\sqrt{g}} \\ \frac{\pi F^2\sqrt{2}T}{8L\sqrt{g}} \left(1 - \frac{v_x\sqrt{2}T}{\sqrt{g}}\right) e^{v_x\sqrt{2}T/\sqrt{g}} \end{cases} \qquad \ldots.(45)$$

(iii) $\beta = n$ (positive integer) (p.413 3.737(i))

$$I(\theta_2) = \frac{F^2}{2L}\int_{-\infty}^{\infty} \frac{\cos(v_x\tau)}{\{1 + g\tau^2/nT^2\}^n} d\tau \qquad \ldots.(46)$$

$$= \frac{F}{2L}\int_{-\infty}^{\infty} \frac{\cos(v_x\tau)}{(g/nT^2)^n \left\{\frac{nT^2}{g} + \tau^2\right\}^n} d\tau$$

$$\begin{cases} \left(\frac{\pi F^2}{2L}\,\frac{1}{2^{2n-1}}\,\frac{\sqrt{n}T}{\sqrt{g}}\,\frac{1}{(n-1)!}\sum_{k=0}^{n-1}\frac{(2n-k-2)!(2v_x\sqrt{n}T/g)^k}{k!(n-k-1)!}\right).\ e^{-v_x\sqrt{n}T/\sqrt{g}}, & v_x>0 \\ \left(\frac{\pi F^2}{2L}\,\frac{1}{2^{2n-1}}\,\frac{\sqrt{n}T}{\sqrt{g}}\,\frac{1}{(n-1)!}\sum_{k=0}^{n-1}\frac{(2n-k-2)!(-2v_x\sqrt{n}T/g)^k}{k!(n-k-1)!}\right) e^{v_x\sqrt{n}T/\sqrt{g}}, & v_x<0. \end{cases} \quad \ldots.(47)$$

(N.B. (ii) is simply a special case of (iii)),

The expression for the intensity curve can be compared with the p.d.f. for the difference of two gammas (p.272 of Kendall & Stuart, Vol. 1 [1969]), confirming the description in terms of geometrical scattering.

For small v_x,

$$\begin{cases} \frac{\pi F^2}{2L}\,\frac{1}{2^{2n-1}}\,\frac{\sqrt{n}T}{\sqrt{g}}\,\frac{1}{(n-1)!}\left\{\frac{(2n-2)!}{(n-1)!}+\frac{(2n-3)!}{(n-2)!}\left(\frac{2v_x\sqrt{n}T}{\sqrt{g}}\right)\right\}e^{-v_x\sqrt{n}T/\sqrt{g}} \\ \frac{\pi F^2}{2L}\,\frac{1}{2^{2n-1}}\,\frac{\sqrt{n}T}{\sqrt{g}}\,\frac{1}{(n-1)!}\left\{\frac{(2n-2)!}{(n-1)!}+\frac{(2n-3)!}{(n-2)!}\left(\frac{-2v_x\sqrt{n}T}{\sqrt{g}}\right)\right\}e^{v_x\sqrt{n}T/\sqrt{g}} \end{cases}$$

$$\begin{cases} \frac{\pi F^2}{2L}\,\frac{1}{2^{2n-1}}\,\frac{\sqrt{n}T}{\sqrt{g}}\,\frac{(2n-3)!2}{(n-1)!(n-2)!}\left\{1+\frac{v_x\sqrt{n}T}{\sqrt{g}}\right\}e^{-v_x\sqrt{n}T/\sqrt{g}}, & v_x>0 \\ \frac{\pi F^2}{2L}\,\frac{1}{2^{2n-1}}\,\frac{\sqrt{n}T}{\sqrt{g}}\,\frac{(2n-3)!2}{(n-1)!(n-2)!}\left\{1-\frac{v_x\sqrt{n}T}{\sqrt{g}}\right\}e^{v_x\sqrt{n}T/\sqrt{g}}, & v_x<0. \end{cases}$$

$$\propto\ (1 - nv_x^2T^2/g), \quad \ldots.(48)$$

which is locally quadratic at $v_x = 0$.

(iv) $\beta = \mu + 1$ (μ not integer)

p.429 3.773(4) of G. & R. offers some help in this case, although the analytic solution involves several advanced mathematical functions.

For the graphs of intensity versus angle, the most noticable change is the removal of the cusp in the specular direction for $\beta \geq 2$; less apparent is the inflexion in the curves. The rate of decay at larger off-specular angles (for fixed surface roughness parameters T and g, is of

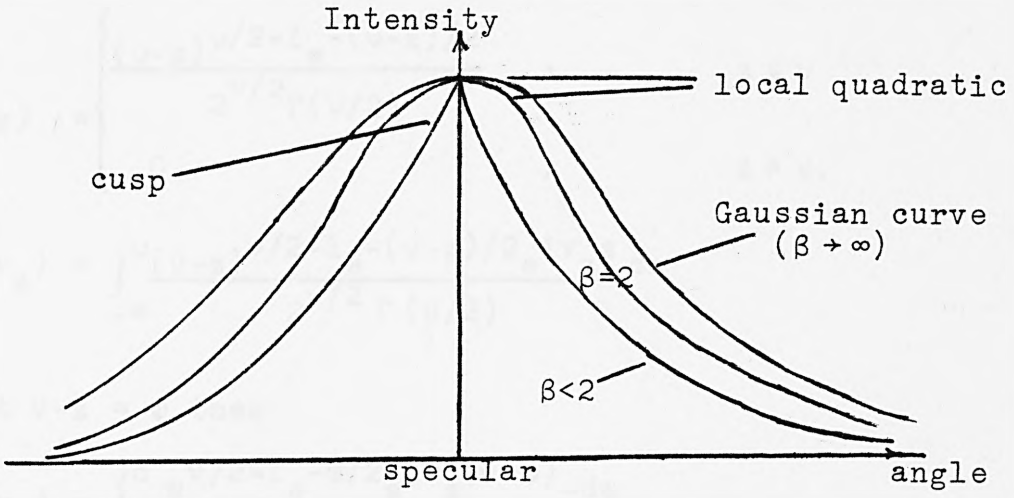

FIG. 8.3.4. Scattering from Type (C) Surface - Gamma Height Distribution

order $e^{-\sqrt{\beta}v_x T/\sqrt{g}}$ i.e. the exponent varies as $\sqrt{\beta}$. The local behaviour in the specular direction is quadratic, the curvature being proportional to β.

N.B. $\sqrt{\beta}v_x T/\sqrt{g} \sim \sqrt{\beta}T/(2\sigma)\tilde{\theta}$ ($\tilde{\theta}$ = off-specular angle) and for large β, the gamma distribution tends to the normal, as the expression $\{\frac{1+g\tau^2/T^2}{\beta}\}^{-\beta} \rightarrow e^{-g\tau^2/T^2}$ which leads to the Gaussian output curve.

8.3.3. Surface Height Distribution: zero mean negatively skewed, transformed Chi-squared

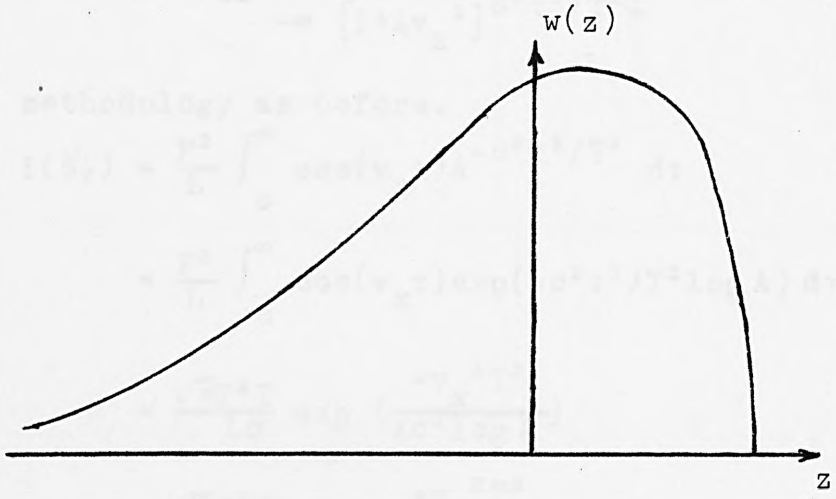

FIG. 8.3.5. Chi-Squared Distribution of Surface Heights

$$w(z) = \begin{cases} \dfrac{(\nu-z)^{\nu/2-1} e^{-(\nu-z)/2}}{2^{\nu/2}\Gamma(\nu/2)}, & z \leqslant \nu \\ 0, & z > \nu. \end{cases}$$

$$\chi(v_z) = \int_{-\infty}^{\nu} \frac{(\nu-z)^{\nu/2-1} e^{-(\nu-z)/2} e^{iv_z z}}{2^{\nu/2}\Gamma(\nu/2)}\, dz$$

Put $\nu - z = \psi$ then

$$\chi(v_z) = \int_{\infty}^{0} \frac{\psi^{\nu/2-1} e^{-\psi/2} e^{iv_z(\nu+\psi)}}{2^{\nu/2}\Gamma(\nu/2)} -d\psi$$

$$= e^{iv_z\nu} \int_0^{\infty} \frac{\psi^{\nu/2-1} e^{-(1+2iv_z)\psi/2}}{2^{\nu/2}\Gamma(\nu/2)} d\psi$$

$$= \frac{e^{iv_z\nu}}{[1+2iv_z]^{\nu/2}} \int_0^{\infty} \frac{\phi^{\nu/2-1} e^{-\phi/2}}{2^{\nu/2}\Gamma(\nu/2)} d\phi \Big| \phi = (1+2iv_z)\psi$$

$$= 1$$

$$= \frac{e^{iv_z\nu}}{[1+2iv_z]^{\nu/2}}$$

$$\therefore \quad \chi(v_z)\chi^*(v_z) = \frac{1}{[1+4v_z^2]^{\nu/2}} \qquad \ldots.(49)$$

For the Chi-squared distribution $\sigma^2 = 2\nu$ and so we propose that $\chi_2(v_z, -v_z; \tau) = \dfrac{1}{[1+4v_z^2]^{\sigma^2(1-C(\tau))/4}}$ $\ldots.(50)$

Whence $I(\theta_2) = \dfrac{F^2}{2L} \displaystyle\int_{-\infty}^{\infty} \frac{\cos(v_x\tau)}{[1+4v_z^2]^{\sigma^2\tau^2/T^2 4}} dz$, using the same methodology as before.

Then $I(\theta_2) = \dfrac{F^2}{L} \displaystyle\int_0^{\infty} \cos(v_x\tau) A^{-\sigma^2\tau^2/T^2}\, d\tau$

$$= \frac{F^2}{L} \int_0^{\infty} \cos(v_x\tau) \exp(-\sigma^2\tau^2/T^2 \log A)\, d\tau$$

$$= \frac{\sqrt{\pi} F^2 T}{L\sigma} \exp\left(\frac{-v_x^2 T^2}{4\sigma^2 \log A}\right)$$

i.e. $I(\theta_2) = \dfrac{\sqrt{\pi} F^2 T}{L\sigma} \exp\left(\dfrac{-v_x^2 T^2}{\sigma^2 \log[1+4v_z^2]}\right)$ $\ldots.(51)$

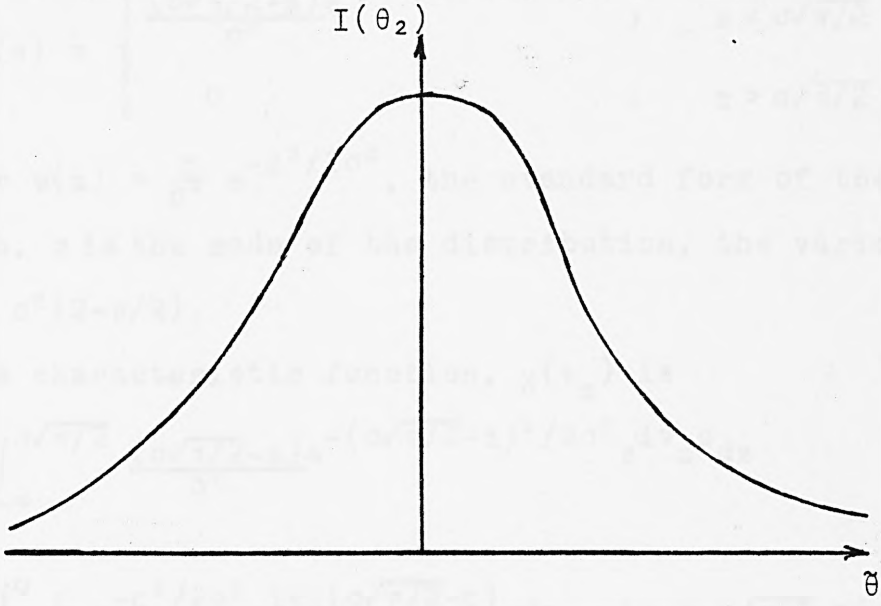

FIG. 8.3.6. Scattering from Type (C) Surface - Chi-Square Height Distribution

8.3.4. Surface Height Distribution : zero mean negatively skewed, Rayleigh

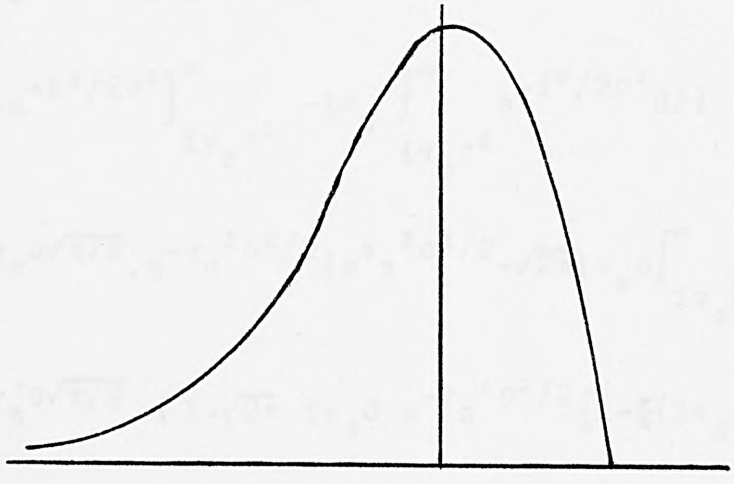

FIG. 8.3.7. Rayleigh Distribution of Surface Heights

$$w(z) = \begin{cases} \dfrac{(\sigma\sqrt{\pi/2}-z)}{\sigma^2} e^{-(\sigma\sqrt{\pi/2}-z)^2/2\sigma^2}, & z < \sigma\sqrt{\pi/2} \\ 0, & z > \sigma\sqrt{\pi/2}. \end{cases}$$

N.B. For $w(z) = \frac{z}{\sigma^2} e^{-z^2/2\sigma^2}$, the standard form of the Rayleigh, σ is the mode of the distribution, the variance is in fact $\sigma^2(2-\pi/2)$.

The characteristic function, $\chi(v_z)$ is

$$= \int_{-\infty}^{\sigma\sqrt{\pi/2}} \frac{(\sigma\sqrt{\pi/2}-z)}{\sigma^2} e^{-(\sigma\sqrt{\pi/2}-z)^2/2\sigma^2} e^{iv_z z} dz$$

$$= \int_{-\infty}^{0} \frac{\zeta}{\sigma^2} e^{-\zeta^2/2\sigma^2} e^{iv_z(\sigma\sqrt{\pi/2}-\zeta)} -d\zeta \quad (z = \sigma\sqrt{\pi/2}-\zeta)$$

$$= e^{iv_z\sigma\sqrt{\pi/2}} \int_{0}^{\infty} \frac{\zeta}{\sigma^2} e^{-(\zeta+iv_z\sigma^2)^2/2\sigma^2} e^{-iv_z{}^2\sigma^2/2} d\zeta$$

$$= e^{iv_z\sigma\sqrt{\pi/2}} . e^{-v_z{}^2\sigma^2/2} \int_{iv_z\sigma^2}^{\infty} \frac{(\S - iv_z\sigma^2)}{\sigma^2} e^{-\S^2/2\sigma^2} d\S$$

on substituting $\zeta + iv_z\sigma^2 = \S$.

$$= e^{iv_z\sigma\sqrt{\pi/2}} . e^{-v_z{}^2\sigma^2/2} \times$$

$$\{ \left[-e^{-\S^2/2\sigma^2} \right]_{iv_z\sigma^2}^{\infty} - iv_z \int_{iv_z\sigma^2}^{\infty} e^{-\S^2/2\sigma^2} d\S \}$$

$$= e^{iv_z\sigma\sqrt{\pi/2}} . e^{-v_z{}^2\sigma^2/2} \{ e^{v_z{}^2\sigma^2/2} - \sqrt{2\pi} iv_z\sigma \int_{iv_z\sigma}^{\infty} \frac{1}{\sqrt{2\pi}} e^{-\S^2/2} d\S \}$$

$$= e^{iv_z\sigma\sqrt{\pi/2}} . \{ 1 - \sqrt{2\pi}\, iv_z\sigma\, e^{-v_z{}^2\sigma^2/2} [1 - \underline{\Phi}(iv_z\sigma)] \} \quad \ldots\ldots (52)$$

For the probability integral $\underline{\Phi}(iv_z\sigma) = \int_{-\infty}^{iv_z\sigma} \frac{1}{\sqrt{2\pi}} e^{-y^2/2} dy$,

$\underline{\Phi}(0) = 1/2$ and we propose to expand $\phi(iv_z\sigma)$ as a Maclaurin power series about $v_z = 0$.

$$\underline{\Phi}'(iv_z\sigma) = 1/\sqrt{2\pi}\ e^{v_z^2\{^2/2}(i\sigma) \quad ; \quad \underline{\Phi}'(0) = i\sigma/\sqrt{2\pi}$$

$$\underline{\Phi}''(iv_z\sigma) = (v_z\sigma^2)\ \frac{1}{\sqrt{2\pi}}\ e^{v_z^2\sigma^2/2}(i\sigma) \ ; \ \underline{\Phi}''(0) = 0$$

$$\underline{\Phi}''(iv_z\sigma) = (v_z\sigma^2)\underline{\Phi}'(iv_z\sigma)$$

Differentiating n times (Leibniz),

$$\underline{\Phi}^{(n+2)}(iv_z\sigma) = (v_z\sigma^2)\underline{\Phi}^{(n+1)}(iv_z\sigma) + n\sigma^2\underline{\Phi}^{(n)}(iv_z\sigma)$$

$$\underline{\Phi}^{(n+2)}(0) = n\sigma^2\underline{\Phi}^{(n)}(0)$$

Since $\underline{\Phi}''(0) = 0$, it follows that $\underline{\Phi}^{(2m)}(0) = 0$ for m=1,2, ..., whilst $\underline{\Phi}^{(2m+1)}(0) = (2m-1)(2m-3).\ 3.1\ \sigma^{2m+1}\frac{i}{\sqrt{2\pi}}$ m=1,1,2 ..., for the odd derivatives.

$$\therefore\ \underline{\Phi}(iv_z\sigma) = \tfrac{1}{2} + \frac{i}{\sqrt{2\pi}}\left(\sigma v_z + \sum_{m=1}^{\infty} \frac{(2m-1)(2m-3)..3.1(\sigma v_z)^{2m+1}}{(2m+1)!}\right)$$

$$= \tfrac{1}{2} + \frac{i}{\sqrt{2\pi}}\,\psi(\sigma v_z) \text{ say, } (\psi(\sigma v_z) \text{ is real})$$

$$\chi(v_z) = e^{iv_z\sigma\sqrt{\pi/2}}\left\{1-(\sqrt{2\pi}iv_z\sigma\ e^{-v_z^2\sigma^2/2})\left[\tfrac{1}{2} - \frac{i}{\sqrt{2\pi}}\psi(\sigma v_z)\right]\right\}$$

$$= e^{i\sqrt{g\pi/2}}\left\{1-i\sqrt{2\pi g}\ e^{-g/2}\left[\tfrac{1}{2} - \frac{i}{\sqrt{2\pi}}\psi(\sqrt{g})\right]\right\}, \quad ....(53)$$

on writing $\sqrt{g} = \sigma v_z$ as is our usual practice, although σ is not the S.D. of height p.d.f. in this case remember.

$$x(v_z) = e^{i\sqrt{g\pi/2}}\left\{1-\sqrt{g}e^{-g/2}\psi(\sqrt{g}) - i\sqrt{g\pi/2}\ e^{-g/2}\right\}$$

$$\chi(v_z)\chi^*(v_z) = \{1-\sqrt{g}e^{-g/2}\psi(\sqrt{g})\}^2 + (\sqrt{\pi g/2}\ e^{-g/2})^2$$

$$= 1-2\sqrt{g}e^{-g/2}\psi(\sqrt{g}) + ge^{-g}\psi^2(\sqrt{g}) + \frac{\pi g}{2}e^{-g}$$

....(54)

We now propose the two-dimensional characteristic function

$$\chi_2(v_z,-v_z;\rho) = 1-2\sqrt{g}(1-\rho)e^{-g/2(1-\rho)}\psi(\sqrt{g(1-\rho)})$$
$$+g(1-\rho)\psi^2(\sqrt{g(1-\rho)}) + \frac{\pi g}{2}(1-\rho)e^{-g(1-\rho)}$$

....(55)

and $\chi_2(v_z,-v_z;\tau)$

$$\simeq 1-2\sqrt{g\tau^2/T^2}e^{-g\tau^2/2T^2}\psi(\sqrt{g\tau^2/T^2})$$

$$+ g\tau^2/T^2\psi^2(\sqrt{g\tau^2/T^2}) + \pi g\tau^2/2T^2\ e^{-g\tau^2/T^2} \quad ....(56)$$

The intensity, $I(\theta_2) = \frac{F^2}{2L}\int_{-\infty}^{\infty} \cos v_x\tau\chi_2(v_z,-v_z;\tau)d\tau.$

We include as many terms in $\psi(\sqrt{g})$ as is deemed desirable.

$\psi(\sqrt{g}) = \sqrt{g}+g^{3/2}/3! + \ldots$ and we may check our working by evaluating the early terms of $\chi(v_z)\chi^*(v_z)$ as a power series in g, and then compare the result with equ (3) of Appendix 8I computed on the basis of moments μ'_r from Appendix 8A.

8.3.5. <u>Surface Height Distribution : zero mean, negatively skewed; Poisson, Neg. Binomal</u>

In the past the Poisson distribution has been used to fit surface height data (Tanner and Fahoum [1976]). A joint characteristic function $\chi_2(v_z,-v_z)$ can be deduced from the bivariate Poisson distribution on p.298 of Johnson & Kotz [1969];

$$\chi_2(v_z,-v_z) = \exp[-(\sigma^2-\S)(1-e^{iv_z})-(\sigma^2-\S)(1-e^{-iv_z})]$$

$$= \exp[-2\sigma^2+2\S + (\sigma^2-\S)(e^{iv_z}+e^{-iv_z})]$$

$$= \exp[-2\sigma^2(1-\S/\sigma^2)(1-\cos v_z)] \quad ....(57)$$

The marginals of the above are Poisson, with variance σ^2 and covariance §. Thus $\S/\sigma^2$ is the correlation.

We may then write

$$\chi_2(v_z,-v_z;\tau) = \exp[-2\sigma^2(1-C(\tau))(1-\cos v_z)] \quad ....(58)$$

Therefore, $I(\theta_2) = \frac{F^2}{2L}\int_{-\infty}^{\infty}\cos(v_x\tau)\exp\left[-\frac{2\sigma^2\tau^2}{T^2}(1-\cos v_z)\right]d\tau,$ ....(59)

which is an integral form closely resembling that for the

normal case of Chapter 4. (If we take v_z small so that $1-\cos v_z \simeq v_z^2/2$ the solution leads precisely to equation (46) of Chapter 4.

Tanner [1976] introduced the Poisson to model the skewness of actual distributions of surface height. He also used a 3-Gaussian model to achieve the same ends. The negative binomial is, in some circumstances, a compound distributions of Poissons. Its characteristic function may be expressed as $\chi(v_z) = (Q - Pe^{iv_z})^{-N}$, and so

$$\chi(v_z)\chi^*(v_z) = \frac{1}{\left[(Q-Pe^{iv_z})(Q-Pe^{-iv_z})\right]^N} \quad \ldots.(60)$$

$$= \frac{1}{\left[Q^2+P^2 - 2PQ\cos v_z\right]^N} \quad \ldots.(61)$$

Since $Q-P = 1$, we have $\chi(v_z)\chi^*(v_z)$

$$= \frac{1}{\left[1 + 2PQ(1-\cos v_z)\right]^N}$$

$$= \frac{1}{\left[1 + 2\sigma^2/N(1-\cos v_z)\right]^N}$$

We take $\chi_2(v_z,-v_z;\rho) = \dfrac{1}{\left[1 + \dfrac{2\sigma^2}{N}(1-\rho)(1-\cos v_z)\right]^N}$ $\ldots.(62)$

which leads to

$$I(\theta_2) = \frac{F^2}{2L}\int_{\infty}^{\infty} \frac{\cos v_x \tau d\tau}{\left[1 + \dfrac{2\sigma^2\tau^2}{NT^2}(1-\cos v_z)\right]^N} \quad \ldots.(63)$$

with N not necessarily an integer. Here the integral closely resembles that for the gamma distribution of heights described in 8.3.2

The vast majority of statistical distributions do not have a simple form of characteristic function although in certain important cases the full set of moments is readily available. A case in point is the Beta distribution, a

modified form of which, namely the Pearson type I frequency distribution, has been verified as accurately modelling actual surface profile data Watson et al [1979].

8.3.6. Surface Height Distribution : zero mean, negatively skewed, Beta

$$w(z) = \begin{cases} \dfrac{(z+\frac{m}{m+n})^{m-1}(\frac{n}{m+n}-z)^{n-1}}{B(m,n)}, & \frac{-m}{m+n} < z < \frac{n}{m+n} \\ 0, & \text{otherwise.} \end{cases}$$

Then $\chi(v_z) = E\left[e^{iv_z z}\right]$

$$= \int_{\frac{-m}{m+n}}^{\frac{n}{m+n}} \frac{(z+\frac{m}{m+n})^{m-1}(\frac{n}{m+n}-z)^{n-1}}{B(m,n)} e^{iv_z z} dz$$

$$= \frac{1}{B(m,n)} \int_{\frac{-m}{m+n}}^{\frac{n}{m+n}} (z+\frac{m}{m+n})^{m-1}(\frac{n}{m+n}-z)^{n-1} e^{iv_z(z+\frac{m}{m+n}-\frac{m}{m+1})} dz$$

$$= \frac{e^{\left[-iv_z \frac{m}{m+n}\right]}}{B(m,n)} \int_{\frac{-m}{m+n}}^{\frac{n}{m+n}} (z+\frac{m}{m+n})^{m-1}(\frac{n}{m+n}-z)^{n-1} \sum_{r=0}^{\infty} \frac{\{iv_z(z+\frac{m}{m+n})\}^r}{r!} dz$$

$$= \frac{e^{\left[-iv_z \frac{m}{m+n}\right]}}{B(m,n)} \sum_{r=0}^{\infty} \frac{(iv_z)^r}{r!} \int_{\frac{-m}{m+n}}^{\frac{n}{m+n}} (z+\frac{m}{m+n})^{m+r-1}(\frac{n}{m+n}-z)^{n-1} dz$$

$$= \frac{e^{\left[-iv_z \frac{m}{m+n}\right]}}{B(m,n)} \sum_{r=0}^{\infty} B(m+r,n) \frac{(iv_z)^r}{r!}$$

$$= e^{\left[-iv_z \frac{m}{m+n}\right]} \sum_{r=0}^{\infty} \frac{B(m+r,n)(iv_z)^r}{B(m,n)\ r!}$$

$$= e^{\left[-iv_z \frac{m}{m+n}\right]} \sum_{r=0}^{\infty} \frac{\Gamma(m+n)/\Gamma(m)\Gamma(n)}{\Gamma(m+r+n)/\Gamma(m+r)\Gamma(n)} \frac{(iv_z)^r}{r!}$$

$$= e^{\left[-iv_z \frac{m}{m+n}\right]} \sum_{r=0}^{\infty} \frac{\Gamma(m+n)\Gamma(m+r)}{\Gamma(m)\Gamma(m+r+m)} \frac{(iv_z)^r}{r!}$$

$$= e^{\left[-iv_z \frac{m}{m+n}\right]} \{1 + \frac{m}{m+n}\frac{(iv_z)}{1!} + \frac{m(m+1)}{(m+n)(m+n+1)}\frac{(iv_z)^2}{2!} + \ldots\}$$

$$= e^{\left[-iv_z \frac{m}{m+n}\right]} \Phi(m,m+n;iv_z) \qquad \ldots.(64)$$

where $\underline{\Phi}(m,m+n;iv_z)$ is termed a degenerate hyper-geometric function).

$$\chi(v_z)\chi^*(v_z) = \underline{\Phi}(m,m+n;iv_z)\underline{\Phi}(m,m+n;-iv_z) \qquad ....(65)$$

We forego the general case and explore the special case when $m = n = p+\frac{1}{2}$ as this offers some prospect of a tractable solution.

N.B. The beta distribution is now symmetrical about zero.

We use the identity $\underline{\Phi}(p+\frac{1}{2},\ 2p+1;\ 2iz)$

$$= \Gamma(p+1)\ (\tfrac{z}{2})^{-p}\ e^{iz}J_p(z) \qquad \text{(p.1059 of G. and R.)}$$

$$\chi(v_z)\chi^*(v_z) = \{\Gamma(p+1)\}^2(\tfrac{v_z}{2^2})^{-2p}\ \{J_p(v_z/2)\}^2$$

$$\{\Gamma(p+1) = \{\Gamma(p+1)\ (\tfrac{v_z}{2^2})^{-p}\ J_p(^{v}z/2)\}^2$$

$$= \{\Gamma(p+1)\}^2(\tfrac{v_z}{2^2})^{-2p} \sum_{k=0}^{\infty} \frac{(-1)^k(v_z/2^2)^{2p+2k}\Gamma(2p+2k+1)}{\Gamma(2p+k+1)\Gamma(p+k+1)\Gamma(p+k+1)}$$

(c.f. p.960 of G. and R.)

$$= \sum_{k=0}^{\infty} (-1)^k\ (\tfrac{v_z}{2^2})^{2k}\ \frac{\Gamma(2p+2k+1)}{\Gamma(2p+k+1)}\left\{\frac{\Gamma(p+1)}{\Gamma(p+k+1)}\right\}^2 \qquad ....(66)$$

$$= 1 - \frac{(2p+2)}{(p+1)}\ \frac{v_z^2}{16} + \frac{(2p+4)(2p+3)}{\{(p+2)(p+1)\}^2}\ \frac{(^{v}z)^4}{256} - \ldots$$

$$= 1 - \frac{1}{(p+1)}\ \frac{v_z^2}{8} + \frac{(2p+3)}{\{(p+2)(p+1)\}^2}\frac{(^{v}z)^4}{128} \qquad ....(67)$$

But $\sigma^2 = \dfrac{mn}{(m+n)^2(m+n+1)}$ $\qquad m = n = p+\frac{1}{2}$

$$= \frac{n^2}{4n^2(2n+1)} = \frac{1}{4(2p+2)} = \frac{1}{8(p+1)}$$

$$\chi(v_z)\chi^*(v_z) = 1 - \sigma^2 v_z{}^2 + \frac{(2p+3)}{(p+2)}\ \frac{(\sigma^2 v_z{}^2)^2}{2} - \ldots$$

$$= 1 - g + \frac{2(p+1)+1}{(p+1+1)} \cdot \frac{g^2}{2} - \ldots$$

$$= 1 - g + \frac{1/4+\sigma^2}{1/8+\sigma^2}\ \cdot \frac{g^2}{2} - \ldots \qquad ....(68)$$

Take $\chi_2(v_z,-v_z;\tau)$ to be

$$= 1 - g\tau^2/T^2 + \frac{\frac{1}{4}+\sigma^2\tau^2/T^2}{\frac{1}{8}+\sigma^2\tau^2/T^2}\cdot\frac{(g\tau^2/T^2)^2}{2} - \ldots \qquad \ldots.(69)$$

$$\simeq 1 - g\tau^2/T^2 + (g\tau^2/T^2)^2 - \ldots \text{ for } \sigma^2/T^2 \text{ small (small slopes)}$$

$$\simeq \frac{1}{[1+g\tau^2/T^2]}$$, which leads to the negative exponential solution of 8.3.1.

For interest, the rectangular distribution:

$w(z) = \frac{1}{2h}$, $a-h < z < a+h$ is such that

$$\chi(v_z) = e^{iv_z a}\left(\frac{\sin v_z h}{v_z h}\right) = e^{iv_z a}\,\mathrm{sinc}\, v_z h\,. \qquad \ldots.(70)$$

$$\therefore\ \chi(v_z)\chi^*(v_z) = \sin^2 c v_z h = \sin^2 c v_z\sqrt{3}\sigma = \sin^2 c\sqrt{3g} \qquad \ldots.(71)$$

From which $\chi_2(v_z,-v_z;\rho) = \sin^2 c\sqrt{3g(1-\rho)}$ $\ldots.(72)$

and $\chi_2(v_z,-v_z;\tau) = \sin^2 c\sqrt{3g\tau^2/T^2}$ $\ldots.(73)$

Then $I(\theta_2) = \frac{F^2}{2L}\int_{-\infty}^{\infty} \frac{\cos(v_x\tau)\sin^2\sqrt{3g}\ \tau/T}{(\sqrt{3g}\tau/T)^2}\, d\tau$, $\ldots.(74)$

leads to the triangular function:

$$I(\theta_2) = \begin{cases} \frac{\pi}{2}\ \frac{T}{\sqrt{3g}}\left(1 - \frac{T}{\sqrt{3}\sigma}\,\frac{\tilde{\theta}}{2}\right) & 0 < \tilde{\theta} < 2\sqrt{3}\sigma/T \\ \frac{\pi}{2}\ \frac{T}{\sqrt{3g}}\left(\frac{T}{\sqrt{3}\sigma}\,\frac{\tilde{\theta}}{2} + 1\right) & -2\sqrt{3}\sigma/T < \tilde{\theta} < 0 \end{cases} \qquad \ldots.(75)$$

The distribution of slopes, based on the difference of rectangular random variables, is well understood to be the corresponding triangular density.

8.4 Conclusions

The wave theory of scattering provides an adequate explanation of the speckle intensity distributions, illustrated in Figures 8.1.2 and 8.1.3, obtained from the interrogation of sheet steel material by an incident laser beam. In addition the theory suggests simple probability distributions which describe both specular and off-specular scattering. Such distributions enable thesholds to be set when monitoring and detecting surface defects and would precisely quantify the false alarm rate when employing an automatic detection system.

The distribution of light scattered from very smooth ground glass mirror surfaces, as portrayed in Figures 8.2.7. and 8.2.8., can be substantiated by the Kirchhoff wave theory of scattering. The mathematical justification presented, was based on a particular form of autocorrelation of the surface texture, and whilst it remains to check whether talysurf traces of the specimens employed formally validate this supposition, the form of the autocorrelation is commonly met in ground metal surfaces. The mathematical model autocorrelation function could be modified, to allow for a periodic component for instance, and the same general results could be derived.

The grinding process, by which the glass surfaces are prepared, frequently creates anisotropic surfaces whose texture have a definite lay. For such surfaces the one-dimensional surface roughness model is appropriate, and the empirical fitting of $\text{cosec}^2\theta$ to log (intensity) has been granted theoretical support as an approximation to part of the range of a Lorenzian-type scatter function. For truely

isotropic surfaces, theory suggests that the order of the fit is in fact $\text{cosec}^3\theta$.

The discussion of surfaces possessing non-Gaussian height distributions has been largely confined to very rough Type (C) surfaces. Although in most instances non-Gaussian Type (A) and Type (B) surfaces could have been incorporated in the discussion. As an illustration, negative exponential Type (A) and Type (B) surfaces are treated in Appendix 8G.

Intensity curves from non-Gaussian Type (C) surfaces are not over sensitive to slight deviations from normality. The indication therefore, is that the estimation procedures considered in Chapter 9 would still yield useful comparative estimates of surface roughness parameters should assumptions of normality be invalid.

APPENDIX 8A

Statistics of the Rayleigh Distribution

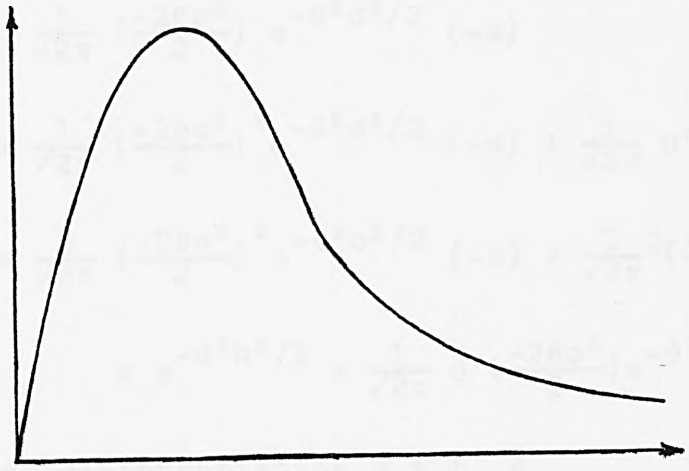

$$\begin{cases} \frac{x}{\sigma^2} e^{-x^2/2\sigma^2}, & x > 0 \\ 0, & x > 0 \end{cases}$$

$$M_x(\theta) = \int_o^\infty \frac{x}{\sigma^2} e^{-x^2/2\sigma^2} e^{x\theta} dx \qquad \ldots.(1)$$

$$= \int_o^\infty \frac{x}{\sigma^2} e^{-(x-\theta\sigma^2)^2/2\sigma^2} e^{\theta^2\sigma^2/2} dx$$

$$= e^{\frac{\theta^2\sigma^2/2}{\sigma^2}} \int_{-\theta\sigma^2}^\infty (y + \theta\sigma^2) e^{-y^2/2\sigma^2} \qquad y = x-\theta\sigma^2$$

$$= e^{\frac{\theta^2\sigma^2/2}{\sigma^2}} \{ \left[-\sigma^2 e^{-y^2/2\sigma^2} \right]_{-\theta\sigma^2}^\infty + \theta\sigma^2 \int_{-\theta\sigma^2}^\infty e^{-y^2/2\sigma^2} dy \}$$

$$= e^{\theta^2\sigma^2/2} \cdot e^{-\theta^2\sigma^2/2} + e^{\theta^2\sigma^2/2} \theta\sqrt{2\pi}\sigma \int_{-\theta\sigma^2}^\infty \frac{1}{\sqrt{2\pi}} \frac{1}{\sigma} e^{-y^2/2\sigma^2} dy$$

$$= 1 + \theta\sigma\sqrt{2\pi}\, e^{\theta^2\sigma^2/2} \int_{-\theta\sigma}^\infty \frac{1}{\sqrt{2\pi}} e^{-z^2/2} dz \qquad z = y/\sigma$$

$$\therefore \underline{M_x(\theta) = 1 + \theta\sigma\sqrt{2\pi}\, e^{\theta^2\sigma^2/2} \left[1-\Phi(-\theta\sigma)\right]} \qquad \ldots.(2)$$

where $\underline{\Phi}(-\theta\sigma) = \int_{-\infty}^{-\theta\sigma} \frac{1}{\sqrt{2\pi}} e^{-z^2/2} dz \qquad (\underline{\Phi}(0) = \frac{1}{2})$

Then $\underline{\Phi}'(-\theta\sigma) = \frac{1}{\sqrt{2\pi}} e^{-\theta^2\sigma^2/2} . (-\sigma).$

$$\underline{\Phi}''(-\theta\sigma) = \frac{1}{\sqrt{2\pi}} \left(\frac{-2\theta\sigma^2}{2}\right) e^{-\theta^2\sigma^2/2} (-\sigma)$$

$$\underline{\Phi}'''(-\theta\sigma) = \frac{1}{\sqrt{2\pi}} \left(\frac{-2\theta\sigma^2}{2}\right)^2 e^{-\theta^2\sigma^2/2} (-\sigma) + \frac{1}{\sqrt{2\pi}} \sigma^3 e^{-\theta^2\sigma^2/2}$$

$$\underline{\Phi}'''(-\theta\sigma^2) = \frac{1}{\sqrt{2\pi}} \left(\frac{-2\theta\sigma^2}{2}\right)^3 e^{-\theta^2\sigma^2/2} (-\sigma) + \frac{1}{\sqrt{2\pi}} 2\left(\frac{-2\theta\sigma^2}{2}\right).\sigma^3$$

$$\times e^{-\theta^2\sigma^2/2} + \frac{1}{\sqrt{2\pi}} \sigma^3 \left(\frac{-2\theta\sigma^2}{2}\right) e^{-\theta^2\sigma^2/2}$$

where $'$ denotes differentiation w.r.t. θ.

$$\Phi'(0) = -\sigma/\sqrt{2\pi}$$

$$\Phi''(0) = 0$$

$$\Phi'''(0) = \frac{1}{\sqrt{2\pi}}\sigma^3$$

$$\Phi''''(0) = 0$$

$$\therefore M_x(\theta) \simeq 1 + \theta\sigma\sqrt{2\pi}\, e^{\theta^2\sigma^2/2} \left[\frac{1}{2} + \frac{1}{\sqrt{2\pi}}\sigma\theta + \frac{1}{\sqrt{2\pi}}\sigma^3\theta^3/3! + 0 \ldots \right]$$

$$= 1 + \theta\sigma\sqrt{2\pi} \left(1 + \frac{\theta^2\sigma^2}{2} + \frac{\theta^4\sigma^4}{4} . \frac{1}{2!} + \ldots\right) \left[\frac{1}{2} + \frac{1}{\sqrt{2\pi}}\sigma\theta - \frac{\sigma^3\theta^3}{\sqrt{2\pi}} \frac{1}{3!} + \ldots \right.$$

$$= 1 + \tfrac{1}{2}\sqrt{2\pi}\theta\sigma + \sigma\theta^2 + \left(\frac{\sqrt{2\pi}}{2} . \frac{1}{2}\right)\sigma^3\theta^3 + \left(\frac{1}{2} - \frac{1}{6}\right)\sigma^3\theta^3 + \ldots$$

$$= 1 + \sqrt{\frac{\pi}{2}}\sigma\theta + 2\sigma^2 \frac{\theta^2}{2!} + 3\sqrt{\frac{\pi}{2}} \frac{\sigma^3\theta^3}{3!} + \frac{8\sigma^4\theta^4}{4!} + \ldots$$

$$\ldots.(3)$$

From which we read $\mu_1 (= \text{mean}) = \sqrt{\frac{\pi}{2}}\sigma$

$$\mu_2' = 2\sigma^2$$

$$\mu_3' = 3\sqrt{\frac{\pi}{2}}\,\sigma^3$$

$$\mu_4' = 8\sigma^4$$

For moments of the Rayleigh distribution in general, we may use direct methods:

$$\mu_2' = \int_0^\infty x^{2m} \frac{x}{\sigma^2} e^{-x^2/2\sigma^2} dx$$

$$= \left[x^{2m} \cdot e^{-x^2/2\sigma^2}\right]_0^\infty + \int_0^\infty (2m)x^{2m-1} e^{-x^2/2\sigma^2} dx$$

$$= (2m)\sigma^2 \int_0^\infty x^{2m-2} \frac{x}{\sigma^2} e^{-x^2/2\sigma^2} dx$$

$$= (2m)\sigma^2 \mu'_{2m-2}$$

$$= (2m)\sigma^2 \cdot (2m-2)\sigma^2 \cdot \cdots 2\sigma^2 I_2$$

$$= 2^m m!(\sigma^2)^m$$

$$\mu'_{2m} = 2^m m! \sigma^{2m} \quad \ldots\ldots(4), \text{ for the even moments,}$$

$$\mu'_{2m+1} = (2m+1)(2m-1) \cdots (\sigma^2)^m I_1,$$

$$= \frac{(2m+1)!(\sigma^2)^m}{m!\ 2^m}\sqrt{\frac{\pi}{2}}\,\sigma = \frac{(2m+1)!\sigma^{2m+1}}{m!\ 2^m}\sqrt{\frac{\pi}{2}}$$

$\ldots\ldots(5)$, for the odd moments.

APPENDIX 8B

Transformation of the Rayleigh Distribution

Consider the distribution of $I = Z^2$ when Z is Rayleigh-distributed.

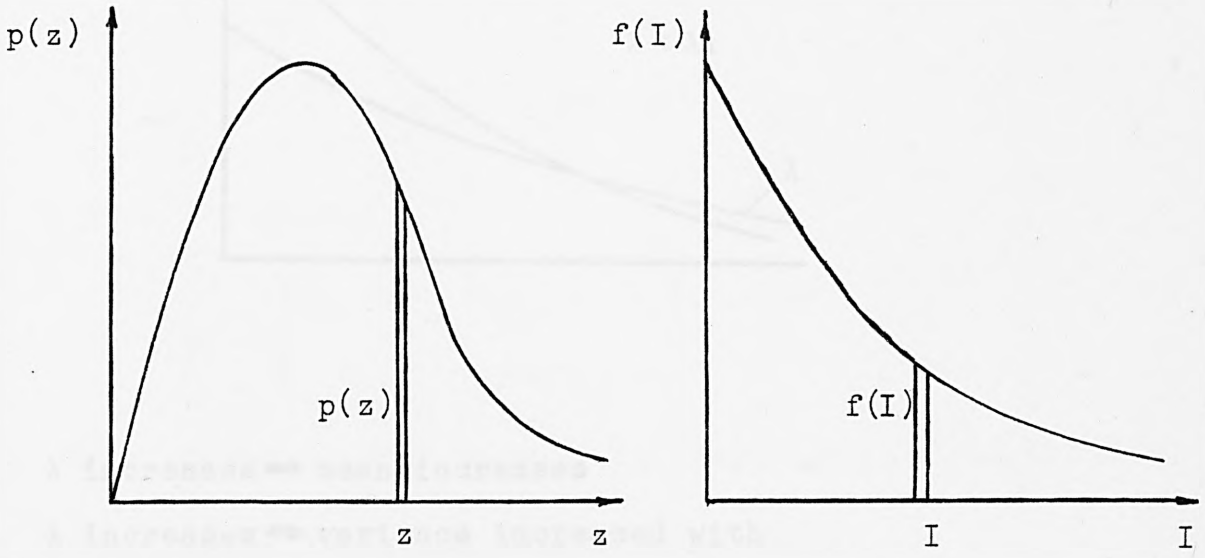

Since the transformation is one-to-one,

$$f(I) = p(z) \left| \frac{dz}{dI} \right|$$

But $I = z^2$, and so $z = \sqrt{I}$.

whence $\left| \frac{dz}{dI} \right| = \frac{1}{2} \frac{1}{\sqrt{I}}$

Thus, $f(I) = \frac{z}{\lambda^2} e^{-z^2/2\lambda^2} \cdot \frac{1}{2} \frac{1}{\sqrt{I}} \quad I > 0$

i.e. $$f(I) = \begin{cases} \frac{1}{2\lambda^2} e^{-I/2\lambda^2}, & I \geq 0 \\ 0, & I < 0. \end{cases}$$

$f(I)$ is the well-known negative exponential distribution with parameter $1/2\lambda^2$.

Mean = $2\lambda^2$; variance = $2\lambda^2$.

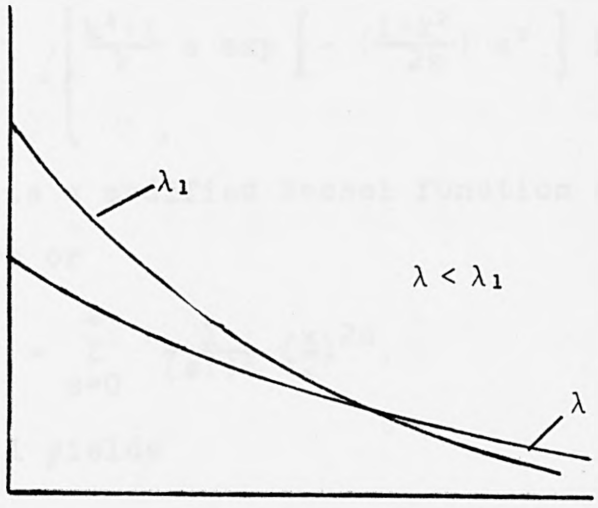

λ increases $\Rightarrow$ mean increases

λ increases $\Rightarrow$ variance increased with

$\frac{\text{mean}}{\text{variance}} = 1$, independent of λ.

APPENDIX 8C

The Hoyt Distribution

$$p(z) = \begin{cases} \frac{k^2+1}{k}\, z \exp\left[-\left(\frac{1+k^2}{2k}\right) z^2 \right] I_0\left(\frac{k^4-1}{4k^2} z^2\right), & \text{for } z > 0 \\ 0, & \text{for } z < 0 \end{cases}$$

where I_0 is a modified Bessel function of the first kind of order zero or

$$I_0 = \sum_{s=0}^{\infty} \frac{1}{(s!)^2} \left(\frac{x}{2}\right)^{2s}.$$

N.B. $k = 1$ yields

$$p(z) = \begin{cases} 2ze^{-z^2} & \text{for } z > 0, \\ 0 & \text{for } z < 0, \end{cases}$$

which is the special case of the Rayleigh distribution.

Verification that p(z) is a genuine p.d.f.

To show $\int_0^{\infty} p(z)dz = 1$

Write

$$v = \left(\frac{1+k^2}{2k}\right)z, \quad \therefore \quad dv = \left(\frac{1+k^2}{2k}\right)dz.$$

Then

$$\int_0^{\infty} p(z)dz = \int_0^{\infty} 2ve^{-v^2} I_0\left[\frac{(k^2-1)(k^2+1)}{4k^2} \cdot \frac{4k^2}{(1+k^2)^2} v^2\right] \cdot \frac{2k}{1+k^2} dv$$

$$= \frac{2k}{k^2+1} \int_0^{\infty} 2ve^{-v^2} I_0\left[\frac{k^2-1}{k^2+1} v^2\right] dv$$

Let $w = v^2$, then $dw = 2vdv$ and write $\eta = \frac{k^2-1}{k^2+1}$.

$$\text{R.H.S.} = \frac{2k}{k^2+1} \int_0^{\infty} e^{-w} I_0(\eta w) dw$$

$$= \frac{2k}{k^2+1} \int_0^{\infty} e^{-w} \sum_{s=0}^{\infty} \frac{1}{(s!)^2} \left(\frac{\eta w}{2}\right)^{2s}$$

$$= \frac{2k}{k^2+1} \sum_{s=0}^{\infty} \frac{1}{(s!)^2} \left(\frac{\eta}{2}\right)^{2s} \int_0^{\infty} e^{-w} w^{2s} dw$$

$$= \frac{2k}{k^2+1} \sum_{s=0}^{\infty} \frac{1}{(s!)^2} \left(\frac{\eta}{2}\right)^{2s} \Gamma(2s+1)$$

$$= \frac{2k}{k^2+1} \sum_{s=0}^{\infty} \frac{(2s)!}{(s!)^2} \left(\frac{\eta}{2}\right)^{2s}$$

But $\sum_{s=0}^{\infty} \frac{(2s)!}{(s!)^2} \left(\frac{\eta}{2}\right)^{2s}$, expanding term by term

$$= 1 + 2\left(\frac{\eta}{2}\right)^2 + \frac{4!}{4}\left(\frac{\eta}{2}\right)^4 + \frac{6!}{(3!)}\left(\frac{\eta}{2}\right)^6 + \ldots$$

$$= 1 + \frac{\eta^2}{2} + \frac{3}{8}\eta^4 + \frac{5}{16}\eta^6 + \ldots$$

Also

$$(1-\eta^2)^{-1/2} = \frac{1+\eta^2}{2} + \frac{(-1/2)(-3/2)\eta^4}{2!} - \frac{(-1/2)(-3/2)(-5/2)\eta^6}{3!} + \ldots$$

$$= 1 + \frac{\eta^2}{2} + \frac{3}{8}\eta^4 + \frac{5}{16}\eta^6 + \ldots$$

Thus $\int_0^{\infty} p(z)dz = \frac{2k}{k^2+1}(1-\eta^2)^{-1/2}$

and

$$1-\eta^2 = 1 - \left(\frac{k^2-1}{k^2+1}\right)^2$$

$$= \frac{(k^2+1)^2 - (k^2-1)^2}{(k^2+1)^2}$$

$$= \frac{4k^2}{(k^2+1)^2}$$

$$\therefore \int_0^{\infty} p(z)dz = \frac{2k}{(k^2+1)} \cdot \frac{k^2+1}{2k}$$

$$= 1, \text{ as required.}$$

APPENDIX 8D

Transformation of the Hoyt Distribution

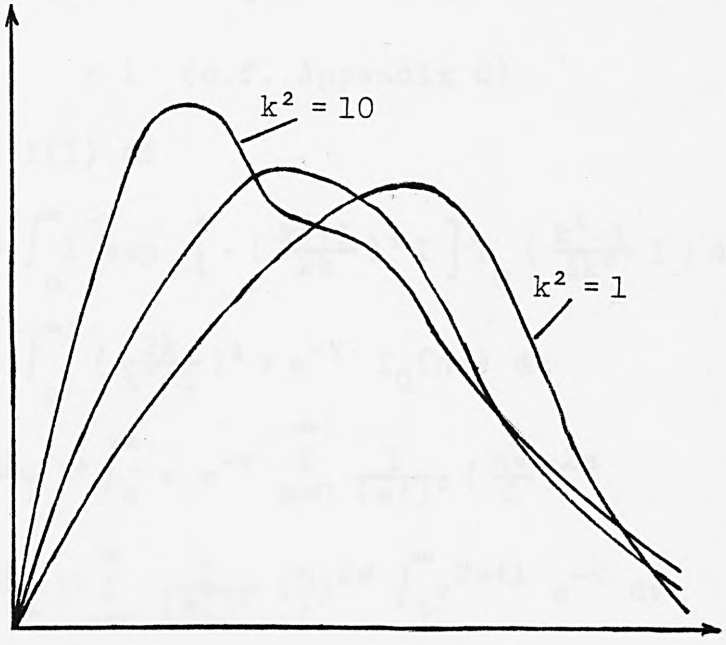

$$p(z) = \begin{cases} \frac{k^2+1}{k}\, z \exp\left[-\left(\frac{1+k^2}{2k}\right)^2 z^2\right] I_0\left(\frac{k^4-1}{4k^2} z^2\right), & z > 0 \\ 0, & z < 0 \end{cases}$$

Consider once more the distribution of $I = z^2$. Then in this case,

$$f(I) = \frac{k^2+1}{k} \sqrt{I} \exp\left[-\left(\frac{k^2+1}{2k}\right)^2 I\right] I_0\left(\frac{k^4-1}{4k^2} I\right) \cdot \frac{1}{2} \frac{1}{\sqrt{I}}$$

$$= \frac{k^2+1}{2k} \exp\left[-\left(\frac{k^2+1}{2k}\right)^2 I\right] I_0\left(\frac{k^4-1}{4k^2} I\right)$$

N.B. for $k = 1$, $f(I)$ reduces to e^{-I}, the negative exponential distribution.

Check:

$$\int_0^\infty f(I)\, dI = \frac{k^2+1}{2k} \int_0^\infty \exp\left[-\left(\frac{k^2+1}{2k}\right)^2 I\right] I_0\left(\frac{k^4-1}{4k} I\right) dI$$

Write:

$$v = \left(\frac{k^2+1}{2k}\right)^2 I, \quad \therefore \quad dv = \left(\frac{k^2+1}{2k}\right)^2 dI$$

Then

$$\int_o^\infty f(I)\, dI = \frac{2k}{k^2+1} \int_o^\infty e^{-v}\, I_0 \left[\frac{k^2-1}{k^2+1}\, v \right] dv$$

$$= \frac{2k}{k^2+1} \int_o^\infty e^{-v}\, I_0 (\eta v)\, dv$$

$$= 1 \quad \text{(c.f. Appendix C)}$$

Mean $\mu = \int_o^\infty I\, f(I)\, dI$

$$= \frac{k^2+1}{2k} \int_o^\infty I \exp \left[-\left(\frac{k^2+1}{2k} \right)^2 I \right] I_0 \left(\frac{k^4-1}{4k^2}\, I \right) dI$$

$$= \frac{2k}{k^2+1} \int_o^\infty \left(\frac{2k}{k^2+1} \right)^2 v\, e^{-v}\, I_0(\eta v)\, dv$$

$$= \left(\frac{2k}{k^2+1} \right)^3 \int_o^\infty v\, e^{-v} \sum_{s=0}^{\infty} \frac{1}{(s!)^2} \left(\frac{\eta v}{2} \right)^{2s}$$

$$= \left(\frac{2k}{k^2+1} \right)^3 \sum_{s=0}^{\infty} \frac{1}{(s!)^2} \left(\frac{\eta}{2} \right)^{2s} \int_o^\infty v^{2s+1}\, e^{-v}\, dv$$

$$= \left(\frac{2k}{k^2+1} \right)^3 \sum_{s=0}^{\infty} \frac{1}{(s!)^2} \left(\frac{\eta}{2} \right)^{2s} \Gamma(2s+2)$$

$$= \left(\frac{2k}{k^2+1} \right)^3 \sum_{s=0}^{\infty} \frac{(2s+1)!}{(s!)^2} \left(\frac{\eta}{2} \right)^{2s}$$

Via Appendix C,

$$\sum_{s=0}^{\infty} \frac{(2s)!}{(s!)^2} \left(\frac{\eta}{2} \right)^{2s} = \frac{1}{\sqrt{(1-\eta^2)}} = (1-\eta^2)^{-1/2}$$

Then

$$\sum_{s=0}^{\infty} \frac{(2s)!}{(s!)^2} \left(\frac{\eta}{2} \right)^{2s+1} = \frac{\eta/2}{(1-\eta^2)^{1/2}}$$

Differentiating w.r.t. η:

$$\sum_{s=0}^{\infty} \frac{(2s+1)!}{(s!)^2} \left(\frac{\eta}{2} \right)^{2s} \cdot \frac{1}{2} = \frac{(1-\eta^2)^{1/2}\, \frac{1}{2} - \frac{\eta}{2} \cdot \frac{1}{2} (1-\eta^2)^{-1/2} (-2\eta)}{(1-\eta^2)}$$

$$= \frac{1}{2}\, \frac{1 - \eta^2 + \eta^2}{(1-\eta^2)^{3/2}} = \frac{1}{2(1-\eta^2)^{3/2}}$$

$$\therefore \mu = \left(\frac{2k}{k^2+1} \right)^3 \times \frac{1}{(1-\eta^2)^{3/2}}$$

$\mu = 1$, independent of η (or k).

Result is obvious from normalisation considerations.

Also

$$E(I^2) = \frac{2k}{k^2+1} \int_o^\infty \left(\frac{2k}{k^2+1} \right)^4 v^2 \, e^{-v} \, I_0 (\eta v) \, dv$$

$$= \left(\frac{2k}{k^2+1} \right)^5 \sum_{s=0}^{\infty} \frac{1}{(s!)^2} \left(\frac{\eta}{2}\right)^{2s} \int_o^\infty v^{2s+2} \, e^{-v} \, dv$$

$$= \left(\frac{2k}{k^2+1} \right)^5 \sum_{s=0}^{\infty} \frac{(2s+2)!}{(s!)^2} \cdot \left(\frac{\eta}{2}\right)^{2s}$$

Using the identity:

$$\sum_{s=0}^{\infty} \frac{(2s+1)!}{(s!)^2} \left(\frac{\eta}{2}\right)^{2s} = \frac{1}{(1-\eta^2)^{3/2}}$$

we have

$$\sum_{s=0}^{\infty} \frac{(2s+1)!}{(s!)^2} \left(\frac{\eta}{2}\right)^{2s+2} = \frac{(\eta/2)^2}{(1-\eta^2)^{3/2}}$$

Differentiating,

$$\sum_{s=0}^{\infty} \frac{(2s+2)!}{(s!)^2} \left(\frac{\eta}{2}\right)^{2s+1} \cdot \frac{1}{2} = \frac{(1-\eta^2)^{3/2} \cdot 2\left(\frac{\eta}{2}\right)\frac{1}{2} - \left(\frac{\eta}{2}\right) \frac{3}{2}(1-\eta^2)^{1/2}(-2\eta}{(1-\eta^2)^3}$$

$$= (1-\eta^2)^{1/2} \; \frac{\frac{1}{2}\eta\,(1-\eta^2) + \frac{3}{4}\eta^3}{(1-\eta^2)^3}$$

$$= \frac{\eta}{2} \; \frac{1 - \eta^2 + \frac{3}{2}\eta^2}{(1-\eta^2)^{5/2}}$$

$$= \frac{\eta}{2} \; \frac{(1 + \frac{1}{2}\eta^2)}{(1-\eta^2)^{5/2}}$$

$$\therefore \quad \sum_{s=0}^{\infty} \frac{(2s+2)!}{(s!)^2} \left(\frac{\eta}{2}\right)^{2s} = \frac{2 + \eta^2}{(1-\eta^2)^{5/2}}$$

$$\therefore \quad E(I^2) = \left(\frac{2k}{k^2+1} \right)^5 \times \left(\frac{k^2+1}{2k} \right)^5 \times (2 + \eta^2)$$

$$= 2 + \eta^2.$$

$$\therefore \quad V(I) = E(I^2) - \mu^2.$$

$$= 1 + \eta^2.$$

V(I) has minimum when $\eta = 0$ or $k = 1$

Check: $k = 1$ $E(I) = 1$; $V(I) = 1$

in agreement with e^{-I} distribution.

V(I) is the variance of <u>normalised</u> intensity.

Actual intensity variance

$$= D\{\rho\} \cdot V(I)$$

$$= (s_1 + s_2)(1 + \eta^2)$$

(c.f. Beckmann [1963] for full explanation of the notation adopted.

$$= s_2(s_1/s_2 + 1)(1 + \eta^2)$$

$$= s_2\left(\frac{1+k^2}{k^2}\right)\left(1 + \left(\frac{k^2-1}{k^2+1}\right)^2\right)$$

$$= s_2\frac{2(k^4+1)}{k^2(k^2+1)}$$

$$= D\{I_m u\} \times 2\,\frac{(1+1/k^4)}{(1+1/k^2)}$$

increases as roughness increases and $k \searrow 1$ or Intensity variance

$$= D\{I_m \rho\} \cdot 2\,\frac{(1+1/k^4)}{1+1/k^2}$$

In the case where roughness height obeys a normal distribution law:

$$s_2 = D\{I_m \rho\} = 1 - e^{-2g} \text{ with } k^2 = \frac{1+e^{-g}}{1-e^{-g}}$$

whence $e^{-g} = \frac{k^2-1}{k^2+1} = \eta$

$$\text{Intensity variance} = \left(1 - \left(\frac{k^2-1}{k^2+1}\right)^2\right)\frac{2(k^4+1)}{k^2(k^2+1)}$$

$$= \frac{4k^2}{(k^2+1)^2} \cdot \frac{2(k^4+1)}{k^2(k^2+1)}$$

$$= 8\,\frac{(k^4+1)}{(1+k^2)^3}$$

$\nearrow 2$ as $k \searrow 1$.

APPENDIX 8E

Moments of the Normal Distribution

The moment generating function, $M_x(\theta)$ of the normal distribution $N(\mu,\sigma^2)$ is $e^{\mu\theta + \frac{1}{2}\sigma^2\theta^2}$ from which all moments can be derived.

$$M_x(\theta) = 1 + (\mu\theta + \tfrac{1}{2}\sigma^2\theta^2) + \frac{(\mu\theta + \frac{1}{2}\sigma^2\theta^2)^2}{2!} + \frac{(\mu\theta + \frac{1}{2}\sigma^2\theta^2)^3}{3!}$$

$$+ \frac{(\mu\theta + \frac{1}{2}\sigma^2\theta^2)^4}{4!} + \ldots \qquad \ldots.(1)$$

In general $M_x(\theta) = 1 + \mu_1' \theta + \frac{\mu_2' \theta^2}{2!} + \frac{\mu_3' \theta^3}{3!} + \frac{\mu_4' \theta^4}{4!} +$

in terms of moments μ_r' about the origin.

From (1), coefficient of θ^4:

$$\frac{1\sigma^4}{8} + \frac{3\mu^2 \frac{1}{2}\sigma^2}{3!} + \frac{\mu^4}{4!} = \frac{3\sigma^4 + 6\mu^2\sigma^2 + \mu^4}{4!}$$

$$\rightarrow \mu^4 = 3\sigma^4 + 6\mu^2\sigma^2 + \mu^4 \qquad \ldots.(2)$$

Again, coefficient of θ^2

$$\frac{\sigma^2}{2} + \mu^2/2! = \frac{\sigma^2 + \mu^2}{2!}$$

$$\rightarrow \mu_2' = \sigma^2 + \mu^2 \qquad \ldots.(3)$$

In terms of the notation of the paper,

$x \sim N(\alpha, s_1)$ whence

$$\begin{aligned} V(x^2) &= E(x^4) - [E(x^2)]^2 \\ &= \mu_4' - (\mu_2')^2 \\ &= \alpha^4 + 6\alpha^2 s_1 + 3{s_1}^2 - (\alpha^2 + s_1)^2 \\ &= \sigma^4 + 6\alpha^2 s_1 + 3{s_1}^2 - \alpha^4 - 2\alpha^2 s_1 - {s_1}^2 \\ &= 4\alpha^2 s_1 + 2{s_1}^2 \qquad \ldots.(4) \end{aligned}$$

$y \sim N(0, s_2)$

$\therefore V(y^2) = 2{s_2}^2$

Since x and y are independent $\rightarrow x^2$ and y^2 are independent.

Thus, $$V(r^2) = V(x^2 + y^2)$$
$$= V(x^2) + V(y^2)$$
$$= 4\alpha^2 s_1 + 2s_1^2 + 2s_2^2. \qquad \ldots.(5)$$

APPENDIX 8F

Bivariate Negative Exponential Distribution

Consider the bivariate probability density function:

$$f(x_1,x_1) = \frac{1}{\sigma^2(1-\rho)} \exp\left[-\frac{1}{\sigma(1-\rho)}(x_1+x_2)\right] \cdot I_o\left(\frac{2\sqrt{\rho}}{\sigma(1-\rho)}\sqrt{x_1x_2}\right)$$

The characteristic function $\chi_2(v_z,-v_z;\rho)$ is defined as

$$\chi_2(v_z,-v_z;\rho) = \iint \frac{1}{\sigma^2(1-\rho)} e^{iv_z(x_1-x_2)} e^{-\frac{1}{\sigma(1-\rho)}(x_1+x_2)} \cdot I_o\left(\frac{2\sqrt{\rho}}{\sigma(1-\rho)}\sqrt{x_1x_2}\right)dx_1dx_2$$

$$= \int_{x_2} \frac{1}{\sigma^2(1-\rho)} e^{-x_2/\sigma(1-\rho)} e^{-iv_zx_2} dx_2 \int_{x_1} e^{-x_1/\sigma(1-\rho)} e^{iv_zx_1} I_o(.)\, dx_2$$

For the second integral,

$$\int_{x_1} e^{-x_1/\sigma(1-\rho)} e^{iv_zx_1} \sum_{r=0}^{\infty} \frac{1}{r!\Gamma(r+1)} \left(\frac{\sqrt{\rho}}{\sigma(1-\rho)}\sqrt{x_1x_2}\right)^{2r} dx_1$$

$$= \sum_{r=0}^{\infty} \frac{x_2^{\,r}}{r!\Gamma(r+1)} \left\{\frac{\rho}{\sigma^2(1-\rho)^2}\right\}^r \int_{x_1} x_1^{\,r} e^{-\left(\frac{1}{\sigma(1-\rho)} - iv_z\right)x_1} dx_1$$

$$= \sum_{r=0}^{\infty} \frac{x_2^{\,r}}{r!} \left\{\frac{\rho}{\sigma^2(1-\rho)^2}\right\}^r \int_{x_1} \frac{x_1^{\,r} e^{-\alpha x_1}}{\Gamma(r+1)} dx_1 \text{ where we have written}$$

$$\alpha = \frac{1}{\sigma(1-\rho)} - iv_z$$

$$= \sum_{r=0}^{\infty} \frac{x_2^{\,r}}{r!} \left\{\frac{\rho}{\sigma^2(1-\rho)^2}\right\}^r \frac{1}{\alpha^{r+1}}$$

$$= \frac{1}{\alpha} \sum_{r=0}^{\infty} \left\{\frac{x_2}{\alpha} \frac{\rho}{\sigma^2(1-\rho)^2}\right\}^r / r! = \frac{1}{\alpha} \exp\left\{\frac{x_2\rho}{\alpha\sigma^2(1-\rho)^2}\right\}$$

Thus $\chi_2(v_z,v_z;\rho)$

$$= \int_{x_2} \frac{1}{\sigma^2(1-\rho)\alpha} e^{-\left(\frac{1}{\alpha(1-\rho)} + iv_z\right)x_2} \cdot e^{\frac{\rho x_2}{\sigma(1+\rho)-iv_z{}^2\sigma^2(1-\rho)^2}} dx_2$$

As a check so far put $v_z = 0$:

Marginal distribution for X_2 is

$$\frac{1}{\sigma^2(1-\rho)}\, e^{-x_2/\sigma(1-\rho)} \cdot \frac{1}{\alpha^*} \exp\left(\frac{\rho x_2}{\sigma(1-\rho)}\right) \qquad \alpha^* = \frac{1}{\sigma(1-\rho)}$$

$$= \frac{1}{\sigma} \exp\left(-\frac{(1-\rho)}{\sigma(1-\rho)} x_2\right) = \frac{1}{\sigma} e^{-x_2/\sigma}$$

which is negative exponential with variance σ^2.

Continuing the derivation of $\chi_2(v_z, -v_z;\rho)$:

$$\chi_2(v_z - v_z;\rho) = \int_{x_2} \frac{1}{\sigma - iv_z\sigma^2(1-\rho)}$$

$$\cdot \exp\left[-\left(\frac{1}{\sigma(1-\rho)} + iv_z - \frac{\rho}{\sigma(1-\rho) - iv_z\sigma^2(1-\rho)^2}\right)x_2\right] dx_2$$

$$= \frac{1}{\sigma - iv_z\sigma^2(1-\rho)} \times \frac{1}{\frac{1}{\sigma(1-\rho)} + iv_z - \frac{\rho}{\sigma(1-\rho) - iv_z\sigma^2(1-\rho)^2}}$$

$$= \frac{1-\rho}{(1-iv_z\sigma(1-\rho))(1+iv_z\sigma(1-\rho)) - \rho}$$

$$= \frac{1-\rho}{1+v_z{}^2\sigma^2(1-\rho)^2 - \rho}$$

$$= \frac{1}{1+v_z{}^2\sigma^2(1-\rho)}$$

$$= \frac{1}{1+g(1-\rho)}$$

i.e. $\chi_2(v_z, -v_z;\rho) = \frac{1}{1+g(1-\rho)}$

Finally, $E(X_1X_2)$

$$= \frac{1}{\sigma^2(1-\rho)} \iint x_1x_2\, e^{-(x_1+x_2)/\sigma(1-\rho)} \sum_{r=0}^{\infty} \frac{1}{r!\Gamma(r+1)} \left\{\frac{\rho\, x_1x_2}{\sigma^2(1-\rho)^2}\right\}^r dx_1dx_2$$

$$= \frac{1}{\sigma^2(1-\rho)} \int_{x_2} x_2 e^{-x_2/\sigma(1-\rho)} dx_2 \sum \frac{1}{r!\Gamma(r+1)} \left\{\frac{\rho}{\sigma^2(1-\rho)^2}\right\}^r \int_{x_1} x_1{}^{r+1} e^{-x_1/\sigma(1-\rho)} dx_1$$

$$= \frac{1}{\sigma^2(1-\rho)} \int_{x_2} x_2 e^{-x_2/\sigma(1-\rho)} \sum_{r=0}^{\infty} \frac{x_2^r}{r!\Gamma(r+1)} \left\{ \frac{\rho}{\sigma^2(1-\rho)^2} \right\}^r \cdot \frac{\Gamma(r+2)}{(\alpha^*)^{r+2}} \, dx_2$$

$$= \frac{1}{\sigma^2(1-\rho)} \int_{x_2} \frac{x_2 e^{-x_2/\sigma(1-\rho)}}{(\alpha^*)^2} \sum_{r=0}^{\infty} \frac{(r+1)}{r!} \left\{ \frac{\rho x_2}{\alpha^* \sigma^2 (1-\rho)^2} \right\}^r$$

$$= (1-\rho) \int_{x_2} x_2 e^{-x_2/\sigma(1-\rho)} \left(\frac{\rho x_2}{\sigma(1-\rho)} + 1 \right) e^{\rho x_2/\sigma(1-\rho)} dx_2$$

$$= (1-\rho) \int \left\{ \frac{x_2^2 \rho}{\sigma(1-\rho)} e^{-x_2/\sigma} + x_2 e^{-x_2/\sigma} \right\} dx_2$$

$$= \rho \int x_2^2 \frac{1}{\sigma} e^{-x_2/\sigma} \, dx_2 + (1-\rho)\sigma \int x_2 \frac{1}{\sigma} e^{-x_2/\sigma} \, dx_2$$

$$= 2\rho . \sigma^2 + (1-\rho) . \sigma^2$$

But $\quad \mathrm{Cov}(X_1 X_2) = E(X_1 X_2) - E(X_1)E(X_2)$

$\therefore \quad \mathrm{Cov}(X_1 X_2) = 2\rho\sigma^2 + (1-\rho)\sigma^2 - \sigma^2$

$$= \underline{\rho\sigma^2}$$

i.e. Correlation of X_1 and X_2 is ρ.

APPENDIX 8G

Scattering from Surfaces Possessing Negative Exponential Properties

Supposing a normal distribution of surface height we may quote equation 4.41:

$$I(\theta_2) = \rho_o^2 e^{-g} + \frac{F^2}{2L}\int_{-L}^{L} e^{iv_x\tau} e^{-g}\{ e^{gC(\tau)} - 1 \}\, d\tau$$

$$= \rho_o^2 e^{-g} + \frac{F^2}{2L}\int_{-L}^{L} e^{iv_x\tau} e^{-g} \sum_{m=1}^{\infty} \frac{\{gC(\tau)\}^m}{m!}\, d\tau$$

$$= \rho_o^2 e^{-g} + \frac{F^2}{2L}\, e^{-g} \sum_{m=1}^{\infty} \frac{g^m}{m!} \int_{-L}^{L} e^{iv_x\tau} e^{-m|\tau|/T} d\tau,$$

taking $C(\tau) = e^{-|\tau|/T}$, a pure negative exponential auto correlation function. In this case,

$$I(\theta_2) = \rho_o^2 e^{-g} + \frac{F^2}{2L} e^{-g} \sum_{m=1}^{\infty} \frac{g^m}{m!}\{ \int_{o}^{L} e^{(iv_x - m/T)\tau} d\tau + \int_{-L}^{o} e^{(iv_x + m/T)\tau} d\tau \}$$

$$= \rho_o^2 e^{-g} + \frac{F^2 e^{-g}}{2L} \sum_{m=1}^{\infty} \frac{g^m}{m!}\{ \left[\frac{1}{iv_x - M/T}\, e^{(iv_x - m/T)\tau} \right]_o^L + \left[\frac{e^{(iv_x + m/T)\tau}}{iv_x + m/T} \right]_{-L}^{L} \}$$

$$= \rho_o^2 e^{-g} + \frac{F^2 e^{-g}}{2L} \sum_{m=1}^{\infty} \frac{g^m}{m!(v_x^2 + m^2/T^2)}\{ (-iv_x - m/T)(e^{(iv_x - m/T)L} - 1)$$

$$+ (-iv_x + m/T)(1 - e^{(iv_x + m/T)L}) \}$$

$$= \rho_o^2 e^{-g} + \frac{F^2 e^{-g}}{2L} \sum_{m=1}^{\infty} \frac{g^m}{m!(v_x^2 + m^2/T^2)}\{ \frac{2m}{T} + e^{-mL/T}(-\frac{m}{T}(e^{iv_xL} + e^{-iv_xL})$$

$$-iv_x(e^{iv_xL} - e^{-iv_xL})) \}$$

$$= \rho_o^2 e^{-g} + \frac{F^2 e^{-g}}{2L} \sum_{m=1}^{\infty} \frac{g^m}{m!(v_x^2 + m^2/T^2)}\{ \frac{2m}{T}(1 - \cos(v_xL) e^{-mL/T})$$

$$+ 2v_x \sin(v_xL) e^{-mL/T} \}$$

For type(A) surface $g \ll 1$ we take the first term only:

$$I(\theta_2) = \rho_o^2 e^{-g} + \frac{F^2 e^{-g} g}{L(v_x^2 + 1/T^2)}\{ \frac{1}{T}(1 - \cos(v_xL) e^{-L/T}) + v_x \sin(v_xL) e^{-L/T} \}$$

In particular $I(\text{spec}) = e^{-g} + g e^{-g}$.

For Type (B) $g \simeq 1$ simply take as many terms as necessary.

For Type (C) $g \gg 1$ use saddle point integration:

$$I(\theta_2) = \frac{F^2 T}{2Lg(1+T^2 v_x^2/g^2)} \qquad \text{(c.f.(21) Chapter 8)}$$

If, on the other hand, the distribution of surface heights is negative exponential,

$$I(\theta_2) = \rho_o^2 \frac{1}{1+g} + \frac{F^2}{2L} \int_{-L}^{L} e^{iv_x\tau} \left\{ \frac{1}{1+g[1-C(\tau)]} - \frac{1}{1+g} \right\} d\tau$$

$$= \rho_o^2 \frac{1}{1+g} + \frac{F^2}{2L} \int_{-L}^{L} \frac{1}{(1+g)} \left\{ \left[\frac{1}{1-\frac{C(\tau)}{1+g}} \right] - 1 \right\} e^{iv_x\tau} d\tau$$

$$= \rho_o^2 \frac{1}{1+g} + \frac{F^2}{2L} \frac{1}{(1+g)} \int_{-L}^{L} e^{iv_x\tau} \sum_{m=1}^{\infty} \left\{ \frac{C(\tau)}{1+g} \right\}^m$$

For a Gaussian form : $C(\tau) = e^{-\tau^2/T^2}$,

$$I(\theta_2) = \rho_o^2 \frac{1}{1+g} + \frac{F^2}{2L(1+g)} \sum_{m=1}^{\infty} \frac{1}{(1+g)^m} \int_{-L}^{L} e^{iv_x\tau} e^{-m\tau^2/T^2} d\tau$$

$$= \rho_o^2 \frac{1}{1+g} + \frac{F^2}{L(1+g)} \sum_{m=1}^{\infty} \frac{1}{(1+g)^m} e^{-T^2 v_x^2/4m} \times T\sqrt{\frac{\pi}{m}}$$

$$I(\theta_2) = \rho_o^2 \frac{1}{1+g} + \frac{\sqrt{\pi} F^2 T}{L(1+g)} \sum_{m=1}^{\infty} \frac{e^{-T^2 v_x^2/4m}}{\sqrt{m}(1+g)^m}$$

For a negative exponential form : $C(\tau) = e^{-|\tau|/T}$,

$$I(\theta_2) = \rho_o^2 \frac{1}{1+g} + \frac{F^2}{2L(1+g)} \sum_{m=1}^{\infty} \frac{1}{(1+g)^m} \int_{-L}^{L} e^{iv_x\tau} e^{-m|\tau|/T} d\tau$$

$$= \rho_o^2 \frac{1}{1+g} + \frac{F^2}{L(1+g)} \sum_{m=1}^{\infty} \frac{1}{(1+g)^m (v_x^2 + m^2/T^2)} \cdot \frac{m}{T} \left(1 - \cos(v_x L) e^{-mL/T} + v_x \sin(v_x L) e^{-\frac{mL}{T}}\right)$$

The result for a surface possessing exclusively negative exponential properties.

APPENDIX 8H

Derivation of results for two-dimensional roughness:

$$D\{\rho\} = \frac{2\pi F_3^2}{A^2} \int_o^\infty J_o(v_{xy}\tau)\left[\chi_2(v_z,-v_z) - (v_z)\chi^*(v_z)\right]\tau d\tau$$

(c.f. Beckmann [1963] equation (33) p.79)

$F_3 \equiv 1$ for normal incidence, $v_{xy} = \sqrt{v_x^2 + v_y^2}$

with $v_x = \frac{2\pi}{\lambda}\sin\theta_2$, $v_y = \frac{2\pi}{\lambda}\sin\theta_2\sin\theta_3$ (θ_3 is the orientation of observation angle with respect to the incident plane) and $J_o(.)$ is the Bessel function of order zero.

For weak scatters (small $g << 1$),

$$D\{\rho\} = \frac{2\pi F_3^2}{A^2} \int_o^\infty J_o(v_{xy}\tau)\, e^{-g} g C(\tau)\tau d\tau$$

$$= \frac{2\pi F_3^2}{A^2} e^{-g}\, g \left\{\int_o^\varepsilon \tau J_o(v_{xy}\tau)d\tau + \int_\varepsilon^\infty A_1 e^{-\tau/T}\tau J_o(v_{xy}\tau)d\tau\right\}$$

employing the same mathematical model function for $C(\tau)$ as before.

$$D\{\rho\} = \frac{2\pi F_3^2}{A^2} e^{-g} g \left\{\int_o^\varepsilon \tau J_o(v_{xy}\tau)d\tau + \left(\int_o^\infty - \int_o^\varepsilon A_1 e^{-\tau/T}\tau J_o(v_{xy}\tau)d\tau\right)\right\}$$

$$= \frac{2\pi F_3^2}{A^2} e^{-g} g \left\{\int_o^\varepsilon (1-A_1 e^{-\tau/T})\tau J_o(v_{xy}\tau)d\tau + \int_o^\infty A_1 e^{-\tau/T}\tau J_o(v_{xy}\tau)d\tau\right\}$$

$$\sim \frac{2\pi F_3^2}{A^2} e^{-g} g \left\{\int_o^\varepsilon (1-A_1+A_1\tau/T)\left(1-\frac{\frac{1}{4}v_{xy}^2\tau^2}{1!^2}\right)\tau d\tau\right.$$

$$\left. + \int_o^\infty A_1\tau e^{-\tau/T} \sum_{n=0}^{\infty} (-1)^n \frac{(\frac{1}{4}v_{xy}^2\tau^2)^n}{(n!)^2}\right.$$

$$= \frac{2\pi F_3^2}{A^2} e^{-g} g\{(1-A_1)\varepsilon^2/2 + A_1 \sum_{n=0}^{\infty} \frac{(-1)^n(\frac{1}{4}v_{xy}^2)^n}{(n!)^2} \int_o^\infty \tau^{2n+1} e^{-\tau/T} d\tau\}$$

$$= \frac{2\pi F_3^2}{A^2} e^{-g} g\{(1-A_1)\varepsilon^2/2 + A_1 \sum_{n=0}^{\infty} (-1)^n \frac{(\frac{1}{4}v_{xy}^2)^n}{(n!)^2} T^{2n+2}\Gamma(2n+2)\}$$

$$= \frac{2\pi F_3^2}{A^2} e^{-g_g} \{(1-A_1)\varepsilon^2/2 + A_1 T^2 \sum_{n=0}^{\infty} \frac{(-1)^n (v_{xy}^2 T^2)^n}{2^n n!} \frac{(2n+1)2n(2n-1)..3.2.1\}}{2^n n!}$$

$$= \frac{2\pi F_3^2}{A^2} e^{-g_g} \{(1-A_1)\varepsilon^2/2 + A_1 T^2 \sum_{n=0}^{\infty} \frac{(-1)^n (v_{xy}^2 T^2)^n}{n!} (\tfrac{1}{2})(3/2)..(n-\tfrac{1}{2})(2n+1)\}$$

$$= \frac{2\pi F_3^2}{A^2} e^{-g_g} \{(1-A_1)\varepsilon^2/2 + A_1 T^2 \sum_{n=0}^{\infty} \frac{(v_{xy}^2 T^2)^n}{n!} (-\tfrac{1}{2})(-3/2)..(-n+\tfrac{1}{2})(2n+1)\}$$

$$= \frac{2\pi F_3^2}{A^2} e^{-g_g} \{(1-A_1)\varepsilon^2/2 + \frac{A_1 T^2}{[1 + (v_{xy} T)^2]^{3/2}} \}$$

Away from specular,

$D\{\rho\} \sim \frac{2\pi F_3^2}{A^2} e^{-g_g} \{ (1-A_1)\varepsilon^2/2 + \frac{A_1 T^2}{v_{xy}^3 T^3} \}$, which may be expressed in the form

$$D\{\rho\} = \frac{2\pi F_3^2}{A^2} e^{-g_g} (1-A_1)\varepsilon^2/2 \{ 1 + \frac{A_2/T}{v_{xy}^3} \}$$

$$\sim \frac{2\pi F_3^2}{A^2} e^{-g_g} (1-A_1)\varepsilon^2/2 \exp\left[\frac{A_2/T}{v_{xy}^3} \right]$$

$$= \exp\left[y + \frac{A_2/T}{v_{xy}^3} \right]$$

whence $\log [D\{\rho\}] = y + \frac{A_2/T}{v_{xy}^3}$.

But $v_{xy} = \sqrt{v_x^2 + v_y^2}$

$= \frac{2\pi}{\lambda} \sin\theta_2 \sqrt{1 + \sin^2\theta_3}$, and thus scanning with θ_3 = constant, together with the dominance of the second term, results in a near linear relationship with $\frac{1}{v_{xy}^3}$ and consequently with $\frac{1}{\sin^3\theta_2} = \operatorname{cosec}^3\theta_2$.

APPENDIX 8I

General Theory

A number of general results from statistical theory are worthy of attention:

Given the two-dimensional characteristic function:

$$\chi_2(v_z,-v_z;\tau) = \int_{-\infty}^{\infty}\int_{-\infty}^{\infty} W(z_1,z_2;\tau)e^{iv_z(z_1-z_2)}dz_1dz_1$$

$$\frac{\partial\chi_2}{\partial v_z} = \int_{-\infty}^{\infty}\int_{-\infty}^{\infty} W(z_1,z_2;\tau)i(z_1-z_2)e^{iv_z(z_1-z_2)}dz_1dz_2$$

$$\frac{\partial^2\chi_2}{\partial v_z^2} = -\int_{-\infty}^{\infty}\int_{-\infty}^{\infty} W(z_1,z_2;\tau)(z_1-z_2)^2e^{iv_z(z_1-z_2)}dz_1dz_2$$

$$\left[\frac{\partial^2\chi_2}{\partial v_z^2}\right]_{v_z=0} = -\int_{-\infty}^{\infty}\int_{-\infty}^{\infty} W(z_1,z_2;\tau)(z_1-z_2)^2dz_1dz_2$$

$$= -E\left[(z_1-z_2)^2|\tau\right]$$

$$= -E\left[(z_1^2-2z_1z_2+z_2^2)|\tau\right]$$

$$= -2\sigma^2 + 2C(z_1,z_2;\tau)$$

where $C(z_1,z_2;\tau)$ is the covariance of z_1 and z_2 for heights z_1 (x_1, y_1) and $z_2(x_2, y_2)$, when the points (x_1, y_1) and (x_2, y_2) are separated by a distance τ.

$$\therefore\ C(z_1,z_2;\tau) = \sigma^2 + \frac{1}{2}\left[\frac{\partial^2\chi^2}{\partial v_z^2}\right]_{v_z=0}$$

$$\text{or}\quad B(\tau) = \sigma^2 + \frac{1}{2}\left[\frac{\partial^2\chi_2(v_z,-v_z;\tau)\tau}{\partial v_z^2}\right]_{v_z=0} \qquad \ldots.(1)$$

This is somewhat at odds with (77) p.96 of Beckmann [1963]

Check: The normal distribution.

The two-dimensional characteristic function $\chi_2(v_z,-v_z;\tau) = \exp\left[-v_z^2\sigma^2(1-C(\tau))\right]$ for the normal distri-

bution $N(0,\sigma^2)$ is well known.

Then $\frac{\partial \chi_2}{\partial v_z} = -2v_z\sigma^2(1-C)\exp\left[-v_z{}^2\sigma^2(1-C)\right]$

$$\frac{\partial^2 \chi_2}{\partial v_z{}^2} = -2\sigma^2(1-C)\exp\left[-v_z{}^2\sigma^2(1-C)\right] + 4v_z{}^2\sigma^4(1-C)^2 \exp\left[-v_z{}^2\sigma^2(1-C)\right]$$

$$\therefore \left[\frac{\partial^2 \chi_2}{\partial v_z{}^2}\right]_{v_z=0} = -2\sigma^2(1-C)$$

$$\therefore \quad B(\tau) = \sigma^2 + \frac{1}{2}\left(-2\sigma^2(1-C)\right)$$

$$= \sigma^2 - \sigma^2 + \sigma^2 C$$

$$= \sigma^2 C(\tau) \quad , \text{ as required.}$$

Again $\chi_2(v_z,-v_z;\tau) = \int_{-\infty}^{\infty}\int_{-\infty}^{\infty} W(z_1,z_1;\tau)\ e^{iv_z(z_1-z_2)}dz_1dz_2$

Then $\lim_{\tau\to\infty} \chi_2(v_z,-v_z;\tau) = \int_{-\infty}^{\infty}\int_{-\infty}^{\infty}\{\lim_{\tau\to\infty} W(z_1,z_2;\tau)\}e^{iv_z(z_1-z_2)}dz_1dz_2$

$$= \int_{-\infty}^{\infty} W(z_1)e^{iv_z z_1}dz_1 \int_{-\infty}^{\infty} W(z_2)e^{-iv_z z_2}\ dz_2$$

$$= \chi(v_z)\chi^*(v_z) \quad , \qquad \ldots.(2)$$

since $\left[\sqrt{\lim_{\tau\to\infty} W(z_1,z_2;\tau)}\right]_{z_1=z_2=\tau} = W(z)$, the one-dimensional distribution function.

In terms of moments we may write,

$$\chi(v_z) = E\left[e^{iv_z z}\right]$$

$$= 1 + i\mu_1'v_z - \frac{\mu_2'}{2!}v_z^2 - \frac{i\mu_3'v_z^3}{3!} + \frac{\mu_4'v_z^4}{4!} +$$

and $\chi^*(v_z) = 1 - i\mu_1'v_z - \frac{\mu_2'v_z^2}{2!} + \frac{i\mu_3'v_z^3}{3!} + \frac{\mu_4'v_z^4}{4!} -$

$$\therefore \chi(v_z)\chi^*(v_z) = 1 - \left(\frac{\mu_2'}{2!} - \frac{\mu_1'}{1!}\frac{\mu_1'}{1!} + \frac{\mu_2'}{2!}\right) v_z^2$$

$$+ \left(\frac{\mu_4'}{4!} - \frac{\mu_3'}{3!}\frac{\mu_1'}{1!} + \frac{\mu_2'}{2!}\frac{\mu_2'}{2!} - \frac{\mu_1'}{1!}\frac{\mu_3'}{3!} + \frac{\mu_4'}{4!}\right) v_z^4$$

$$= \sum_{r=0}^{\infty} (-1)^r C_{2r} v_z^{2r} \quad ,$$

where $C_{2r} = \frac{\mu_{2r}'}{(2r)!} - \frac{\mu_{2r-1}'}{(2r-1)!}\frac{\mu_1'}{1!} + \frac{\mu_{2r-2}'}{(2r-2)!}\frac{\mu_2'}{2!} - \ldots + \frac{\mu_{2r}'}{(2r)!}$

$$= \sum_{k=0}^{2r} (-1)^k \frac{\mu_{2r-k}'}{(2r-k)!}\frac{\mu_k'}{k!}$$

Note: $\left(\frac{\mu_2'}{2!} - \frac{\mu_1'}{1!}\frac{\mu_1'}{1!} + \frac{\mu_2'}{2!}\right) = \mu_2' - \mu_1'^2 = \mu_2$

But μ_2 is, in fact, σ^2 and so

$$\chi(v_z)\chi^*(v_z) = 1 - g + \left(\frac{\mu_4'}{4!} - \frac{\mu_3'}{3!}\frac{\mu_1'}{1!} + \frac{\mu_2'}{2!}\frac{\mu_2'}{2!} - \frac{\mu_1'}{1!}\frac{\mu_3'}{3!} + \frac{\mu_4'}{4!}\right) v_z^4 - \ldots$$

$$= 1 - g + \frac{1}{12}(\mu_4' - 4\mu_3'\mu_1' + 3\mu_2'^2)v_z^4 - \ldots$$

(for zero mean distribution)

$$= 1 - g + \frac{1}{12}\left(\frac{\mu_4'}{(\mu_2)^2} + 3\right)(\mu_2')^2 v_z^4 - \ldots$$

$$= 1 - g + \frac{1}{12}(\beta_2 + 3)g^2 - \ldots \qquad \ldots.(3)$$

where $\beta_2 = \frac{\mu_4'}{(\mu_2)^2}$ is the coefficient of kurtosis and

$$\sqrt{g} = v_z\sigma.$$

In the case of the normal, $\beta_2 = 3$ and we have $1 - g + g^2/2$, the first three terms of exp $(-g)$.

We return to $\chi_2(v_z, -v_z)$ and investigate this in terms of moments:

$$\chi_2(v_z, -v_z) = E\left[e^{iv_z(\zeta_1 - \zeta_2)}\right]$$

$$= E\left[1 + iv_z(\zeta_1 - \zeta_2) - \frac{v_z^2}{2!}(\zeta_1 - \zeta_2)^2 - \frac{iv_z^3}{3!}(\zeta_1 - \zeta_2)^3 + \frac{iv_z^4}{4!}(\zeta_1 - \zeta_2)^4 + \ldots\right]$$

$$= 1 + iv_z 0 - \frac{v_z^2}{2!} E(\zeta_1-\zeta_2)^2 - i\frac{v_z^3}{3!}.0 + \frac{v_z^4}{4!} E(\zeta_1-\zeta_2)^4 - \ldots$$

(N.B. all odd powers of $(\zeta_1-\zeta_2)$ will have zero expectation.)

$$\chi_2(v_z,-v_z;\tau) = 1 - \frac{v_z^2\tau^2}{2!} E\left\{\frac{(\zeta_1-\zeta_2)^2}{\tau}\right\} + \frac{v_z^4\tau^4}{4!} E\left\{\frac{(\zeta_1-\zeta_2)^4}{\tau}\right\} - \ldots$$

Now $\frac{\zeta_1-\zeta_2}{\tau}$ is a measurement of a 'chord' of the surface profile, whilst $\lim_{\tau\to\infty} E\left[\frac{(\zeta_1-\zeta_2)}{\tau}\right]^2 = {}_s\sigma^2$, the second moment of the distribution of slopes etc. Then for small τ, we have:

$$\chi_2(v_z,-v_z;\tau) \simeq 1 - \frac{v_z^2\tau^2}{2!} {}_s\sigma^2 + \frac{v_z^4\tau^4}{4!} {}_s\mu_4 - \ldots$$

$$\simeq \sum_{r=0}^{\infty} (-1)^r \, {}_s\mu_{2r} \frac{(v_z^2)^{2r}\tau^{2r}}{(2r)!}$$

where, in general, ${}_s\mu_r$ is the rth moment of the distribution of <u>slopes</u>.

Write $K_2(v_z,-v_z;\tau) = \log\{\chi_2(v_z,-v_z;\tau)\}$

$$= \log\left\{1 - \frac{v_z^2\tau^2}{2!} {}_s\sigma^2 + \frac{v_z^4\tau^4}{4!} {}_s\mu_4 - \ldots\right\}$$

$$= \log\left\{1 - \left(\frac{v_z^2\tau^2}{2!}{}_s\sigma^2 - \frac{v_z^4\tau^4}{4!} {}_s\mu_4 + \ldots\right)\right\}$$

$$= -\left[\left(\frac{v_z^2\tau^2 {}_s\sigma^2}{2!} - \frac{v_z^4\tau^4 {}_s\mu_4}{4!} + \ldots\right) + \frac{\left(\frac{v_z^2\tau^2 {}_s\sigma^2}{2!} - \frac{v_z^4\tau^4 {}_s\mu_4}{4!} + \ldots\right)^2}{2!} + \ldots\right]$$

$$= -\frac{v_z^2\tau^2 {}_s\sigma^2}{2!} + \frac{v_z^4\tau^4 {}_s\mu_4}{4!} - \frac{v_z^4\tau^4 ({}_s\sigma^2)^2}{8}$$

$$= -\frac{v_z^2\tau^2 {}_s\sigma^2}{2!} + \frac{v_z^4\tau^4}{4!}\{{}_s\mu_4 - 3({}_s\sigma^2)^2\}$$

Then ${}_s\kappa_2 = {}_s\sigma^2$ and ${}_s\kappa_4 = {}_s\mu_4 - 3({}_s\sigma^2)^2$ are the cumulants of the distribution of slopes and ${}_s\beta_2 = \frac{{}_s\mu_4}{({}_s\sigma^2)^2}$ is the kurtosis

of the distribution of slopes.

$$\chi_2(v_z,-v_z;\tau) = 1 - \frac{v_z^2}{2!} E[(\zeta_1-\zeta_2)^2] + \frac{v_z^4}{4!} E[(\zeta_1-\zeta_2)^4] - \ldots$$

$$= 1 - \frac{v_z^2}{2!}\{\sigma^2+\sigma^2-2\sigma^2 C(\tau)\} + \frac{v_z^4}{4!} 2\{\mu_4' - 4E[\zeta_1{}^3\zeta_2] + 3E[\zeta_1{}^2\zeta_2{}^2]\} - \ldots$$

$$= 1 - \sigma^2 v_z{}^2\{1-C(\tau)\} + \frac{v_z^4}{12}\{\mu_4 - 4E[\zeta_1{}^3\zeta_2] + 3E[\zeta_1{}^2\zeta_2{}^2]\} - .$$

The higher order moments $E[\zeta_1{}^2\zeta_2]$ and $E[\zeta_1{}^2\zeta_2{}^2]$ involve the autocorrelation functions of higher orders.

Defining, $\zeta' = \lim_{\tau\to 0} \frac{\zeta(x+\tau) - \zeta(x)}{\tau}$,

$$V(\zeta') = \lim_{\tau\to 0} V\{\frac{\zeta(x)+\tau) - \zeta(x)}{\tau}\}$$

$$= \lim_{\tau\to 0} \frac{1}{\tau_2}\{V\zeta(x+\tau) - (\zeta(x))\}$$

$$= \lim_{\tau\to 0} \frac{1}{\tau_2}\{V(\zeta(x+\tau) + V(\zeta(x) - 2C(\zeta(x+\tau),\zeta(x))\}$$

$$= \lim_{\tau\to 0} \{\frac{2\sigma^2 - 2\sigma^2 C(\tau)}{\tau^2}\}$$

Using L' Hospital's rule:

$$V(\zeta') = \lim_{\tau\to 0} - \frac{2\sigma^2 C'(\tau)}{2\tau}$$

Again, $V(\zeta') = \lim_{\tau\to 0} - \frac{2\sigma^2 C''(\tau)}{2}$

$$= -\sigma^2 C''(0).$$

CHAPTER 9

APPLICATIONS

Abstract

This chapter summarises the results and observations accrued, during the study to the applications of:

(i) optical inspection instrumentation,

(ii) defect detection and classification from polar intensity diagrams, and

(iii) surface roughness parameter estimation.

Comment is made on the following instrument design features: the nature of the interrogating source, the incident and receiver angles, and the transducer system.

Use can be made of knowledge of the speckle intensity distributions in selecting thresholds for detecting surface flaws, so as to work to desired detection and false alarm rates.

Polar diagrams demonstrate clear discrimination between scratch and indentation defects, as well as showing evidence of periodicity in the macrostructure.

In addition, a variety of surface roughness parameter estimates are derived for Type (A) and Type (C) surfaces.

9.1 Instrument Design

The optical rig used in the study was built for the the purpose of studying the interaction of a laser beam and a rough surface, and at no stage was it conceived as a prototype surface inspection instrument. It demonstrated the feasibility however, of automatic data gathering by an optical scanning sensor. Traditional optical scanners have a serious disadvantage in that they are constrained to move in a fixed path. A roving scanner, tracking under control

in three dimensions, is a higher order of magnitude of instrumentation, and there would be great difficulty in protecting the receiver device, in the severe industrial environment in which it would operate commercially.

An alternative, as with the SIRA system, is to use fixed sensors at strategic points. The obvious drawback is the partial information that this provides. For mild steel strip the reflected field is scattered over a large solid angle, whereas for some types of highly finished stainless steel, it is confined to a solid angle of 1-2 degrees only. A diode array nowadays offers a better alternative. Thwaite's instrument (c.f. Thwaites [1982]), employed a linear diode array successfully, and there is no reason why this could not be augmented to a planar diode array matrix. For our specimens, gross defects resulted in variations in the specular lobe, within a fraction of one degree, and the indications are that the dimensions of this array need not be extensive. A comprehensive appraisal of scanning instruments versus diode array devices is to be found in Norton-Wayne [1982].

Another design option is the choice of wavelength of the incident radiation. Practical measurements, supported by the analyses of Chapter 8, have shown that better contrast is available if incoherent illumination is utilised, rather than coherent illumination. A 2:1 improvement in the signal-to-noise ratio has been observed if we opt for an incoherent source. The practical importance of this result is that low contrast defects might now be detected, since the threshold bounds (c.f. 9.2.1.) can be tightened for greater sensitivity, without introducing unacceptably high false alarm rates.

An alternative method of detecting low contrast defects is to align both source and sensor at grazing incidence. The background surface roughness fades to a smoother roughness type enabling the defect signal to be extracted. Sawatari [1972] described such a mode of operation. One can simulate this effect by holding up a surface near a light source and tilting the surface towards grazing incidence.

The effect is easily explained in terms of the wave theory since,

$$g = \sigma^2 v_z^2 = \left\{ \frac{2\pi\sigma}{\lambda} (\cos\theta_1 + \cos\theta_2) \right\}^2 \qquad \ldots.(1)$$

and θ_1, $\theta_2 \to 90^\circ \implies g \to 0$ as we approach grazing incidence.

In the laboratory, grazing incidence can be easily achieved. However, with the actual rig the maximum available movement of the scanner only allowed angles of θ_2 up to about 60 degrees or so. Nevertheless, the 'smoothing effect' of oblique illumination was plainly discernable and for strong scatterers, such as surfaces bearing semi-circular indentations, it was necessary to operate at as wide an angle as possible to detect the scattered field above the background radiation. (Mundy and Porter [1981] actually reverse this technique in estimating the depth of scratch etc., in searching for the angle of zero contrast.)

There are additional benefits in operating in a smoother roughness mode, in that the scattered field no longer purely imitates the distribution of surface slopes. If we transpose to a Type (A) surface, the extra term available from the wave theory becomes significant from which the RMS roughness, σ, can be estimated (c.f. Chapter 9.3.).

Unfortunately, in the application to moving surfaces, there are operational difficulties at grazing incidence because of the 'flap' of the surface material. This causes the reflected beam to fluctuate wildly out of the field of view of any would-be receiver.

Another way of achieving the same ends, namely of transforming from a Type (C) to Type (A) surface, is to operate with a different incident wavelength.

Clearly to make g small in (1) we can let θ_1, $\theta_2 \to 90^\circ$ or allow λ to become large compared with the RMS roughness σ. Thwaite achieved this by using infra-red radiation, not only to estimate σ, but also to estimate the autocorrelation function of surface heights.

We can adapt the work of Wirgin [1975], by matching the wavelength of the incident light, to the dimension of defect type we are interested in. However, to achieve this resonance mode, the size of the laser spot must be reduced to, say, three times the dimensions of the defect type. This is virtually a matched filter optimally designed for one specific size of defects. The Kirchhoff model evaluation, using the deterministic term for geometrical defects, verifies the discrimination of polar diagrams to defect shapes, but the indication of 9.2.2., is that this would be rapidly obscured when the ideal geometry is disturbed by random fluctuations.

9.2 Defect Detection and Classification

9.2.1. Thresholding

For the past ten years optical methods have been employed to aid the problem of detecting surface flaws. Trigger signals, activated by a loss in intensity

amplitude, indicate the presence of a gross defect. The SIRA institute devised an empirical method of implementing a trigger pulse, see Brook [1971]. Their method was to smooth the output of a specularly positioned transducer, by means of a low pass filter. Attenuation by 10% of the filtered signal provided a suitable reference; should the specular signal fall below this threshold a trigger pulse was transmitted.

This system was modelled by using time series methods to obtain the expected specular output (c.f. Obray [1973]). The surface roughness imparts a noise to the monitored intensity level, and this noise was estimated by the MAD (mean absolute deviation) of the output intensity using the technique of exponential smoothing. The decision threshold for defect detection could then be set at ±2MAD.

However, we can now incorporate the knowledge of Chapter 8, namely, that for the off-specular receiver the intensity output is negative exponential, whilst the random component in the specular direction is given by the transformed Hoyt distribution. Thus thresholds can be set for different receivers so as to operate with prescribed false alarm probabilities for each detector.

The outputs of individual detectors are not independent, since light scattered away from one sensor will fall upon another. Crosscorrelation of output from the specular sensor, with that of a sensor 5 degrees off-specular, shows a significant negative correlation. (A typical crosscorrelation plot obtained from the SIRA system is given in Fig. 9.2.1.). False

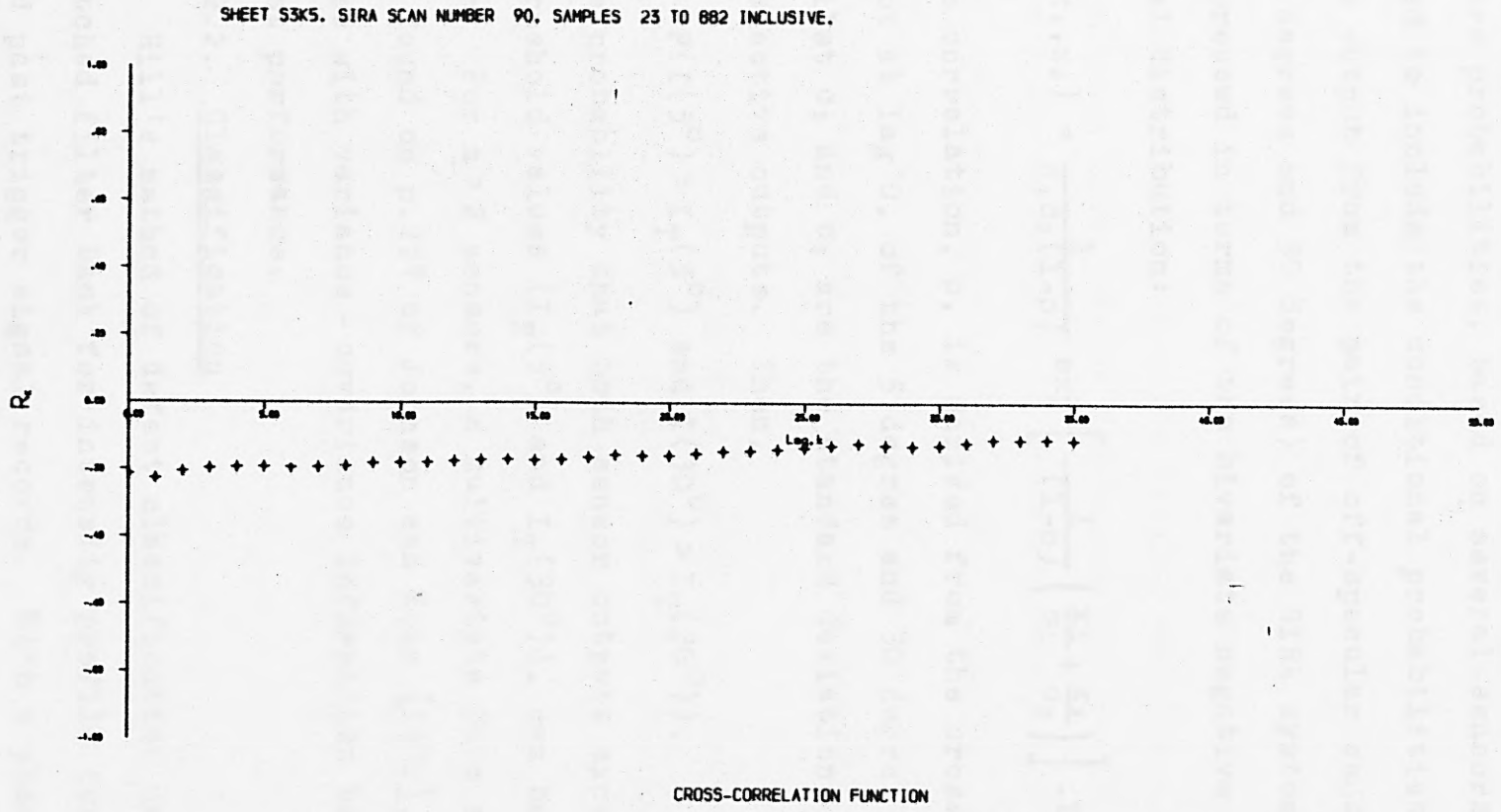

FIG. 9.2.1. Crosscorrelation Function of Specular and 5° off-specular Sensor Outputs from SIRA system

alarm probabilities, based on several sensors would need to include the conditional probabilities involved. The output from the pair of off-specular sensors (5 degrees and 30 degrees) of the SIRA system can be expressed in terms of the bivariate negative exponential distribution:

$$f(x_1,x_2) = \frac{1}{\sigma_1\sigma_2(1-\rho)} \exp\left[-\frac{1}{(1-\rho)}\left(\frac{x_1}{\sigma_1}+\frac{x_2}{\sigma_2}\right)\right] . I_o\left[\frac{2\sqrt{\rho}}{1-\rho}\sqrt{\frac{x_1x_2}{\sigma_1\sigma_2}}\right]$$

The correlation, ρ, is derived from the cross correlation plot at lag 0, of the 5 degree and 30 degree sensors, whilst σ_1 and σ_2 are the standard deviations of their respective outputs. Then,

$$P(I(5^o) > I_T(5^o) \text{ and } I(30^o) > I_T(30^o)),$$

the probability that both sensor outputs exceed their threshold values ($I_T(5^o)$ and $I_T(30^o)$), can be derived, etc. For $m > 2$ sensors, a multivariate form such as to be found on p.227 of Johnson and Kotz [1972], should be used with variance - covariance information based on past performance.

9.2.2. Classification

Hill's method of defect classification used a matched filter bank for intensity profile comparisons, and past trigger signal records. With a planar photodiode array detector device, to monitor the reflected polar diagram, the signal processing involved could be considerably less in terms of the volume of information. A simple integrator to monitor the total received power, would distinguish between a geometric defect and an oil drop for example, where much more light energy

would be absorbed.

Scratch Defects

A scratch defect scatters light in all directions but, as we have reported in Chapter 7, if the scratch is orientated approximately perpendicular to the incident light, the polar diagram reveals a major secondary lobe. Rules for bimodality can be devised, for instance whether or not a quartic polynomial leads to a significantly improved fit. Moreover, the turning points of the polynomial could locate the lobe maxima more precisely should there be an accompanying surface noise.

The interpretation of the polar diagram from the geometrical profile is not completely straightforward. It is tempting to treat the defect as a mixed model of Chapter 4, imposing a random facet micro-structure upon a deterministic half-plane macro-structure. For such a model we would expect to see preferred scattering directions with Gaussian dispersion about those directions. In reality, we do see a secondary lobe and, furthermore, this is far more substantial than anticipated. The lobe separation however is of the order of 0.5 degrees, and not, judging by the slope of the flanks, 45 degrees or more.

The lobe position does not vary substantially with variation of the angle of incidence (consistent with facet theory), but the relative amplitude of the lobes can vary, believed to be an effect of shadowing.

Debris material along the run of the scratch exacerbates shadowing. For this reason there is some

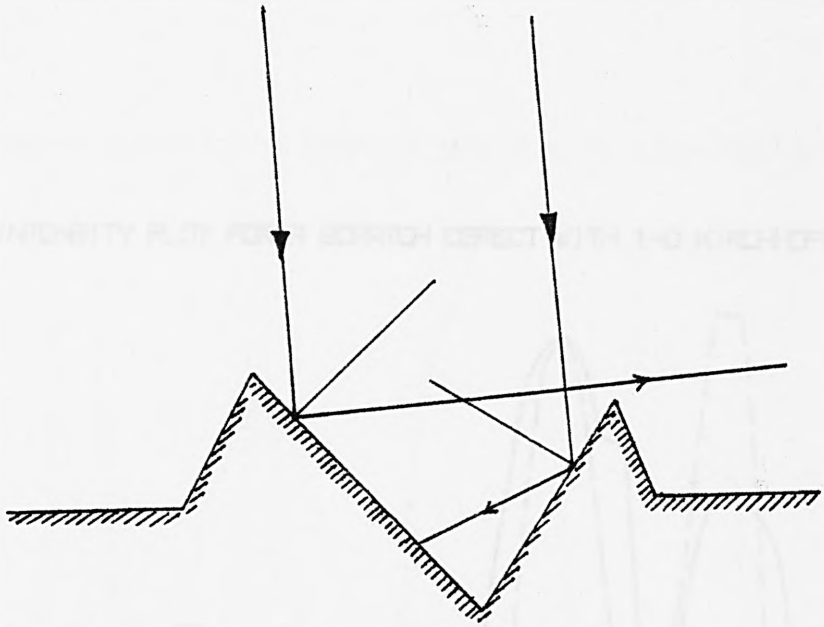

FIG. 9.2.2. Half-plane scratch scattering

evidence to suggest that near normal incidence is preferable, in order to obtain a clear bimodal graph, although the result is by no means conclusive. Secondary reflection, on the other hand, is thought to be the reason for only one secondary lobe and not two. Gaussian or non-Gaussian dispersion about the preferred directions is of the same order as for non defect specimens of the same RMS roughness.

The half-plane model is too rigid to explain the close proximity of the lobes. The groove was not precisely machined but crudely scribed. The randomness of the scattering is, in consequence, very much greater than suggested by the model. In effect, there is much more scattering away from specular, and the specular lobe is much diminished. This accounts for a more substantial secondary lobe. Scratch defect

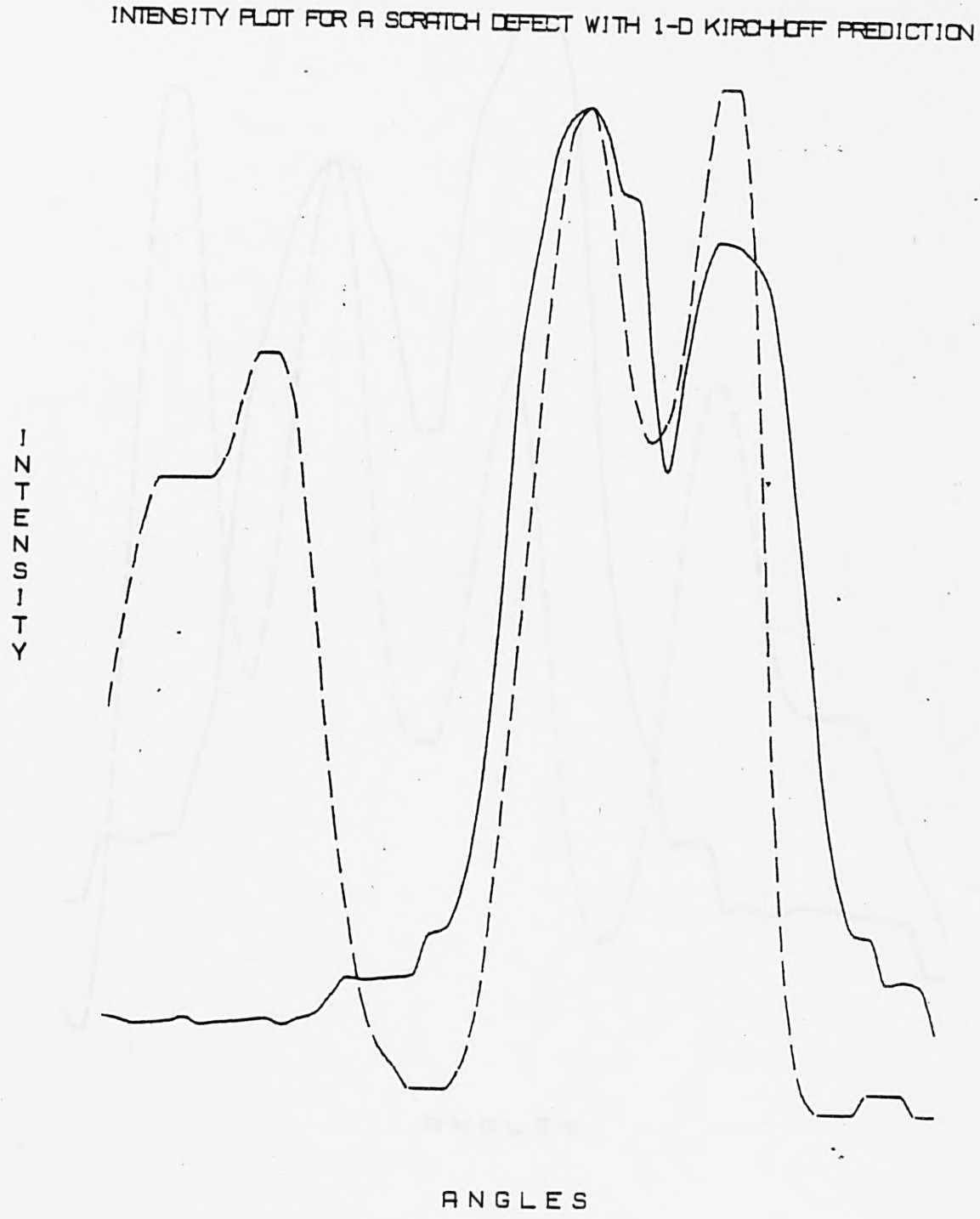

FIG. 9.2.3. Scratch defect specimen M2T4 scan 90°: angle of incidence 30°(perpendicular alignment)

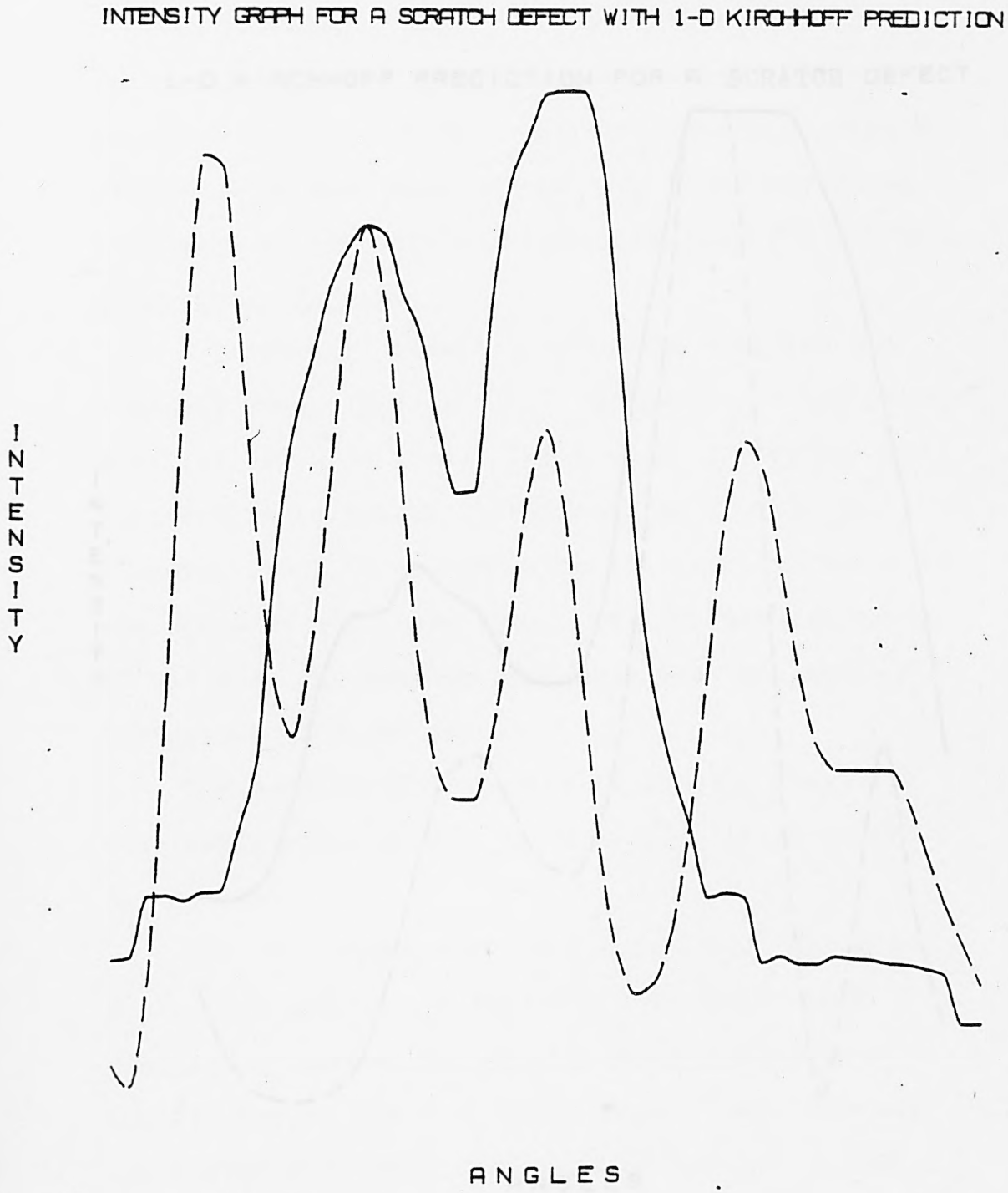

FIG. 9.2.4. Scratch defect specimen M2T4 scan 90.0°: angle of incidence 10° (perpendicular alignment)

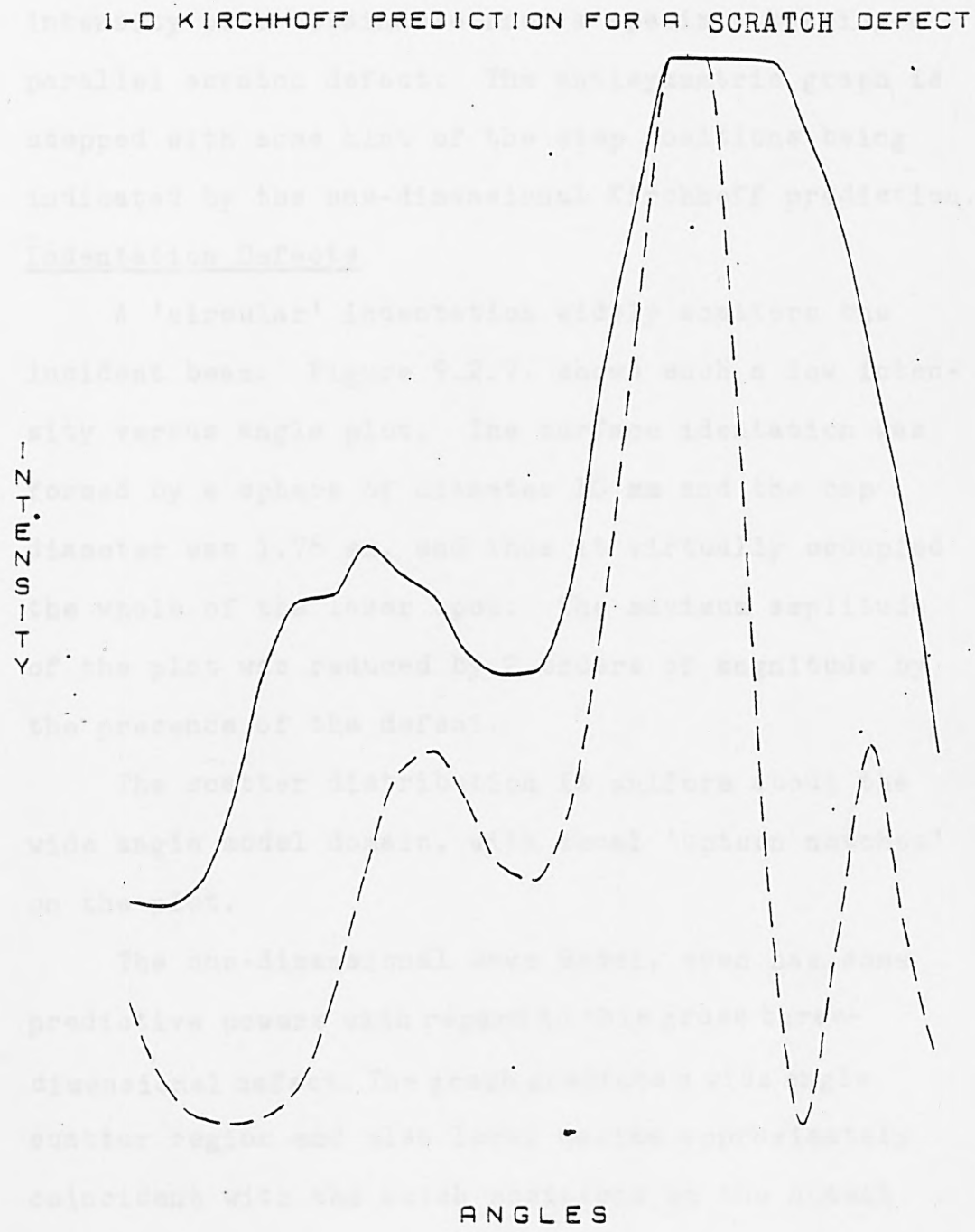

FIG. 9.2.5. Scratch defect specimen M1T4 scan: angle of incidence 30° (perpendicular alignment)

intensity plots are reproduced in Figures 9.2.3.-9.2.6. for which the range of scatter is about 2.5 degrees.

In particular figure 9.2.6. illustrates an intensity plot obtainable from a specimen bearing a parallel scratch defect. The antisymmetric graph is stepped with some hint of the step positions being indicated by the one-dimensional Kirchhoff prediction.

Indentation Defects

A 'circular' indentation widely scatters the incident beam. Figure 9.2.7. shows such a low intensity versus angle plot. The surface identation was formed by a sphere of diameter 10 mm and the cap diameter was 1.76 mm, and thus it virtually occupied the whole of the laser spot. The maximum amplitude of the plot was reduced by 2 orders of magnitude by the presence of the defect.

The scatter distribution is uniform about the wide angle model domain, with local 'upturn notches' on the plot.

The one-dimensional wave model, even has some predictive powers with regard to this gross three-dimensional defect. The graph predicts a wide angle scatter region and also local maxima approximately coincident with the notch positions on the actual intensity plot.

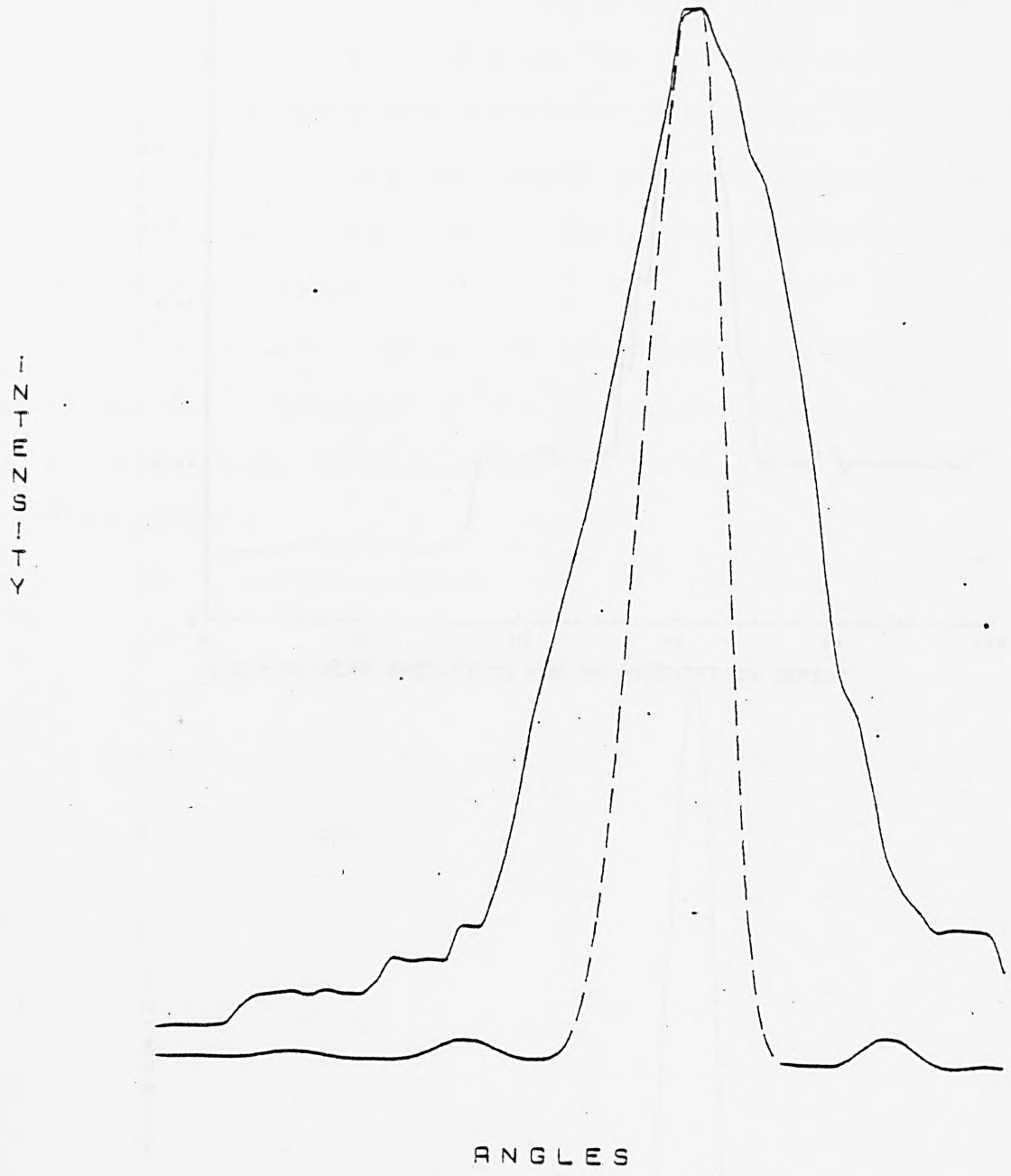

FIG. 9.2.6. Parallel scratch defect specimen M3T5 (perpendicular alignment)

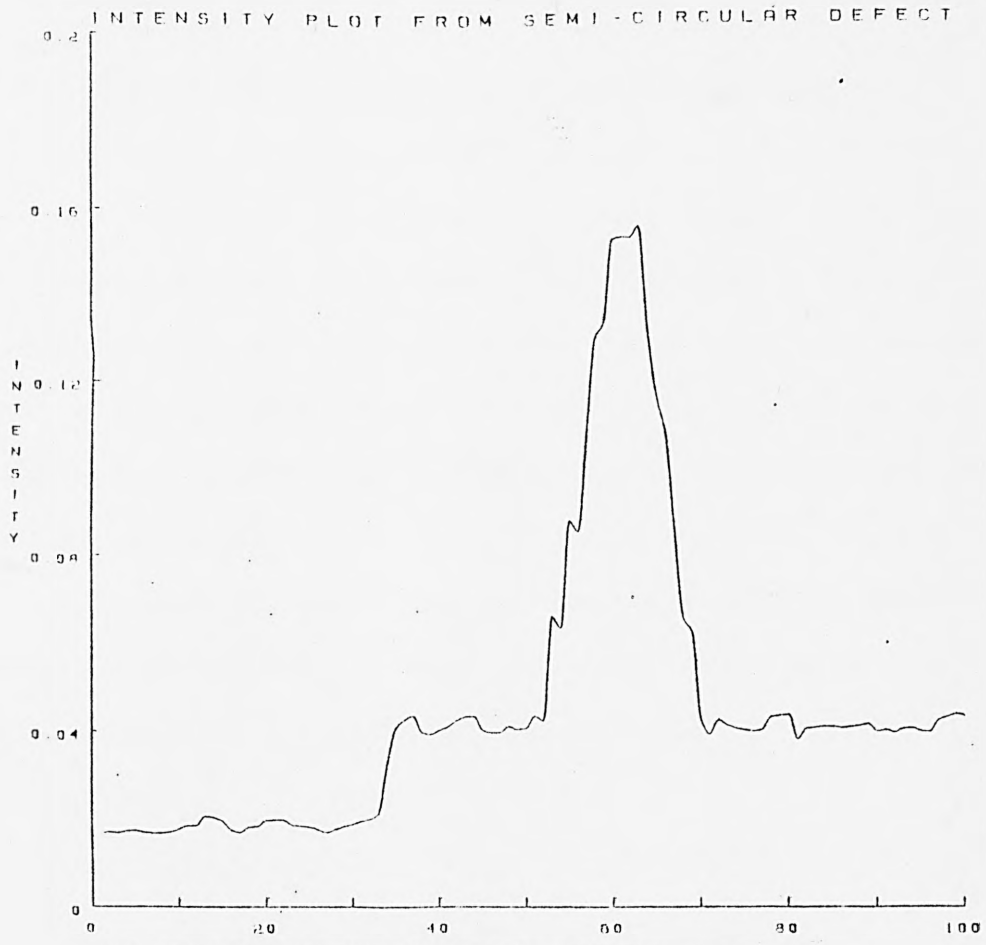

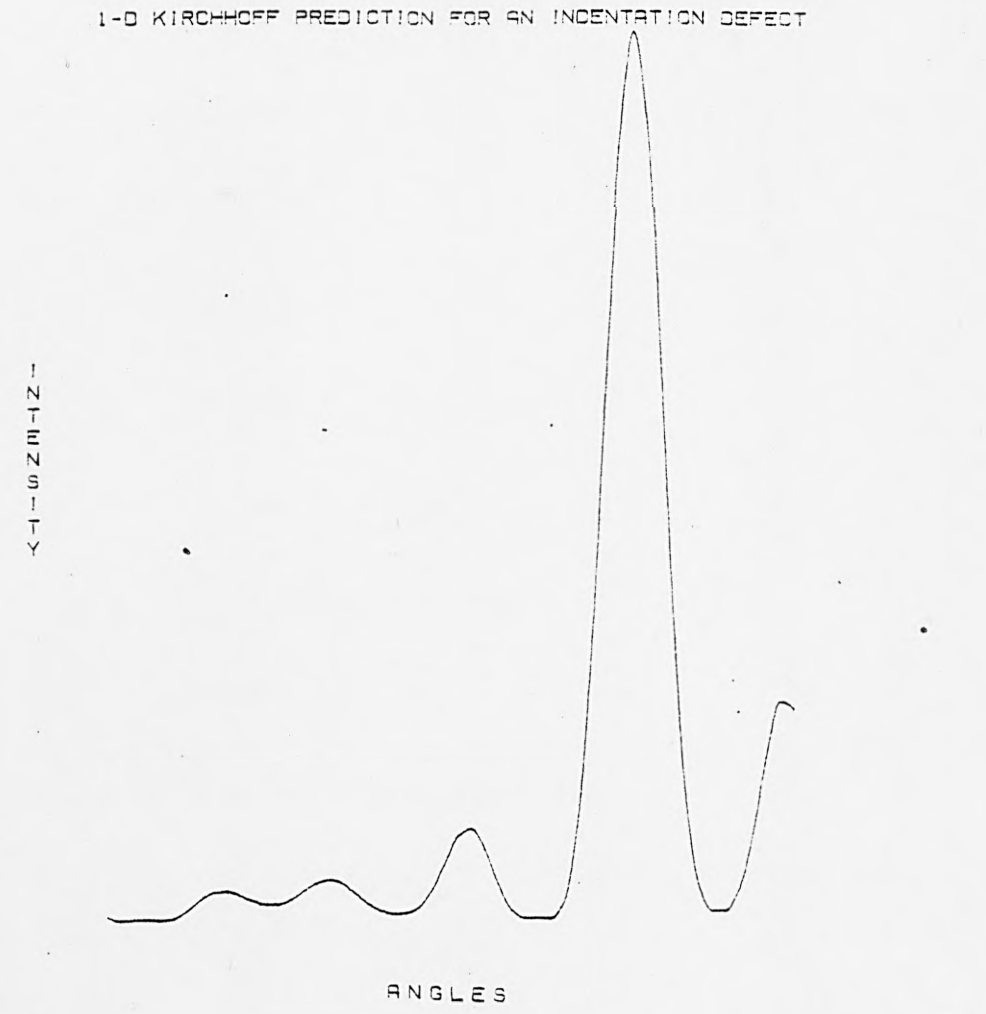

FIG. 9.2.7. Intensity plot from 'circular' indentation

9.3 Estimation of Surface Roughness Parameters

As we have seen for Type (C) surfaces the reflected field is a function of surface slopes. Since most practical surfaces are of this type, the discussion focuses on the retrieval of slope statistics. However, in the course of the study various peripheral analyses suggested methods whereby other surface parameters might be estimated for suitable surfaces.

For instance, returning to our work on incoherent and coherent illumination of the previous chapter, we have a possible means of estimating the variance of surface roughness heights:

For a smooth surface

$$R^2 \text{ (say)} = \frac{S/NR \text{ (specular)}}{S/NR \text{ (off specular)}} \simeq \frac{1}{2(1 - e^{-\sigma^2})^2} \quad \ldots.(2)$$

Measurement of the L.H.S., R^2, in practice gives

$$R = \frac{1}{\sqrt{2}(1 - e^{-\sigma^2})}$$

$$1 - e^{-\sigma^2} = \frac{1}{\sqrt{2}R}$$

$$e^{-\sigma^2} = \frac{1}{\sqrt{2}R}$$

$$-\sigma^2 = \log\left(1 - \frac{1}{\sqrt{2}R}\right)$$

$$= -\left[\frac{1}{\sqrt{2}R} + \frac{1}{2}\left(\frac{1}{2R}\right)^2 + \ldots\right]$$

$$\therefore \quad \sigma^2 \simeq -\log\left(1 - \frac{1}{\sqrt{2}R}\right) \quad \ldots.(3)$$

or as a further approximation,

$\sigma_\phi^2 \simeq \frac{1}{\sqrt{2}R}$ on returning to our earlier notation. Thus from equation (5) of Chapter 8

$$\frac{16\pi^2}{\lambda^2} \cos^2\theta_1 \, \sigma_z^2 \simeq \frac{1}{\sqrt{2}R}$$

$\therefore$ The standard deviation of surface heights, σ_z

$$= \frac{\lambda}{4\pi\cos\theta_1(\sqrt{2}R)^{\frac{1}{2}}} \qquad \ldots.(4)$$

A laboratory method to estimate σ_z would be to view the specimen at the same specular angle θ_1, alternatively with a coherent and an incoherent light source. After each pair of readings the specimen would be moved so that a different region of the surface would be illuminated. The mean/variance ratios of the data sets would allow R^2 to be derived.

Again, an algorithm for parameter extraction emerges from Cox's work on smooth mirrors.

Given that the log (intensity) scatter can be modelled adequately (at least qualitatively), it would be of interest to attempt a qualitative fit and estimate certain parameters.

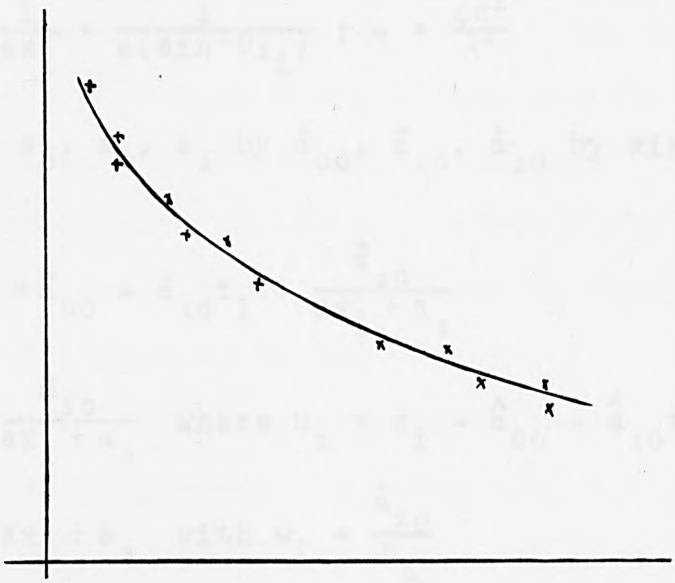

FIG. 9.3.1. Log (Intensity) Plot with Model. Curve. Fit.

Model : z_i (say) $= \log\left[I(\theta_2)_i\right]$

$$= a_o - 2\log(1+\cos\theta_{2i}) - a_1(1+\cos\theta_{2i})^2 + \frac{3}{a\sin^2\theta_{2i} + a_3} \qquad \ldots.(5)$$

Initially estimate a_o, a_1, B, a_3 by least squares to provide $\hat{a}_o$, $\hat{a}_1$, $\hat{B}$ and $\hat{a}_3$.

a_o is of no interest but $\hat{\sigma}^2 = \frac{\lambda^2 \hat{a}_1}{4\pi^2}$

(N.B. $\hat{a}_1 > o$ to be meaningful.)

Also $\hat{T} = 1/\sqrt{\hat{a}}$ and $\hat{B}$ carries information on A_1 and e to provide useful surface texture autocorrelation data. If this is encouraging, enhance the method to breakdown B into its separate features.

The estimation is non-linear but the following algorithm, essentially a two-stage linear process should be tried:

(1) Reduce model to $z_i = a_o - a_1 t_i + \frac{a_2}{a x_i}$

or $z_i = a_o - a_1 t_i + a_2 s_i$ where $t_i = 2\log(1 + \cos\theta_{2_i})$

and $s_i = \frac{1}{a x_i} = \frac{1}{a(\sin^2\theta_{2_i})}$; $a = \frac{4\pi^2}{\lambda^2}$

Estimate a_o, a_1, a_2 by $\hat{a}_{oo}$, $\hat{a}_{1o}$, $\hat{a}_{2o}$ by simple least squares.

(2) Model $z_i = \hat{a}_{oo} - \hat{a}_{1o} t_i + \frac{\hat{a}_{2o}}{a x_i + a_3}$

or $u_i = \frac{\hat{a}_{2o}}{a x_i + a_3}$ where $u_i = z_i - \hat{a}_{oo} - \hat{a}_{1o} t_i$

and $w_i = a x_i + a_3$ with $w_i = \frac{\hat{a}_{2o}}{u_i}$

Estimate a_3 from w_i model to obtain $\hat{a}_{3o}$.

Now update s_i to $\frac{1}{a x_i + \hat{a}_{3o}}$ and go to (1).

Stop when estimates have converged.

9.3.1. Half-width of Intensity Distribution

A simple processing statistic is to compute the angular deflection for which the intensity falls to half the specular value. The absolute value of the specular intensity, or for that matter the absolute value of off-specular intensity, is a function of the reflective properties of the material and the dimensions of the illuminated region, as well as surface roughness. As we have seen before, a ratio of intensity values removes difficulties of interpretation.

An exploratory paper by Thomas and Clarke [1978] reports half-width measurements performed in the laboratory. Thomas and Clarke used a laser scanner developed by Ferranti, the details of which are to be found in Clarke and Bedford [1978]. The quoted conclusions have been discredited, but the potential capability of the device is not in question. Half-width measurements varied from about 0.2 degrees for finely finished surfaces to almost 50 degrees for coarsely finished surfaces.

For our laboratory samples half-widths were about 0.1 degrees (regardless of material), except for specimen MOT3 (cold rolled stainless steel) which was approximately 0.4 degrees. The intensity in fact dropped by 1 order of magnitude at approximately 0.25 degrees from specular.

Cold-rolled mild steel is coarsely textured and measurements by Barker and Brook [1978] on this material showed a 1 order of magnitude drop at about

15 degrees, a 2 orders of magnitude drop at about 40 degrees. Further, using a data bank of successive scan data held on magnetic tape, the intensity at 5 degrees off-specular is three-quarters of the specular value. (In practice the mean values of the sensor outputs can be computed as the SIRA scanner automatically inspects a sheet: Chandley [1976] physically moved a specimen 4000 times in order to remove speckle effects and obtain ensemble mean intensity values.)

Combining the information we have the incomplete plot shown, on normalising the intensity value to 1 at specular.

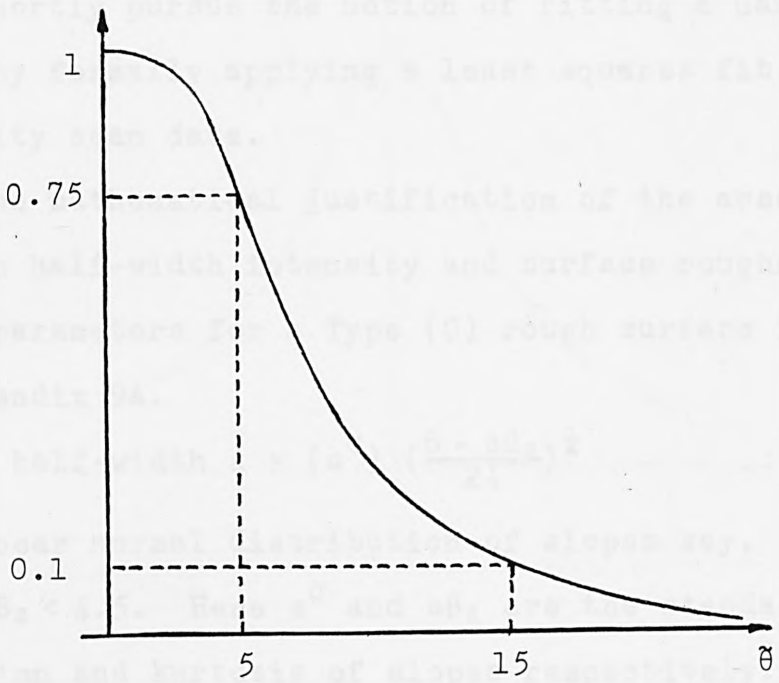

FIG. 9.3.2. Partial Scatter Information of SIRA Sensors

If we assume a Gaussian distribution of surface height, the intensity scatter from a Type (C) rough surface is given by

$$I(\tilde{\theta}) \propto \exp\left(-\frac{T^2\tilde{\theta}^2}{16\sigma^2}\right) \qquad \ldots.(6)$$

(c.f. equation (46) of Chapter 6.)

for reasonably small angles $\tilde{\theta}$ from specular. An adequate fit of a Gaussian curve can be made if we discard the 40 degree value. (We would not expect the approximation to still hold in this remote diffuse region in any event.)

$$\frac{3}{4} = \exp\left[-\frac{T^2}{16\sigma^2}\left(\frac{5\pi}{180}\right)^2\right]$$

$$(\hat{\sigma}/T) = \frac{1}{4}\left[-\log_e(3/4)\right]^{\frac{1}{2}} \cdot \frac{5\pi}{180}$$

$$= 0.040$$

i.e. a mean surface slope statistic of 0.040 (0.043 if we use the 15 degree value) or 2.29 degrees. We will shortly pursue the notion of fitting a Gaussian curve by formally applying a least squares fit to our intensity scan data.

The mathematical justification of the association between half-width intensity and surface roughness slope parameters for a Type (C) rough surface is given in Appendix 9A.

$$\text{A half-width } \Lambda \simeq (s^{\sigma})\left(\frac{6 - s\beta_2}{24}\right)^{\frac{1}{4}} \qquad \ldots.(7)$$

for a near normal distribution of slopes say, $2.5 < s\beta_2 < 4.5$. Here s^{σ} and $s\beta_2$ are the standard deviation and kurtosis of slopes respectively. Thus the expression (7) for half-width comprises two characteristics: a measure of spread (s^{σ}) and a measure of shape ($s\beta_2$) of the slope, distribution in keeping with the dominant geometrical nature of Type (C) scattering.

Incidently Porter and Mundy [1981], estimate s^{σ} from the half-width point assuming, albeit unstated, a Gaussian distribution of surface heights. However, half-width estimates are reasonably robust as demonstrated in Appendix 9A.

9.3.2. Mean Slope Roughness by Intensity Curve Fitting

The Gaussian function: $I(\theta_2) \propto \frac{T}{\sigma} \exp\left(-\frac{T^2\vartheta^2}{16\sigma^2}\right)$ ....(8) has been established as the mean intensity for Type (C) surfaces with Gaussian height statistics. The strategy now adopted to obtain an estimate of mean slope is to fit a Gaussian curve to intensity scan data by the method of least squares.

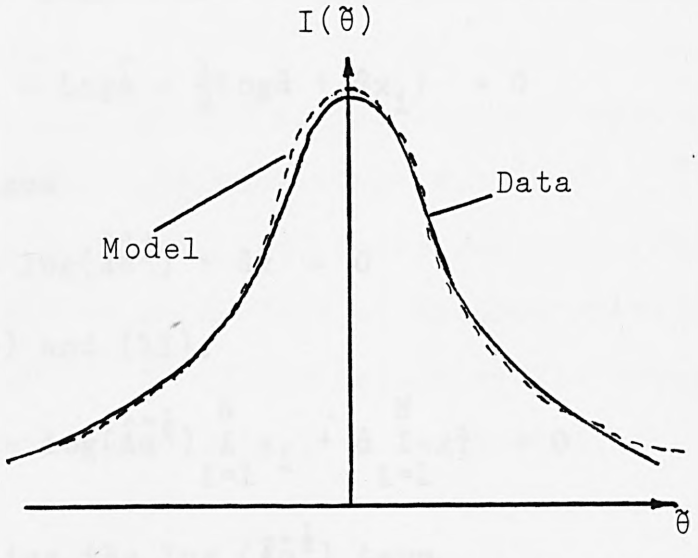

FIG. 9.3.3. Least Squares Fit to Gaussian Intensity Plot

The model fitting function is of the form

$$E[I(\vartheta)] = A\sqrt{\alpha}\exp(-\alpha\vartheta^2) \quad \ldots.(9)$$

on introducing the dimensionless variable $\alpha = \frac{T^2}{16\sigma^2}$

Take logarithms to produce, after a little algebra, a linear relationship.

$$\log\left[I(\theta)\right] = \log A + \frac{1}{2}\log\alpha - \alpha\theta^2.$$

With N data points, S, sum of squared errors

$$= \sum_{i=1}^{N} \{y_i - (\log A + \frac{1}{2}\log\alpha - \alpha x_i)\}^2 \quad \text{on writing}$$

$$y_i = \log\left[I(\theta)\right] \text{ and } x_i = \theta_i^2.$$

Whence, $\frac{\partial S}{\partial \alpha} = \Sigma\, 2\{y_i - (\log A + \frac{1}{2}\log\alpha - \alpha x_i)\}.(-\frac{1}{2\alpha} - x_i)$

$$\therefore \frac{1}{2\hat{\alpha}} \sum_{i=1}^{N} \{y_i - \log\hat{A} - \frac{1}{2}\log\hat{\alpha} + \hat{\alpha}x_i\} - \sum_{i=1}^{N} \{y_i x_i - (\log\hat{A} + \frac{1}{2}\log\hat{\alpha})\, x_i + \hat{\alpha}x_i^2\}$$

$$= 0 \text{ , for minimum} \qquad \ldots.(10)$$

Also $\frac{\partial S}{\partial A} = \sum_{i=1}^{N} 2\{y_i - (\log A + \frac{1}{2}\log\alpha - \alpha x_i)\}\frac{1}{A}$

$$\therefore \sum_{i=1}^{N} \{y_i - \text{Log}\hat{A} - \frac{1}{2}\log\hat{\alpha} + \hat{\alpha}x_i\} = 0 \qquad \ldots.(11)$$

for minimum

i.e. $\bar{y} - \log(\hat{A}\hat{\alpha}^{\frac{1}{2}}) + \hat{\alpha}\bar{x} = 0 \qquad \ldots.(12)$

From (10) and (11),

$$\sum_{i=1}^{N} y_i x_i - \log(\hat{A}\hat{\alpha}^{\frac{1}{2}}) \sum_{i=1}^{N} x_i + \hat{\alpha} \sum_{i=1}^{N} x_i^2 = 0$$

Eliminating the $\log(\hat{A}\hat{\alpha}^{\frac{1}{2}})$ term

$$\Sigma y_i x_i - (\bar{y} + \alpha\bar{x}) \sum_{i=1}^{N} x_i + \hat{\alpha}\Sigma x_i^2 = 0$$

$$\hat{\alpha} = -\frac{\{\Sigma y_i x_i - (\Sigma y_i)(\Sigma x_i)/N\}}{\Sigma x_i^2 - (\Sigma x_i)^2/N}, \qquad \ldots.(13)$$

which is the usual form of the estimate of the slope parameter in simple linear regression.

To complete the fitting,

$$\log (\hat{A}\hat{\alpha}^{\frac{1}{2}}) = \bar{y} + \hat{\alpha}\bar{x}$$

$$\hat{A}\hat{\alpha}^{\frac{1}{2}} = \exp (\bar{y} + \hat{\alpha}\bar{x}). \qquad \ldots.(14)$$

The surface roughness statistic, σ/T is then estimated by $1/4\sqrt{\hat{\alpha}}$.

A Gaussian curve has been fitted to a number of intensity data scans employing program SCATGH.FOR (c.f. Appendix 5A for program listing). Figure 6.1.14 shows a Gaussian curve fit to an intensity graph from specimen M1T2, from which σ/T is estimated to be 0.00113.

Such a value would indicate a scatter spread of about 0.8 degrees. In fact the observed range is about 1.2 degrees.

The derived σ/T values are used next in 9.3.3. to obtain σ RMS roughness heights.

The expression (8) above was formulated on the basis of a Gaussian form of autocorrelation $C(\tau) = e^{-\tau^2/T^2}$. If the nature of the autocorrelation is negative exponential instead, then

$$I(\theta_2) \quad \frac{2T/g}{1 + \frac{T^2}{g^2}\theta^2} \qquad \ldots.(15)$$

is the appropriate intensity model.

Then $E[I(\theta)] = \frac{A}{1 + \alpha\theta^2}$ $\ldots.(16)$

is the requisite fitting function.

Whence, $\frac{1}{A} + \frac{\alpha}{A}\theta^2 = \frac{1}{E[I(\theta)]}$ $\ldots.(17)$

Writing $y = \frac{1}{I(\theta)}$ and $x = \theta^2$, we have again a simple linear regression with the slope parameter = $\frac{\alpha}{A}$ and the intercept parameter = $\frac{1}{A}$.

The ratio of the linear regression parameters enables $\alpha = T/g$ to be estimated.

This least squares fitting routine was utilised in a simulation exercise in Appendix 9B. Whilst the tails of actual intensity plots do decay more slowly than Gaussian, reflecting the negative exponential portion of surface autocorrelations, a Lorenzian type curve fit is manifestly inadequate.

Many of the intensity plots obtained experimentally were extremely leptokertic, indicating that neither Gaussian nor Lorenzian curves are suitable bases for model fitting. Such intensity plots were modelled by Pearson VII curves using the method of moments, and we appeal to the geometric nature of Type (C) roughness scattering to derive an estimate of mean slope. For specimen M1T2, the Pearson parameters are $c^2 = 0.1355$ and $m = 3.04$, from which we estimate the mean slope to be 0.10 degrees which compares directly with 0.13 degrees from the Gaussian fit.

9.3.3. Estimation of RMS of Surface Heights

In the literature review of Chapter 3, we noted in 3.2, methods of obtaining RMS of surface roughness heights. Often the method methodology required some degree of extra sophistication, such as the use of two modes of incidence or two nearly coincident wavelengths of illumination.

We have seen that the first order surface statistics gives rise to a specular spike, whilst the mechanism for scattering about the specular spike, is the second order statistics of the surface. Many of the test specimens were too rough to distinguish the spike feature, but for more moderately rough specimens the specular spike is just discernable, as seen in Figure 9.3.4. for example. We approximate the diffuse component by a Gaussian scatter curve, and consider the ratio of the intensities in the specular direction

$$\frac{I\ (\text{first order})}{I\ (\text{second order})} = \frac{e^{-g}}{T/L\ \frac{\sqrt{\pi}}{\sqrt{g}}} \qquad \ldots.(18)$$

$$= \frac{e^{-g}}{\sqrt{\pi}/L\ \frac{T}{\sigma v_z}}$$

$$= \frac{(Lv_z e^{-g})(\sigma/T)}{\sqrt{\pi}} \qquad \ldots.(19)$$

For a specimen such as M3T2 on the Type (B)/Type (C) boundary, the methods of 9.3.2. enable a reasonable estimate of σ/T to be found independently. The relative magnitude of the specular spike to the broad diffuse intensity component then allows for the determination of g and thence σ.

For the scan shown:

$$\frac{I(\text{spike})}{I(\text{diffuse})} = \frac{1.15 - 1.14}{1.14} = \frac{0.04}{1.14}$$

$$= \frac{2000}{3}\ \frac{2\pi}{0.628}\ (\sqrt{3})\ 0.00164\ e^{-g}$$

$$= \frac{4}{114}$$

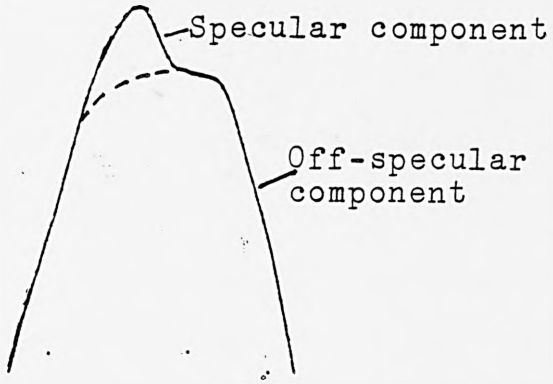

FIG. 9.3.4. Specular component and off-specular component for specimen M3T2

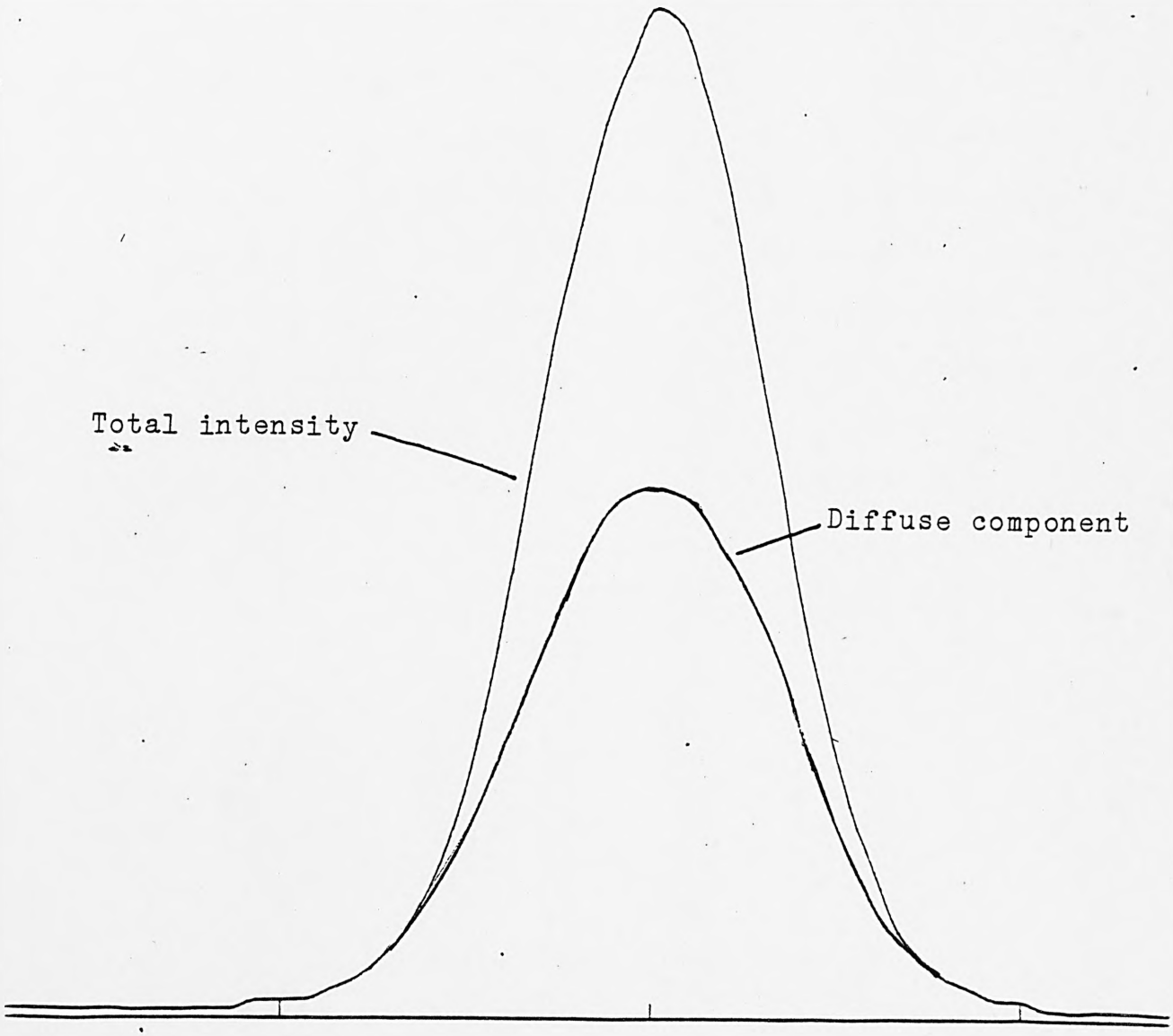

FIG. 9.3.5. Diffuse component and total intensity plot for Type (B) specimen M3T1

$\Rightarrow g = 7.10$

$\Rightarrow \sigma = 0.138$ μm, which compares with the talysurf value of 0.09 μm.

For a super-smooth specimen M3T1 (a smoother brass specimen), the relative contributions are vastly different. The diffuse component is a relatively disperse, low amplitude field. The 'specular spike', for reasons explained in Chapter 7, appears broadly Gaussian. The method in this case is to use the 'tails' of the intensity plot, to estimate the diffuse contribution of the field attributable to the second order statistics. The intensity ratio is used in the same manner to estimate the value of g etc. The ratio in this instance is approximately 1. Whence $\hat{\sigma} = 0.0747$. Table 9.3.1. gives estimated and observed RMS values. In general, the estimated values $\hat{\sigma}$, are approximately 1.4 times larger than the measured talysurf-5 values. Although for the anisotropic rolled steel surface, there was exact agreement.

Specimen	Estimated $\hat{\sigma}$	Observed σ
M3T2	0.138	0.09
M3T1	0.07	0.05
M1T2	0.137	0.10
M0T2	0.12	0.12 (rolled)

TABLE 9.3.1. Estimated and Observed RMS Values of Surface Heights

9.3.4. Estimation of the Autocorrelation Function of Surface Heights

For smooth Type (A) surfaces, equation (24) of Chapter 8 provides a useful result for Fourier inversion. We thus obtain:

$$C(\tau) = \frac{1}{2\pi} \int_{-\infty}^{\infty} g\, e^{-iv_x\tau} \frac{2L}{F^2} I(v_x)dv_x. \qquad ....(20)$$

In the case of Type (C) surfaces the corresponding approximate result, as seen from equation (22) of Chapter 8, is

$$K(\tau) = \frac{1}{2\pi} \int_{-\infty}^{\infty} e^{-iv_x\tau} \frac{2L}{F^2} I(V_x)dv_x \qquad ....(21)$$

where $K(\tau) = \exp\left[-g(1 - C(\tau))\right]$ if in this case g and F, in reality functions of θ_2 (and consequently of v_x), can be treated as reasonably constant.

To appreciate the potential usefulness of (21) two special cases are analysed in Appendix 9B : specifically when $C(\tau)$ takes the form (i) $e^{-\tau^2/T^2}$ and (ii) $e^{-|\tau|/T}$. Case (ii) is further pursued in a simulation exercise.

However the apparent simplicity of equations (20) and (21) above is deceptive. Since the intensity $I(v_x)$ of (20) is the component of the scattered field about the specular direction, and the component due to the first order statistics must be removed first. In (21), an intensity model based on the Pearson fit yields a global autocorrelation function, but cannot realise the micro/macro structure components of observed autocorrelation functions. From our work in 7.1, the significant micro component contribution to

the scatter field is confined to the near specular region. One approach would be to attempt to fit the near specular region separately, and use a semi-empirical method of assessing the relative contributions to the autocorrelation integral from knowledge of the g parameter.

However this is unconvincing as a methodology since it is formulated by virtue of hindsight. Inversion of the actual intensity for Type (C) surfaces yields Gaussian-type autocorrelations, and in view of the approximations involved, would be meaningful for relatively few lags, say $\tau < 50$ μm. Over the lags 10 μm to 50 μm the derived autocorrelations are linear and agree reasonably well with talysurf autocorrelograms listed in Chapter 6. For longer lags the autocovariance of the scattered waves drops much more rapidly than the autocovariance of actual surface heights. (In agreement with the work of Chandley [1976b].)

Near $\tau = 0$ the talysurf and normalised autocorrelation functions from light scattering measurements differ considerably. The immediate fall registered in the talysurf graphs is not echoed by the light scattering graphs. For smoother surfaces the talysurf autocorrelograms register a less dramatic step at zero lag, and consequently light based autocorrelograms show better agreement near lag zero, but nonetheless fall more rapidly than their talysurf counterparts.

Lag	Specimen Type (C) M1T2	M3T2	M0T2	Specimen Type (B) M3T1
6.5	0.99	0.99	0.98	0.99
13	0.98	0.97	0.96	0.97
19.5	0.97	0.94	0.92	0.95
26	0.95	0.91	0.88	0.92
32.5	0.93	0.88	0.85	0.90
39	0.90	0.84	0.83	0.86
45.5	0.87	0.81	0.81	0.82
52	0.84	0.76	0.78	0.77
58.5	0.80	0.72	0.73	0.71

TABLE 9.3.2. Normalised Autocorrelations based on light intensity measurements

9.3.5. Periodicity of the Surface Roughness

Model surfaces having exact periodicity were closely examined in Chapter 4.3.1. Intensity plots demonstrate periodicity in their diffraction pattern away from the specular lobe. The separation of diffraction maxima gives a measure of an underlying periodicity in the surface roughness macro-structure.

A measure of the power spectrum, λq, defined by

$$\lambda q = 2\pi \frac{\sigma}{s\sigma}$$

is termed the 'average wavelength', so called since for a sinusoidal surface this parameter takes the value of the wavelength of the sinusoid.

A wavelength value λq^* is available from the separation of the specular lobe (order zero) and the first order diffraction lobe.

For the specimen M0T2 (cold rolled steel sample) this separation is 0.4 degrees.

$$\sin 30.4^{o} = \sin 30^{o} + \frac{\lambda}{\Lambda q^{*}}$$

$$\Rightarrow \lambda q^{*} = 104 \ \mu m$$

For specimen M3T1, employing the scan listed in Table 5.1.1., the separation is 0.92 degrees

$$\sin 10.92^{o} = \sin 10^{o} + \frac{\lambda}{\Lambda q^{*}}$$

$$\Rightarrow \lambda q^{*} = 40 \ \mu m$$

These values are approximately half the corresponding values obtainable from talysurf power spectra, and are consistent with the differences in light scattering and mechanical estimates of slopes and autocorrelograms.

Adjacent off-specular diffraction maxima gives higher harmonics of the surface periodicity.

9.3.6. Depth of Scratch Defects

If a scratch defect is aligned parallel to the incident laser beam the intensity plot is a broad Gaussian distribution. The ratio of the σ/T estimate for this plot with that obtained from defect free material enables an estimate of the scratch depth to be made provided the delineation of the scratch is known (e.g. from SIRA laser trace scanner). From

$$\frac{\sigma_{SC}}{\sigma_{RMS}} = 5 \times \frac{2L}{W} \quad , (W = \text{scratch width})$$

since the scratch roughness is smoothed over the area of the spot.

For the M2T4 sample, $\sigma_{SC} \simeq 40 \ \mu m$ which reasonably compares with the talysurf value.

9.4 Conclusions

Discrimination between the polar diagrams of circular indentations, can be partially explained in terms of simple geometry. Quantitatively, however, details of the polar diagram cannot be trivially inferred from talysurf profiles. The one-dimensional wave theory model can anticipate the whereabouts of defect-related polar diagram features and this represents a potential tool for developing more efficient classification algorithms.

The work has also shown the necessity of modelling non-Gaussian processes. The vast majority of slope distributions encountered were non-Gaussian, obeying a Pearson type IV or VII frequency law, for which the high kurtosis leads to a revision of the Gaussian based estimate of slope variance.

Prior knowledge of the form of the slope distributions should in fact determine the appropriate fitting routine for the extraction of the mean absolute slope statistic. Furthermore, if a negative exponential distribution of heights was envisaged the R.H.S. of (18) of 9.3.3. should read

$$\frac{1/(1+g)}{\pi T/4Lg}$$

and the estimation of σ_{RMS} should proceed accordingly.

The estimation of σ_{RMS} height from a single intensity scan appears feasible under conditions which enable components of the field due to the first and second order height statistics to be clearly differentiated. The results agree with talysurf values to within the sampling variation of σ_{RMS} of mechani-

cally measured heights. The methodology offers obvious advantages of instrumentation should the results be confirmed by further work.

Autocorrelograms based on light scattering measurements show much the same linear decay over the range 10 μm-50 μm as talysurf autocorrelograms. In general, for longer lags the light scatter autocorrelograms decay to zero more rapidly than corresponding talysurf autocorrelograms, which are much more influenced by the longer surface wavelengths. For Type (C) surfaces, $K(\tau) = \exp\left[1+g(1-C(\tau))\right]$ is based on the assumption of a Gaussian height distribution. If a negative exponential is adopted, the requisite form is

$$\frac{1}{\left[1+g(1-C(\tau))\right]}$$

and the decay to zero is more rapid still.

The cusp feature of the talysurf graphs eluded those based on light scattering. Whilst the cusp feature is apparent rather than real, and noting the different wavelength resolutions of the two measurements involved, the discrepancy demonstrates some conflict in the contacting and non-contacting results. For very smooth surfaces (20) is more robust than (21) in relation to the statistical distribution of surface height. Nevertheless, higher powers of g have been neglected in its formulation with the underlying assumptions of the Beckmann theory being presupposed.

APPENDIX 9A

Half-width of Intensity Distribution

Although half-width is s simple processing statistic of actual intensity data, there is no simple model intensity curve on which to compute a theoretical half-width parameter: the functional forms of intensity curve being determined by the statistical distributions of surface height. Here the approach is to evaluate the following integral for intensity:

$$I(.) = \int_{-\infty}^{\infty} \cos(v_x\tau)\chi_2(v_z,-v_z;\tau)\, d\tau, \qquad \ldots.(1)$$

using early terms of the $\chi_2(v_z,-v_z;\tau)$ expansion.
(N.B. For g>>1 Type (C) roughness, the only significant contribution to the integral is close to τ=0.)

Applying the general results of Appendix 8I,

$$\chi_2(v_z,-v_z;\tau) \simeq 1 - \frac{v_z^2\tau^2}{2!}s^{\sigma^2} + \frac{v_z^4\tau^2}{4!}s^{\mu_4} - \ldots$$

$$\simeq \sum_{r=0}^{\infty} (-1)^r \frac{s^{\mu_{2r}} v_z^{2r} \tau^{2r}}{(2r)!}, \qquad \ldots.(2)$$

where s r is the rth moment of the distribution of slopes.

Thus $I(.) \alpha \int_{-\infty}^{\infty} \cos v_x z \{ 1 - \frac{v_z^2\tau^2 s^{\sigma^2}}{2!} + \frac{v_z^4\tau^4}{4!}s^{\mu_4} - \ldots \} d\tau$

$$\simeq \int_{-\infty}^{\infty} \frac{\cos v_x\tau d\tau}{\{1+a\tau^2+b\tau^4\}} \qquad \ldots.(3)$$

We require as near as possible,

$$\{1 - \frac{v_z^2\tau^2}{2!}s^{\sigma^2} + \frac{v_z^4\tau^4}{4!}s^{\mu_4} - \ldots\{ \{1 + a\tau^2 + b\tau^2\} = 1 \quad \ldots.(4)$$

$$\Rightarrow \quad a - \frac{v_z^2 s^{\sigma^2}}{2} = 0 \qquad \text{(coeff. of } \tau^2) \qquad \ldots.(5)$$

$$b + \frac{v_z^4 {}_s\mu_4}{4!} - a\,\frac{v_z^2 {}_s\sigma^2}{2!} = 0 \quad \text{(coeff. of } \tau^4\text{)} \qquad \ldots.(6)$$

$$\therefore\ a = \frac{v_z^2 {}_s\sigma^2}{2!} \qquad \ldots.(7)$$

$$b = \frac{v_z^2 {}_s\sigma^2}{2!} \cdot \frac{v_z^2 {}_s\sigma^2}{2!} - \frac{v_z {}_s\mu_4}{4!}$$

$$= \frac{v_z^4 ({}_s\sigma^2)}{4!} \left\{ 6 - \left(\frac{{}_s\mu_4}{{}_s\sigma^2}\right)^2 \right\}$$

$$= \frac{v_z^4 ({}_s\sigma^2)^2}{4!} \{ 6 - {}_s\beta_2 \}, \qquad \ldots.(8)$$

where ${}_s\beta_2$ is the kurtosis of the slope distribution.

As a check on the working so far ${}_s\beta_2 = 3$ for a normal distribution, and therefore,

$$1 + a\tau^2 + b\tau^4 = 1 + \frac{{}_sg\tau^2}{2!} + \frac{{}_sg\tau^4}{8} \quad \text{on writing } {}_sg = v_z^2 {}_s\sigma^2.$$

The R.H.S. is the first three terms of $e^{sg\tau^2/2}$ and so

$$I \propto \int \cos v_x \tau e^{-{}_sg\tau^2/2} d\tau \qquad \ldots.(9)$$

If we further suppose that surface heights are correlated to $C(\tau) = e^{-\tau^2/T^2}$, then ${}_sg = 2\sigma^2/T^2 v_z^2 = 2g/T^2$.

$$\therefore\ I(.) \propto \int_{-\infty}^{\infty} \cos v_x \tau e^{-g\tau^2/T^2} d\tau \qquad \ldots.(10)$$

which is of the form of (28) p.85 of Beckmann [1963].

As a second check, for a negative exponential distribution, ${}_s\beta_2 = 6$, which implies b = 0 and

$$I(.) \alpha \int_{-\infty}^{\infty} \frac{\cos v_x \tau d\tau}{\{1 + {}_sg\tau^2/2\}} \qquad \ldots.(11)$$

This leads to the cusp solution as required.

In full, consider $\int_0^{\infty} \frac{\cos v_x \tau d\tau}{\{1 + a\tau^2\}}$.

$$\int_0^\infty \frac{\cos v_x \tau \, d\tau}{\{1 + a\tau^2\}} = \int_0^\infty \frac{\cos v_x \tau \, d\tau}{a\{1/a + \tau^2\}}$$

$$= \int_0^\infty \frac{\cos v_z \tau \, d\tau}{a\{(a')^2 + \tau^2}, \quad a' = 1/\sqrt{a}$$

$$= \frac{1}{a} \frac{\pi}{2a'} e^{-v_x a'}, \quad v_x > 0$$

$$= \frac{\pi}{2\sqrt{a}} e^{-v_x/\sqrt{a}} \qquad \ldots.(12)$$

But $a = s^g/2 = \frac{1}{2} s\sigma^2 v_z^2$

$$= \frac{\pi}{\sqrt{2}\, s\sigma v_z} e^{-\sqrt{2}/s\sigma(v_x/v_z)}$$

$$= \frac{\pi}{\sqrt{2}\, s\sigma v_z} e^{-\sqrt{2}/s\sigma \tan(\frac{\theta_1 - \theta_2}{2})}, \quad \theta_1 > \theta_2 \qquad \ldots.(13)$$

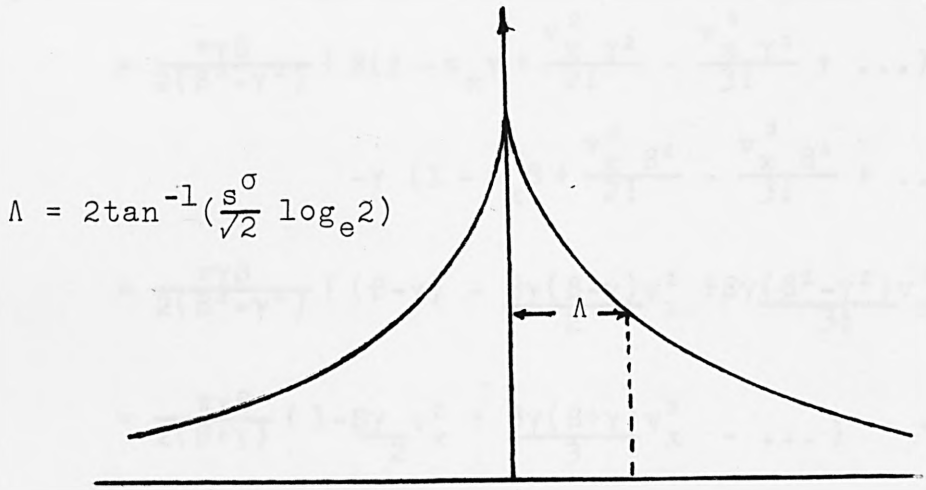

That is a cusped function with halfwidth Λ satisfying $\frac{\sqrt{2}}{s^\sigma} \tan \frac{\Lambda}{2} = \log_e 2$

$$\Lambda = 2\tan^{-1}\left(\frac{s^\sigma}{\sqrt{2}} \log_e 2\right) \qquad \ldots.(14)$$

$$\simeq s^\sigma$$

Returning to $\int_c^\infty \frac{\cos v_x \tau}{\{1 + a\tau^2 + b\tau^4\}} d\tau$, we have

$$\int_c^\infty \frac{\cos v_x \tau d\tau}{\{1 + a\tau^2 + b\tau^4\}} = \int_o^\infty \frac{\cos v_x \tau d\tau}{(1 + \frac{1}{\beta^2}\tau^2)(1 + \frac{1}{\gamma^2}\tau^2)}$$

$$= \int_o^\infty \frac{\gamma^2\beta^2 \cos(v_x\tau)_{d\tau}}{(\beta^2 + \tau^2)(\gamma^2 + \tau^2)}$$

$$= \gamma^2\beta^2\pi \frac{(\beta e^{-v_x\gamma} - \gamma e^{-v_x\beta})}{2\beta\gamma(\beta^2 - \gamma^2)} \quad , \qquad \ldots.(15)$$

with $\frac{1}{\beta^2} + \frac{1}{\gamma^2} = a$ $\quad \frac{1}{\beta^2\gamma^2} = b$ provided that the factorisation is allowable.

(The solution in the special case with b = 0 can be derived if we take $\frac{1}{\beta^2} = a$ and allow $\gamma \to \infty$).

$$I(.) \propto \frac{\pi\gamma\beta}{2(\beta^2 - \gamma^2)} \{ \beta e^{-v_x\gamma} - \gamma e^{-v_x\beta} \}$$

$$= \frac{\pi\gamma\beta}{2(\beta^2 - \gamma^2)} \{ \beta(1 - v_x\gamma + \frac{v_x^2\gamma^2}{2!} - \frac{v_x^3\gamma^3}{3!} + \ldots)$$

$$-\gamma (1 - v_x\beta + \frac{v_x^2\beta^2}{2!} - \frac{v_x^3\beta^3}{3!} + \ldots)$$

$$= \frac{\pi\gamma\beta}{2(\beta^2 - \gamma^2)} \{ (\beta - \gamma) - \frac{\beta\gamma(\beta - \gamma)}{2} v_x^2 + \beta\gamma\frac{(\beta^2 - \gamma^2)}{3!} v_x^3 - \ldots \}$$

$$= \frac{\pi\gamma\beta}{2(\beta + \gamma)} \{ 1 - \frac{\beta\gamma}{2} v_x^2 + \frac{\beta\gamma(\beta + \gamma)}{3} v_x^3 - \ldots \} \qquad \ldots.(16)$$

If b = 0, we have a function which is locally quadratic at $v_x = 0$ (specular). The half-width Λ is given by $\{.\} = \frac{1}{2}$, but more simply, at least in mathematical terms, would be the 'half-width' condition:

$$\beta\gamma v_x^2 = 1$$

$$v_x^2 = \frac{1}{\sqrt{\beta\gamma}} = \sqrt{b}$$

$$= \frac{v_z^2 s\sigma^2}{(4!)^{\frac{1}{2}}} \{ 6 - s\beta_2 \}^{\frac{1}{2}}$$

$$\frac{v_x^2}{v_z^2} = \frac{{}_s\sigma^2}{(4!)^{\frac{1}{2}}}\{6-{}_s\beta_2\}^{\frac{1}{2}}$$

$$\tan\{\frac{\theta_1-\theta_2}{2}\} = \frac{{}_s\sigma}{(4!)^{\frac{1}{4}}}\{6-{}_s\beta_2\}^{\frac{1}{4}}$$

$$\Lambda^* \text{say} = 2\tan^{-1}\frac{{}_s\sigma}{(4!)^{\frac{1}{4}}}\{6-{}_s\beta_2\}^{\frac{1}{4}}$$

$$\simeq \frac{2{}_s\sigma}{(4!)^{\frac{1}{4}}}\{6-{}_s\beta_2\}^{\frac{1}{4}} \qquad \ldots.(17)$$

In the case of the normal, $\Lambda^* = \frac{2(2\sigma^2/T)^{\frac{1}{2}}3^{\frac{1}{4}}}{(4!)^{\frac{1}{4}}}$,

$= 2^{\frac{1}{4}}(2\sigma^2/T^2)^{\frac{1}{2}}$, which compares with $\Lambda = (2\sigma^2/T^2)^{\frac{1}{2}}(2\log_e 2)^{\frac{1}{2}}$, the true half-width value.

As a working approximation we may take

$$\Lambda^* = {}_s\sigma \times \{6 - {}_s\beta_2\}^{\frac{1}{4}} \qquad \ldots.(18)$$

N.B. (i) In truth, the evaluation of $\int_{-\infty}^{\infty}\cos v_x\tau\chi_2(v_z-v_z;\tau)d\tau$ proceeds by knowledge of the poles of the function $\chi_2(v_z,-v_z;\tau)$, when expressed in terms of the complex variable z.

(ii) If ${}_s\beta_2 > 6$ then $b<0$ from (8) and the quadratic $1+az+bz^2=0$ has real zeros. In which case, $1+a\tau^2+b\tau^4 = (1+\frac{1}{\beta^2}\tau^2)(1-\frac{1}{\gamma^2}\tau^2)$. Then

$$\int_o^{\infty}\frac{\cos v_x\tau d\tau}{\{1+a\tau^2+b\tau^4\}} = \gamma^2\beta^2\int_o^{\infty}\frac{\cos v_x\tau d\tau}{(\beta^2+\tau^2)(\gamma^2-\tau^2)}$$

$$= \frac{\gamma^2\beta^2}{\beta^2+\gamma^2}\{\int_o^{\infty}\frac{\cos v_x\tau d\tau}{(\beta^2+\tau^2)} + \int\frac{\cos v_x\tau d\tau}{\gamma^2-\tau^2}\}$$

$$= \frac{\gamma^2\beta^2}{\beta^2+\gamma^2}\{\frac{\pi}{2\beta}e^{-v_x\beta} + \frac{\pi}{2\gamma}\sin v_x\gamma\} \qquad \ldots.(19)$$

Thus the half-width parameter is insensitive to slope kurtosis for leptokurtic slope distributions.

(iii) The approximations in the above treatment tend to nullify one another and the result

$$\Lambda = {}_s\sigma \left\{ \frac{6 - s\beta_2}{24} \right\}^{\frac{1}{4}}$$

seems acceptable for near normal distributions. However $\Lambda.s\sigma$ is preferred if the slope distribution approaches a Laplacian density.

APPENDIX 9B

Inversion Theorem for Autocorrelation Information

In, $I(\ ) = \frac{F^2}{2L}\int_{-\infty}^{\infty} e^{iv_x\tau} e^{-g[1-C(\tau)]}\,d\tau$, equation (22) of 8.2.2., we take $C(\tau) = e^{-\tau^2/T^2}$.

Then $I(\ ) \simeq \frac{F^2}{2L}\int_{-\infty}^{\infty} e^{iv_x} e^{-g\tau^2/T^2}\,d\tau$

$= \frac{F^2}{L}\int_{-\infty}^{\infty} e^{-g\tau^2/T^2}\cos(v_x\tau)\,d\tau$, since the integral is plainly even. To evaluate the above integral contour integration methods of functions of a complex variable are pursued and confirm in passing equation (45) of Chapter 4.

Consider the integral e^{-gz^2/T^2} around the contour C_R shown below.

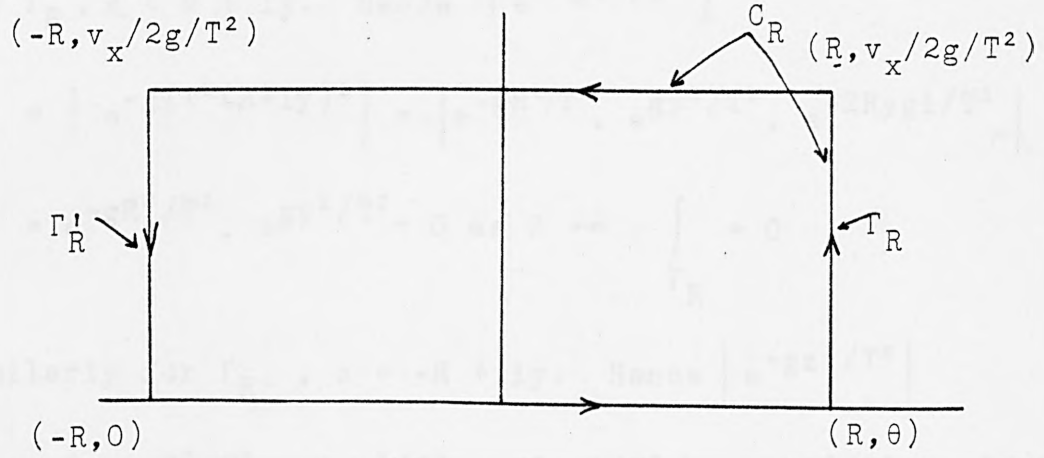

Since no singularities are contained within the contour,

$$\int_{C_R} e^{-gz^2/T^2}\,dz = 0$$

i.e. $\int_{-R}^{R} e^{-g\tau^2/T^2}\,d\tau + \int_{R}^{-R} e^{-g/T^2(\tau+iv_xT^2/2g)}\,d\tau + \int_{\Gamma_R} + \int_{\Gamma_R'} = 0$

Suppose for the moment that $\int_{\Gamma R}$ and $\int_{\Gamma R'} \to 0$ as $R \to \infty$.

Under this supposition we may write,

$$\int_{-\infty}^{\infty} e^{-g\tau^2/T^2}\,d\tau + \int_{-\infty}^{\infty} e^{-g\tau^2/T^2}.e^{iv_x\tau}.\ e^{T^2v_x{}^2/4g}\,d\tau = 0$$

$$\int_{-\infty}^{\infty} e^{-g\tau^2/T^2}\,d\tau = e^{T^2vx^2/4g} \int_{-\infty}^{\infty} e^{-g\tau^2/T^2}\ e^{iv_x\tau}d\tau$$

$$\therefore\quad I(v_x) = \frac{F^2}{2L}\, e^{-T^2v_x{}^2/4g} \int_{-\infty}^{\infty} e^{-g\tau^2/T^2}\,dz$$

$$= \frac{F^2}{2L}\, e^{-T^2v_x{}^2/4g}.\ \sqrt{2\pi}\ \frac{T}{\sqrt{2g}}$$

$$= \frac{TF^2}{2L}\sqrt{\frac{\pi}{g}}\ \exp\ (-v_x{}^2T^2/4g)$$

For Γ_R, $z = R + iy$. Hence $\left| e^{-g\tau^2/T^2} \right|$

$$= \left| e^{-g/T^2(R+iy)^2} \right| = \left| e^{-gR^2/T^2}.\ e^{gy^2/T^2}.\ e^{-2Rygi/T^2} \right|$$

$$= e^{-gR^2/T^2}.\ e^{gy^2/T^2} \to 0 \text{ as } R \to \infty \Rightarrow \int_{\Gamma_R} \to 0$$

Similarly for $\Gamma_{R'}$, $z = -R + iy$. Hence $\left| e^{-gz^2/T^2} \right|$

$$= \left| e^{-gR^2/T^2}.\ e^{+gy^2/T^2}\ e^{2Rygi/T^2} \right| = e^{-gR^2/T^2}\ e^{gy^2/T^2}$$

$$\to 0 \text{ as } R \to \infty \Rightarrow \int_{\Gamma_R'} \to 0.$$

As a test of the inversion theorem take the result for $I(v_x)$ and attempt to recover the Gaussian autocorrelation function:

$$K(\tau) = \frac{1}{2\pi}\int_{-\infty}^{\infty} e^{-iv_x\tau}\, T\sqrt{\frac{\pi}{g}}\exp\left(-\frac{v_x^2T^2}{4g}\right)dv_x$$

$$= \frac{1}{2\pi}\, T\sqrt{\frac{\pi}{g}}\int_{\infty}^{\infty}\exp\left(-\frac{v_x^2T^2}{4g}\right)\cos\left(v_x\tau\right)dv_x$$

$$= \frac{1}{2\pi}\, T\sqrt{\frac{\pi}{g}}\,.\sqrt{\pi}.\sqrt{\frac{4g}{T}}\exp\left(-\tau^2g/T^2\right)$$

$$= e^{-g\tau^2/T^2}$$

In the course of deriving $I(v_x)$, $C(\tau) = e^{-\tau^2/T^2}$, was approximated by $1 - \tau^2/T^2$ and so

$$K(\tau) = e^{-g[1 - C(\tau)]} \simeq e^{-g\tau^2/T^2}$$

which is reconciled with the above.

As a second illustration, consider the case of a negative exponential autocorrelation function

$$C(\tau) = e^{-|\tau|/T}.$$

$$I(v_x) = \frac{F^2}{2L}\int_{-L}^{L} e^{iv_x\tau}\, e^{-g[1 - C(\tau)]}d\tau$$

To a first approximation,

$$I(v_x) \simeq \frac{F^2}{2L}\int_{-L}^{L} e^{iv_x\tau}\, e^{-g|\tau|/T}d\tau$$

$$\simeq \frac{F^2}{2L}\left\{\int_{o}^{\infty} e^{iv_x\tau}\, e^{-g\tau/T}d\tau + \int_{-\infty}^{o} e^{iv_x\tau}\, e^{g\tau/T}d\tau\right\}$$

justifying the limits to be $\pm\infty$ as previously.

Note however $\left| e^{\left[iv_x - g/T\right]\tau}\right| = \left| e^{iv_x\tau}\right|\left|e^{-g\tau/T}\right|$

$$= e^{-g\tau/T} \to 0 \text{ as } \tau \to \infty$$

In summary $I(v_x) \sim \frac{F^2T}{Lg}\,\frac{1}{1 + v_x^2T^2/g^2}$, a function which is of the form of the Cauchy distribution in statistics.

Can the Inversion theorem now be used to recover $K(\tau) = e^{-g|\tau|/T}$?

We have $K(\tau) = \frac{1}{2\pi} \int_{\infty}^{\infty} e^{-iv_x\tau} \frac{2T}{g} \frac{1}{1 + v_x^2 T^2/g^2} dv_x$

In particular, $K(0) = \frac{1}{2\pi} \int_{-\infty}^{\infty} \frac{2T}{g} \frac{1}{1 + \frac{v_x^2 T^2}{g^2}} dv_x$

Setting $s = \frac{v_x T}{g}$, we have

$$K(0) = \frac{1}{2\pi} \int_{-\infty}^{\infty} \frac{2T}{g} \frac{ds}{1 + s^2} \frac{g}{T}$$

$$= \int_{-\infty}^{\infty} \frac{1}{\pi} \frac{ds}{1 + s^2} = 1 \text{ , (from property of the}$$

Cauchy p.d.f.) as required.

In general, for the evaluation of $K(\tau)$ we again resort to contour integration techniques.

For $\tau > 0$ we consider the complex function

$$\frac{e^{-i\tau z}}{1 + T^2 z^2/g^2} = \frac{e^{-i\tau z}}{T^2/g^2 (z^2 + g^2/T^2)} = \frac{g^2/T^2 \; e^{-i\tau z}}{(z + ig/T)(z - ig/T)}$$

taken round the contour C_R as shown. There is a simple pole at $z = \frac{-ig}{T}$ within C_R with residue

$$\frac{g^2}{T^2} \frac{e^{-i\tau(-ig/T)}}{-2ig/T} = \frac{-g}{T} \frac{e^{-g\tau/T}}{2i}$$

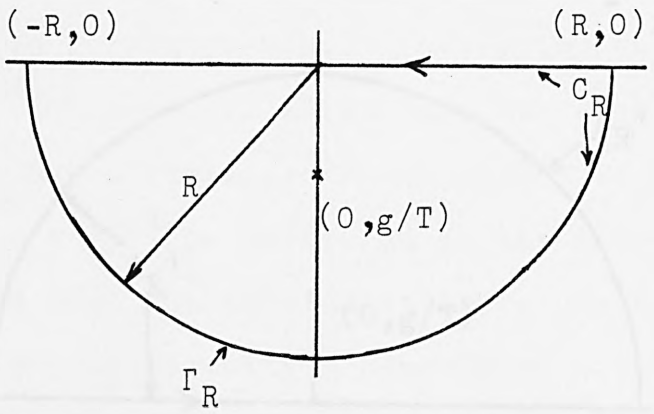

By Cauchy's residue theorem,

$$\int_{C_R} \frac{e^{-i\tau z}}{1 + z^2T^2/g} = 2\pi i \times \frac{-g/T \; e^{-g\tau/T}}{2i}$$

$$\int_{\Gamma_R} \frac{e^{-i\tau z}dz}{1 + z^2T^2/g^2} + \int_{R}^{-R} \frac{e^{-i\tau x}}{1 + x^2T^2/g^2}\,dx = -\frac{\pi g}{T}\, e^{-g\tau/T}$$

Suppose as $R \to \infty$ $\int_{\Gamma_R} \to 0$, then

$$\int_{-\infty}^{\infty} \frac{e^{-i\tau x}}{1 + x^2T^2/g^2}\,dx = \frac{\pi g}{T}\, e^{g\tau/T}$$

$$\therefore \quad K(\tau) = \frac{1}{2\pi} \int_{\infty}^{\infty} \frac{2T}{g} \cdot \frac{e^{-iv_x\tau}}{1 + v_x{}^2T^2/g^2}\,dv_x$$

$$= \frac{1}{2\pi} \cdot \frac{2T}{g} \times \frac{\pi g}{T}\, e^{g\tau/T}$$

$$K(\tau) = e^{g\tau/T} \quad \text{as required.}$$

On Γ_R, $\left| \frac{e^{-i\tau z}}{1 + z^2T^2/g^2} \right| \leq \left| \frac{e^{-i\tau R(\cos\theta + i\sin\theta)}}{T^2/g^2(R^2-1)} \right|$

$$= \frac{e^{\tau R\sin\theta}}{T^2/g^2(R^2-1)} < \frac{1}{T^2/g^2(R^2-1)} \quad (R\sin\theta < 0 \text{ remember})$$

$$\therefore \quad \left| \int_{\Gamma_R} \frac{e^{-i\tau z}}{1 + z^2T^2/g^2} dz \right| \leq \frac{1}{T^2/g^2(R^2-1)} \cdot \pi R \quad \text{and this tends}$$

to zero as $R \to \infty$.

For $\tau < 0$ we consider the same function but taken round C_R'.

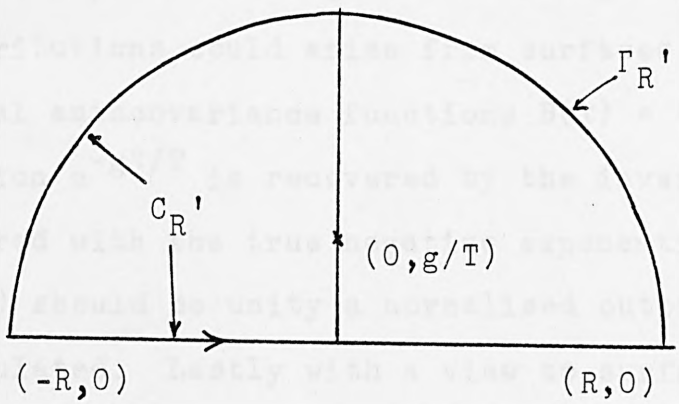

By the residue theorem

$$\int_{C_R'} \frac{e^{-i\tau z}dz}{1 + z^2T^2/g^2} = 2\pi i \frac{g}{T} \frac{e^{\tau g/T}}{2i}$$

$$\therefore \int_{\Gamma_R'} \frac{e^{-i\tau z}dz}{1 + z^2T^2/g^2} + \int_{-R}^{R} \frac{e^{-i\tau x}dx}{1 + x^2T^2/g^2} = \frac{\pi g}{T} e^{\tau g/T}$$

Again if $\int_{\Gamma_R'} \to 0$ as $R \to \infty$, we have

$$\int_{-\infty}^{\infty} \frac{e^{-i\tau x}dx}{1 + x^2T^2/g^2} = \frac{\pi g}{T} e^{\tau g/T} .$$

Thus $K(\tau) = \frac{1}{2\pi} \frac{2T}{g} \cdot \frac{\pi g}{T} e^{\tau g/T} = e^{\tau g/T}$ $(\tau \to o)$.

It remains to verify that $\int_{\Gamma_R'} \to 0$ as $R \to \infty$

On Γ_R' , $z = R\cos\theta + i\, R\sin\theta$ and so

$$\left| \frac{e^{-i\tau z}}{1 + z^2T^2/g^2} \right| \leq \frac{e^{\tau R\sin\theta}}{T^2/g^2(R^2 - 1)} < \frac{1}{T^2/g^2(R^2 - 1)} \quad (\tau < o)$$

$$\therefore \left| \int_{\Gamma_R'} \frac{e^{-i\tau z}}{1 + z^2T^2/g^2} dz \right| \leq \frac{1}{T^2/g^2(R^2-1)} \cdot \pi R \to 0 \text{ as } R \to \infty$$

Simulation Exercise

As a further investigation of inversion, Cauchy type intensity distributions,

$I(x) = \frac{2T/g}{1 + T^2/g^2x^2}$, are generated for different values of the parameter T/g. According to theory remember, such distributions could arise from surfaces having negative exponential autocovariance functions $B(\tau) = \sigma^2 e^{-|\tau|/T}$. The function $e^{-g\tau/T}$ is recovered by the inversion theorem and compared with the true negative exponential values. Since K(0) should be unity a normalised output $K(\tau)/K(0)$ is also calculated. Lastly with a view to surface parameter

estimation applications, T/g is estimated from the intensity data by a least squares routine.

The results show close agreement between $K(\tau)$, as obtained by the inversion algorithm and the true negative exponential values, and validates the least squares parameter extraction procedure.

Input T/g parameter = 20

Lag	Normalised correlation fn.	Neg. exponential model
0	1.00	1.00
3	0.87	0.86
6	0.74	0.74
9	0.53	0.64
12	0.53	0.55
15	0.45	0.47

Least squares. estimate T/g = 20.000

Input T/g parameter = 40

Lag	Normalised correlation fn.	Neg. exponential model
0	1.00	1.00
8	0.81	0.82
16	0.65	0.67
24	0.52	0.55
32	0.40	0.45
40	0.30	0.37

Least squares estimate T/g = 40.000

TABLE 9.B.1. Recovery of correlation function from Cauchy 'intensity' plot with theoretical neg. exponential model

CHAPTER 10

CONCLUSIONS AND SUGGESTIONS FOR FURTHER RESEARCH

10.1 Summary of Research Achievement

The principal conclusion arising from the study, is that the Kirchhoff theory adequately predicts the back scatter from reflective metal surfaces of the order of 0.07-0.5 RMS roughness investigated, if we apply the full two-dimensional treatment. The full model is not merely a refinement of the simpler one-dimensional model, employed to explain short-comings of the one-dimensional model, as was thought to be the case when the project was initiated. Isotropic surfaces required AREA statistics to be input into the model: the one-dimensional model fails to hold.

For the roughness grades specified the scattering is believed to be virtually geometric, although talysurf profile slopes indicate otherwise. Our conclusion is that numerical values of slopes are likely to be substantially too large if the autocorrelation function of surface heights is near negative exponential.

For typical defect-free surfaces $\sim .2\mu m$, the two-dimensional Kirchhoff theory model provided an adequate fit to observation, on the basis of a small representative sample of the surface topography. Furthermore, the fit was not materially improved by the inclusion of the local reflectance properties, and the simplification of perfect conductivity was justifiable. These remarks are important, since the evaluation of the fourth order integral over 100,000 sample heights is a daunting task, and an insatiable user of CPU time. The two-dimensional model captured the broad features of observed intensity curves and indicated

the extent of fine features at the tip of the specular lobe for instance. The diffraction features at the foot of the lobe were exaggerated however.

Scattered intensity showed itself to be sensitive, both to the lay of the surface texture of rolled surfaces, and to the orientation of scratch defects. For defect specimens it is ambitious to hope for a totally adequate prediction, in view of the presence of sharp surface irregularities and the associated problems of shadowing and secondary reflections.

Simple model geometries are deficient in the explanation of the order of observed scattering. It is impossible to relate the position of a 'defect' lobe from a scratch defect for instance, from a talysurf trace record of the scratch. For such a linear defect, the one-dimensional Kirchhoff model provides useful, albeit partial, information. The predicted intensity curve requires a degree of interpretation, but the model appears capable of accurately forecasting the separation of the central lobe from the defect lobe. The accuracy of the prediction of the relative lobe amplitudes is an open question. The relative amplitude not only depends on the size of the scratch, but also its position beneath the laser spot due to the Gaussian profile characteristics of the laser beam. A pair of parallel scratches of different dimensions, can give rise to a 'tiered' structure of intensity. The one-dimensional model suggests the location of the individual tiers.

The project also demonstrates the recovery of certain rough surface parameters and defect measurements. This is not entirely new ground in some instances, but the reliance

on Gaussian statistics, a methodological requirement of several previous analyses, has been relaxed in many of the procedures.

10.2 Areas of Further Research

In the field of optical instrumentation, a rectangular diode array device of small aperture, functioning with incoherent light, ought to be considered. There is considerable scope for research in appraising such an instrument, and in developing suitable computer software, both for decision threshold subroutines for defect detection and classification, and for on-line parameter estimation procedures, which would grade and control the quality of surfaces.

The sensitivity of polar diagrams to the orientation of scratch defects is easily understood. The precise interpretation of near specular polar diagram information should be studied using the one-and two-dimensional Kirchhoff scattering models. The simple one-dimensional model has shown itself capable of locating an adjacent lobe arising from a scratch deformation. On this evidence simulation studies on surfaces bearing scratch or grooved defects, whereby the predicted scatter is computed on the basis of a single profile only, should be performed to investigate how the position and relative amplitude of the 'defect' lobe, varied with the width and depth of the scratch.

The models perform a particularly useful function, since it does not appear possible to link the slopes of profile heights with scatter dispersion directly. We need to resort to a regression technique as in Chapter 7.

The two-dimensional Kirchhoff model performed well in modelling non-defect scatter patterns, but less well in modelling defect scatter patterns. A prime reason is that the disordered nature of defect surfaces exposes limitations in the reference map: the lack of resolution in the across trace direction, together with a lack of precise control over the start up point of each trace, introduces too much error variation. It would be of interest to improve the mapping procedures by utilising the laser application of exact distance measurement. By suitable gearing, a stepping motor could advance an X/Y table so that the same resolution (of the order of 2-3μm), applies in both 'X and Y' directions, whilst a static laser beam could provide an exact start up reference. Having demonstrated the feasibility of using Kirchhoff wave theory models to study defects, and with defect geometries specified more precisely, samples of industrial defects should be mapped and the predicted scatter patterns computed. Such patterns would assist in the interpretation of polar diagrams obtained on-line, and would aid defect detection and classification decision-making.

A useful by-product of this line of research, is a high integrity data base for studies in the area of surface metrology, such as to investigate the relationship of profile parameters to area parameters, or modelling three-dimensional surfaces by spatial time series analysis.

REFERENCES

AMENT, W. S. [1956]
The forward and back scattering from certain rough surfaces.
Trans. I.R.E. AP-4 : 369-373.

AMENT, W. S. [1960]
Reciprocity and scattering by certain rough surfaces.
Trans. I.R.E. AP-8 : 167-174.

BARKER, A. and BROOK, R. [1978]
A design study of automatic systems of on-line detection and classification of defects on cold-rolled steel strip.
Optica Acta 25(12) : 1189-1196.

BECKMANN, P. [1957]
A new approach to the problem of reflection from rough surfaces.
Acta Technica 2(4) : 311-355.

BECKMANN, P. [1959]
The probability distribution of the vector sum of n unit vectors and arbitrary phase distributions.
Acta Technica 4 : 323-334.

BECKMANN, P. and SPIZZICHINO, A. [1963]
The scattering of electromagnetic waves from rough surfaces
(London : Pergamon)

BECKMANN, P. [1973]
Scattering by non-Gaussian surfaces.
IEEE Trans. AP-21 : 169-175.

BENNETT, H. E. and PORTEOUS, J. O. [1961]
Relation between surface roughness and specular reflectance at normal incidence.
J. Opt. Soc. Am. 51 : 123-219.

BERNY, F. [1976]
Optical methods for rough surface measurements.
In : IMEKO PRACTICAL MEASUREMENT FOR IMPROVING EFFICIENCY, 7th, London 1976, preprint BDM-234.

BITZ, G. [1978]
Optical on-line measurement of surface roughness using coherent light.
In : IMEKO MEASUREMENT FOR PROGRESS IN SCIENCE AND TECHNOLOGY, 8th, Moscow 1979, preprint FRG-124.

BORN, M. and WOLF, E. |1975|
Principles of Optics (London and New York : Pergamon)

BROOK, R. [1971]
An experimental automatic surface inspection system
Metron 3(8) : 219-223.

BROWNLEE, K. A. [1965]
Statistical theory and methodology in science and engineering
(London : Wiley).

CHANDLEY, P. J. and WELFORD, W. T. [1975]
A re-formulation of some results of P. Beckmann for scattering from rough surfaces.
Opt. and Quant. Elec. 7 : 393-397.

CHANDLEY, P. J. [1976a]
Surface roughness measurements of coherent light scattering.
Opt. and Quant. Elec. 8 : 323-327.

CHANDLEY, P. J. [1976b]
Determination of the autocorrelation function of height on a rough surface from coherent light scattering.
Opt. and Quant. Elec. 8 : 329-333.

CHANDLEY, P. J. and ESCAMILLA, H. M. [1979]
Speckle from a rough surface when the illuminated region contains few correlation areas: the effect of changing the surface variance.
Opt. Comm. 29(2) : 151-154.

CLARKE, G. M. and BEDFORD, J. [1978]
Laser scanning for defects, dimensions and surface finish.
In: INTERNATIONAL CONFERENCE ON AUTOMATED INSPECTION AND PRODUCT CONTROL, 3rd, Nottingham 1978.

CLARKE, G. M. and THOMAS, T. R. [1980]
Roughness measurement with a laser scanning analyser.
In: INTERNATIONAL CONFERENCE OF METROLOGY AND PROPERTIES OF ENGINEERING SURFACES, 1st, Leicester 1980.

DAINTY, J. C [1970]
Some statistical properties of random speckle patterns in partially coherent illumination.
Optica Acta 17(10) : 761-772.

DAINTY, J. C. [1976]
The statistics of speckle patterns. In: Progress in Optics 14 ed. E. Wolf (Amsterdam, New York: North-Holland)

DERYUGIN, L. N. [1960]
The reflection of a longitudinally polarised plane wave from a surface of rectangular corrugations.
Radiostekhn 15(5).

Du CASTEL, F. and SPIZZICHINO, A, et al [1962]
On the role of the process of reflection in radio wave propagation
J Res. Nat. Bur. Stand. (USA), 66(3): 273-84.

ELSON, J. M. and BENNETT, J. M. [1979]
Relation between the angular dependence of scattering and the statistical properties of optical surfaces.
J. Opt. Soc. Am. 69(1) : 31-47.

ESCAMILLA, H. M. [1978]
Speckle contrast from weak diffusers with a small number of correlation areas.
Optica Acta 25(8) : 777-785

FUJII, H. and ASAKURA, T. [1977]
Effect of the point spread function on the average contrast of image speckle patterns.
Optics Comm, 16:68.

FUJII, H. and LIT, J. W. Y. [1978]
Surface roughness measurement using dichromatic speckle patterns.
App. Opt. 17 : 2690-2694.

FUJII, H, et al [1976]
Measurements of surface roughness properties by means of laser speckle techniques.
Opt. Commun. 16(1) : 68-72.

GEORGE, A. F. and RADCLIFFE, S. J. [1982]
Automated wear measurement on a computerised profilometer.
In: INTERNATIONAL CONFERENCE OF METROLOGY AND PROPERTIES OF ENGINEERING SURFACES, 2nd, Leicester 1980.

GOODMANN, J. W. [1963]
Stanford Electronics Lab. Tech. Report No. 2303-1.

GOODMANN, J. W. [1975]
In: Laser speckle and related phenomena, ed. J. C. Dainty. (Berlin, New York: Springer-Verlag).

GRADSHTEYN, I. S. and RYZIK, I. M. [1965]
Tables of integrals, series and products. (New York: Academic Press).

HARIHARAN, P [1977]
Statistics of speckle patterns produced by a rough metal surface.
Optica Acta 24(9) : 979-987.

HILDEBRAND, B. P. et al [1974]
Instrument for measuring the roughness of supersmooth surfaces.
Appl. Optics. 13(1) : 177-180.

HILL, W. J. [1977]
Defect recognition in automated surface inspection. Ph. D. thesis: The City University, Department of Systems Science.

HORN, [1975]
In: The psycology of computer vision, ed. P. Winston (New York: McGraw-Hill).

JAKEMANN, E. and PUSEY, P. N. [1973a]
The statistics of light scattered by a random phase screen.
J. Phys. A 6(7),: L88-92.

JAKEMAN, E. and PUSEY, P. N. [1973b]
Idem. Phys. Lett. 44A : 456-458.

JAKEMANN, E. and PUSEY, P. N.[1975]
Non-Gaussian fluctuations in electromagnetic radiation scattered by random phase screen. I theory, II application to dynamic scattering in liquid crystal.
Idem. Phys. A8(3). 369-391 : 392-410.

JOHNSON, N. L. and KOTZ, S. [1969]
Discrete distributions (Chichester: Wiley).

JOHNSON, N. L. and KOTZ, S. [1972]
Distributions in statistics : continuous multivariate distributions (New York :Wiley).

KENDAL, M. G. and STUART, A. [1969]
Advanced Theory of Statistics, Vol. 1 (London: Griffin).

KIBBLE, W. F. [1940]
A two-variate gamma type distribution
SANKHYA Ind. J. of Stat. 5 : 137-150.

KOECHNER, W [1976]
Solid-state laser engineering (New York: Springer-Verlag).

LEADER, J. C. [1971]
The relationship between the Kirchhoff approach and small perturbation analysis in rough surface scattering theory.
IEEE trans. AP-19(6) : 786-788.

LEADER, J. C. [1976]
An analysis of the spatial coherence of laser light scattered from a surface with two scales of roughness.
J. Opt. Soc. Am. 66(6) : 536-546.

LEADER, J. C. [1979]
Analysis and prediction of laser scattering from rough surface material.
J. Opt. Soc. Am. 69(4) : 610-627.

LÉGER, D. et al [1975]
Optical surface roughness determination using speckle correlation technique.
Appl. Opt. 14(4) : 872-877.

LONGUET-HIGGINS, M. S. [1957]
The statistical analysis of a random moving surface.
Phil. Trans. Roy. Soc. 1957, A 249, 321.

McKECHNIE, T. S. [1974]
Measurement of some second order statistical properties of speckle.
Optik 39(3) : 258-267.

MILANA, E. and RASELL, F. [1981]
An optical method for on-line evaluation of machined surface finishing.
Optica Acta 28(1) : 111-123.

MILLER, M. G. et al [1975]
Second-order statistics of laser-speckle patterns.
J. Opt. Soc. Am. 65(7) : 779-785

MORAN, P. A. P. [1969]
Statistical inference with bivariate gamma distributions.
Biometrika, 56 : 627-634.

MUNDY, J. L. [1979]
Visual inspection of metal surfaces. In: NATIONAL COMPUTER CONFERENCE, 1979; preprints 227-231.

NORTON-WAYNE, L. [1982]
The detection of defects in automated visual inspection.
Ph. D thesis: The City University Department of Systems Science.

OBRAY, C. D. [1973]
Detection of surface defects by automatic inspection. M.Sc. thesis: The City University, Department of Mathematics.

PARRY, G. [1974]
Some effects of temporal coherence on the first order statistics of speckle.
Optica Acta 21(10) : 763-722.

PARRY, G. [1975]
The scattering of polychromatic light from rough surfaces : first order statistics.
Idem. Opt. Quant. Elect. 7 : 311-318.

PEARSON, K [1914]
Tables for Statisticians and Biometricians, Part 1
(Cambridge : Cambridge University Press).

PEDERSON, H. M. [1976]
Object-roughness dependence of partially developed speckle patterns in coherent light.
Idem. Opt. Commun. 16(1) : 63-67.

PORTER, G. B. and MUNDY, J. L. [1981]
Automatic visual inspection of metal surfaces
SPIE Tech. and App. of Im. Understanding 281 : 176-181.

ROSS, G. and FIDDY, M. A. [1978]
The speckle effect : a reappraisal
Optica Acta, 25(3) : 205-217.

SAWATARI, T. [1971]
Surface flaw detection using oblique angle illumination
Appl. Optics, 11(6) : 1337-1343.

SAYLES, R. S. and THOMAS, T. R. [1976]
Mapping a small area of a surface.
J. Phys. E, Sci. Instrum. 9 : 855-861.

SAYLES, R. S. et al [1977]
Measurement of the surface microgeometry of articular cartilage.
J. Biomech.

SMOLKA, F. M. and CAUDELL, T. P. [1978]
Surface profile measurement and angular deflection monitoring using a scanning laser beam: a noncontact method.
Appl. Optics, 17(20) : 3284 - 3289.

SPRAGUE, R. A. [1972]
Surface roughness measurements using whitelight speckle.
Appl. Opt. 11 : 2811-2816.

STANSBERG, C. T. [1981a]
Surface roughness dependence of the first-order statistics of polychromatic speckle patterns.
Optica. Acta, 28(4) : 471-488.

STANDBERG, C. T. [1981b]
On the first-order probability density function of integrated laser speckle.
Optica Acta, 28(7) : 917-932.

STOVER, J. C. [1975]
Roughness characterisation of smooth machined surfaces by light scattering.
Appl. Optics, 14(8) : 1796-1802.

TANNER, L. H. and FAHOUM, M [1976a]
A study of the surface parameters of ground and lapped metal surfaces, using speckle and diffuse reflection of laser light.
Wear, 36 : 299-316.

TANNER, L. H. [1976b]
The use of laser light in the study of metal surfaces.
Optics and Laser Tech. June 1976 : 113-116.

TANNER, L. H. [1980]
A comparison between talysurf 10 and optical measurements of roughness and surface slope. In: INTERNATIONAL CONFERENCE OF METROLOGY AND PROPERTIES OF ENGINEERING SURFACES, 1st, LEICESTER 1980.

TEAGUE, E. C. et al [1982]
Three-dimensional stylus profilometry. In: INTERNATIONAL CONFERENCE OF METROLOGY AND PROPERTIES OF ENGINEERING SURFACES, 2nd, Leicester 1982.

THOMAS, T. R. [1975]
Recent advances in the measurement and analysis of surface microgeometry.
Wear, 33 : 203-233.

THOMAS, T. R. and SAYLES, R. S. [1978]
Some problems in the tribology of rough surfaces.
Tribology (June 1978) : 163-166.

THWAITE, E. G. [1982]
A quantitative comparison of the wavelength spectrum of a surface obtained by optical Fourier transformation with calculations of profile measurements. In: INTERNATIONAL CONFERENCE OF METROLOGY AND PROPERTIES OF ENGINEERING SURFACES, 2nd, Leicester 1982.

TWERSKY, V [1957]
On scattering a reflection of sound by rough surfaces.
J. Acoust. Soc. Am. 29(2) : 209-255.

WATSON, W. et al [1979]
The machined surface - time series modelling. In: INTERNATIONAL CONFERENCE OF METROLOGY AND PROPERTIES OF ENGINEERING SURFACES, 1st, Leicester 1979.

WELFORD, W. T. [1977]
Review optical estimation of surface roughness from light scattering measurements.
Opt. Quant. Elect. 9 : 269-287.

WHITEHOUSE, D. J. and ARCHARD, J. F. [1970]
The properties of random surfaces of significance in their contact.
Proc. Roy. Soc. A. 316 : 97-121.

WHITEHOUSE, D. J. [1974]
The measurement and analysis of surfaces
Tribology Int., Dec. 1974 : 249-259.

WHITEHOUSE, D. J. and PHILLIPS, M. J. [1978]
Discrete properties of random surfaces.
Phil. Trans. of Roy. Soc. 290.

WHITEHOUSE, D. J. and PHILLIPS, M. J. [1982]
Two dimensional properties of random surfaces
Phil. Trans. of Roy. Soc.

WILLIAMSON, J. B. P. [1968]
Microtopography of surfaces
Proc. Inst. Mech. Eng. 182(3K) : 21-30.

WIRGIN, A. [1975]
Resonance scattering from an arbitrary shaped protuberance on a ground plane.
Optica Acta 22(1) : 47-58.

ADDENDA AND CORRIGENDA